Dynamics of impurities and trapped Bose-Einstein condensates

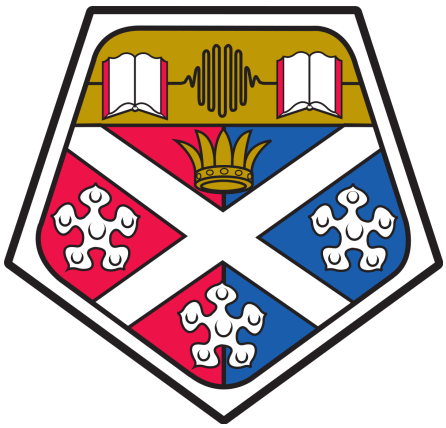

Rosaria Gabriella Lena

Thesis submitted in partial fulfilment of requirements for the degree of
Doctor of Philosophy

University of Strathclyde

Department of Physics and SUPA

June 2020

This thesis is the result of the author's original research. It has been composed by the author and has not been previously submitted for examination which has led to the award of a degree.

Signed:

Date:

Abstract

The high degree of control that exists in experiments with cold atoms, and Bose-Einstein condensates, in particular, allows us to design systems with chosen geometries. These provide us with simple model systems that are well understood from first principles microscopically, and with parameters controlled by external fields, as tools to explore new frontiers in the context of non-equilibrium dynamics. These possibilities can be used for a wide variety of applications, ranging from quantum simulations to quantum metrology. In this thesis, we investigate designing the confinement of tightly trapped impurities in a BEC reservoir to study their dissipative dynamics, and to study non-equilibrium dynamics of BECs confined in a tilted ring trap (both with ultracold atoms and polaritons).

In the first part we explore tightly confined impurities, immersed in a weakly trapped BEC and initially excited in the strongly confined direction, to study cooling of the impurities to low-temperature states under realistic experimental conditions. This scheme, combined with dissipative state engineering, sets the basis for adaption of laser cooling techniques for the production of low-entropy states in quantum simulators. We can also use this system to access non-Markovian dynamics by changing the ratios of relevant timescales using control over the trapping of the impurities and the reservoir.

In the second part we study the dynamics of a BEC confined in a 1D tilted ring trap, both with ultracold atoms and long-lifetime polaritons. We study the collective oscillations of a BEC in a tilted ring trap to characterise the effects generated by the interplay between non-linearities due to anharmonicity and non-linearities due to interactions. In the case of polaritons, we make comparison with experimentally observed features, and gain an understanding of the thermalisation process in such systems.

Contents

Acknowledgements

I would like to thank all the people who supported me during my PhD, but the list would be too long to individually mention everyone.
Foremost, I am extremely grateful to my supervisor Andrew Daley, for giving me the chance to be part of his group, for his kindness, his constant support and for his patience.
Huge thanks go to all the former and current members of the QOQMS group (and CNQO) at the University of Strathclyde that I had the luck to cross paths with.
Special mentions go to Eduardo Mascarenhas and Françcois Damanet, for the motivating and interesting physics and non-physics conversations at both "offices", to Jacopo Surace for always being supportive, and to Jorge Yago, who has been there through all the stages of my PhD, bearing with me during good and bad times for four years.
I am grateful to my friends, especially the ones I met in Glasgow, who made me feel at home. Particular thanks go to Leire Elzaurdia and to my flatmate Alessia Abbati, who also contributed to keep me somehow sane during a lockdown, in extraordinary times.
Last but not least, the biggest thanks go to my parents Mario and Lidia, who made this possible with their unconditional support and love, and to my brothers Antonino, Ersilia and Daniele. I dedicate this thesis to my family.

Thank you all,
Rosaria Lena

Chapter 1

Introduction

The Bose-Einstein Condensate (BEC) phase, a macroscopic quantum state of matter, was theorised by Bose and Einstein in 1924 [1, 2]. This consists of the prediction that, when the thermal de Broglie wavelength of a gas of bosons is comparable to the interparticle spacing, the gas undergoes a transition where a large fraction of bosons occupy the lowest-energy single-particle state, forming a matter wave. This allows the observation of microscopic quantum phenomena, such as wavefunction interference, on a macroscopic scale.

The formation of Bose-Einstein Condensation of weakly interacting dilute gases of alkali atoms was achieved in 1995 with ^{87}Rb [3], ^{23}Na [4] and ^{7}Li [5, 6], obtaining densities of $\sim 10^{13} - 10^{15}$ cm^{-3} and temperatures of the order of nK. This was possible thanks to the progress in both theoretical studies and experimental techniques for trapping and cooling of atoms [7], with methods such as laser cooling [8–10], evaporative cooling [11] and later on sympathetic cooling for BEC mixtures [12–14]. Following experimental realisations of BECs, besides alkali atoms, now include a wide variety of alkaline-earth and lanthanide atoms.

In the last few decades we have witnessed remarkable progress in the field of ultracold many-body quantum systems, strongly motivated by the fact that, because of the exceptional control over their implementation, these experimental platforms can be used as quantum simulators [15–17]. This means that a wide range of Hamiltonians can be engineered using ultracold atoms, to simulate other more complex quantum

and many-body models, such as systems related to strongly interacting electrons in condensed matter physics [18].

This progress was made possible also thanks to the available experimental tools for probing and manipulating cold atoms, which offer unique opportunities in the study of the time dependent out-of-equilibrium dynamics. In fact, appropriate engineering of optical and magnetic fields leads to the possibility to create a wide variety of configurations and geometries for the motion and trapping potentials of the atoms, accessing different dimensionalities, and it also makes it possible to tune and control relevant parameters such as the interaction strength between the atoms, via either optical or magnetic Feshbach resonances [19, 20].

This high tunability, both for the engineering of the trapping potentials and the interaction strength, relies on the fact that we can build microscopic models from first principles. The diluteness of cold atoms allows to model their interaction with scattering theory, based on an effective interaction that we can describe, in the low energy limit, with s-wave scattering. This makes it possible to control the interaction strength, either attractive or repulsive, by changing a single parameter, the scattering length. The realisation of traps for neutral atoms, on the other side, is achieved with magnetic fields and with laser beams that generate a spatial dependent intensity profile for the potential. The physical origin of the neutral atoms confinement by laser fields is determined by the AC-Stark shift that the atoms experience in the off-resonant laser field having a frequency larger than the recoil energy of the atoms. Changing the detuning between the laser frequency and the atomic frequency (determined by the difference in energy between its ground and excited state), we can create potentials that are attractive (for red detuning) or repulsive (for blue detuning) for atoms, so they sit respectively on the maxima or minima of the intensity profile. With this possibility, combining lasers with different orientations, allows to construct a rich variety of trapping potentials.

These experimental opportunities have made it possible to realise different trapping potentials where the dynamics of cold atoms can be restricted to desired dimensions, by engineering the trapping frequencies along the different directions. Disk shaped trapping potentials can be obtained by tightening the confinement in one dimension,

resulting in an effective dynamics in 2D. Similarly, cigar shaped configurations, realised with tight confinement along two directions, lead to the realisation of an effective 1D system. Other potentials inlcude toroidal traps [21–23] and optical lattices, which allow to study many-body physics and can be used to probe the Mott insulator to superfluid phase transition [24], but also to realise bosonic Josephson junctions with double-well potentials [25, 26].

On top of that, recently, the development of quantum gas microscopes [27, 28] have made it possible to achieve an improved single-atom resolution in cold atom experiments. This provides further control of the trapping and addressing of individual atoms in lattice sites.

Being able to control the dimensionality of the system, under appropriate conditions, also makes it possible to explore different phases of the BEC. For instance, this allows us to observe long-range order features in weakly interacting BEC in 3D geometrical confinements, but also leads to the possibility to observe other exotic states beyond the mean-field regime in lower dimensions, such as the Berezinskii-Kosterlitz-Thouless (BKT) superfluid in 2D [29] and bosonic Luttinger Liquids in 1D with Tonks-Girardeau gases [30], achieved with strong interactions between the atoms.

On the other side, tuning atom-atom interactions and engineering particular geometries for trapping atoms is of interest in the context of "atomtronics" [31, 32] for the development of quantum technologies and quantum devices for measurement and sensing, as well as quantum computation. The idea behind this is to use the coherent flow of a trapped Bose gas and its analogy to solid-state platforms to obtain cold atom analogues of electronic devices, such as diodes and transistors, using the transport properties of ultracold atoms instead of electrons. It has been shown for example, how atom transistors can be engineered using ultracold atoms in double-well [33, 34] and triple-well potentials [35], or in few lattice sites coupled to multiple reservoirs, for which open quantum system descriptions can be used to study the transport properties [33, 36]. In this context, spin impurities have also been shown to be powerful tools in the control of the transport between different subsystems [37, 38]. Other examples of atomtronics systems consist in the realization of analogues of diodes [39, 40] and atomtronic cir-

cuits using ring shaped trapping potentials [41–43]. Ring traps interrupted by weak links offer also valid platforms for the realisation of atomtronics analogues of SQUIDs (Superconducting Quantum Interference Devices) [42, 44–48].

Motivated by all these possibilities in the progress of quantum technologies, in this thesis we dedicate particular attention to the study of impurities in superfluid reservoirs and the dynamics of BEC in ring potentials, both with cold atoms and with exciton-polariton condensates, which offer another possible platform for the study of superfluidity and condensation in solid state systems [49], complementing ultracold gases.

Neutral impurities in Bose-Einstein Condensates

Since the first experimental realisation of a BEC mixture with two different spin states of ^{87}Rb [12], obtained through sympathetic cooling of one hyperfine state in contact with another cooled state, there has been significant progress in the realisation of other two-component BECs, including mixtures of dual atomic species. Examples of these include Bose-Bose [13, 50], Fermi-Fermi [51, 52] and Bose-Fermi mixtures [53–56]. One of the interesting features in the study of two-component BECs is given by the phase separation determined by the inter-species interaction strength, with the possibility to observe miscibility and immiscibility of the two species [57, 58], with spatial overlap or separation.

Among the mixtures, the Bose-Fermi case is particularly interesting because it merges systems with different statistics, giving rise to new physics that is not accessible in the case of Bose-Bose and Fermi-Fermi gases, such as new phases for mixtures in optical lattices [59]. In these systems, different interesting scenarios can be explored by tuning the interaction strength of the fermionic part from the non-interacting limit, where the Pauli exclusion principle dominates the behaviour of the dynamics, to the strongly correlated regime, where the crossover to the BCS-like superfluid can be accessed, and study the effects that its statistics have on the dynamics.

The realisation of mixtures with Fermi atoms trapped in optical lattices [60, 61] offered

new possibilities also for the achievement of individually trapped impurities [62–65]. The study of single impurity dynamics mediated by the interaction with a many-body reservoir is a central problem in condensed matter physics, therefore the study of this, especially with fermionic species, in a superfluid reservoir, is interesting with both coherent and dissipative dynamics. From the study of the dynamics of impurities in a lattice in contact with a superfluid reservoir, it was shown how the phononic bath can induce decoherence [66, 67] and mediate the interaction between two or more impurities [68].

For strong interactions between the BEC and the impurity, studies of polarons (impurities strongly interacting with the superfluid reservoir and therefore dressed by the phonon modes) have been conducted for both coherent and incoherent dynamics, in the weakly interacting limit, using a Fröhlich's polaron Hamiltonian [69, 70], and also in the strong coupling limit, beyond the mean-field regime [71, 72].

On the other side, the study of dissipative dynamics for atoms in optical lattices has led to developments in cooling techniques, providing possibilities to control unwanted heating [73–78]. In the case of a single trapped impurity, dissipative dynamics can be used to reach cooling to its motional ground state [79] with a sympathetic cooling mechanism, without affecting the internal degrees of freedom under appropriate conditions. This mechanism is analogous to the spontaneous emission of a two-level atom coupled to the vacuum mode of the light field, but relies instead on the coupling to the quasi-particles of the BEC that leads to the relaxation of the motional states of the impurity through the spontaneous emission of Bogoliubov excitations [64, 79, 80]. Beyond that, for atoms in a lattice, cooling within a Bloch band can be obtained through the application of dark-state laser cooling, which can be achieved combining this dissipative dynamics with dissipative state engineering of dark-states [81, 82]. In dual species experiments with bialkali atoms, these cooling processes are contrasted by the collisions between atoms in the higher Bloch band. However, the realisation of mixtures with Alkali atoms and Alkaline-Earth-Metal [54, 63, 83, 84], in particular with spin-polarised fermions, allows the suppression of collisions within the lattice, leading to a preservation of coherence and to dissipative processes induced by the coupling of

the atoms between the Bloch bands. This offers new perspectives in the development of novel cooling methods, and motivated us to study the dissipative dynamics of impurities with trapping confinements in different dimensions, extending the single atom cooling scheme considered for an impurity trapped in a 1D harmonic potential and immersed in a reservoir [79]. In Chapter 4 we will discuss the case of harmonically trapped impurities in a 3D configuration with tight confinement along one direction and in a harmonic trap with anisotropic tight confinement along two directions, giving an effective 2D configuration with weak confinement in one direction, analogous to a cigar shaped trap. We extend these studies also to the case of a cluster of impurities in a harmonic trap. These calculations, especially for the 2D configuration with tight trapping along one direction, are relevant in the perspective of achieving dark-state cooling within a Bloch band, as the transitions between motional states in the tightly confined directions can be mapped into the coupling to different Bloch bands.

Other possibilities for the study of this kind of system come from investigating impurities in a BEC reservoir, in the context of reservoir engineering [85]. It has been shown, for instance, how a non-Markovian superfluid reservoir can be used to control the entanglement between two impurities [86]. This has applications in quantum information protocols and quantum computing, involving preparation of qubits and entanglement [87], but the study of impurities has also shown to be a potentially valuable tool for probing the BEC [88, 89], for instance with non-demolition thermometry [90–92]. Due to the high control that we have on the trapping geometry of the reservoir, non-Markovian dynamics can be studied by tweaking the interaction strength of the impurity with the BEC, going to the strong coupling limit, by changing the trapping confinement of the impurity, as we show in Chapter 5, or changing the size of the reservoir, which can have implications such as coupling to few modes and backflows of information due to edge effects.

Motivated by these possibilities, and by experimental success in creating two-component Bose gases in particular structured geometries, such as in ring potentials [93], a study of impurities immersed in BEC with particular confinements that go beyond the case of a homogeneous gas, or harmonic trapping, can be a very powerful resource in the context

of reservoir engineering, to explore new physics determined by the specific confinement of the BEC. In fact, as the excitation spectrum of the Bogoliubov excitations depends on the form of the trapping potential, the dynamics of impurity atoms, as well as the memory effects of the reservoir [94], are affected by different confinements [95, 96]. From this perspective, studying the collective excitations of a BEC in anharmonic traps and tilted ring traps, to understand the features determined by the particular geometry, is essential to understand how these can affect the dynamics of impurities and lead to observations of new physics.

Dynamics of trapped BEC

As discussed in the previous section, the study of BECs in different trapping potentials offers a plethora of possibilities for the study of many-body physics and out-of-equilibrium dynamics with useful applications for quantum computing and the development of quantum technologies. From this perspective, the study of the elementary excitations of a trapped BEC is important to develop an understanding of the effects that both the interactions and the confinement in different configurations have on the dynamics of the system.

Since the observation of BEC, the study of low-lying collective excitations, both theoretically [97–104] and experimentally [105–107] has been one of the most natural ways to characterise the superfluidity and the effects that the interaction between the atoms have on the dynamics and on the thermodynamic properties of the BEC.

Experimentally, the observation of the dynamics of the system in real time is made possible by the fact that the trapping frequencies are in the range of ∼Hz-kHz, corresponding to dynamical time scales below the typical lifetimes (of the order of seconds) of the trapped atomic gases.

From a theoretical point of view, the static and dynamical proprerties of weakly-interacting trapped BECs can be described with a mean-field description provided by the Gross-Pitaevskii Equation [108].

The ability to change the confinement in different directions allowed these studies in both spherically symmetric harmonic traps [97] and in axially symmetric harmonic po-

tentials, In the latter case it was observed how the trap anisotropy, the symmetry of the system and the interaction strength change the excitation modes of a perturbed condensate [105, 107]. Probing the dynamics of the system in axially symmetric harmonic trap is particularly interesting especially in the cigar-shaped configuration. Here in fact, by changing parameters such as the anisotropy, the density and the interaction strength, one can explore transitions between different phases, such as a 3D cigar shape (with a wavepacket in the Thomas-Fermi approximation radially), 1D mean-field, and a Tonks-Girardeau gas. One of the ways used to characterise the frequency of the low-lying modes experimentally consists of driving the condensate out of equilibrium, for instance shaking it via modulation of the trapping magnetic fields, then letting it evolve for a variable time and finally switching the potential off to obtain the image of the condensate after a given time [105].

Among the most important features observed in the probing of the collective excitations of trapped BECs is the shift of their frequency modes, determined by the interaction that gives rise to non-linearity and by the geometry of the system [97–99, 103, 105, 106, 109–112]. Theoretically, however, finding analytical solutions for these is not an easy task and most of the approaches used consist in solving the hydrodynamic equations [97, 103, 109–111]. The limitation of this approach, however, is that the hydrodynamic approximation considered in these works is valid in the local density approximation and therefore for a large number of atoms. Other possibilities are offered by numerical methods, either for the solution of the equations obtained from the Bogoliubov-Hartree theory [102], or for the simulation of the dynamics with a time-dependent Gross-Pitaevskii Equation.

Previous studies of collective excitations were mainly conducted for harmonic trapping potentials in both isotropic and anisotropic conditions, and less attention has been given to the characterisation of collective oscillations in anharmonic trapping potentials. However, the interest in these is now increasing, motivated for instance by experiments that use tilted ring traps [22, 113], both with cold atoms and with exciton-polariton BEC [114]. The attention directed to the study of BEC in toroidal geometric potentials (both flat and tilted) increased drastically in the last two decades, leading to

the achievement of neutral atom storage in ring traps [21–23, 115, 116]. These constitute promising platforms for applications in quantum metrology and sensing, because of the possibility to use them for Sagnac atom interferometry [117–119], but also in quantum computing. As previously mentioned, the achievement of stable persistent flow in the rings [23, 45] makes these platforms good candidates for atomic circuits in the context of atomtronics and for possible implementations of qubits [120].

For the study of the dynamics of BEC in tilted ring potentials, and more generally in anharmonic traps, more fundamental questions on the investigation of the non-linear dynamics arise, as a result of the mixing between two kind of non-linearities having different origins: one is given by the anharmonic part of the potential, as in the case of the quantum pendulum for a single particle, and the other one is determined by the interaction between the particles. Furthermore, the presence of periodic boundary conditions in the ring gives rise to other features, such as interference, when the rotational motion around the ring leads to interaction between the tails of the condensate.

It is therefore important to gain a detailed understanding of the aforementioned contribution to the non-linearity, studying the induced dynamics of BECs in this geometry, and individuating features that do not appear for the harmonic potential trapped dynamics. These include, for instance, the frequency shift of the dipole mode (unaffected by the interaction within the BEC in the harmonic potential case, where the center of mass motion is decoupled from the internal excitations), and changes in the collapse and revivals of the density in time [121, 122]. All these features will be subject of further discussions in Chapter 6.

These studies allow us also to have insights on the excitation spectrum in this kind of geometry, which, as mentioned in the previous section, is needed for the possibility to study impurity atoms in BECs confined in ring traps, as we have stressed how the geometry and dimensionality of the system affect these.

1.1 Thesis Outline

In this section we present an overview of this thesis, which is divided into three parts. In the first part, Chapters 2-3, we discuss some background concepts on cold atoms and open quantum systems, which provide a basis for the research presented here. In the second part (Chapter 4-5) we study a system of impurities in a BEC, for two different purposes: to study the cooling rates induced by dissipative dynamics of the impurities trapped in different geometries, and to investigate the effects of a non-Markovian environment on it. In the third part (Chapter 6 and 7) we study the dynamics of BECs in a tilted ring potential, motivated by current experiments in both exciton-polariton and cold-atom platforms. Finally, in Chapter 8 we summarise the main conclusions of the research presented in this thesis, as well as some final remarks on the outlook and future possible work. In the following we give more specific details about the content of each chapter.

In Chapter 2 we give an overview of the background in the field of weakly interacting Bose-Einstein condensates, focusing on a mean-field description that we used for the studies reported in this thesis. In particular, we derive the Bogoliubov excitation spectrum, which we use in the context of trapped impurities to describe the superfluid reservoir. Depending on their momentum, Bogoliubov excitations can have the character of phonon-like or particle-like excitations. The other topic we cover is the Gross-Pitaevskii equation and its derivation, as we use it in the description of the dynamics of a BEC in the harmonic oscillator and ring potentials. Based on the mean-field approximation, this can be thought of as a Schrödinger equation with a non-linear term consisting of the interaction term generated by the scattering between the atoms in the BEC.

In Chapter 3 we introduce some concepts in the theory of open quantum systems, such as the master equation in the Lindblad form, giving an overview of its derivation in order to explain the main approximations, used to describe the system of impurities

coupled to the superfluid reservoir in the following chapter. We also give a brief description of the Monte-Carlo wavefunction method, as this is used in Chapter 4 to describe the induced dissipative dynamics of a cluster of impurities with stochastic methods using trajectories.

In Chapter 4 we present results published in [123]. Here, motivated by the possibilities provided by sympathetic cooling techniques discussed above, together with opportunities to achieve dark-state cooling of impurities in an optical lattice, we study the dissipative dynamics of neutral atoms in different trap geometries, and immersed in a 3D superfluid gas. We extend previous studies [79] that considered the sympathetic cooling of a single impurity trapped in a 1D harmonic potential, and study the cooling and reheating rates for the cases of impurities trapped in a 3D harmonic potential tightly confined in one direction, and in a harmonic trap tightly confined in two directions, with a quasi-one dimensional cigar shape geometry where we consider two available modes in the radial direction. The latter case is of particular relevance in the context of laser dark-state cooling for atoms in an optical lattice, as the coupling with the tight confined direction can be mapped to the coupling between different Bloch bands.

In Chapter 5 we consider the system of an impurity in a BEC and the ability to tune the trapping parameters of both the impurity and the BEC potentials, in order to access non-Markovian regimes by changing the trapping frequency of the impurity immersed in a one-dimensional BEC. This produces different ratios between the timescales of the system relaxation and of the bath correlations, which leads to the emergence of non-Markovian effects with backflow of information to the system. Preliminary results shown in this chapter pave the way to a variety of studies where reservoir engineering can be used to access non-Markovian dynamics.

In Chapter 6 we study the dynamics of a wavepacket in a one-dimensional anharmonic tilted ring trap, characterising the frequencies of the low-lying modes by looking at the

oscillations of the BEC density for small angles around the bottom of the ring, and comparing them with those obtained for the same kind of dynamics in harmonic potentials, for different values of the interaction strength. We characterise the difference between the dynamics in the two kinds of potentials in different initial configurations and compare, for each of them, results obtained from both numerical and analytical or semi-analytical approaches for the frequency shifts generated by the non-linearities.

In Chapter 7 we describe the dynamics of exciton-polariton condensates in a tilted microcavity ring, motivated by recent experiments in the group of David Snoke at the University of Pittsburgh [124], where particularly long polariton lifetimes have been achieved. Aiming to describe the features observed experimentally, we simulate the out-of-equilibrium dynamics of the condensate with a modified GPE that includes a generation and a dissipation term, accounting for the creation of polaritons and their finite lifetime. Furthermore, we consider the effect of interactions with an excitonic reservoir on the dynamics of the polaritons, and account for the relaxation due to this with the introduction of a phenomenological term in the GPE.

We conclude in Chapter 8 with an overview of the key findings discussed in this thesis, together with some possible interesting future directions of these studies.

1.2 Contributions during the PhD

1. S. Mukherjee, D. M. Myers, R. G. Lena, B. Ozden, J. Beaumariage, Z. Sun, M. Steger, L. N. Pfeiffer, K. West, A. J. Daley, and D. W. Snoke, *Observation of nonequilibrium motion and equilibration in polariton rings*, Phys. Rev. B 100, 245304 (2019)

2. R. G. Lena and A. J. Daley, *Dissipative dynamics and cooling rates of trapped impurity atoms immersed in a reservoir gas*, Phys. Rev. A 101, 033612 (2020)

3. R. G. Lena and A. J. Daley, *Collective oscillations of a BEC in a tilted ring*, in preparation

Conference talk presentations

- *"Cooling of impurity atoms in a 2D lattice by a reservoir gas"* QuProCS II workshop, Palma De Mallorca (April 2017)

- *"Cooling of impurity atoms in different dimensions by a reservoir gas"* Quantum Emitters in Non-Conventional Baths, Garching (January 2019)

- *"Cooling of neutral impurities in different dimensions by a reservoir gas"* Polaron Day, Vienna (May 2019)

- *"Induced dissipative dynamics and cooling of impurities by a reservoir gas"* QUISCO Meeting, Edinburgh (April 2019)

- *"Cooling of neutral impurities in different dimensions by a reservoir gas"* SUPA Annual Gathering, Glasgow (May 2019)

Chapter 2

Weakly interacting Bose gas

2.1 Introduction

In this chapter we aim to introduce some of the main concepts that we use in the following chapters, in the context of superfluid reservoirs with trapped impurities in Chapter 4-5 and out-of-equilibrium dynamics of BECs in trapping potentials, in Chapter 6-7. For a broader overview of BECs, see [108, 125].

This chapter is organised as follows. We start by giving some general background about Bose-Einstein condensates, introducing their properties to give a brief overview on how the scales of the physical quantities compare in these systems, treating the most simple case of a 3D homogeneous weakly interacting dilute gas. We then derive the Bogoliubov excitation spectrum of a homogeneous BEC in a box potential and the Gross-Pitaevskii equation, which we use to describe the dynamics of weakly interacting trapped gases.

2.2 Bose-Einstein Condensation

Bose-Einstein Condensation is a macroscopic phase transition a system of bosons undergoes when the interparticle distance $d = n^{-1/3}$ (where $n = N/V$ is the average density of N atoms in a volume V) is of the same order of magnitude as the de Broglie wavelength

$$\lambda_{dB} = \sqrt{\frac{2\pi\hbar^2}{mk_BT}}, \tag{2.1}$$

where m is the mass of the atom, k_B is the Boltzmann constant and T is the temperature of the system. This condition, for a very weakly interacting gas of identical bosons in a 3D box potential, is found for temperatures below

$$T_c \approx \frac{2\pi\hbar^2}{k_B m}\left(\frac{n}{2.612}\right)^{2/3}, \tag{2.2}$$

which is the critical temperature, below which the lowest single-particle energy state is macroscopically occupied and Bose-Einstein Condensation occurs. The number of particles in the condensate, for this, is given by

$$N_0(T) = N\left[1 - \left(\frac{T}{T_c}\right)^{3/2}\right], \tag{2.3}$$

with N the total number of particles. This result is valid for a 3D box potential but varies for different trapping geometries and dimensions. For a 3D harmonic potential, for example, this is $N_0(T) = N\left[1 - \left(\frac{T}{T_c}\right)^3\right]$ [126].
In this chapter we discuss weakly interacting BECs. By this we mean that the range of atom-atom interaction force r_a satisfies the relation

$$r_a \ll n^{-1/3}, \tag{2.4}$$

which also implies that interactions of three or more particles can be neglected. Furthermore, as the distance between the atoms is much larger than the effective range of the interparticle potential, the interactions of the atoms can be described by their scattering amplitude. The condition of condensation is that the temperature of the gas is below T_c. As this is achieved for $\lambda_{dB} \sim n^{-1/3}$, from Eq. (2.4) we obtain the inequality $r_a \ll \lambda_{dB}$, which in terms of the momentum of the atoms $p = 2\pi\hbar/\lambda_{dB}$ can be rewritten as

$$\frac{r_a p}{2\pi\hbar} \ll 1. \tag{2.5}$$

The consequence of this relation is that the energy of the particles is so low that it is sufficient to consider an s-wave scattering potential, with the advantage that the interaction strength can be defined by the a single parameter, the scattering length a,

which determines the interaction range r_a defined here. Therefore Eq. (2.4) reduces to the diluteness condition[1]

$$n|a|^3 \ll 1, \tag{2.6}$$

where $n|a|^3$ is often referred to as the gas parameter.

2.3 Bogoliubov excitation spectrum

We use now the field operators $\hat{\psi}$ to describe the many-body Hamiltonian

$$\hat{H} = \int d^3r \hat{\psi}^\dagger(\mathbf{r}) \left[-\frac{\hbar^2}{2m}\nabla^2 + V_{ext}(r) \right] \hat{\psi}(\mathbf{r}) + \frac{1}{2}\int d^3r \int d^3r' \hat{\psi}^\dagger(\mathbf{r})\hat{\psi}^\dagger(\mathbf{r'})V(\mathbf{r}-\mathbf{r'})\hat{\psi}(\mathbf{r})\hat{\psi}(\mathbf{r'}), \tag{2.7}$$

where V_{ext} is the external potential, which in the following of this section we can neglect (but we use it in the next section for the Gross-Pitaevskii Equation), as we are considering the case of a box trap, where the condensate can be considered homogeneous, and $V(\mathbf{r}-\mathbf{r'})$ is the interaction potential between the atoms. In order to be able to use perturbation theory to describe the interaction with the s-wave, it is convenient to substitute $V(\mathbf{r}-\mathbf{r'})$ with an effective pseudopotential V_{eff}, due to the fact that the form of the real potential at short distances does not allow it to be treated perturbatively. The idea to use a pseudopotential, introduced by Fermi [127], is that if we are interested in the long-range behaviour of the wavefunction, we do not need to get the correct details of the potential in the short-range. Therefore we can simplify the model by considering a simple pseudopotential that has the same behaviour at long range and the specific form of the potential does not really matter, as long as it gives rise to the same scattering amplitude, described by the scattering length a.

Moving to momentum operators description by means of the Fourier transform, we can write the field operator as

$$\hat{\psi}(\mathbf{r}) = \frac{1}{\sqrt{V}} \sum_{\mathbf{p}} e^{i\mathbf{p}\cdot\mathbf{r}/\hbar} \hat{a}_{\mathbf{p}}, \tag{2.8}$$

where $\hat{a}_{\mathbf{p}}$ are the bosonic annihilation operators for a particle with momentum p. For the Fourier transform of the effective potential, considering only the $p = 0$ momentum

[1] This is however not true near Feshbach resonances.

justified by the fact that only small momenta are involved, we have

$$V_0 = \int d^3 r V_{\text{eff}}(\mathbf{r}). \tag{2.9}$$

Eq. (2.7) then reduces to

$$\hat{H} = \sum_{\mathbf{p}} \frac{p^2}{2m} \hat{a}_{\mathbf{p}^\dagger} \hat{a}_{\mathbf{p}} + \frac{V_0}{2V} \sum_{\mathbf{p}_1, \mathbf{p}_2, \mathbf{q}} \hat{a}^\dagger_{\mathbf{p}_1+\mathbf{q}} \hat{a}^\dagger_{\mathbf{p}_2-\mathbf{q}} \hat{a}_{\mathbf{p}_1} \hat{a}_{\mathbf{p}_2}. \tag{2.10}$$

We apply now the Bogoliubov approximation

$$\hat{a}_0 = \sqrt{N_0}, \tag{2.11}$$

which captures the assumption that the ground state is macroscopically occupied and the occupation of other states can be treated perturbatively, describing it as fluctuations to the mean-field. This approximation is valid under the condition that the average range of the the real and effective potentials is much smaller than the interparticle average distance $n^{-1/3}$ (i.e. for a dilute gas). In this case we can use the effective potential and remove the potential problems for the applicability of the perturbation theory.

Starting from Eq. (2.10), we now calculate the ground state energy and then consider corrections to this, determined by a perturbation theory to the first order in the fluctuations. When considering only the contribution coming from the ground state occupation ($p = 0$) in Eq. (2.10), using the Bogoliubov approximation Eq. (2.11), we find the ground state energy

$$\hat{H} = \frac{g}{2V} \hat{a}_0^\dagger \hat{a}_0^\dagger \hat{a}_0 \hat{a}_0 = \frac{V_0 N_0^2}{2V} \tag{2.12}$$

$$E_0 = \frac{N^2 V_0}{2V} = \frac{N^2 g}{2V} = \frac{4\pi\hbar^2 a}{2mV} N^2 = \frac{1}{2} N n g, \tag{2.13}$$

where $n = N/V$ is the density, and where we defined the interaction as

$$V_0 = g = 4\pi\hbar^2 a/m, \tag{2.14}$$

as a result of the Born approximation on the effective potential, which holds for weak interactions and when we assume the macroscopic occupation of the ground state. When considering occupation beyond the mean-field approximation, however, this term has corrections that depend on p and takes the form

$$V_0 = g\left(1 + \frac{g}{V}\sum_{p\neq 0}\frac{m}{p^2}\right). \tag{2.15}$$

The divergence for large momentum of this term comes from the fact that in the Fourier transform of the effective potential (Eq. (2.9)) we considered only the contributions with zero momentum. The correction of Eq. (2.15) is however important as it changes the ground state energy and ensures this is a convergent quantity.

Including fluctuations in Eq. (2.10), and therefore the terms with $\mathbf{p} \neq 0$, we obtain

$$\hat{H} = \frac{V_0}{2V}\hat{a}_0^\dagger\hat{a}_0^\dagger\hat{a}_0\hat{a}_0 + \sum_{\mathbf{p}}\frac{p^2}{2m}\hat{a}_{\mathbf{p}}^\dagger\hat{a}_{\mathbf{p}} + \frac{V_0}{2V}\sum_{\mathbf{p}\neq 0}(4\hat{a}_0^\dagger\hat{a}_{\mathbf{p}}^\dagger\hat{a}_0\hat{a}_{\mathbf{p}}^\dagger + \hat{a}_{\mathbf{p}}^\dagger\hat{a}_{-\mathbf{p}}^\dagger\hat{a}_0\hat{a}_0 + \hat{a}_0^\dagger\hat{a}_0^\dagger\hat{a}_{\mathbf{p}}^\dagger\hat{a}_{-\mathbf{p}}^\dagger), \tag{2.16}$$

where the terms containing only one particle having non zero momentum have been neglected as they do not guarantee the conservation of momentum.

Here we can still use the Bogoliubov approximation of Eq. (2.11), implying $N \approx N_0$, however, in the first term we have to take particular care as the this approximation does not include the terms that are second order in $\hat{a}_{\mathbf{p}}^\dagger$ and $\hat{a}_{\mathbf{p}}$, with $p \neq 0$. Therefore, we have to renormalize the population by imposing the condition

$$N = \hat{a}_0^\dagger\hat{a}_0 + \sum_{\mathbf{p}\neq 0}\hat{a}_{\mathbf{p}}^\dagger\hat{a}_{\mathbf{p}} = N_0 + \sum_{\mathbf{p}\neq 0}\hat{a}_{\mathbf{p}}^\dagger\hat{a}_{\mathbf{p}}. \tag{2.17}$$

Neglecting higher order terms, this gives

$$\hat{a}_0^\dagger\hat{a}_0^\dagger\hat{a}_0\hat{a}_0 = N^2 - 2N\sum_{\mathbf{p}\neq 0}\hat{a}_{\mathbf{p}}^\dagger\hat{a}_{\mathbf{p}}. \tag{2.18}$$

Replacing this result, together with Eq. (2.15) in Eq. (2.16), we obtain the Hamiltonian

in the form

$$\hat{H} = \frac{gN^2}{2V} + \sum_p \frac{p^2}{2m}\hat{a}^\dagger_{\mathbf{p}}\hat{a}_{\mathbf{p}} + \frac{gn}{2}\sum_{\mathbf{p}\neq 0}\left(2\hat{a}^\dagger_{\mathbf{p}}\hat{a}_{\mathbf{p}} + \hat{a}^\dagger_{\mathbf{p}}\hat{a}^\dagger_{-\mathbf{p}} + \hat{a}_{\mathbf{p}}\hat{a}_{-\mathbf{p}} + \frac{mgn}{p^2}\right). \tag{2.19}$$

This Hamiltonian can be diagonalised by using the Bogoliubov transformations

$$\hat{a}_{\mathbf{p}} = u_{\mathbf{p}}\hat{b}_{\mathbf{p}} + v_{\mathbf{p}}\hat{b}^\dagger_{-\mathbf{p}} \tag{2.20}$$

$$\hat{a}^\dagger_{\mathbf{p}} = u_{\mathbf{p}}\hat{b}^\dagger_{\mathbf{p}} + v_{\mathbf{p}}\hat{b}_{-\mathbf{p}}, \tag{2.21}$$

where the bosonic creation operator $\hat{b}^\dagger_{\mathbf{p}}$ describes the creation of a quasiparticle (Bogoliubov excitation) with momentum $\mathbf{p}$. The coefficients $u_{\mathbf{p}}$ and $v_{\mathbf{p}}$ are called Bogoliubov coefficients and, imposing the bosonic commutation relations for both the operators $\hat{b}_{\mathbf{p}}$ and $\hat{a}_{\mathbf{p}}$, it can be shown that they must satisfy the relation

$$u^2_{\mathbf{p}} - v^2_{\mathbf{p}} = 1. \tag{2.22}$$

It is useful at this point to introduce some functions that depend on one parameter and satisfy this condition, so that we can reduce the number of variables. For instance, we consider

$$u_{\mathbf{p}} = \cosh\theta_{\mathbf{p}}, \qquad v_{\mathbf{p}} = \sinh\theta_{\mathbf{p}}. \tag{2.23}$$

Using the Bogoliubov transformations in Eq. (2.19), we obtain a Hamiltonian containing a term proportional to the non-diagonal elements $\hat{b}^\dagger_{\mathbf{p}}\hat{b}^\dagger_{-\mathbf{p}} + \hat{b}_{\mathbf{p}}\hat{b}_{-\mathbf{p}}$, so we need to impose the condition for their coefficient to be null in order to have a diagonal Hamiltonian. Therefore we impose

$$\left(\frac{p^2}{2m} + gn\right)u_{\mathbf{p}}v_{\mathbf{p}} + \frac{gn}{2}(u^2_{\mathbf{p}} + v^2_{\mathbf{p}}) = 0, \tag{2.24}$$

and by using Eq. (2.23), this can be turned into an equation for a single variable $\theta_{\mathbf{p}}$. Using the relations $\cosh(2\theta_{\mathbf{p}}) = \cosh^2\theta_{\mathbf{p}} + \sinh^2\theta_{\mathbf{p}}$ and $\sinh(2\theta_{\mathbf{p}}) = 2\cosh\theta_{\mathbf{p}}\sinh\theta_{\mathbf{p}}$,

we can rewrite Eq. (2.24) as

$$\coth(2\theta_{\mathbf{p}}) = -\frac{p^2/2m + gn}{gn}, \tag{2.25}$$

and obtain the Bogoliubov coefficients in the form

$$u_{\mathbf{p}}^2 = 1 - v_{\mathbf{p}}^2 = \frac{1}{2}\left[\frac{p^2/2m + ng}{\epsilon(p)} + 1\right]. \tag{2.26}$$

Here,

$$\epsilon(p) = \left[\left(\frac{p^2}{2m}\right)^2 + 2ng\frac{p^2}{2m}\right]^{1/2}, \tag{2.27}$$

is the Bogoliubov dispersion relation, corresponding to the eigenvalues of the Hamiltonian (2.16) obtained in the diagonal form

$$\hat{H} = E_0 + \sum_{\mathbf{p}} \epsilon(p)\hat{b}_{\mathbf{p}}^\dagger \hat{b}_{\mathbf{p}}, \tag{2.28}$$

with

$$E_0 = \frac{gN^2}{2V} + \frac{1}{2}\sum_{\mathbf{p}\neq 0}\left[\epsilon(p) - gn - \frac{p^2}{2m} + \frac{mg^2n^2}{p^2}\right] \tag{2.29}$$

$$= \frac{gN^2}{2V}\left[1 + \frac{128}{15\sqrt{\pi}}(na^3)^{1/2}\right], \tag{2.30}$$

where in the last line we carried the integration over the momentum.

These results mean that the superfluid, initially described as a system of interacting particles in Eq. (2.16), can be thought as an ensemble of non-interacting quasiparticles (Eq. (2.28)), the Bogoliubov excitations, whose creation and annihilation operators are given by $\hat{b}_{\mathbf{p}}^\dagger$ and $\hat{b}_{\mathbf{p}}$, and with energy $\epsilon(p)$, given by their dispersion relation Eq. (2.27). For small momenta $p \ll mc$, where $c = \sqrt{gn/m}$ is the velocity of sound in the superfluid, the dispersion relation is linear with p and takes the form

$$\epsilon(p) \sim cp, \tag{2.31}$$

and the quasi-particles have a phonon nature. In this case the Bogoliubov coefficients diverge, as $u_{\mathbf{p}} \to -v_{\mathbf{p}} \to \sqrt{mc/2p}$. In the opposite limit, for $p \gg mc$, the quasi-particles are particle-like and have the dispersion relation

$$\epsilon(p) \approx \frac{p^2}{2m} + gn = \frac{p^2}{2m} + \mu, \tag{2.32}$$

where we defined the chemical potential $\mu = gn = mc^2$, and in this case $v_{\mathbf{p}} \ll u_{\mathbf{p}} \sim 1$.

2.4 Gross-Pitaevskii equation

In this section we derive the Gross-Pitaevskii Equation (GPE), which is a mean-field theory used to describe the dynamics of a weakly interacting gas. We use the Hamiltonian of Eq. (2.7) as a starting point and, as we are dealing with field operators, we describe the evolution of the system using the Heisenberg equation

$$\begin{aligned} i\hbar\frac{\partial}{\partial t}\hat{\psi}(\mathbf{r},t) &= [\hat{\psi}(\mathbf{r},t), \hat{H}] \\ &= \left[-\frac{\hbar^2\nabla^2}{2m} + V_{\text{ext}}(\mathbf{r}) + \int d\mathbf{r'}\hat{\psi}^\dagger(\mathbf{r'},t)V(\mathbf{r}-\mathbf{r'})\hat{\psi}(\mathbf{r'},t)\right]\hat{\psi}(\mathbf{r},t), \end{aligned} \tag{2.33}$$

where the last term was obtained using the commutation relations for the bosonic field operators.

Under the considerations made in the previous section, we substitute $V(\mathbf{r}-\mathbf{r'})$ with the pseudo potential $V_{\text{eff}}(\mathbf{r}-\mathbf{r'})$. As discussed, the important thing is that both these potentials define the same scattering amplitude in the dilute gas, where the condition $a \ll |\mathbf{r}-\mathbf{r'}|$ is satisfied. In the mean-field approximation, we can replace the field operator $\hat{\psi}(\mathbf{r})$ with a wavefunction $\psi_0(\mathbf{r})$, and the soft pseudo potential introduced ensures that the wavefunction varies slowly on the range of the interparticle interaction, therefore we can substitute $\mathbf{r'}$ with $\mathbf{r}$ in $\psi_0(\mathbf{r'})$. The Born approximation is valid in the weakly interacting limit (for $ka \ll 1$, where k is the relative wave vector of the particles approaching each other) and, as seen in the previous section, the interaction in this regime can be described by the interaction strength g, as defined in Eq. (2.14). Under these assumptions, from Eq. (2.33) we derive the Gross-Pitaevskii Equation, of

the form

$$i\hbar\frac{\partial}{\partial t}\psi_0(\mathbf{r},t) = \left[-\frac{\hbar^2\nabla^2}{2m} + V_{\text{ext}}(\mathbf{r}) + g|\psi_0(\mathbf{r},t)|^2\right]\psi_0(\mathbf{r},t), \tag{2.34}$$

where, for interactions in 3D, $g = 4\pi\hbar^2 a/m$, as defined previously.

The GPE is therefore a Schrödinger equation with a non-linear term determined by the scattering between two particles. It is important to stress that this derivation relies on the macroscopic occupation of the ground state, which is described by a wavefunction, while any perturbations populating higher moments are neglected. This is typically valid for large, weakly interacting gases, and for $T < T_c$.

In Eq. (2.34) the only interaction process is the scattering between pairs of atoms, so the number of particles is conserved and given by

$$N = \int n(\mathbf{r},t)d\mathbf{r} = \int |\psi_0(\mathbf{r},t)|^2 d\mathbf{r}, \tag{2.35}$$

where $n = |\psi_0|^2$ is the density of the gas.

In the previous section we discussed the conditions needed to have a dilute gas and a weakly interacting condensate. It is important to remark that the diluteness condition $na^3 \ll 1$ does not necessarily imply weak interactions, when comparing the different energy scales. In fact, in order to understand if a gas is weakly interacting, we would need to compare the kinetic and the interaction energy.

The energy functional of the system, for the ground state ψ_0, is given by the equation

$$E = \int \left(\frac{\hbar^2}{2m}|\nabla\psi_0|^2 + V_{\text{ext}}(\mathbf{r})|\psi_0|^2 + \frac{g}{2}|\psi_0(\mathbf{r})|^4\right) \tag{2.36}$$

$$= \int \left(\frac{\hbar^2}{2m}|\nabla\sqrt{n}|^2 + V_{\text{ext}}(\mathbf{r})n^2 + \frac{g}{2}n^4\right) \tag{2.37}$$

$$= E_{kin} + E_{pot} + E_{int}, \tag{2.38}$$

where the first term, which is zero in uniform gases, is the "quantum pressure" and is a consequence of the Heisenberg ucertainty principle, the second term is the potential energy and the last one is the interaction energy. Using this, from the definition of the

chemical potential $\mu = \frac{\partial E}{\partial N}$, we obtain the time-independent GPE

$$\left[-\frac{\hbar^2\nabla^2}{2m} + V_{\text{ext}}(\mathbf{r}) + g|\psi_0(\mathbf{r},t)|^2\right]\psi_0(\mathbf{r}) = \mu\psi_0(\mathbf{r}). \tag{2.39}$$

In a 3D isotropic harmonic potential of frequency $\hbar\omega_{ho}$, $E_{kin} \approx N\hbar\omega_{ho} \propto N/a_{ho}^2$, and the interaction energy evaluated on the ground state is $E_{int} = gNn \propto N^2 a/a_{ho}^3$. Comparing the two terms, we have

$$\frac{E_{int}}{E_{kin}} \propto \frac{Na}{a_{ho}}. \tag{2.40}$$

This term can be larger than one even in the case of a dilute gas, so the word "weakly interacting" can be misleading. When the kinetic energy is much smaller than the interaction energy, we are in the so called Thomas-Fermi limit. If we neglect the kinetic term in Eq. (2.39), we obtain

$$\mu = V(\mathbf{r}) + g|\psi(\mathbf{r})|^2, \tag{2.41}$$

which results in the form of the stationary wavefunction determined by

$$|\psi(\mathbf{r})|^2 = \frac{\mu - V(\mathbf{r})}{g}. \tag{2.42}$$

The Gross-Pitaevskii equation (2.34) derived here will be used to simulate the dynamics of a BEC in Chapters 6-7, following the numerical method illustrated in Appendix 6.3.2.

Chapter 3

Open quantum system dynamics

Despite the advanced progress in experiments to create platforms with single atoms or photons coherently prepared in a well defined state, quantum systems cannot be considered completely isolated from an environment, as there are always sources of decoherence and dissipation present. For a complete description of the system, interactions with the environment must be considered.

Theories of open quantum systems (OQS) provide toolboxes for the study of a system interacting with an environment, where the environment degrees of freedom are traced out in order to retain only the information about the system dynamics after the interaction. These methods, broadly used in quantum optics and atomic physics [128–130] to describe, for instance, the interaction of atoms with light, have found applications in other different fields, such as molecular physics [131, 132], solid state physics, quantum information [133], biophysics [134], quantum chemistry [135], and nuclear physics [136]. In the context of quantum optics and solid state physics systems, the coupling is commonly with bosonic (or fermionic) environments, such as photons in the description of an atom interacting with the light field, or phonons, for instance for atoms in crystals, while in the context of atomic physics some environments can be represented by spins. A complete description of a system coupled to an environment is difficult to give in some cases, due to the fact that the size of the Hilbert space for an environment with N degrees of freedom increases exponentially as 2^N. Therefore describing the dynamics of both system and reservoir with the Schrödinger equation, in such cases,

becomes prohibitive. However, depending on the characteristics of both system and environment, for appropriate separation of time or frequency scales, we can use some approximations to facilitate the evaluation of the dynamics of the total system. The idea is that, instead of studying the joint closed dynamics of system and environment, we can study the non-unitary dynamics of the system alone, using a dynamical equation that accounts for the influence of the reservoir on the system state, but where we do not need to keep track of the evolution of the environment.

These dynamical methods describing the evolution of the density operator for the system are called master equations. Under certain assumptions, we can have some simplified versions of these, called Markovian master equations, where we neglect the correlations between system and reservoir and, under the assumption that the correlation time of the reservoir is much smaller than the typical timescales of the system, we can treat the environment as being static. In the following we present the derivation of the master equation in the Gorini-Kossakowski-Sudarshan-Lindblad (GKSL) [137, 138] form (commonly known as the Lindblad equation), to describe the evolution of the system under the aforementioned approximations, and describe the Monte Carlo methods, as these methods have been used in the results presented in Chapter 4, where we consider a neutral atom immersed in a superfluid reservoir.

3.1 Master equation

There are different methods to derive the GKSL master equation, using various approaches and mathematical descriptions that lead to the same results [130, 139–141], based on some assumptions that will be discussed in this section. Here we report the derivation of the GKSL master equation using a microscopic approach. Although we are aware that the word “reservoir” is used by some authors to describe environments with an infinite number of degrees of freedom, and therefore with a continuum of frequency modes, we interchange it with the term “environment” without any distinction. The Hamiltonian of a system interacting with the environment is

$$H = H_{\mathrm{S}} + H_{\mathrm{R}} + H_{\mathrm{I}}, \tag{3.1}$$

defined by the sums of the Hamiltonians respectively for the system, the environment and their interaction. We define, in the Hilbert space of system and reservoir $\mathcal{H}_{\mathrm{S}} \otimes \mathcal{H}_{\mathrm{R}}$, the density operator ρ that describes both the system and the environment, which in the Schrödinger picture, evolves according to the equation

$$\dot{\rho} = -\frac{i}{\hbar}[H, \rho]. \tag{3.2}$$

Moving to the interaction picture, an operator (generally described by the symbol $\mathcal{O}$) acquire a time dependence according to

$$\mathcal{O}^{(I)}(t) = \mathcal{U}^{\dagger}(t)\mathcal{O}\mathcal{U}(t) = e^{\frac{i}{\hbar}(H_{\mathrm{S}}+H_{\mathrm{R}})t}\mathcal{O}e^{-\frac{i}{\hbar}(H_{\mathrm{S}}+H_{\mathrm{R}})t}. \tag{3.3}$$

This definition applies also to the density operator, therefore Eq. (3.2) takes the form

$$\dot{\rho}^{(I)} = -\frac{i}{\hbar}[H_I^{(I)}(t), \rho^{(I)}(t)], \tag{3.4}$$

which is the von Neumann equation. As in the following we keep working in the interaction picture, to lighten the notation, we remove the superindex "(I)" in the operators. Eq. (3.4) can be rewritten in the integro-differential form

$$\rho(t) = \rho(0) - \frac{i}{\hbar}\int_0^t dt'[H_{\mathrm{I}}(t'), \rho(t')], \tag{3.5}$$

and after inserting this into Eq. (3.4), we obtain

$$\dot{\rho}(t) = -\frac{i}{\hbar}[H_{\mathrm{I}}(t), \rho(0)] - \frac{1}{\hbar^2}\int_0^t dt'[H_{\mathrm{I}}(t), [H_{\mathrm{I}}(t'), \rho(t')]]. \tag{3.6}$$

It is important to remark that up to this point we did not make any assumptions. The first approximation that we make now consists of considering the system and the reservoir not entangled at the initial time $t = 0$, so that the total density operator can be factorised into one part for the system and one for the environment, as

$$\rho(0) = \rho_{\mathrm{S}}(0) \otimes \rho_{\mathrm{R}}(0). \tag{3.7}$$

However, this is not generally true at $t > 0$, after the system and environment start interacting and correlations between them set in. This can be accounted for, in the total density operator at later times

$$\rho(t) = \rho_{\mathrm{S}}(t) \otimes \rho_{\mathrm{R}}(t) + \delta\rho(t), \tag{3.8}$$

with the addition of a term $\delta\rho(t) \propto O(H_{\mathrm{I}})$ that defines the correlations between the system and the reservoir, at the second order in H_{I}. At this stage we use the first approximation, namely the Born approximation, where we stop at the lowest order of the perturbation neglecting the correlations term $\delta\rho(t)$. This approximation is justified by the condition of weak coupling between system and reservoir. Furthermore, under the assumption that the reservoir contains a large number of degrees of freedom and interacts weakly with the system, we can consider the density matrix of the reservoir to be only slightly affected by the interactions with the system. More precisely, the correlation functions in the equation of motion that are relevant to the time evolution of the system involve the same bath contribution at the time t as they do at time zero, and we can consider, for simplicity $\rho_{\mathrm{R}}(t) = \rho_{\mathrm{R}}(0) = \rho_{\mathrm{R}}$.

As we are interested in the dynamics of the system, Eq. (3.6) can be traced over the environment to obtain an equation of motion for the density operator of the system only, and based on the *Born approximation*, keeping only the lowest order terms, we obtain

$$\dot{\rho}_{\mathrm{S}}(t) = -\frac{i}{\hbar}\mathrm{Tr}_{\mathrm{R}}\{[H_{\mathrm{I}}(t), \rho_{\mathrm{S}}(0) \otimes \rho_{\mathrm{R}}]\} - \frac{1}{\hbar^2}\int_0^t dt' \mathrm{Tr}_{\mathrm{R}}\{[H_{\mathrm{I}}(t), [H_{\mathrm{I}}(t'), \rho_{\mathrm{S}}(t') \otimes \rho_{\mathrm{R}}]]\}. \tag{3.9}$$

The other assumption that we make is $-\frac{i}{\hbar}\mathrm{Tr}_{\mathrm{R}}[H_{\mathrm{I}}(t), \rho(0)] = 0$ in Eq. (3.6). This is true given $\mathrm{Tr}_{\mathrm{R}}[H_{\mathrm{I}}(t), \rho_{\mathrm{R}}] = 0$, which can be satisfied by considering an effective Hamiltonian for the system that includes the term $\mathrm{Tr}_{\mathrm{R}}\{H_{\mathrm{I}}(t)\rho_{\mathrm{R}}\}$. Eq. (3.9) can then be written as

$$\dot{\rho}_{\mathrm{S}}(t) = -\frac{1}{\hbar^2}\int_0^t dt' \mathrm{Tr}_{\mathrm{R}}\{[H_{\mathrm{I}}(t), [H_{\mathrm{I}}(t'), \rho_{\mathrm{S}}(t') \otimes \rho_{\mathrm{R}}]]\}. \tag{3.10}$$

This form is clearly non-local in time, as the density operator of the system at the time

t depends on its past history (denoted by the integration over the times t' in an interval t). We now make the third approximation, consisting in making this local in time by replacing $\rho_{\rm S}(t')$ with $\rho_{\rm S}(t)$, so that the system evolution $\dot{\rho}_{\rm S}(t)$ does not depend on its past dynamics anymore, but only on its state at the time t. This is called *Markov approximation* and in order to justify it we need to introduce two distinct timescales involved in our assumptions:

1. the correlation time of the reservoir τ_C, defined as the interval of time needed for the reservoir to restore its initial conditions. More formally, given a set of operators b_α of the reservoir, τ_C is that time needed for the correlation function, defined as $\langle b^\dagger_\alpha(t) b_\beta(t-t')\rangle = {\rm Tr}_{\rm R}\{b^\dagger_\alpha(t) b_\beta(t-t')\rho_{\rm R}\}$, to go to zero. Assuming that the environment covers an energy range $\hbar\delta\omega$, then the correlation time is of the order $\tau_C = \hbar/\delta\omega$;

2. the typical relaxation timescales of the system τ_R, which can be defined as the timescale over which the density matrix of the system changes appreciably, e.g. for an excited atom, this is the decay time $\tau_R \sim 1/\Gamma$.

The Markov approximation consists of the assumption that $\tau_C \ll \tau_R$, meaning that the system can not resolve any changes in the environment as the correlations in this decay in a time smaller than the timescale of the system. Under this condition, Eq. (3.10) becomes

$$\dot{\rho}_{\rm S}(t) = -\frac{1}{\hbar^2}\int_0^t dt' {\rm Tr}_{\rm R}[H_{\rm I}(t),[H_{\rm I}(t'),\rho_{\rm S}(t)\otimes\rho_{\rm R}]]. \tag{3.11}$$

This equation is called the Redfield equation, and although it is now local in time, it is still not Markovian, as the dynamics of the system still depend on the choice of the initial condition at $t = 0$ [139]. A second step then consists of applying the substitution $t' \to (t-t')$ and extending the integral limit to infinity, under the assumption that correlations in the environment decay rapidly on a timescale corresponding to the system dynamics, which implies $\int_t^\infty dt' {\rm Tr}_{\rm R}\{[H_{\rm I}(t),[H_{\rm I}(t'),\rho_{\rm S}(t)\otimes\rho_{\rm R}]]\} \approx 0$. This corresponds to the assumption that the system density matrix does not change significantly within the environment correlation time τ_C. From the Redfield equation we therefore obtain

the master equation in the Markovian form

$$\dot{\rho}_{\mathrm{S}}(t) = -\frac{1}{\hbar^2}\int_0^\infty dt' \mathrm{Tr}_{\mathrm{R}}[H_{\mathrm{I}}(t), [H_{\mathrm{I}}(t-t'), \rho_{\mathrm{S}}(t)\otimes\rho_{\mathrm{R}}]]. \tag{3.12}$$

However, this equation does not guarantee the definition of a dynamical semigroup [139]. For this purpose, we need to do the secular approximation, which is fulfilled by the condition $\tau_{\mathrm{S}} \ll \tau_R$, where τ_{S} is the characteristic evolution time of the system and τ_R is the relaxation time, as previously discussed. In order to have a better understanding of the motivation and implications of this approximation, we now proceed to the derivation of the Lindblad master equation. Decomposing the interaction Hamiltonian in a part given by operators of the system and one by operators of the reservoir, respectively s_α and b_α, we can write

$$H_{\mathrm{I}} = \hbar\sum_\alpha s_\alpha \otimes b_\alpha. \tag{3.13}$$

Under the assumption that the spectrum of the system is discrete with eigenvalues ϵ [139], we can define projectors $\Pi(\epsilon)$ in this eigenspace, so that the eigenoperators of the system are given by

$$s_\alpha(\omega) = \sum_{\epsilon'-\epsilon=\omega} \Pi(\epsilon) s_\alpha \Pi(\epsilon'), \tag{3.14}$$

therefore fulfilling the condition $[H_{\mathrm{S}}, s_\alpha(\omega)] = -\omega s_\alpha(\omega), [H_{\mathrm{S}}, s_\alpha^\dagger(\omega)] = \omega s_\alpha^\dagger(\omega)$, and having the properties

$$s_\alpha(\omega) = s_\alpha^\dagger(-\omega), \tag{3.15}$$

$$\sum_\omega s_\alpha(\omega) = \sum_\omega s_\alpha^\dagger(\omega) = s_\alpha, \tag{3.16}$$

where the last equation follows from the completeness relation. We transform the operators of the system and the reservoir into the interaction picture, where according to Eq. (3.3) we obtain $b_\alpha^{(I)}(t) = e^{iH_{\mathrm{R}}t} b_\alpha e^{-iH_{\mathrm{R}}t}$ and use the property of the eigenoperators of the system $s_\alpha^{(I)}(\omega) = e^{-i\omega t} s_\alpha(\omega), s_\alpha^{\dagger(I)}(\omega) = e^{i\omega t} s_\alpha^\dagger(\omega)$. Removing, for convenience of notation, the superindex (I) in the operators above, the interaction Hamiltonian can

then be written in the form

$$H_{\mathrm{I}}(t) = \hbar^2 \sum_{\alpha,\omega} e^{-i\omega t} s_\alpha(\omega) \otimes b_\alpha(t) = \hbar^2 \sum_{\alpha,\omega} e^{i\omega t} s_\alpha^\dagger(\omega) \otimes b_\alpha^\dagger(t). \tag{3.17}$$

Going back to Eq. (3.12), after expanding the commutators and using the cyclic property of the trace, we can write

$$\dot{\rho}_{\mathrm{S}}(t) = \frac{1}{\hbar^2} \int_0^\infty dt' \mathrm{Tr}_{\mathrm{R}}\{H_{\mathrm{I}}(t-t')\rho_{\mathrm{S}}\rho_{\mathrm{R}}H_{\mathrm{I}}(t) - H_{\mathrm{I}}(t)H_{\mathrm{I}}(t-t')\rho_{\mathrm{S}}(t)\rho_{\mathrm{R}} + \mathrm{h.c.}\}. \tag{3.18}$$

where h.c. denotes the Hermitian conjugate, and after replacing in Eq. (3.18) the interaction Hamiltonian with the form derived in Eq. (3.17), we obtain the master equation in the form

$$\dot{\rho}_{\mathrm{S}}(t) = \sum_{\alpha,\beta} \sum_{\omega,\omega'} e^{i(\omega'-\omega)t} \left[\Gamma_{\alpha\beta}(\omega)(s_\beta(\omega)\rho_{\mathrm{S}}(t)s_\alpha^\dagger(\omega') - s_\alpha^\dagger(\omega')s_\beta(\omega)\rho_{\mathrm{S}}(t)) + \mathrm{h.c.}\right], \tag{3.19}$$

where we have defined

$$\Gamma_{\alpha\beta}(\omega) = \int_0^\infty dt' e^{i\omega t'} \left\langle b_\alpha^\dagger(t) b_\beta(t-t') \right\rangle, \tag{3.20}$$

corresponding to the one-sided Fourier transform of the reservoir correlation functions

$$\langle b_\alpha^\dagger(t) b_\beta(t-t') \rangle = \mathrm{Tr}_{\mathrm{R}}\{b_\alpha^\dagger(t) b_\beta(t-t')\rho_{\mathrm{R}}\}. \tag{3.21}$$

Here we want to make some remarks about the properties of the reservoir and its correlation function. If the environment is stationary, as we assumed so far, then $[H_{\mathrm{R}}, \rho_{\mathrm{R}}] = 0$, implying that $\langle b_\alpha^\dagger(t) b_\beta(t-t') \rangle = \langle b_\alpha^\dagger(t') b_\beta(0) \rangle$. This means that the correlation functions are homogeneous, as they do not depend on the particular time t, but only on the interval t'.

Going back to the motivation behind the secular approximation, Eq. (3.19) gives now a more solid ground for further discussions. The typical evolution timescale of the system, τ_S, should be considered of the order $1/(|\omega' - \omega|)$ with $\omega' \neq \omega$. However,

under the assumption that $\tau_R \gg \tau_S$, where τ_R is the relaxation time of the system, the frequencies $|\omega' - \omega|$ with $\omega' \neq \omega$ will be highly oscillating and average out to zero in the timescale τ_R. We therefore keep only the energy conserving terms with $\omega' = \omega$, so that we can write the master equation as

$$\dot{\rho}_{\mathrm{S}}(t) = \sum_{\alpha,\beta} \sum_{\omega} \left[\Gamma_{\alpha\beta}(\omega)(s_\beta(\omega)\rho_{\mathrm{S}}(t)s_\alpha^\dagger(\omega) - s_\alpha^\dagger(\omega)s_\beta(\omega)\rho_{\mathrm{S}}(t)) + \mathrm{h.c.} \right], \tag{3.22}$$

with $\Gamma_{\alpha,\beta}(\omega)$ defined as in Eq. (3.20). We do not report the next passages here, but it can be shown [139] that this master equation can be rewritten in the GKSL form [137, 138]

$$\dot{\rho}_{\mathrm{S}} = \mathcal{L}\rho_{\mathrm{S}} = -\frac{i}{\hbar}[H_{\mathrm{S}}, \rho_{\mathrm{S}}] + \sum_i \frac{\gamma_i}{2}(2L_i\rho_{\mathrm{S}}L_i^\dagger - \{L_i^\dagger L_i, \rho_{\mathrm{S}}\}), \tag{3.23}$$

where L_i are jump (or Lindblad) operators and $\gamma_i \geq 0$ are decay rates associated with the dissipative part of the dynamics.

3.2 Monte-Carlo Wavefunction method

In the previous section we derived the GKSL master equation. This can be used to describe the evolution of the system interacting with an environment in a wide variety of problems, as mentioned at the beginning of this chapter. However, in the numerical implementation of the Lindblad equation, a direct propagation of the density matrix ρ_{S} can be challenging due to the fact that its matrix representation has dimension $\dim(\mathcal{H}_{\mathrm{S}})^2$ and the Hilbert space dimension $\mathcal{H}_{\mathrm{S}}$ grows exponentially with the size of the system. Some other approaches alternative to the direct propagation of the reduced density matrix have therefore been developed to circumvent this problem. One of these is the quantum Monte-Carlo Wavefunction method (also known as the Quantum Trajectories method) [142, 143] (see [144] for a review), where a pure state of the system (that can be represented with $\dim(\mathcal{H}_{\mathrm{S}})$ variables), randomly sampled from the initial density matrix of the system, is subject to a stochastic evolution that combines quantum jumps and the evolution under an effective Hamiltonian. The density matrix is therefore reconstructed after averaging over many realisations (trajectories). From the

Lindblad master equation Eq. (3.23) we have seen that the dissipation is determined by the action of jump operators L_i that occur at rates γ_i. We expand the anti-commutator in the Lindblad equation and define the effective Hamiltonian

$$H_{\text{eff}} = H_{\text{S}} - \frac{i\hbar}{2}\sum_j \gamma_j L_j^\dagger L_j, \tag{3.24}$$

to write Eq. (3.23) in the more convenient form

$$\dot{\rho}_{\text{S}} = -\frac{i}{\hbar}[H_{\text{S}}, \rho_{\text{S}}] + \sum_i \frac{\gamma_i}{2}[2L_i\rho_{\text{S}}L_i^\dagger - L_i^\dagger L_i\rho_{\text{S}} - \rho_{\text{S}}L_i^\dagger L_i] \tag{3.25}$$

$$= -\frac{i}{\hbar}[H_{\text{eff}}, \rho_{\text{S}}] + \sum_i \gamma_i L_i\rho_{\text{S}}L_i^\dagger. \tag{3.26}$$

These two terms can be interpreted as follows: the first term determines the system evolution under the non-Hermitian Hamiltonian H_{eff}, therefore removing amplitude from a certain state, and the last term of Eq. (3.26) restores the population into other states. We can imagine this as the effect of an environment acting on the system with measurements after time intervals δt, and instead of tracing over the environment, the outcomes of the measurements are recorded, so the system at the time $t + \delta t$ is projected into a new state[1], which becomes the initial condition for the next time step. At this point the memory of the environment simulator is reset (reflecting the Markovian approximation) and the system is in a new pure state. After repeating this procedure for the entire evolution and for many trajectories, the density matrix of the system can be restored by averaging the projector on the state of the system, over all the number of trajectories.

In the following we describe more precisely how to implement the first-order Monte Carlo wavefunction method, used in Chapter 4.

For each trajectory we start with the system initially in the pure state $|\phi(t = 0)\rangle$, sampled from the density matrix $\rho_{\text{S}}(0)$. We can expand the master equation to the

[1] in the numerical implementation, the state at $t+\delta t$ is sampled from the distribution of the transition probabilities

first order in a time step δt, and this gives a time evolution determined by

$$|\phi^{(1)}(t+\delta t)\rangle = \left(1 - \frac{i}{\hbar} H_{\text{eff}} \delta t\right) |\phi(t)\rangle \,, \tag{3.27}$$

where t is the initial time at each time step. As the evolution of the system is non-unitary, it does not preserve the norm and this decreases by a quantity δp:

$$\langle \phi^{(1)}(t+\delta t) | \phi^{(1)}(t+\delta t)\rangle = 1 - \delta p, \tag{3.28}$$

with $\delta p = \frac{i}{\hbar}\delta t \, \langle \phi(t)|(H_{\text{eff}} - H_{\text{eff}}^{\dagger})\phi(t)\rangle + O(\delta t^2) \simeq \delta t \sum_j \gamma_j \, \langle \phi(t)|L_j^{\dagger} L_j|\phi(t)\rangle = \sum_j \delta p_j$, determined by the total decay probability given by the sum over the probabilities to decay to the other states determined by the channels allowed by the dissipator. Based on this observation, for the next step we have to determine if the jump happens or not. Numerically, this is done by randomly generating a number $r_1 \in [0,1]$, and based on this outcome we propagate the state as follows:

1. $r_1 > \delta p$: no jump occurs. The probability that this happens is given by $1 - \delta p$, as we have just seen, and in this case we simply renormalise the state:

$$|\phi(t+\delta(t))\rangle = \frac{|\phi^{(1)}(t+\delta t)\rangle}{\sqrt{1-\delta p}}. \tag{3.29}$$

2. $r_1 < \delta p$: a jump occurs. With probability δp, the system jumps to another state and the population is removed from the initial state

$$|\phi(t+\delta t)\rangle = \frac{\sqrt{\gamma_j} L_j \, |\phi(t)\rangle}{\sqrt{\delta p_j / \delta t}}. \tag{3.30}$$

   The new state occupied is sampled from the probability distribution of all the possible states $\Pi_j = \delta p_j / \delta p$, by generating a random number r_2 weighted over this.

After iterating this method for the whole evolution, we can determine the stochastic average over different trajectories and reconstruct the density matrix evolution, as explained below.

We follow the previous steps explained for the evolution of the pure state, mapping that to a density matrix formulation. The pure state at each initial time step t corresponds to a density operator given by

$$\sigma(t) = |\phi(t)\rangle \langle\phi(t)| . \tag{3.31}$$

After propagating in a time δt, this can be written in the form

$$\overline{\sigma(t+\delta t)} = (1-\delta p)\frac{|\phi^{(1)}(t+\delta t)\rangle}{\sqrt{1-\delta p}}\frac{\langle\phi^{(1)}(t+\delta t)|}{\sqrt{1-\delta p}} + \delta p \sum_j \gamma_j \Pi_j \frac{L_j |\phi(t)\rangle}{\sqrt{\delta p_j/\delta t}}\frac{\langle\phi(t)| L_j^\dagger}{\sqrt{\delta p_j/\delta t}}, \tag{3.32}$$

to be interpreted as the statistical average of $\sigma(t+\delta t)$ over all the trajectories. Substituting Eq. (3.27) here, at the first order in δt, the above equation is

$$\overline{\sigma(t+\delta t)} = \sigma(t) - \frac{i}{\hbar}\delta t(H_{\text{eff}}\sigma(t) - \sigma(t)H_{\text{eff}}^\dagger) + \delta t \sum_j \gamma_j L_j \sigma(t) L_j^\dagger + O(\delta t^2), \tag{3.33}$$

that can be rewritten, neglecting higher order terms, as

$$\frac{\overline{\sigma(t+\delta t)} - \sigma(t)}{\delta t} \simeq -\frac{i}{\hbar}(H_{\text{eff}}\sigma(t) - \sigma(t)H_{\text{eff}}^\dagger) + \sum_j \gamma_j L_j \sigma(t) L_j^\dagger \tag{3.34}$$

which can be generalised to the case of a mixed operator $\sigma(t)$. Taking a statistical average over the different trajectories is therefore equivalent to evaluating the evolution by means of the master equation (Eq. (3.26)).

It is worthwhile noting that in general we sample the observables that interest us from the trajectories, rather than directly reconstructing the density operator. Furthermore, these are independent samples, so that the statistical error scales as $\sigma/\sqrt{N}$, with σ the standard deviation of the observable across the trajectories, and N the number of samples.

Chapter 4

Cooling of neutral impurity atoms immersed in a BEC

4.1 Introduction

The achievement of dual-species mixtures in the last years [53, 54, 145] has paved the way to the study of individually trapped impurities in a BEC [62–64, 68] exploring both coherent many-body dynamics and dissipative dynamics. In particular, the study of dissipative dynamics [146, 147] has led to progress in the cooling of atoms, improving the control over unwanted dissipation of trapped atoms in optical lattices [73–78], and also applications in the context of many-body state engineering by means of dissipative driving [148–151]. The study of dissipative dynamics of a single neutral impurity atom immersed in a BEC, in particular, has been shown to be useful for its cooling to the motional ground state, without affecting its internal states under certain conditions [79].

This process relies on the relaxation of the motional excitations when coupled to the BEC, determined by the spontaneous emission of excitations in the reservoir, analogously to the case of an atom in an excited electronic state that decays by emitting a photon. In a lattice, this spontaneous emission process, combined with engineered excitations of the motional state can find applications in dark-state laser cooling, aiming to achieve cooling within a Bloch band [81, 82]. This is motivated in particular

by recent dual-species experiments with alkaline-earth-metal atoms and alkali atoms [54, 63, 152], especially with spin-polarised fermions, where the collisions within the same band are suppressed, so that coherence is preserved and the dissipative dynamics is related to the coupling between different bands.

Sympathetic cooling by a gas of neutral atoms has also been studied for single ion impurities, motivated also by recent experiments with hybrid traps for ions and neutral atoms [153, 154]. In contrast to the neutral impurity case, the radio-frequency field of the ion trap induces micromotion, on top of the harmonic oscillations, as a consequence of the oscillating electrical forces. The presence of this time-dependent trapping potential leads to injection and loss of energy in the system over a single trapping cycle, with limitations in cooling and heating that are still argument of discussion [155, 156].

Given the above motivations, we study the dissipative dynamics of neutral spin-polarised fermionic impurities trapped in anisotropic traps in different geometrical configurations, going beyond the 1D trapping potential models of previous studies [79, 82], and immersed in a 3D bosonic reservoir gas.

Experimentally the confinements of the two species in different dimensions is obtained using, for instance, the technique of species-selective dipole potential [64, 157]. The dynamics of impurities, in this setup, can be observed experimentally using fermions in an optical lattice in the Mott insulator regime where the tunneling is tuned to zero, so that the harmonic oscillators are independent [64]. Besides that, experiments that use trapping of a single impurity were realised, for example, preparing separately the reservoir atoms and the impurity and then transferring the impurity in the bath [158, 159].

Here, for the impurities, we consider a range of trapping conditions in the transverse direction with respect to the direction along which an atom is initially excited. This sets the basis for experimental applications in 1D or 2D optical lattices, and also offers a possible method for cooling distributions of fermions on single sites of a lattice.

This chapter contains results published in [123][1] and is organised as follows. In Sec. 4.2

[1]The author of this thesis performed all of the calculations and produced all of the figures in Ref. [123]

we introduce the model, describing the Hamiltonian and the approximations made in our study, where we use an open quantum system approach. In Sec. 4.3 we start by considering the case of a single impurity in a pancake-shaped trapping potential, and coupled to a BEC, which acts as a reservoir for the impurity atoms. We evaluate the decay rates associated with the spontaneous emission process for excitations in the reservoir, for the case of the impurity initially excited in the axial (tightly confined) direction. We see how these rates depend on the geometry of the system and the trapping frequencies, as well as the properties of the reservoir, such as the chemical potential. Setting parameters used in current experiments, we estimate realistic decay times. In Sec. 4.4 we estimate the decay rates for a different geometrical trapping potential weakly confined in the radial direction, effectively studying a 2D harmonic trap. Furthermore, we consider finite temperature reservoir effects and in Sec. 4.5 we extend these results to study the dynamics of spin-polarised fermions in a cigar-shaped trapping potential. In Sec. 4.6 we summarise this work and discuss future interesting perspectives.

4.2 Introduction to the model and derivation of the master equation

The system we study is an impurity neutral atom trapped in a harmonic potential, immersed in a 3D superfluid gas of bosons. For simplicity, we consider the reservoir to be confined in a square well potential of volume V (we assume that the size of the reservoir is much larger than the oscillation length of the impurity in different directions), and the fermionic impurity in a well-defined internal state during the whole investigated dynamics. This choice is justified by the fact that the internal states are not be affected by the cooling process if there are no spin-changing collisions and if the atoms are prepared in a single internal state, or in a superposition of states with the same scattering lengths for collisions with the reservoir atoms [79]. This model is

described by the total Hamiltonian

$$\hat{H} = \hat{H}_{\mathrm{a}} + \hat{H}_{\mathrm{b}} + \hat{H}_{\mathrm{int}}, \tag{4.1}$$

where

$$\hat{H}_{\mathrm{a}} = \hbar \left(\omega_x \hat{n}_x + \omega_y \hat{n}_y + \omega_z \hat{n}_z + \frac{1}{2}(\omega_x + \omega_y + \omega_x) \right), \tag{4.2}$$

is the Hamiltonian describing the vibrational motion of the impurity, approximated by a 3D quantum harmonic oscillator of frequency ω_i along the i-direction ($i = x, y, z$). The Hamiltonian describing the superfluid reservoir is

$$\hat{H}_{\mathrm{b}} = E_0 + \sum_{k \neq 0} \epsilon(k) \hat{b}_k^\dagger \hat{b}_k, \tag{4.3}$$

which is obtained from the Bogoliubov diagonalisation as described in Chapter 3, where we introduced the creation and annihilation operators $\hat{b}_{\mathbf{k}}^\dagger$ and $\hat{b}_{\mathbf{k}}$ for Bogoliubov excitations with energy $\epsilon(k) = \epsilon_k$ and momentum $\hbar\mathbf{k}$. Here, E_0 is the ground state energy of the superfluid. The interaction between the reservoir and the system is described by a contact interaction term, given by the Hamiltonian

$$H_{int} = g_{ab} \int \delta\hat{\rho}(\mathbf{r}_b) \delta(\mathbf{r} - \mathbf{r}_b) d\mathbf{r}_b = g_{ab} \delta\hat{\rho}(\mathbf{r}), \tag{4.4}$$

where $\mathbf{r}$ is the position operator of the atom, and $\mathbf{r}_b$ and $\delta\hat{\rho}$ are respectively the position and the density fluctuation operator of the reservoir. The coupling constant between the atom in the lattice (with mass m_a) and the atoms of the BEC (with mass m_b) is given by the interaction strength $g_{ab} = 4\pi\hbar^2 a_{ab}/2\tilde{m}$, where a_{ab} is the scattering length between the impurity and the superfluid, and $\tilde{m} = \frac{m_a m_b}{m_a + m_b}$ is the reduced mass.
By using the mean field description, the field operator for the superfluid can be written as

$$\hat{\Psi} = \sqrt{\rho_0} + \delta\hat{\Psi}, \tag{4.5}$$

where ρ_0 is the mean condensate density and the density fluctuation operator is there-

fore given by

$$\delta\hat{\rho} = \hat{\Psi}^\dagger\hat{\Psi} - \rho_0 = \sqrt{\rho_0}(\delta\hat{\Psi} + \delta\hat{\Psi}^\dagger) + \delta\hat{\Psi}^\dagger\delta\hat{\Psi}, \tag{4.6}$$

determined by the fluctuations of the field operator, which can be rewritten in terms of Bogoliubov operators as

$$\delta\hat{\Psi} = \frac{1}{\sqrt{V}}\sum_{\mathbf{k}}(u_k\hat{b}_{\mathbf{k}}e^{i\mathbf{k}\cdot\mathbf{r}} + v_k\hat{b}^\dagger_{\mathbf{k}}e^{-i\mathbf{k}\cdot\mathbf{r}}), \tag{4.7}$$

where V is the normalisation volume and u_k and v_k the coefficients obtained moving to the momentum space using Eq. (2.8) and using the Bogoliubov transformations of Eq. (2.20)-(2.21). The Bogoliubov coefficients of Eq. (2.26) can be rewritten in the form

$$u_k^2 = \frac{R_k^2}{1-R_k^2}, \qquad v_k^2 = \frac{1}{1-R_k^2}, \tag{4.8}$$

where we defined $R_k = \frac{\epsilon_k - (\hbar k)^2/2m_b - m_b u^2}{m_b u^2}$. Here $u = \sqrt{g_{bb}\rho_0/m_b}$ is the speed of sound in the condensate (with $g_{bb} = 4\pi\hbar^2 a_{bb}/m_b$ the interaction within the BEC) and ϵ_k the energy of the Bogoliubov excitations, given by

$$\epsilon_k = \sqrt{(\hbar u k)^2 + \left(\frac{\hbar^2 k^2}{2m_b}\right)^2}. \tag{4.9}$$

Using the definition of the chemical potential of the reservoir

$$\mu_b = g_{bb}\rho_0 = m_b u^2, \tag{4.10}$$

we observe that, depending on the momentum of the excitations, the Bogoliubov excitations can either have a particle-like spectrum in the supersonic regime (when $\epsilon_k \gg \mu_b$, therefore $k \gg m_b u$), or a phonon-like one in the subsonic regime (for $\epsilon_k \ll \mu_b$, implying $k \ll m_b u$). The energy spectra in the two cases are respectively given by

$$\epsilon_k^{(sup)} = \frac{\hbar^2 k^2}{2m_b} + \mu_b, \tag{4.11}$$

$$\epsilon_k^{(sub)} = \hbar u k, \tag{4.12}$$

and are shown in Fig. 4.1.

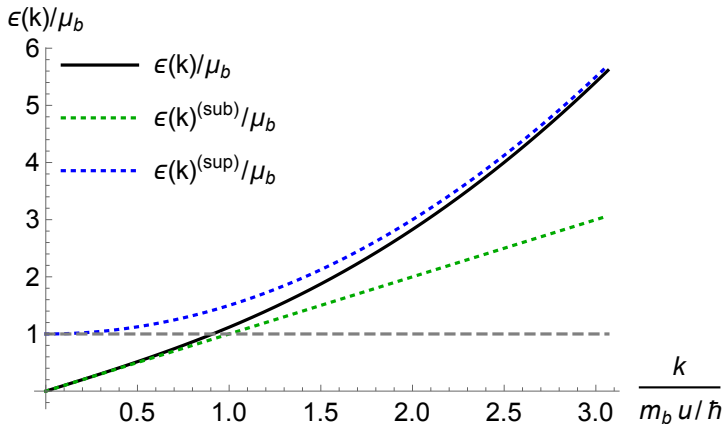

Figure 4.1: Bogoliubov excitation spectrum, as given by Eq. (4.9) (solid black line). The dashed grey line determines the value of the chemical potential μ_b, while the blue and green dotted lines represent the excitation spectrum respectively in the supersonic limit (Eq. (4.11)) and in the subsonic limit (Eq. (4.12)).

The different dispersion relations in the two regimes imply a change also in the structure factor $S(k) = (u_k + v_k)^2$, with $S(k) \sim 1$ in the supersonic limit and $S(k) \simeq \dfrac{\hbar k}{2m_b u}$ in the subsonic limit, as shown in Fig. 4.2. In the following we will see that this quantity represents an important role in the evaluation of the transition rates, and therefore in the dynamics of the system.

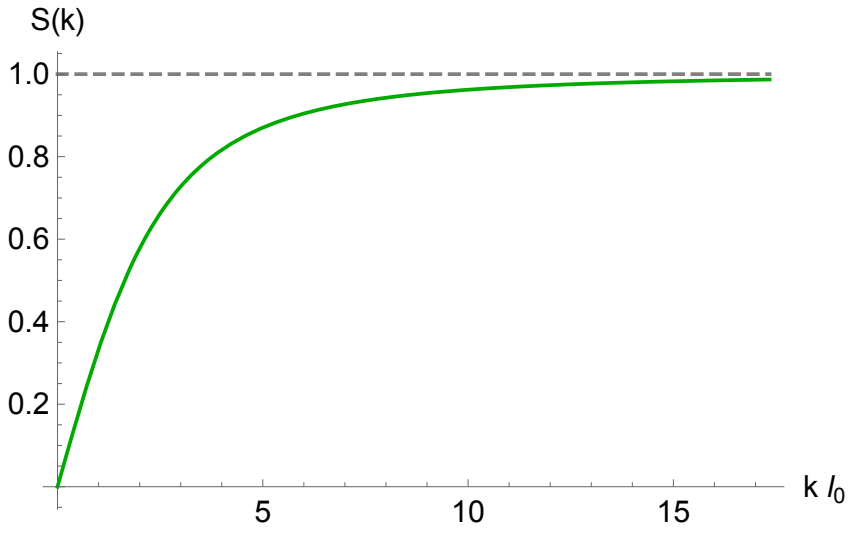

Figure 4.2: Structure factor $S(k) = (u_k + v_k)^2$.

Under the assumption of low temperatures, the term $\delta\hat{\Psi}^\dagger\delta\hat{\Psi}$ of Eq. (4.6) can be neglected [79], and using the definition in Eq. (4.7), the density fluctuation operator takes the form

$$\delta\hat{\rho} = \sqrt{\rho_0}(\delta\hat{\Psi}^\dagger + \delta\hat{\Psi}) = \sqrt{\frac{\rho_0}{V}}\sum_{\mathbf{k}}[(u_k + v_k)(\hat{b}_{\mathbf{k}}e^{i\mathbf{k}\cdot\mathbf{r}} + \hat{b}^\dagger_{\mathbf{k}}e^{-i\mathbf{k}\cdot\mathbf{r}})]. \tag{4.13}$$

The interaction Hamiltonian of Eq. (4.4) therefore reduces to

$$H_{int} = g_{ab}\sqrt{\rho_0}[\delta\hat{\Psi}^\dagger(\hat{r}) + \delta\hat{\Psi}(\hat{r})] = g_{ab}\sqrt{\frac{\rho_0}{V}}\sum_{\mathbf{k}}[(u_k + v_k)(\hat{b}_{\mathbf{k}}e^{i\mathbf{k}\cdot\hat{\mathbf{r}}} + \hat{b}^\dagger_{\mathbf{k}}e^{-i\mathbf{k}\cdot\hat{\mathbf{r}}})]. \tag{4.14}$$

We consider the impurity atom initially in an excited state, and in order to consider its dynamics we use an open quantum system description (see Chapter 3), where the impurity is the system, interacting with the BEC reservoir. In the following we present the derivation of the master equation describing the dynamics of the system. We move to the interaction picture and use the Born-Markov approximation, motivated by the fact that, in addition to weak coupling, we assume that the correlation time of the reservoir is much smaller than the relaxation time of the system (further discussions on this are presented in the next chapter). We start with the Redfield equation

$$\dot{\rho}_{\mathrm{S}} = -\frac{1}{\hbar^2}\int_0^t dt' \mathrm{Tr}_{\mathrm{R}}[\hat{H}_{int}(t), [\hat{H}_{int}(t'), \hat{\rho}_{\mathrm{S}}(t)\otimes\hat{\rho}_{\mathrm{R}}]], \tag{4.15}$$

where the density matrix of the system, factorised in the different directions, is

$$hat\rho_{\mathrm{S}} = \hat{\rho}^{(x)}_{\mathrm{S}}\otimes\hat{\rho}^{(y)}_{\mathrm{S}}\otimes\hat{\rho}^{(z)}_{\mathrm{S}}, \tag{4.16}$$

and where we assume that the coherences can be neglected, under the assumption that the oscillation frequency ω_i is much larger than the frequency associated to the characteristic interaction timescale, so that, along every direction we can project the density operator on the diagonal and consider $\hat{\rho}^{(i)}_{\mathrm{S}} = \sum_{n_i} p_{n_i}|n_i\rangle\langle n_i|$, where $i = x, y, z$ is the index for the different spatial directions, which can be factorised. In the interaction picture, the operators $\hat{b}_{\mathbf{k}}$ and $\hat{r}_i$ of Eq. (4.14) are now $\hat{b}_{\mathbf{k}}(t) = e^{-\frac{i}{\hbar}\epsilon_k t}\hat{b}_{\mathbf{k}}$ and $\hat{r}_i(t) =$

$\sqrt{\frac{\hbar}{2m_a\omega_i}}[\hat{a}_i(t)+\hat{a}_i^\dagger(t)]$, with $\hat{a}_i(t)=e^{-i\omega_i t}\hat{a}_i$.
Defining $g_k = g_{ab}\sqrt{\frac{\rho_0}{V}}(u_k+v_k)$, $\Gamma_{\mathbf{k},1}(t) = b_{\mathbf{k}}(t)$, $\Gamma_{\mathbf{k},2}(t) = b_{\mathbf{k}}^\dagger(t)$, $s_{\mathbf{k},1}(t) = e^{i\mathbf{k}\cdot\mathbf{r}(t)}$, $s_{\mathbf{k},2}(t) = e^{-i\mathbf{k}\cdot\mathbf{r}(t)}$, the interaction Hamiltonian can be rewritten in the more compact form

$$H_{int} = \sum_{\mathbf{k}} g_k(\Gamma_{\mathbf{k},1}s_{\mathbf{k},1} + \Gamma_{\mathbf{k},2}s_{\mathbf{k},2}) = \sum_{\mathbf{k}} g_k \sum_{\alpha}\Gamma_{\mathbf{k},\alpha}s_{\mathbf{k},\alpha}. \tag{4.17}$$

By expanding the commutator in the master equation and using the cyclic property of the trace, $\mathrm{Tr_R}\{ABC\} = \mathrm{Tr_R}\{CAB\} = \mathrm{Tr_R}\{BCA\}$, Eq. (4.15) can be written as

$$\begin{aligned}\dot{\rho}_{\mathrm{S}}(t) = -\sum_k g_k^2 \sum_{\alpha,\beta}\int_0^t dt'[&(s_\alpha(t)s_\beta(t')\rho_{\mathrm{S}}(t) - s_\beta(t')\rho_{\mathrm{S}}(t)s_\alpha(t))\left\langle\Gamma_\alpha(t)\Gamma_\beta(t')\right\rangle_{\mathrm{R}} \\ &+ (\rho_{\mathrm{S}}(t)s_\beta(t')s_\alpha(t) - s_\alpha(t)\rho_{\mathrm{S}}(t)s_\beta(t'))\left\langle\Gamma_\beta(t)\Gamma_\alpha(t')\right\rangle_{\mathrm{R}}],\end{aligned} \tag{4.18}$$

where we removed the index k in the operators, after using the property

$$\left\langle\Gamma_{k,\alpha}(t)\Gamma_{k',\beta}(t')\right\rangle_{\mathrm{R}} = \delta_{k,k'}\left\langle\Gamma_\alpha(t)\Gamma_\beta(t')\right\rangle_{\mathrm{R}}. \tag{4.19}$$

Furthermore, using the relations

$$\langle b_k b_k\rangle_{\mathrm{R}} = \langle b_k^\dagger b_k^\dagger\rangle_{\mathrm{R}} = 0, \tag{4.20}$$

$$b_k(t)b_k^\dagger(t') = e^{-\frac{i}{\hbar}\epsilon_k t}e^{\frac{i}{\hbar}\epsilon_k t'}b_k b_k^\dagger = e^{-\frac{i}{\hbar}\epsilon_k(t-t')}b_k b_k^\dagger, \tag{4.21}$$

and changing the integration variable from t' to $\tau = t - t'$, after considering also the secular approximation, the master equation takes the form

$$\begin{aligned}\dot{\rho}_{\mathrm{S}} = -\sum_{\mathbf{k}}\int_0^t d\tau\Bigg[&\prod_{i=x,y,z}\sum_{n_i,m_i}\left(|m_i\rangle\langle m_i|e^{-ik_i r_i}|n_i\rangle\langle n_i|e^{ik_i r_i}|m_i\rangle\langle m_i|\, p_{m_i}e^{i\omega_i\tau(m_i-n_i)}\right) \\ &- \prod_{i=x,y,z}\sum_{n_i,m_i}\left(|m_i\rangle\langle m_i|e^{ik_i r_i}|n_i\rangle\langle n_i|e^{-ik_i r_i}|m_i\rangle\langle m_i|\, p_{n_i}e^{i\omega_i\tau(n_i-m_i)}\right)\Bigg] \\ &\times\left(e^{-i\epsilon_k\tau/\hbar}\left\langle\hat{b}_{\mathbf{k}}\hat{b}_{\mathbf{k}}^\dagger\right\rangle_{\mathrm{R}} + e^{i\epsilon_k\tau/\hbar}\left\langle\hat{b}_{\mathbf{k}}^\dagger\hat{b}_{\mathbf{k}}\right\rangle_{\mathrm{R}}\right)\frac{2g_{ab}^2\rho_0}{V\hbar^2}(u_k+v_k)^2.\end{aligned} \tag{4.22}$$

Under the assumption that the correlation time of the reservoir is much smaller than

the typical times of the system's dynamics, the Markov approximation allows us to extend the integration limit $t \to \infty$, hence we obtain

$$\int_0^\infty d\tau e^{i\tau[\sum_j \omega_j(n_j-m_j)-\epsilon_k/\hbar]} = \pi\hbar\delta\left[\hbar\sum_j \omega_j(n_j-m_j)-\epsilon_k\right] + i\frac{p.v.}{\hbar\sum_j \omega_j(n_j-m_j)-\epsilon_k}, \tag{4.23}$$

where, as before, j runs on the components in the different directions and where $p.v.$ in the second term indicates the Cauchy principal value [160] and it only gives an energy shift (the counterpart to the Lamb shift in electrodynamics), so it can be discarded by means of a renormalisation of the system frequencies ω_j. The occupation probability p_{m_x,m_y,m_z} of the impurity in the state $|m_x, m_y, m_z\rangle$ is given by

$$\begin{aligned}\dot{p}_m =& \frac{2\pi g_{ab}^2\rho_0}{\hbar V}\sum_{\mathbf{k}}(u_k+v_k)^2\sum_{n_{x,y,z}}\left(\prod_i |\langle m_i|e^{-ik_i r_i}|n_i\rangle|^2\right) \\ &\times\left\{\left[\delta\left(\sum_i \omega_i(n_i-m_i)-\epsilon_k\right)p_n-\delta\left(\sum_i \omega_i(m_i-n_i)-\epsilon_k\right)p_m\right]\langle\hat{b}_{\mathbf{k}}\hat{b}_{\mathbf{k}}^\dagger\rangle_{\mathrm{R}}\right. \\ &\left.+\left[\delta\left(\sum_i \omega_i(m_i-n_i)-\epsilon_k\right)p_n-\delta\left(\sum_i \omega_i(n_i-m_i)-\epsilon_k\right)p_m\right]\langle\hat{b}_{\mathbf{k}}^\dagger\hat{b}_{\mathbf{k}}\rangle_{\mathrm{R}}\right\},\end{aligned} \tag{4.24}$$

where we used the notation $p_m = p_{m_{x,y,z}}$. The terms in the trace over the bath give $\langle\hat{b}_{\mathbf{k}}^\dagger\hat{b}_{\mathbf{k}}\rangle_{\mathrm{R}} = N(\mathbf{k})$ and $\langle\hat{b}_{\mathbf{k}}\hat{b}_{\mathbf{k}}^\dagger\rangle_{\mathrm{R}} = N(\mathbf{k})+1$, describing respectively the processes of absorption of Bogoliubov thermal excitations from the reservoir and stimulated and spontaneous emission, where the distribution of excitations with momentum $\mathbf{k}$ is given by the Bose distribution $N(\mathbf{k}) = \frac{1}{e^{\beta\epsilon_k}-1}$, which is taken into account when considering a finite temperature reservoir.

Considering the matrix elements given by the term

$$T_{n,m}(\mathbf{k}) = g_{ab}\sqrt{\frac{\rho_0}{V}}(u_k+v_k)\,\langle m_x, m_y, m_z|e^{-i\mathbf{k}\cdot\mathbf{r}}|n_x, n_y, n_z\rangle\,, \tag{4.25}$$

we can define the decay rates, given by the Fermi's golden rule, as

$$\Gamma_{n_{x,y,z}\to m_{x,y,z}} = \frac{2\pi}{\hbar}\sum_{\mathbf{k}}\left|T_{n,m}(\mathbf{k})\right|^2\delta(\tilde{\epsilon}-\epsilon_{\mathbf{k}}), \tag{4.26}$$

where $\tilde{\epsilon} = \hbar \sum_j \omega_j (n_j - m_j)$ is the difference of energy between initial and final states of the impurity. Analogously, for a finite temperature reservoir, the transition rates for absorption and stimulated emission processes, are given by

$$H_{n_{x,y,z};m_{x,y,z}} = \frac{2\pi}{\hbar} \sum_{\mathbf{k}} N(\mathbf{k}) \left| T_{n,m}(\mathbf{k}) \right|^2 \delta(\tilde{\epsilon} - \epsilon_{\mathbf{k}}). \tag{4.27}$$

We can therefore rewrite the form of Eq. (4.24) for the evolution of the occupation probabilities of an impurity in the state $|m_x, m_y, m_z\rangle$ as

$$\begin{aligned} \dot{p}_{m_{x,y,z}} = & \sum_{\substack{n_{x,y,z}: \\ \sum_i \omega_i (n_i - m_i) > 0}} \Gamma_{n_{x,y,z} \to m_{x,y,z}} p_{n_{x,y,z}} - \sum_{\substack{m'_{x,y,z}: \\ \sum_i \omega_i (m_i - m'_i) > 0}} \Gamma_{m_{x,y,z} \to m'_{x,y,z}} p_{m_{x,y,z}} \\ & + \sum_{n_{x,y,z}} H_{n_{x,y,z};m_{x,y,z}} (p_{n_{x,y,z}} - p_{m_{x,y,z}}). \end{aligned} \tag{4.28}$$

As illustrated in Fig. 4.3, the first two terms in Eq. (4.28) define the decay with the spontaneous emission of a Bogoliubov excitation, while the third term describes stimulated emission and absorption of thermal excitations that can bring the atom to higher motional states, as defined in Eq. (4.26) and Eq. (4.27).

Depending on the temperature of the environment compared to the separation of the system energy levels, the absorption of thermal excitations can in principle be neglected if $k_B T_B \ll \hbar\omega$ for all relevant trapping frequencies ω, so that the reservoir at this extent could be considered as an effective zero temperature gas. However, depending on the geometry of the system, this condition may not be fulfilled. In Sec. 4.4 we study how finite temperature effects modify the dynamics of the system and what conditions must be fulfilled in order to be able to minimise or neglect them.

Aiming to study the evolution of the state of the impurity in different geometrical confinements, in the following we focus our attention on the derivation of the transition rates, for the specific case of impurities initially excited in the first excited state along a tightly confined direction.

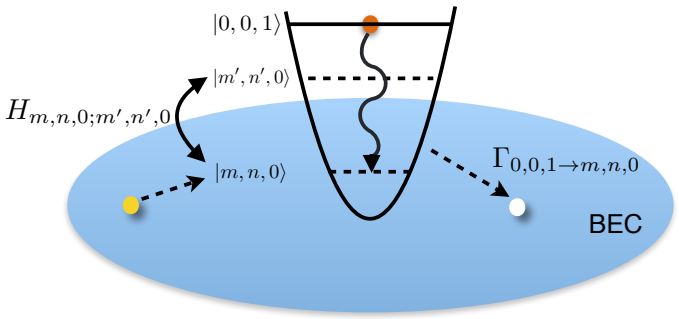

Figure 4.3: Schematic representation of level transition mechanisms for an atom initially excited along one direction in a 3D harmonic trap immersed in a superfluid. At $T = 0$ the only possible transitions are given by the decay from the state $|0,0,1\rangle$ to the state $|m,n,0\rangle$ with the creation of Bogoliubov excitations and are described by the coefficients $\Gamma_{001\to mn0}$ in the equations of motion. At finite temperature, an additional contribution due to the interaction with thermal excitations can induce stimulated transitions and excite the atoms to higher motional states either radially or axially. This contribution is represented by the coefficients $H_{m,n,\alpha;m',n',\alpha'}$.

4.3 Single atom cooling in a 3D harmonic potential tightly confined in one direction

In this section we study the case of an impurity trapped in a 3D harmonic potential tightly confined in the axial direction z and weakly confined isotropically in the other directions, so that $\omega_z \gg \omega_r = \omega_x = \omega_y$. Referring to the symmetry of a pancake shaped potential, we will refer to the tightly confined direction as the axial direction, and to the others as the radial directions. We consider the atom initially excited in the first state along the axial direction, and we study the spontaneous emission of the atom decaying towards the radial directions.

For this purpose, we confine our study to the case where the chemical potential of the BEC is much smaller than the separation of the energy levels in the different directions. This allows us to consider the dynamics of the system in the supersonic regime ($\epsilon_k \gg \mu_b$), where the Bogoliubov excitations, emitted after the decay of the excited impurities, are particle-like having energy $\epsilon_k = \hbar^2 k^2/(2m_b)$ (neglecting the shift given by the chemical potential). As seen in Fig. 4.2, this allows us to consider the structure factor in the simplified form $S(k) = |u_k + v_k|^2 \simeq 1$.

The spontaneous decay rates are found from Eq. (4.26) after evaluating the matrix elements in Eq. (4.25). For this purpose, we note that the term $e^{-ik_j\hat{r}_j}$ is the displacement operator $\hat{D}(\alpha) = \exp[\alpha\hat{a}_j^\dagger - \alpha^*\hat{a}_j]$, with $\alpha = -\dfrac{ik_j r_{j_0}}{\sqrt{2}}$ and $r_{j_0} = \sqrt{\dfrac{\hbar}{m_a\omega_j}}$ is the oscillation length in the j direction. By using the identity [161]

$$\langle n'|D(\alpha)|n\rangle = \sqrt{\frac{n_>!}{n_<!}}e^{-\frac{|\alpha|^2}{2}}\alpha^{|n-n'|}L_{n_<}^{|n-n'|}(|\alpha|^2), \tag{4.29}$$

we therefore obtain

$$\langle n_j'|e^{-ik_j j_0}|n_j\rangle = \sqrt{\frac{n_<!}{n_>!}}e^{-\frac{r_{j_0}^2k_j^2}{4}}\left(-\frac{ij_0k_j}{\sqrt{2}}\right)^{|n_j-n_j'|}L_{n_<}^{|n_j-n_j'|}\left(\frac{r_{j_0}^2k_j^2}{2}\right), \tag{4.30}$$

with $n_< = \min(n_j, n_j')$ and $n_> = \max(n_j, n_j')$, and where $L_n^{(n_j-n_j')}(x)$ is the generalised Laguerre polynomial, defined as

$$L_n^\alpha(x) = \sum_{m=0}^{n}(-1)^m\binom{n+\alpha}{n-m}\frac{x^m}{m!}. \tag{4.31}$$

After transforming the momentum components from cartesian to spherical coordinates, and after using the delta distribution property to integrate over the momentum, we obtain that the dimensionless decay rates of Eq. (4.26) for the transitions $|0_x, 0_y, 1_z\rangle \to |m_x, n_y, 0_z\rangle$ are given by

$$\begin{aligned}\frac{\Gamma_{001\to mn0}}{\sqrt{\omega_r\omega_0}} =& \frac{2g_{ab}^2\rho_0\sqrt{m_am_b}}{(2\pi)^2\hbar^3u\,m!\,n!\,w}\left(\frac{m_b}{m_a}(w-(m+n))\right)^{m+n+\frac{3}{2}}A_\phi(m,n)\\ &\times\int_0^\pi d\theta\cos^2\theta(\sin^2\theta)^{m+n+1/2}e^{-\frac{m_b}{m_a}(w-(m+n))\left(\sin^2\theta+\frac{1}{w}\cos^2\theta\right)},\end{aligned} \tag{4.32}$$

where $A_\phi(m,n) = \int_0^{2\pi}d\phi\cos^{2m}\phi\sin^{2n}\phi$. We write them in units of $\sqrt{\omega_r\omega_0}$, with $\omega_0 = \mu_b/2\hbar$, to give them an explicit dependence on the ratio $w = \omega_z/\omega_r$.

In Fig. 4.4 we show how these decay rates depend on the final radial states n and m for realistic parameter values, and we observe that the main contributions come from transitions towards low energy states, where the overlap between initial and final

wavefunctions is larger. The transition coefficients are symmetric for n and m, but not radially symmetric in $n-m$ space. This is due to the fact that, with the conservation of the energy, conservation of momentum is also imposed. As a consequence, there is a non-trivial dependence on $n+m$ and $n-m$, since for a fixed value $n+m$, the different projections of the momentum on the two possible directions change significantly the matrix elements.

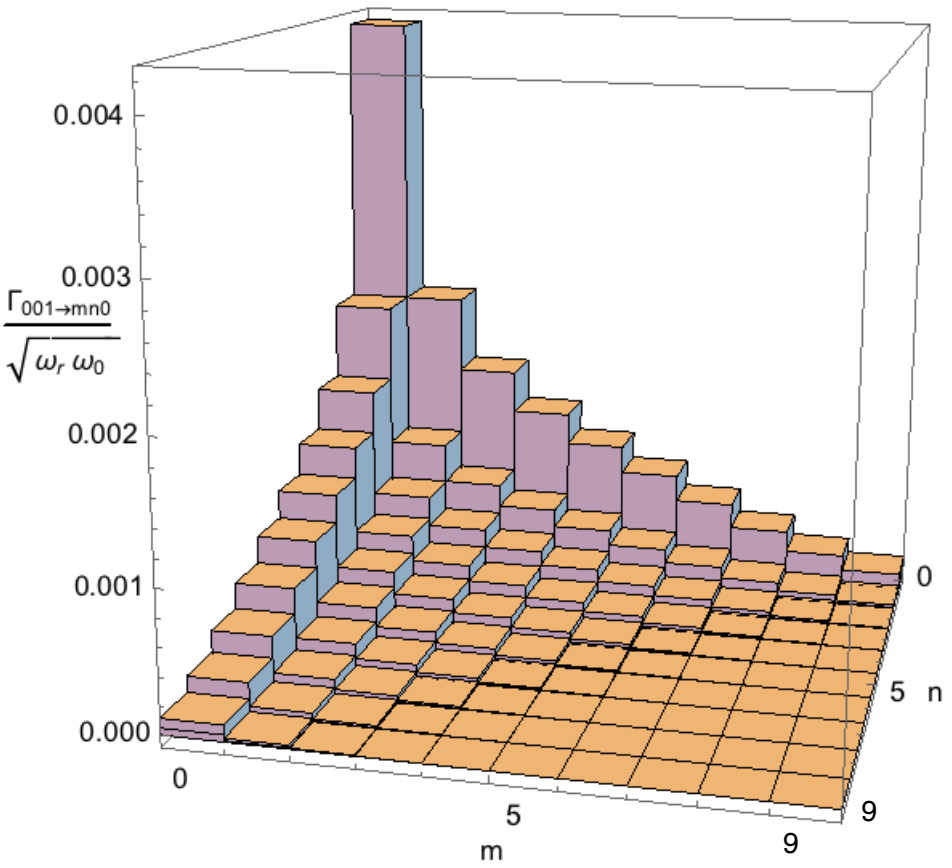

Figure 4.4: Transition coefficients $\Gamma_{001\to mn0}$ in units of $\sqrt{\omega_r\omega_0}$, for $\omega_z/\omega_r = 25$. The transitions contributing the most are the ones to low energy radial states.

The estimation of these transition coefficients is necessary to determine the decay time $\tau = 1/\Gamma_{\text{Tot}}$ from the initial state $|0,0,1\rangle$, as this depends on the sum of the transition

rates for all the possible final states, which gives the total decay rate

$$\Gamma_{\mathrm{Tot}} = \Gamma = \sum_{n,m} \Gamma_{001\to mn0}. \tag{4.33}$$

In Fig. 4.5 we observe the variation of the total decay rate with the ratio between the two trapping frequencies $w = \omega_z/\omega_r$ for different configurations, ranging from 1D ($w < 1$), 3D isotropic ($w = 1$) and 3D anisotropic ($w > 1$). We observe that when increasing the ratio w in the 1D limit, the total decay rate (that in this case is given the only possible transition $\Gamma_{1\to 0}$) increases, as a consequence of the fact that an increase of the trapping frequency along z (keeping ω_r fixed) increases the number of collisions with the reservoir in a given time interval.

In this limit ($w < 1$) the decay rate can be written in the simplified form [79]

$$\begin{aligned}\frac{\Gamma_{1\to 0}}{\sqrt{\omega_r\omega_0}} &= \frac{g_{ab}^2\rho_0\sqrt{m_a m_b}}{\pi\hbar^3 u}\sqrt{\frac{\omega_z}{\omega_r}}\int_{-\sqrt{m_b/m_a}}^{\sqrt{m_b/m_a}} e^{-\xi^2}\xi^2 d\xi \\ &= \frac{g_{ab}^2\rho_0\sqrt{m_a m_b}}{\pi\hbar^3 u}\sqrt{\frac{\omega_z}{\omega_r}}\left[\frac{\sqrt{\pi}}{2}\mathrm{Erf}\left(\sqrt{\frac{m_b}{m_a}}\right) - \sqrt{\frac{m_b}{m_a}}e^{-\frac{m_b}{m_a}}\right].\end{aligned} \tag{4.34}$$

In the 3D isotropic case ($w = 1$), the analytical solution obtained from Eq. (4.32) (for $m = n = 0$) takes the form

$$\frac{\Gamma^{iso}_{001\to 000}}{\sqrt{\omega_r\omega_0}} = \frac{2e^{-m_b/m_a}g_{ab}^2 m_b^2\rho_0}{3\pi u\hbar^3 m_a}. \tag{4.35}$$

In the 3D limit, going towards higher values of $w > 1$, although the single values of the allowed transitions $\Gamma_{001\to mno}$ decrease for increasing w, the total decay rate increases, since the number of available final states contributing to that is given by $w(w+1)/2$. From Fig. 4.5 we see how the decay time $\tau = 1/\Gamma$ varies in the different limits: the 1D asymptotic behaviour obtained from Eq. (4.34) is represented with the dotted line and the value obtained with the 3D isotropic analytical case of Eq. (4.35) is shown for $w = 1$ by the dashed horizontal line. From the decay time plot in Fig. 4.5 we see that, analogously to the 1D case, for the 3D scenario the behaviour of $\Gamma_{\mathrm{Tot}}/\sqrt{\omega_r\omega_0} \propto \sqrt{\omega_z/\omega_r}$ is preserved, but with a different coefficient.

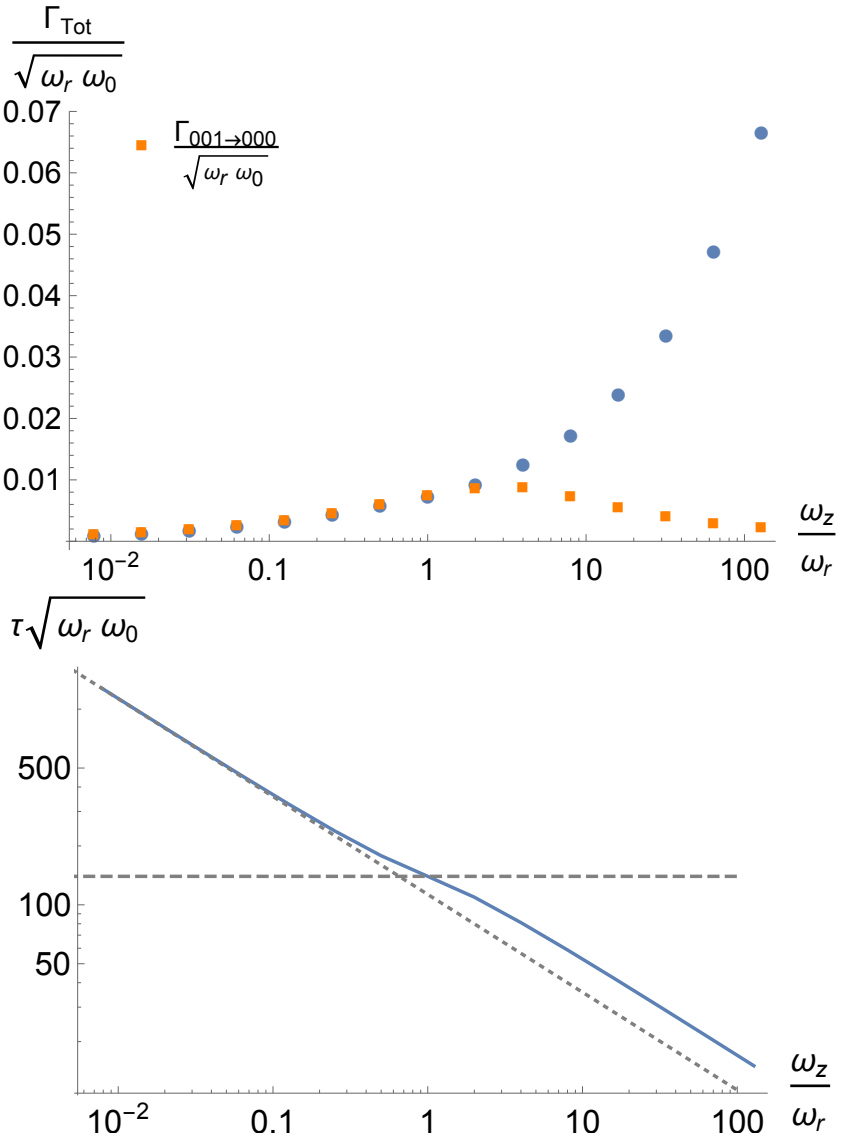

Figure 4.5: (Top) Total decay rate from the initial state $|001\rangle$ (blue dots) and decay rate for the transition $|001\rangle \to |000\rangle$ (orange squares), versus the ratio between the frequencies. (Bottom) Decay time versus the ratio between the frequencies (blue solid line). In the 1D limit and 3D isotropic limit, respectively for $w = \omega_z/\omega_r < 1$ and $w = 1$, the only transition available is the one given by the decay rate $\Gamma_{001\to000}$, for which we have analytical solutions determined by Eq. (4.34) and Eq. (4.35). The corresponding decay times are illustrated in the bottom figure respectively with a dotted and a dashed line. In the 3D limit, for $w > 1$, the number of transitions contributing to the total decay rate is $w(w+1)/2$, giving an increasing total decay rate also in this limit. The value of ω_z used here is always larger than the reference frequency $\omega_0 = \mu/(2\hbar)$, so that we are in the supersonic regime even in the low frequency 1D limit.

4.3.1 Experimental parameters

In this section we make use of the above results to give an estimation of the real timescales of the dynamics by using numerical parameters realistically used in dual species experiments. In particular, we consider the case of ^{171}Yb impurities immersed in a ^{87}Rb superfluid (as realised in [84]) with a density $\rho_0 \sim 10^{14}$ cm^{-3}. Considering a scattering length $a_{bb} = 105\, a_0$, with a_0 being the Bohr radius, we obtain that the chemical potential is $\mu_b = g_{bb}\rho_0 = \frac{4\pi\hbar^2 a_{bb}}{m_b}\rho_0 \sim 3 \times 10^{-11} eV$. This value of the chemical potential determines a speed of sound in the superfluid of $u = \sqrt{\frac{\mu_b}{m_b}} \sim 0.5$ cm/s, and we define the reference frequency as $\omega_0 = \dfrac{\mu_b}{2\hbar} \sim 2\pi \times 4$ kHz. By considering values for the trapping frequencies $\omega_z = 2\pi \times 60$ kHz $\approx 15\omega_0$ and $\omega_r = 2\pi \times 200$ Hz $\approx 0.05\omega_0$, from the results obtained in the previous section, we estimate a decay time of $\tau \sim 2$ ms, shorter than the typical coherence times.

4.4 Single atom cooling in a 2D harmonic trap tightly confined in one direction

In this section we adapt the results derived in the previous section to study the case where one of the previous radial directions is tightly confined, so that the 3D harmonic oscillator is tightly confined in two directions, and the trapping frequencies satisfy the hierarchy $\omega_y \gg \omega_z \gg \omega_x$. In this case we can neglect the dynamics along the tightest direction y and we effectively consider a 2D harmonic trap where in the z direction, as in the previous case, we have only two available modes. Reflecting the geometry of this potential, we now call the direction along z the radial one and we refer to the one along x as the axial direction.

For our purposes, as we excite the atom to the first excited state along z, considering only the two accessible states $|0\rangle_z$ and $|1\rangle_z$ in this direction, we can neglect for the direction y the states at those energies will not be populated during the dynamics. Therefore, we effectively study a 2D harmonic trap with tight confinement in the direction z. We now consider the case where the atom can initially be excited also along the axial direction, therefore taking into account transitions $|n_x, 1_z\rangle \to |m_x, 0_z\rangle$. In the

following we see how this complicates the estimation of the transition rates and discuss some useful approximations. Furthermore, we study the case of a finite temperature reservoir and see how this affects the dynamics of the impurity, depending on the choice of the parameters. From now on we remove the indices x and z to simplify the notation.

4.4.1 Estimation of the transition coefficients

In this case the transitions contributing to the dynamics are:

1. a decay rate $\Gamma_{n,1\to m,0}$ due to the decay from the radially excited state;
2. transitions from and to axial states of the same radial one, given by $\Gamma_{n,\alpha\to m,\alpha}$, with α either 0 or 1, where transitions occur effectively in 1D.

As we still focus on the case $\hbar\omega_z \gg \mu_b$, for the transitions from the excited radial state we can still consider the system to be in the supersonic regime. However, for the transitions between axial states, this assumption is not necessarily valid as the energy spacing $\hbar\omega_x$ in this direction can now be of the same order of the chemical potential μ_b. We therefore need to use the most general form of the structure factor in the estimation of the transition rates, and we will see the effect of this in the different regimes.

Decay rates $\Gamma_{n,1\to m,0}$ In Appendix A we present the derivation of the decay rates $\Gamma_{n,1\to m,0}$ with a procedure analogous to the one presented in the previous section. However, the numerical evaluation of the matrix elements obtained here turns out to be non-trivial and to give convergence problems, due to rapidly oscillating integrands for large values of m and n. Therefore, to evaluate them, we used a semi-classical approximation [162], discussed in more detail in Appendix A, where we compare the results to the full quantum expression.
The decay rates between the states $|n,1\rangle \to |m,0\rangle$ obtained with this method, in the supersonic regime, are given by the equation

$$\Gamma_{n,1\to m,0} = \frac{2g_{ab}^2\rho_0\sqrt{m_a m_b}}{(2\pi)^2\hbar^3 u}\sqrt{\frac{m_b}{m_a}(w+n-m)}\sqrt{\omega_x\omega_0} \times \int_0^\pi d\theta \sin\theta B_\phi(n,m,\theta) J_{n-m}^2\left(\sqrt{2}\frac{x_{max}}{x_0}\xi(\theta)\right), \tag{4.36}$$

are plotted in Fig. 4.6. Here $J_{n-m}(z)$ are the Bessel functions of the first kind, as defined in Eq.(A.7),

$$x_{max} = x_0 \left(\frac{\sqrt{2n+1} + \sqrt{2m+1}}{2} \right), \tag{4.37}$$

is the average between the initial and final maximum position of the impurity and we have defined

$$\xi^2(\theta) = \frac{x_0^2 k^2 \cos^2\theta}{2} = \frac{m_b}{m_a}(w+n-m)\cos^2\theta, \tag{4.38}$$

$$\zeta^2(\theta) = \frac{z_0^2 k^2 \sin^2\theta}{2} = \frac{m_b}{m_a w}(w+n-m)\sin^2\theta, \tag{4.39}$$

and

$$\begin{aligned} B_\phi(n,m,\theta) &= \int_0^{2\pi} d\phi e^{-\zeta^2(\theta)\cos^2\phi}\zeta^2(\theta)\cos^2\phi \\ &= \pi\zeta^2(\theta)e^{-\zeta^2(\theta)/2}\left[I_0\left(\frac{\zeta^2(\theta)}{2}\right) - I_1\left(\frac{\zeta^2(\theta)}{2}\right)\right], \end{aligned} \tag{4.40}$$

with I_0 and I_1 the modified Bessel functions of the first kind, as defined in Eq.(A.5). Despite the small difference, the matrix elements of Fig. 4.6 are not exactly symmetric for n and m around the diagonal $n = m$, as a consequence of the energy and momentum conservation.

Decay rates $\Gamma_{n,\alpha\to m,\alpha}$ The other contribution to the dynamics is effectively in 1D and it comes from the decay between axial states $\Gamma_{n,0\to m,0} = \Gamma_{n,1\to m,1} = \Gamma_{n\to m}$. As going to high m, as mentioned already, makes the numerical estimation of the matrix elements difficult, like in the case of the transitions in 2D, we use the semiclassical approximation, further discussed in Appendix A. The general form, without an assumption that we are in the supersonic limit, as before, is given by the expression

$$\Gamma_{n\to m} = \frac{g_{ab}^2\rho_0}{2\pi\hbar^2}\sqrt{\frac{m_b}{2}}\frac{\tilde{\epsilon}k^2 S(k)}{\sqrt{(\tilde{\epsilon}^2+\mu_b^2)(\sqrt{\tilde{\epsilon}^2+\mu_b^2}-\mu_b)}}\int_0^\pi J_{n-m}^2(k\cos\theta x_{max})\sin\theta d\theta, \tag{4.41}$$

with $\tilde{\epsilon} = \hbar\omega_x(n-m)$ and where from the integration over k of the delta distribution we obtained $k = \frac{\sqrt{2m_b}}{\hbar}\sqrt{\sqrt{\epsilon_k^2 + \mu_b^2} - \mu_b}$.

We plot in Fig. 4.7 the results obtained from this solution, in the semi-classical approximation, for two different values of the frequency ω_x. In Appendix A we investigate in more detail the validity of the semi-classical approximation used here by comparing these results with the ones obtained in the fully quantum limit (Eq. (A.1) and Eq. (A.11). We find that the approximation works reasonably well even beyond the condition $|n-m| \ll n$, with a relative difference between the values obtained via the two methods below 18% for $|n-m|/n \leq 0.9$ and lying in the range $0-38\%$ for $|n-m| \simeq n$.

In the following we consider the case of a finite temperature reservoir, and in order to determine the effects that this has on the dynamics, we compare the spontaneous decay rates obtained in this section with the absorption and stimulated emission coefficients $H_{n_{x,z},m_{x,z}}$, introduced in Eq. (4.28).

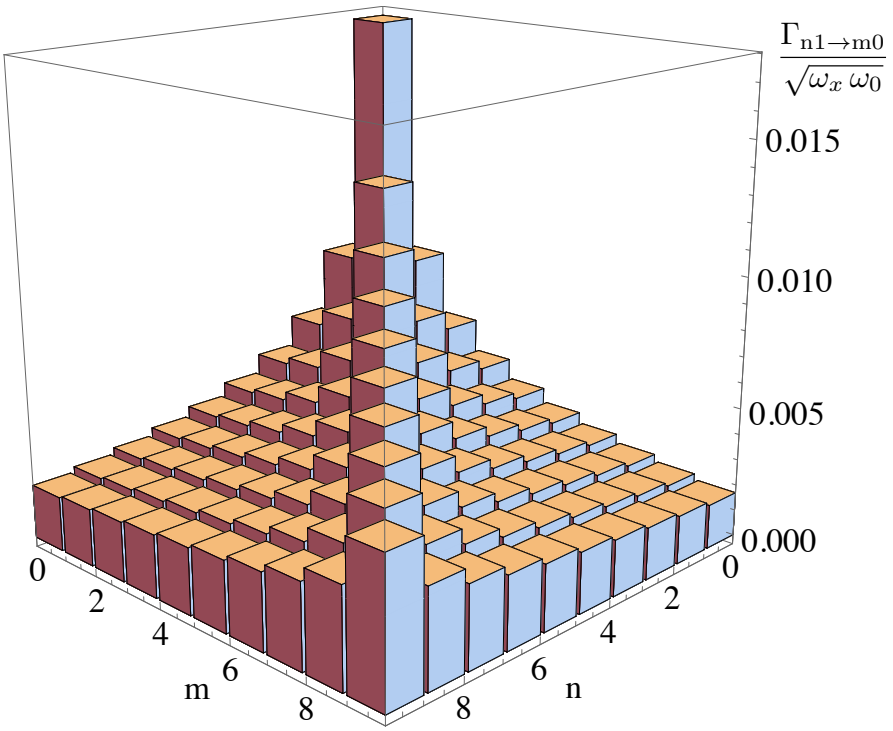

Figure 4.6: Decay rates in 2D in units of $\sqrt{\omega_x\omega_0}$, for $\omega_z/\omega_x = 100$, obtained from Eq. (4.36). The transition coefficients have a maximum for $n = m$.

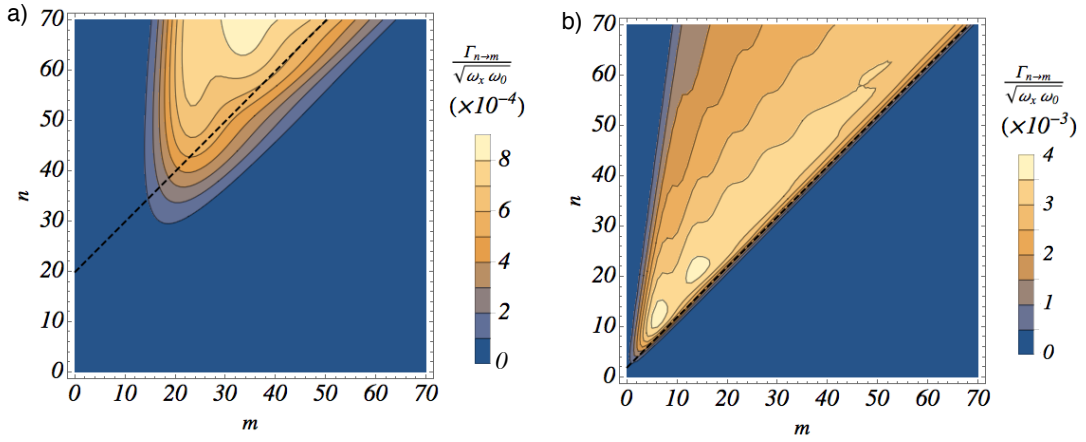

Figure 4.7: Transition coefficients $\Gamma_{n\to m}$ in units of $\sqrt{\omega_x\omega_0}$, with $\omega_x = 0.1\omega_0$ (a) and $\omega_x = \omega_0$ (b), evaluated from the expression Eq. (4.41) in the semiclassical approximation. The dotted black lines define the zones where $\epsilon_k = \mu_b$, i.e. in the limit between the supersonic and subsonic regimes, corresponding respectively to the areas far above and below the line.

4.4.2 Finite temperature reservoir

Here we study the transitions associated to the interaction of the impurity with a BEC at finite temperature, where stimulated emission takes place, and the absorption of thermal excitations can lead to a difference in the dynamics of the system exciting the atoms radially or axially. In order to estimate these effects, we consider different parameters not only for the temperature of the reservoir, but also for its chemical potential, aiming to find in which regimes the reheating effects can be minimised. For this purpose, we calculate the transition rates $H_{n_{x,z},m_{x,z}}$ of stimulated emission and absorption (see Eq. (4.28)) and compare them with the spontaneous decay rates that we already discussed.

We can neglect reheating in the radial direction as we consider the case $k_B T_b \ll \hbar\omega_z$. We therefore study the effects of the finite temperature reservoir for two possible scenarios in the regime $\hbar\omega_x \leq k_B T_b \leq \mu_b \ll \hbar\omega_z$: $k_B T_b = \hbar\omega_x \leq \mu_b \ll \hbar\omega_z$ and $\hbar\omega_x \leq \mu_b = k_B T_b \ll \hbar\omega_z$. The thermal reservoir effects depend on both the temperature and the chemical potential. We therefore change these parameters to see in which of the above regimes the reheating is minimised. As we used the frequency $\omega_0 = \mu_b/(2\hbar)$ related to the chemical potential μ_b as a reference, we do not directly change this parameter, but

we equivalently change it by tweaking both the axial frequency ω_x and the temperature of the reservoir, while keeping fixed the values of ω_z/ω_x and the chemical potential μ_b. Following the same approach used for the estimation of the axial decay rates in Eq. (4.41), we use the semi-classical approximation to evaluate the transition rates for stimulated emission and absorption of excitations. In the most general case, without any assumptions on the structure factor, these have the form

$$H_{n,m} = \frac{g_{ab}^2 \rho_0}{2\pi\hbar^2}\sqrt{\frac{m_b}{2}}\frac{\tilde{\epsilon}k^2 S(k)}{\sqrt{(\tilde{\epsilon}^2+\mu_b^2)(\sqrt{\tilde{\epsilon}^2+\mu_b^2}-\mu_b)}}\frac{1}{e^{\beta\tilde{\epsilon}}-1}\int_0^\pi J_{n-m}^2(k\cos\theta x_{max})\sin\theta d\theta, \tag{4.42}$$

having defined $\tilde{\epsilon} = \hbar\omega_x|n-m|$ and where by using the integration with the delta distribution we obtained $k = \frac{\sqrt{2m_b}}{\hbar}(\sqrt{\tilde{\epsilon}^2+\mu_b^2}-\mu_b)^{\frac{1}{2}}$.

We need to compare these transition rates, represented in Fig. 4.8 for different values of chemical potential and temperature, with the ones obtained in the previous section for the spontaneous decay (shown in Fig. 4.7) in order to determine to which extent and in what regime reheating can be neglected and how stimulated processes would influence the final distribution at the steady state.

For the case $\hbar\omega_x = k_B T_b \leq \mu_b \ll \hbar\omega_z$ [Fig. 4.8(a)], we see that, although the thermal energy and the spacing between the axial energy are of the same order of magnitude, the transition rates of the stimulated emission and absorption are at least two orders of magnitude smaller than the decay rates of Fig. 4.7(a), so reheating effects in this regime can be neglected. We therefore study how increasing the temperature [Fig. 4.8(b)] and decreasing the chemical potential [Fig. 4.8(c)] changes the transition coefficients, in the limit $\hbar\omega_x \leq \mu_b = k_B T_b \ll \hbar\omega_z$.

From Fig. 4.8(b) we can observe that an increase in the temperature of the reservoir increases the values of the stimulated transition rates. By comparing these transition coefficients with the decay rates of Fig. 4.7(a), we now notice that they are of the same order of magnitude, and in particular absorption transitions from lower energy states ($n > 30$ in this case) cannot be neglected. Furthermore, with the increase of the temperature, we notice that the transition coefficients for stimulated processes are

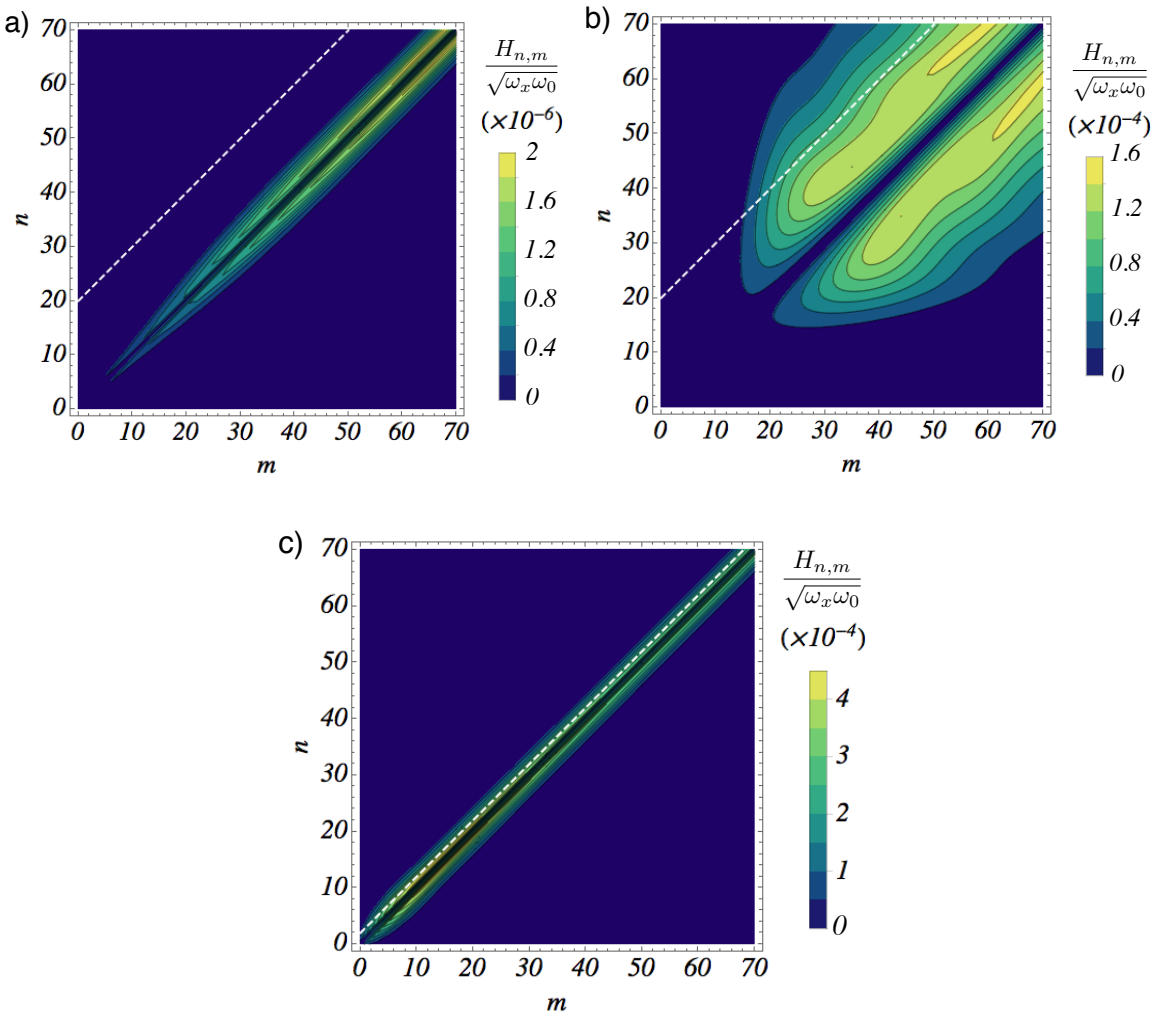

Figure 4.8: Transition coefficients $H_{n,m}$ in units of $\sqrt{\omega_x\omega_0}$, for different values of the trapping frequency in the axial direction ω_x and the reservoir temperature T_b, in the different limits $\hbar\omega_x = k_B T_b \leq \mu_b \ll \hbar\omega_z$ (a), $\hbar\omega_x < \mu_b = k_B T_b \ll \hbar\omega_z$ (b) and $\hbar\omega_x = K_B T_b \simeq \mu_b \ll \hbar\omega_z$ (c). The parameters values are $T_b = 0.1\hbar\omega_0/k_B, \omega_x = 0.1\omega_0$ (a), $T_b = \hbar\omega_0/k_B, \omega_x = 0.1\omega_0$ (b) and $T_b = \hbar\omega_0/k_B, \omega_x = \omega_0$ (c). The white dashed lines set the limit between supersonic regime (far above it) and the subsonic one (below it).

more spread towards farther states. This can be seen from the broadening around the diagonal $n = m$ of the transition coefficients in Fig. 4.8(b). As a consequence, considering transitions from a given initial state $|n\rangle$, absorption will dominate over stimulated emission. This is better shown in Fig. 4.9(a-b), where we compare the rates

$\Gamma_{n\to m}$ and $H_{n,m}$ for some chosen transitions, both at low ($n = 10$) and higher ($n = 50$) energy levels, for different values of the gas temperature. Here the transitions with $m < n$ represent both spontaneous and stimulated decay, while the absorption rates are represented for $m > n$. We observe that for transitions involving higher energy states ($n = 50$ in Fig. 4.9(a)), the absorption effects are balanced by the stimulated emission, with a symmetric distribution of the rates values around $n = m$, and moreover, they are dominated by the spontaneous emission rates. We can therefore neglect reheating effects for higher states. In contrast, in the same regime of parameters, transitions involving lower energy states (e.g. $n = 10$ in Fig. 4.9(b)) show a more asymmetric distribution around the value $n = m$ of the rates related to the stimulated processes, with absorption effects being larger than both the spontaneous and stimulated decay, and therefore inducing reheating.

Conversely, in Fig. 4.8(c) we show the results obtained for the transition rates for a smaller value of the chemical potential (this is equivalently obtained by increasing both the temperature and frequency ω_x as we expressed them in units of $\omega_0 = \mu_b/2\hbar$), and see how these values increase respect to the case in Fig. 4.8(a). However, here it can be seen that the transitions involve less states, determining a narrowing of the transition rates values around the diagonal $n = m$.

A first comparison with the spontaneous emission coefficients estimated for these parameters in Fig. 4.7(b) shows that the absorption can be neglected for states $n \gtrsim 5$. The increased decay rates can be explained as a consequence of the fact that decreasing the chemical potential has moved the transitions towards the supersonic regime, where a higher value of the structure factor enhances them. In addition to this, as can be seen from Fig. 4.9(c), the fact that the transition coefficients are more symmetric around $n = m$ means that the stimulated decay compensates the absorption, being a symmetric counterpart at even lower energy states. In Fig. 4.9(c) the stimulated transition coefficients already compensate the absorption rates until lower energies states at $n \approx 5$ for the given values. The combination of these factors when comparing the absorption rates to the two different decay rates, makes the reheating effects much smaller compared to the case of Fig. 4.8(a).

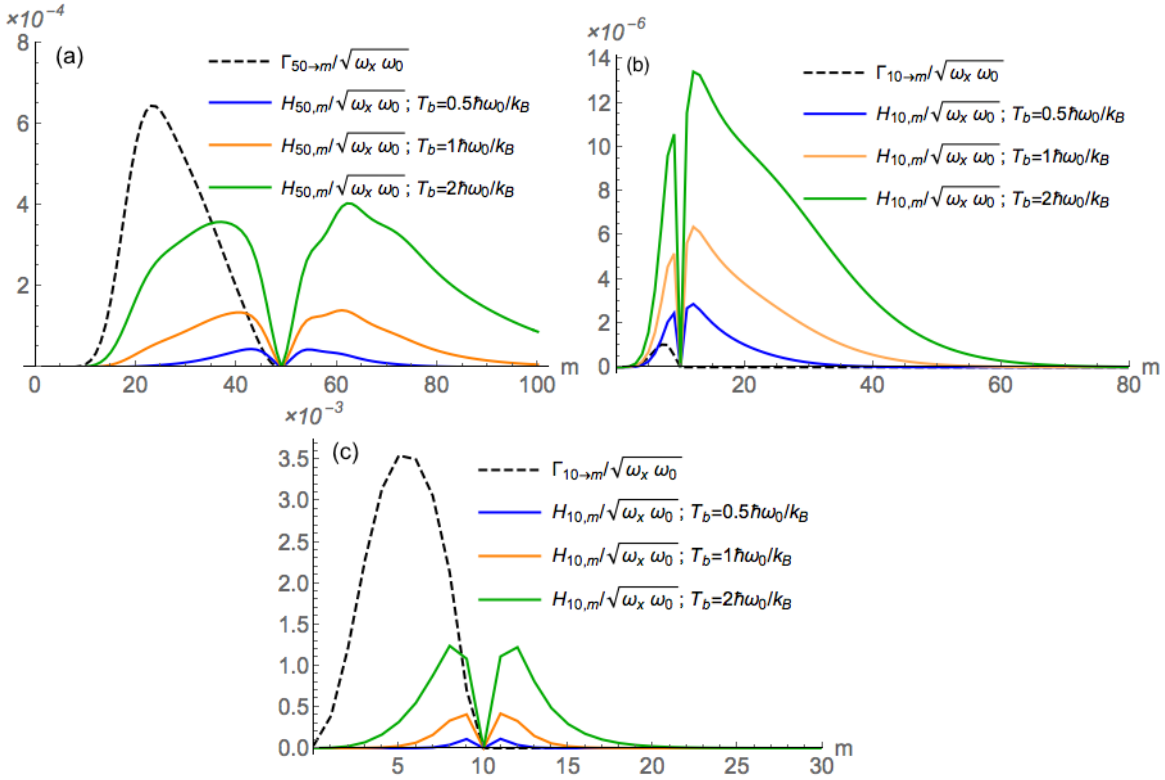

Figure 4.9: Comparison between the decay rates along the axial direction $\Gamma_{n\to m}$ (dashed black lines) and axial stimulated transition rates $H_{n,m}$ between the states having quantum numbers n and m, with n as shown in legends, for different values of the axial frequency ω_x and of the temperature $k_B T_b/(\hbar\omega_0) = 0.5, 1, 2$. The values of the frequency used here are $\omega_x/\omega_0 = 0.1$ (a, b) and $\omega_x/\omega_0 = 1$ (c).

From the results reported in Fig. 4.8 and Fig. 4.9, as shown, we want to stress the fact that, besides the temperature, the chemical potential plays an important role when considering reheating effects. As seen in Fig. 4.8(b), for instance, the radial reheating terms can not be neglected, especially for transitions involving the lower states, and can as a consequence affect the final configuration. We therefore used the detailed balance condition to study how finite temperature effects change the steady state distribution of the system, considering transitions over changes of one unit, obtaining

$$\begin{aligned} \bar{p}_{n+1} &= \frac{H_{n+1,n}}{\Gamma_{n+1\to n} + H_{n+1,n}} \bar{p}_n \\ &= \frac{H_{1,0}}{\Gamma_{1\to 0} + H_{1,0}} \times \ldots \times \frac{H_{n-1,n-2}}{\Gamma_{n-1\to n-2} + H_{n-1,n-2}} \bar{p}_0, \end{aligned} \tag{4.43}$$

with $p_0 = 1 - e^{-\beta\hbar\omega_r}$, which results in a Boltzmann distribution.

4.5 Induced dynamics of fermions in a 2D anisotropic trap

In this section we now consider the impurity system to consist of an ensemble of spin-polarised non-interacting fermions in an anisotropic harmonic trap, again in the cigar-shaped configuration in 2D, for z and x, with $\omega_y \gg \omega_z \gg \omega_x$, still immersed in a 3D reservoir. This is motivated by experiments with fermionic atoms in an optical lattice produced by a single standing wave along one direction [64]. We start with a Fermi distribution of particles in the ground state of the harmonic oscillator along the tightly confined radial direction z (i.e. single particles in the states $|n_x, 0_z\rangle$), we then appropriately excite them to the first excited state along z (to the states $|n_x, 1_z\rangle$) and study the decay back to the ground state of z and towards other states along x ($|m_x, 0_z\rangle$). Since only the dynamics in two directions is involved in these processes, we treat the system in an effective 2D harmonic trap.

We determine the initial distribution of N atoms at temperature T_a in the axial direction given by the Fermi distribution [163]

$$\bar{n}(\epsilon_n) = \frac{1}{\exp[\beta_a(\epsilon_n - \mu_a)] + 1}, \tag{4.44}$$

where $\beta_a = (k_B T_a)^{-1}$, $\epsilon_n = \hbar\omega_x n_x$ is the energy of the n-th excited state of the quantum harmonic oscillator (having set the zero of the energy at $\hbar\omega_x/2$) along the axial direction and in the radial ground state, and

$$\mu_a = \frac{\log[e^{\beta_a \epsilon_F} - 1]}{\beta_a}, \tag{4.45}$$

is the chemical potential, derived by imposing the identity

$$N = \int_0^{\epsilon_F} g(\epsilon) d\epsilon = \int_0^{\infty} \bar{n}(\epsilon) g(\epsilon) d\epsilon, \tag{4.46}$$

where $\epsilon_F = N\hbar\omega_x$ is the Fermi energy and $g(\epsilon) = (\hbar\omega_x)^{-1}$ is the density of states. Considering some typical experimental values, such as $N = 10^4$, $\omega_x = 2\pi \times 200$ Hz and

$T_a \sim 10^{-8}$ K, used for optical lattices in one dimension, we obtain $T_F = N\hbar\omega_x/k_B \sim 2 \times 10^{-6}$ K$\gg T_a$. This means that we can still limit our analysis to the case where, for N particles, all the lower N states are initially occupied, so where $\mu_a \to \epsilon_F$. Under the assumption that we can excite the particles only along the radial direction resonantly with energy $\hbar\omega_z$, the distribution of the particles in the axial states will be left invariant. The equations of motion for the occupation probabilities derived in Eq. (4.28) can again be used in this case, after readapting them for the 2D scenario, so that

$$\dot{p}_{m_x,m_z} = \sum_{\substack{n_x>\alpha \\ n_z\geq m_z}} \Gamma_{n_x,n_z\to m_x,m_z} p_{n_x,n_z} - \sum_{\substack{m'_x<\alpha' \\ m'_z\leq m_z}} \Gamma_{m_x,m_z\to m'_x,m'_z} p_{m_x,m_z} + \sum_{n_x,n_z} H_{n_x,n_z;m_x,m_z}(p_{n_x,n_z} - p_{m_x,m_z}). \tag{4.47}$$

with $\alpha = m_x - \frac{\omega_z}{\omega_x}(n_z - m_z)$, $\alpha' = m_x + \frac{\omega_z}{\omega_x}(m_z - m'_z)$. Since we are dealing with non-interacting fermions, we used a stochastic description given by the Quantum Boltzmann Master Equation (QBME) [164], derived by neglecting the coherences in the density matrix, which leads to the following forms of the transition rates:

$$\Gamma_{n_x,n_z\to m_x,m_z} = \frac{2\pi}{\hbar} \sum_{\mathbf{k}} |T_{n_x,n_z;m_x,m_z}(\mathbf{k})|^2 \delta(\epsilon_f - \epsilon_i - \epsilon_k)\tilde{n}(\epsilon_i)(1 - \tilde{n}(\epsilon_f)) \tag{4.48}$$

$$H_{n_x,n_z;m_x,m_z} = \frac{2\pi}{\hbar} \sum_{\mathbf{k}} N(\mathbf{k})|T_{n_x,n_z;m_x,m_z}(\mathbf{k})|^2 \delta(|\epsilon_i - \epsilon_f| - \epsilon_k)\tilde{n}(\epsilon_i)(1 - \tilde{n}(\epsilon_f)), \tag{4.49}$$

where $T_{n;m}$ are the matrix elements, as defined in Eq. (4.25). Here the statistics of the particles (fermions in our case) is explicitly accounted for in the terms $(1 - \bar{n}(\epsilon_f))$, with $\tilde{n}(\epsilon_i)$ and $\tilde{n}(\epsilon_f)$ the occupation numbers of initial and final state respectively. We simulated the dynamics of the particles using Monte Carlo wavefunction methods with jump operators [144] to reconstruct the final distribution, where the advantage given by the QBME is to automatically forbid the transitions from single-particle non-occupied states and towards already occupied ones.

Given an initial distribution with a defined number of particles in the first excited state along z, we averaged over different repetitions the number of jumps towards the ground radial state in time. This allowed us to evaluate the decay rates in time, for

the dynamics in the two different directions.

The decay rates for the transitions from the particles excited along z were obtained by summing over all the initially occupied and possible final states as

$$\Gamma^{(2D)} = \sum_{n,m} \Gamma_{n,1\to m,0}, \tag{4.50}$$

while the one for axial transitions is given by

$$\Gamma^{(1D)} = \sum_{n',m'} \Gamma_{n'\to m'}. \tag{4.51}$$

Even though the total decay rate is given by the sum of these two contributions, so that the decay time is $\tau = (\Gamma^{(2D)} + \Gamma^{(1D)})^{-1}$, we observed them separately to see the contribution given by each of them in the dynamics. As shown in Fig. 4.10, the decay rate $\Gamma^{(2D)}$ given by the spontaneous emission of particles initially in the excited states $|n,1\rangle$ is maximum at $t = 0$ when all the particles are excited (while $\Gamma^{(1D)} = 0$) and decreases in time whilst the particles decay to $|m,0\rangle$. During this time, on the other side, because states $|m,0\rangle$ start being occupied, $\Gamma^{(1D)}$ starts increasing as a result of the fact that more transitions between axial states become available. It then starts decreasing when the atoms are mostly in the radial ground state, and less lower energy states in the axial direction become available.

We observe that while the radial dynamics is fast, with $\Gamma^{(2D)}$ going to zero in the scale of $\tau\sqrt{\omega_x\omega_0} \simeq 80$ for $\omega_z/\omega_x = 100$ and $N = 8$ particles, the axial dynamics is much slower, so the steady state is approached in a much longer time. This is due to the fact that while the radial decay happens in the supersonic regime where the structure factor has its maximum value ($S(k) = 1$), the decay rates for the axial transitions are smaller even as a consequence of the lower structure factor that tends to suppress them. From Fig. 4.10 it can be observed that the time for all the particles to decay from the excited axial state increases when going to lower ratios ω_z/ω_x, as a consequence of the fact that the total decay rate in 2D decreases with the ratio between the axial and radial frequencies. While the decay rate in 2D, $\Gamma^{(2D)}$ [Eq. (4.50)] in these units does not depend on the choice of ω_x but only on the ratio w, the whole dynamics does depend

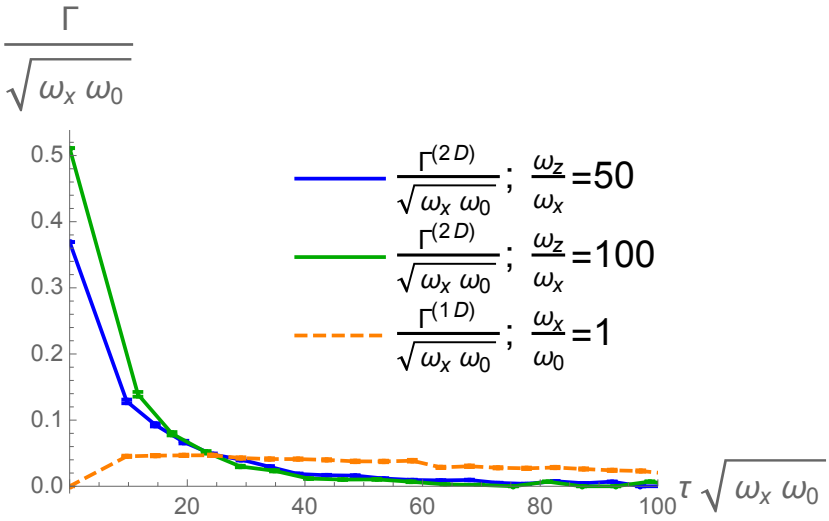

Figure 4.10: Total decay rates from the excited radial state $\Gamma^{(2D)}$ (solid lines) for different values of the frequency ratio ω_z/ω_x and total decay rate between axial states from the ground radial direction $\Gamma^{(2D)}$ (dashed line) and for $N = 8$ atoms. The emergence of a fast and a slow decay in the two different dimensions can be seen clearly.

on the choice of the axial frequency because this will be determined at longer times by the transitions to other axial states in 1D. For the values of the parameters used here, the 1D dynamics in the axial direction becomes dominant from $\tau\sqrt{\omega_x\omega_0} \simeq 20$, where the transition coefficients of the decays in the two different dimensions become comparable.

As a consequence of this, for the same parameters used in Fig. 4.10, in Fig. 4.11 we show the effect that the two kinds of dynamics have on the distribution of the atoms along the axial states $|m, 0\rangle$. In particular, it is possible to see that for earlier times (e.g. $\tau\sqrt{\omega_x\omega_0}$, when the slow dynamics along the axial direction is not dominant yet, as compared to Fig. 4.10), there is no significant effect of Pauli blocking given by the statistics of the impurities, as this starts appearing only at later times when the slower axial dynamics brings the system to the lowest energy state.

4.6 Summary and outlook

We studied the dynamics of spin-polarised fermions harmonically trapped in different configurations of tight confinement along one and two directions, and immersed in

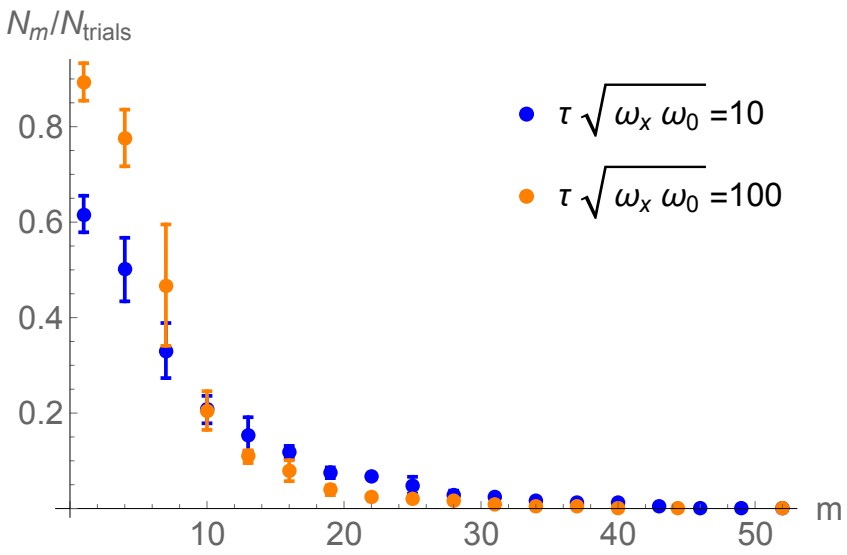

Figure 4.11: Occupation number of the axial modes m, averaged over $N_{trials} = 1000$ runs of 8 atoms, at different times as shown in the legend, having set $w = 100$ and $\omega_x = \omega_0$. No Pauli blockade is observed initially while the dynamics in 1D is still not dominant (see Fig. 4.10), but it starts appearing when the decay between axial modes become more significant. The stationary state is reached for longer times than the one shown in the plot, as the decay rate in 1D approaches the zero more slowly.

a BEC, evaluating the decay rates of their motional states. We observed how the geometry of the trapping potential and the chemical potential strongly affect the decay rates and we estimated the decay rates for the anisotropic 3D trapping. Using the typical experimental parameters reported in Section 4.3.1, we found that the decay times are of the order of ms in the 3D limit, much shorter than typical coherence timescales in experiments and comparable to other dynamical timescales in optical lattices.

Furthermore, we considered a finite temperature reservoir to study reheating effects in different limits given by certain parameters for the temperature and the chemical potential with respect to the energy scales of the system. We showed how conveniently choosing the chemical potential can minimise the absorption of the thermal excitations and how this is not due only to the temperature. We observed that in the limit of trapping frequencies smaller than the chemical potential, reheating effects are relevant and change the steady state distribution, even though the dynamics is much slower

compared to the decay from the axial excited state.

In order to be able to estimate decay and absorption rates of transitions to and from higher levels, we resorted to a semi-classical approach, where the matrix elements were evaluated considering classical trajectories for the motion of the atoms. This provided numerical advantages as, in addition to making possible the evaluation of matrix elements that in their fully quantum form could not be estimated efficiently due to highly oscillating terms, it decreased the time needed for their estimation.

Additionally, we studied the decay of a cluster of non-interacting impurities in a cigar-shaped potential, immersed in the BEC, aiming to export this study to experiments in a one-dimensional lattice of pancakes. In order to derive the dynamics, we used the QBME and the Monte Carlo methods. We observed that this is determined by a fast and a slow decay, respectively in the radial and the axial directions, as a consequence of the change in the structure factor given by the difference in the energy scales along the two directions.

This study offers some useful tools for both numerical and analytical solutions of spontaneous emission of a trapped impurity in a BEC, but also for the implementation of sympathetic cooling of impurity atoms in the context of dual species experiments.

This systems opens interesting possibilities in the context of reservoir engineering and dissipative state preparation [148–151], where by changing the properties of the reservoir and its interaction with the system, we can control the dynamics of the system such that the stationary state is a desired target state (i.e. cooling an atom to the ground state with sympathetic cooling through a reservoir).

Furthermore, because of the high control of the parameters of the reservoir, we can have access to other regimes that go beyond the one treated so far, such as the non-Markovian regime, which we briefly discuss in the next chapter.

Chapter 5

Impurities in a non-Markovian bath

5.1 Introduction

In Chapter 3 we gave an overview of the derivation of a master equation under the Born-Markov approximation, which we then used in Chapter 4 to describe the spontaneous emission of excited impurities immersed in a superfluid gas. There we assumed (within the Markov approximation) that the correlation time of the reservoir was much smaller than the relaxation time of the system, so that we could consider the state of the reservoir to be unaffected by the excitations emitted by the system at any time, with a flow of information going exclusively from the system to the environment and not vice versa. However, this is not generally the case for open quantum systems, and even in systems like our impurity immersed in a reservoir gas, where the Markov approximation is valid in realisable parameter regimes, under certain conditions that we will discuss in the following, the Markov approximation is no longer valid, and the environment can induce backflow of information. The emergence of non-Markovian effects can be found in a plethora of contexts, ranging from AMO (Atomic, Molecular and Optical physics) [130, 165, 166], to solid state physics [167, 168] and quantum biology [169]. The interest in the study of systems coupled to non-Markovian environments is motivated not only by fundamental questions on how to describe the dynamics of open quantum

system in more general terms, without relying on specific approximations, but also on the fact that non-Markovian reservoirs can be used as a powerful resource to combat the detrimental effect of decoherence induced by the interaction of the system with the reservoir, in both pure dephasing and dissipative dynamics regimes. In this context, it was observed that two qubits interacting with a bipartite Markovian reservoir present a phenomen termed "entanglement sudden death" [170, 171] where the entanglement between the qubits disappears after some time, due to the decoherence induced by the coupling to the reservoir. However, the study of the dynamics of systems coupled to non-Markovian reservoirs showed how backflow of information to the system can be used to protect and restore entanglement, via entanglement revivals and oscillations induced by long-memory reservoirs and the quantum Zeno effect [172, 173].

The system of an impurity immersed in a BEC studied in the previous chapter offers an invaluable toolbox for the study of non-Markovian dynamics. In fact, the high degree of control over the parameters of the reservoir allows us to access both Markovian and Non-Markovian regimes in different ways. Non-Markovianity can be accessed, by instance, changing the size of the reservoir, so that boundary effects can lead to backflow of information. Besides that, a non-Markovian dynamics can be accessed also changing the interaction strength between the impurities and the reservoir via Feshbach resonance, where possible, in order to access strong interactions where the Born-Markov approximation is no longer valid, or by changing the confinement of the impurity, as we show in the following. Hence, this system is a promising candidate for the freedom that it gives on the possible parameters that can be changed in order to study non-Markovian environments.

In this chapter, we show preliminary results on the non-Markovian dynamics of an impurity immersed in a bosonic BEC that pave the way for future studies.

5.2 Model

We start by considering, in analogy to the system discussed in Chapter 4, a neutral impurity trapped in a harmonic potential with tight confinement along two directions, so that we can effectively describe the system using the states along one direction

only, and we assume that the bosonic reservoir does not have any excitations at the initial time. This latter approximation is valid under the assumption that thermal excitations can be neglected, satisfied by the condition $k_B T_B \ll \hbar\omega$, where ω is the radial frequency of the impurity trap and T_B is the temperature of the bath, so we are effectively considering a zero temperature reservoir. Here we consider the most simple case where the superfluid gas is trapped in a box trap of volume V. Due to the fact that the potential inside the box is flat, the Bogoliubov parameters u_k and v_k can be considered to be the same as those of a homogeneous gas already considered for the studies in Chapter 4, where in Eq. (4.8) we defined $u_k^2 = \dfrac{R_k^2}{1-R_k^2}$ and $v_k^2 = \dfrac{1}{1-R_k^2}$. Here $R_k = (\epsilon_k - (\hbar k)^2/2m_b - m_b u^2)/m_b u^2$, where we recall that m_b is the mass of the atoms in the reservoir and u is the speed of sound in the superfluid.

The Hamiltonian describing the neutral impurity immersed in a superfluid gas is analogous to the one of Eqs. (4.1)-(4.4) and is given by

$$\hat{H} = \hat{H}_a + \hat{H}_b + \hat{H}_I, \tag{5.1}$$

where

$$\hat{H}_a = \hbar\omega\left(\hat{a}^\dagger\hat{a} + \frac{1}{2}\right) \tag{5.2}$$

$$\hat{H}_b = E_0 + \sum_{\mathbf{k}\neq 0} \epsilon(\mathbf{k})\hat{b}_{\mathbf{k}}^\dagger\hat{b}_{\mathbf{k}} \tag{5.3}$$

$$\hat{H}_I = g_{ab}\sqrt{\frac{\rho_0}{V}}\sum_{\mathbf{k}}(u_k + v_k)(\hat{b}_{\mathbf{k}}e^{i\mathbf{k}\cdot\hat{\mathbf{r}}} + \hat{b}_{\mathbf{k}}^\dagger e^{-i\mathbf{k}\cdot\hat{\mathbf{r}}}) = \sum_{\mathbf{k}} g_{\mathbf{k}}(\hat{b}_{\mathbf{k}}e^{i\mathbf{k}\cdot\hat{\mathbf{r}}} + \hat{b}_{\mathbf{k}}^\dagger e^{-i\mathbf{k}\cdot\hat{\mathbf{r}}}), \tag{5.4}$$

are the Hamiltonians of the impurity, the superfluid bath and the contact interaction between the impurity and the bath, respectively. Here $\hat{a}$ and $\hat{b}_k$ are the bosonic annihilation operators for the impurity harmonic oscillator states and the Bogoliubov excitations of the bath, g_{ab} is the interaction between the impurity and the BEC, ρ_0 is the density of reservoir and $\hat{\mathbf{r}}$ is the position operator of the impurity. As we consider the dynamics of the impurity only along one direction, here we consider the harmonic oscillator Hamiltonian $\hat{H}_a$ in 1D, different to the one used in Eq. (4.2) in Chapter 4.

We start by considering the impurity initially in the first excited state, while no exci-

tations are in the reservoir, so that the total state at the initial time is $|\psi(0)\rangle = |1, 0_k\rangle$. Moving to the interaction picture, the operators take the time dependent forms

$$\hat{a}^\dagger(t) = e^{i\omega t}\hat{a}^\dagger, \qquad \hat{a}(t) = e^{-i\omega t}\hat{a}, \tag{5.5}$$

$$\hat{b}^\dagger_{\mathbf{k}}(t) = e^{\frac{i}{\hbar}\epsilon_{\mathbf{k}} t}\hat{b}^\dagger_{\mathbf{k}}, \qquad \hat{b}_{\mathbf{k}}(t) = e^{-\frac{i}{\hbar}\epsilon_{\mathbf{k}} t}\hat{b}_{\mathbf{k}}, \tag{5.6}$$

$$\hat{r}(t) = \sqrt{\frac{\hbar}{2m_a\omega}}(e^{i\omega t}\hat{a}^\dagger + e^{-i\omega t}\hat{a}), \tag{5.7}$$

so that the interaction Hamiltonian is now given by

$$H_I(t) = \sum_{\mathbf{k}} g_{\mathbf{k}}(\hat{b}_{\mathbf{k}}(t)e^{i\mathbf{k}\cdot\hat{\mathbf{r}}(t)} + \hat{b}^\dagger_{\mathbf{k}}(t)e^{-i\mathbf{k}\cdot\hat{\mathbf{r}}(t)}), \tag{5.8}$$

where $g_{\mathbf{k}} = g_{ab}\sqrt{\frac{\rho_0}{V}}(u_{\mathbf{k}} + v_{\mathbf{k}})$ and we limit our analysis to the case where the excitations are in the supersonic regime, so that the structure factor is $S(k) = |u_{\mathbf{k}} + v_{\mathbf{k}}| \sim 1$. We consider the impurity in a 1D trap where the non-tightly confined direction is along z ($\omega = \omega_z \ll \omega_x, \omega_y$), so that we can restrict the study of the motion of the atom to that along the direction z and $\mathbf{k}\cdot\hat{\mathbf{r}} = k_z\hat{r} = k\cos(\theta)\hat{r}$. Making use of the Baker-Campbell-Hausdorff relation $e^{\hat{A}+\hat{B}} = e^{\hat{A}}e^{\hat{B}}e^{-[\hat{A},\hat{B}]/2}$, the term $e^{i\mathbf{k}\cdot\hat{\mathbf{r}}(t)} = e^{ik_z\hat{r}(t)}$ can be rewritten as

$$e^{ik_z\hat{r}(t)} = e^{ik_z\frac{r_0}{\sqrt{2}}(e^{i\omega t}\hat{a}^\dagger + e^{-i\omega t}\hat{a})} = e^{-\frac{k_z^2 r_0^2}{4}}e^{ik_z\frac{r_0}{\sqrt{2}}e^{i\omega t}\hat{a}^\dagger}e^{ik_z\frac{r_0}{\sqrt{2}}e^{-i\omega t}\hat{a}}, \tag{5.9}$$

where we defined the oscillation length $r_0 = \sqrt{\frac{\hbar}{m_a\omega}}$ and used the commutator relation $\left[ik_z\frac{r_0}{\sqrt{2}}e^{i\omega t}\hat{a}^\dagger, ik_z\frac{r_0}{\sqrt{2}}e^{-i\omega t}\hat{a}\right] = \frac{k_z^2 r_0^2}{2}$. So far, the description of the system is analogous to the one considered in Chapter 4 for an impurity tightly confined in two directions. However, we will consider here situations where the correlation time of the reservoir can be comparable to the relaxation time of the impurity. Under this condition the system can no longer be considered in the weak coupling regime, hampering the use of a Born-Markov master equation. We therefore use a different approach that allows us to keep track of the state of the environment into the global state $|\psi\rangle$. This is done using the Wigner-Weisskopf approach. With this representation, in the interaction picture,

the state of the system at the time t can be written in the form

$$|\psi(t)\rangle = c_{10}(t)e^{i\omega t}\,|1,0_k\rangle + \sum_{\mathbf{k}} c_{0k}(t)e^{\frac{i}{\hbar}\epsilon_{\mathbf{k}}t}\,|0,1_k\rangle\,, \tag{5.10}$$

where $c_{ij}(t)$ describe the probability amplitudes of the system to be in the configuration $|i,j_k\rangle$, with i excitations for the impurity and j in the mode k of the superfluid. In order to use this we used the secular approximation and therefore assumed that the number of excitations in the system is conserved. By using the Schrödinger equation

$$\frac{d}{dt}\,|\psi(t)\rangle = -\frac{i}{\hbar}H_I(t)\,|\psi(t)\rangle\,, \tag{5.11}$$

and inserting into it the definition from Eq. (5.10), the left side gives

$$\frac{d}{dt}\,|\psi(t)\rangle = (\dot{c}_{10}(t)+i\omega c_{10}(t))e^{i\omega t}\,|1,0_k\rangle+\sum_{\mathbf{k}}\left(\dot{c}_{0k}(t)+\frac{i}{\hbar}\epsilon_{\mathbf{k}}c_{0k}(t)\right)e^{\frac{i}{\hbar}\epsilon_{\mathbf{k}}t}\,|0,1_k\rangle\,, \tag{5.12}$$

while from the right side we obtain

$$-\frac{i}{\hbar}H_I(t)\,|\psi(t)\rangle = -\frac{i}{\hbar}\left(c_{10}(t)e^{i\omega t}H_I(t)\,|1,0_k\rangle + \sum_{\mathbf{k}} c_{0k}(t)e^{\frac{i}{\hbar}\epsilon_{\mathbf{k}}t}H_I(t)\,|0,1_k\rangle\right) \tag{5.13}$$

$$= -\frac{i}{\hbar}\left(c_{10}(t)e^{i\omega t}\sum_{\mathbf{k}} g_{\mathbf{k}}e^{\frac{i}{\hbar}\epsilon_{\mathbf{k}}t}e^{-ik_z\hat{r}(t)}\,|1,1_k\rangle + \sum_{\mathbf{k}} g_{\mathbf{k}}c_{0k}(t)e^{ik_z\hat{r}(t)}\,|0,0_k\rangle\right). \tag{5.14}$$

Projecting these onto the states $|0,1_k\rangle$ and $|1,0_k\rangle$ and using the Schrödinger equation, we obtain

$$\dot{c}_{0k}(t) = -i\omega_{\mathbf{k}}c_{0k}(t) - \frac{i}{\hbar}c_{10}(t)e^{i\omega t}g_k\,\langle 0,1_k|\,e^{-ik_z\hat{r}(t)}\,|1,1_k\rangle \tag{5.15}$$

$$\dot{c}_{10}(t) = -i\omega c_{10}(t) - \frac{i}{\hbar}\sum_{\mathbf{k}} g_k c_{0k}(t)e^{-i\omega t}\,\langle 1,0_k|\,e^{-ik_z\hat{r}(t)}\,|0,0_k\rangle\,, \tag{5.16}$$

where we defined $\omega_{\mathbf{k}} = \epsilon_{\mathbf{k}}/\hbar$.

We solve the first differential equation

$$c_{0k}(t) = e^{-i\omega_{\mathbf{k}}t}c_{0k}(0) - \frac{i}{\hbar}g_{\mathbf{k}}\int_0^t c_{10}(s)e^{i\omega s}e^{-i\omega_{\mathbf{k}}(t-s)}\left\langle 0\right|e^{-ik_z\hat{r}(s)}\left|1\right\rangle ds \tag{5.17}$$

$$= -\frac{i}{\hbar}g_{\mathbf{k}}\int_0^t c_{10}(s)e^{i\omega s}e^{-i\omega_{\mathbf{k}}(t-s)}\left\langle 0\right|e^{-ik_z\hat{r}(s)}\left|1\right\rangle ds, \tag{5.18}$$

where we used the initial condition $c_{0k}(0) = 0$, and we insert this into the second differential equation (5.16), obtaining

$$\dot{c}_{10}(t) = -i\omega c_{10}(t) - \sum_{\mathbf{k}}\frac{g_{\mathbf{k}}^2}{\hbar^2}\int_0^t c_{10}(s)e^{-i(\omega_{\mathbf{k}}+\omega)(t-s)}\left\langle 0\right|e^{-ik_z\hat{r}(s)}\left|1\right\rangle\left\langle 1\right|e^{-ik_z\hat{r}(t)}\left|0\right\rangle ds. \tag{5.19}$$

It is convenient to define $c_{10}(t) = e^{-i\omega t}\tilde{c}_{10}(t)$, so that $\dot{\tilde{c}}_{10}(t)e^{-i\omega t} = \dot{c}_{10}(t) + i\omega c_{10}(t)$, and by using the result derived from Eq. (5.9), and the relation

$$e^{-i\frac{k_z r_0}{\sqrt{2}}e^{-i\omega t}\hat{a}}\left|n\right\rangle = \sum_{m=0}^{n}\frac{1}{m!}\left(-i\frac{k_z r_0}{\sqrt{2}}e^{-i\omega t}\hat{a}\right)^m\left|n\right\rangle$$

$$= \sum_{m=0}^{n}\frac{1}{m!}\left(-i\frac{k_z r_0}{\sqrt{2}}e^{-i\omega t}\right)^m\sqrt{\frac{n!}{(n-m)!}}\left|n-m\right\rangle, \tag{5.20}$$

we obtain

$$\left\langle 0\right|e^{-ik_z\hat{r}(s)}\left|1\right\rangle\left\langle 1\right|e^{-ik_z\hat{r}(t)}\left|0\right\rangle = \frac{k_z^2 r_0^2}{2}e^{-k_z^2 r_0^2/2}e^{i\omega(t-s)}. \tag{5.21}$$

Therefore Eq. (5.19) reduces to

$$\dot{\tilde{c}}_{10}(t) = -\sum_{\mathbf{k}}\frac{g_{\mathbf{k}}^2}{\hbar^2}\int_0^t \tilde{c}_{10}(s)e^{-i(\omega_{\mathbf{k}}-\omega)(t-s)}\frac{k_z^2 r_0^2}{2}e^{-k_z^2 r_0^2/2}ds. \tag{5.22}$$

After changing the notation $\tilde{c}_{10}$ to c_{10} and defining the correlation function

$$\alpha(t-s) = \sum_{\mathbf{k}}\frac{g_{\mathbf{k}}^2}{\hbar^2}e^{-i(\omega_{\mathbf{k}}-\omega)(t-s)}\frac{k_z^2 r_0^2}{2}e^{-k_z^2 r_0^2/2}, \tag{5.23}$$

we have the equation of motion for the amplitude probability $c_{10}(t)$ in the more compact

form

$$\dot{c}_{10}(t) = -\int_0^t c_{10}(s)\alpha(t-s)ds. \tag{5.24}$$

This can be computed numerically using different methods, including the finite difference method and the inverse Laplace transform evaluated with the Stehfest algorithm [174].

5.2.1 Finite difference method

In the finite difference method, we have two time steps: δs and δt (with $\delta s < \delta t$), where the first time step $\delta s = \delta t/N_s$ is used for the integration sampling (with N_s the number of subintervals) over a time interval $[t, t+\delta t]$, and δt is the time that we consider for the increments of the probability amplitude $c_{10}(t)$. Using the finite difference method (Euler forward to the first order in δt), starting with an initial time $t = 0$, the evolution of Eq. (5.24) after the first time step at $t_1 = \delta t$, can be written as

$$\frac{c_{10}(\delta t) - c_{10}(0)}{\delta t} \approx -c_{10}(0)\sum_{i=0}^{N_s}\alpha(\delta t - s_i)\delta s, \tag{5.25}$$

where $s_i = i\delta s$, and in the sum over i we approximated $c_{10}(s_i) \approx c_{10}(s_0) = c_{10}(0)$. We can rewrite this in the form

$$c_{10}(\delta t) \approx c_{10}(0) - c_{10}(0)\sum_{i=0}^{\delta t}\alpha(\delta t - s_i)\delta s\,\delta t. \tag{5.26}$$

Following the same rule, at the next time $t_2 = 2\delta t$ we have

$$\begin{aligned}\frac{c_{10}(2\delta t) - c_{10}(\delta t)}{\delta t} &= -\sum_{i=0}^{2N_s} c_{10}(s_i)\alpha(2\delta t - s_i)\delta s \\ &= -c_{10}(0)\sum_{i=0}^{N_s}\alpha(\delta t - s_i)\delta s - c_{10}(\delta t)\sum_{i=N_s}^{2N_s}\alpha(2\delta t - s_i)\delta s,\end{aligned} \tag{5.27}$$

which returns

$$c_{10}(2\delta t) \approx c_{10}(\delta t) - c_{10}(0)\sum_{i=0}^{N_s}\alpha(\delta t - s_i)\delta s\,\delta t - c_{10}(\delta t)\sum_{i=N_s}^{2N_s}\alpha(2\delta t - s_i)\delta s\,\delta t. \tag{5.28}$$

By iterating this process for all the successive time steps, we can see that the occupation probability of the system at a time t does not depend only on the previous time step, but also all the previous ones. This is the signature of a memory process that was not considered in the previous chapter, due to the fact that we do not use a Markov approximation.

5.2.2 Laplace transform

The approach used in the following uses the Laplace transform to obtain, from the integro-differential equation (5.19), an algebraic equation that can be solved analytically. We can rewrite Eq. (5.24) as the convolution product

$$\dot{c}_{10}(t) = -\int_0^t c_{10}(s)\alpha(t-s)ds = -\int_0^t c_{10}(s)\alpha(t-s)ds = -(c_{10} * \alpha)(t). \tag{5.29}$$

The Laplace transform of a function $f(t)$ is defined as

$$\tilde{f}(s) = \mathcal{L}\{f(t)\} = \int_0^\infty e^{-st} f(t)dt, \tag{5.30}$$

and using the convolution property $\mathcal{L}\{c_{10} * \alpha\} = \mathcal{L}\{c_{10}\}\mathcal{L}\{\alpha\}$, Eq. (5.29) can be rewritten as an algebraic equation in the Laplace space, of the form

$$s\tilde{c}_{10}(s) - c_{10}(0) = -\tilde{\alpha}(s)\tilde{c}_{10}(s). \tag{5.31}$$

Using the fact that $c_{10}(0) = 1$, from Eq. (5.31) we obtain the solution

$$\tilde{c}_{10}(s) = \frac{1}{s + \tilde{\alpha}(s)}. \tag{5.32}$$

By calculating the inverse Laplace transform of Eq. (5.32), defined as

$$f(t) = \mathcal{L}^{-1}\{f(s)\} = \frac{1}{2\pi i}\int_{\gamma-i\infty}^{\gamma+i\infty} \tilde{f}(s)e^{st}ds, \tag{5.33}$$

where, in the complex plane, the integration is done along the vertical line $Re(s) = \gamma$, so that $\gamma > \Re(s_0)$, with s_0 the singularities of $F(s)$, one can thus obtain the time-

evolution of $c_{10}(t)$. In general, however, the inverse Laplace transform cannot be done analytically, and one has to use numerical methods. In this thesis we used the Stehfest algorithm [174], which approximates the inverse Laplace transform with the expansion

$$f(t) \approx f_N(t) = \frac{\ln(2)}{t} \sum_{n=1}^{N} K_n \tilde{f}\left(\frac{n\ln(2)}{t}\right), \tag{5.34}$$

where

$$K_n = (-1)^{n+N/2} \sum_{k=(n+1)/2}^{\min(n,N/2)} \frac{k^{N/2(2k)!}}{(N/2-k)!k!(k-1)!(n-k)!(2k-n)!} \tag{5.35}$$

with N even.

The Stehfest method is significantly faster than the finite difference method, however it is more unstable and one must be careful to the choice of N, which gives inaccurate results beyond certain values. We computed and compared both the methods introduced here, finding an excellent agreement between the two for the range of parameters that we use in the next section. Therefore, in the following we report the results obtained with the Laplace method, which is computationally less expensive than the finite difference method.

5.3 1D reservoir

We consider the results of Eq. (5.23) and Eq. (5.24) as a starting point and study the case of the impurity trapped in a 1D reservoir with $l_z \gg l_r$, so that $\mu_b = \frac{\hbar^2}{2m_b\xi^2} = g_{bb}\rho_0 \ll \hbar\omega_r$, where we introduced the healing length $\xi = \frac{1}{\sqrt{8\pi\rho_0 a}} \gg \frac{l_r}{\sqrt{2}}$. We assume the system to be in the limit $l_r > a$, where a is the scattering length of the atoms in the reservoir, so that the interaction strength in 1D is given by

$$g_{ab}^{(1D)} = \frac{g_{ab}^{(3D)}}{(\sqrt{2\pi}l_r)^2} = \frac{4\pi\hbar^2 a_{ab}}{2\tilde{m}} \frac{1}{2\pi l_r^2} = \frac{\hbar^2 a_{ab}}{\tilde{m} l_r^2}, \tag{5.36}$$

where $\tilde{m} = \frac{m_a m_b}{m_a+m_b}$ is the reduced mass. Converting the density to one direction from $\rho_0^{(3D)} = N/l_z l_r^2 = \rho_0^{(1D)}/l_r^2$, we obtain that $g_k^2/\hbar^2$ in the 1D limit can be rewritten

(omitting the superindex "(1D)") as

$$\frac{g_k^2}{\hbar^2} = \frac{(2\pi)^2 g_{ab}^2 \rho_0}{\hbar^2 l_z}. \tag{5.37}$$

Extending the sum over k to the continuum, we obtain the 1D correlation function

$$\begin{aligned}\alpha(t-s) &= \sum_k \frac{g_k^2}{\hbar^2} e^{-i(\omega_k-\omega)(t-s)} \frac{k^2 r_0^2}{2} e^{-k^2 r_0^2/2} \\ &= \frac{(2\pi)^2 g_{ab}^2 \rho_0}{l_z \hbar^2} \frac{l_z}{2\pi} \int_0^\infty \frac{k^2 r_0^2}{2} e^{-k^2 r_0^2/2} e^{-i(\omega_k-\omega)(t-s)} dk \\ &= \frac{2\pi g_{ab}^2 \rho_0}{\hbar^2} \int_0^\infty \frac{k^2 r_0^2}{2} e^{-k^2 r_0^2/2} e^{-i(\omega_k-\omega)(t-s)} dk. \end{aligned} \tag{5.38}$$

Considering the supersonic limit (which is typical for optically trapped impurities in a BEC), i.e., coupling to the particle branch of the dispersion relation, where $\epsilon_k = \frac{\hbar^2 k^2}{2m_b}$, the integration over k of the equation above leads to

$$\alpha(t-s) = \frac{g_{ab}^2 \rho_0}{2\pi\hbar^2} \sqrt{\frac{\pi}{2}} \frac{\hbar\, m_b^{3/2} e^{i\omega(t-s)}}{2m_a\omega \left(\frac{\hbar m_b}{m_a\omega} + i\hbar(t-s)\right)^{3/2}}. \tag{5.39}$$

The power law in the time dependence is typical of non-Markovian systems. In order to understand in what regime the environment is non-Markovian, we need to compare the timescales of the system with the correlation time of the reservoir, that we can obtain from the correlation function.

As discussed in Chapter 3, the Born-Markov approximation relies on the assumption that the correlation time of the bath is much smaller than the relaxation time of the system, so that the contributions of the environment to the dynamics of the system at all times would be the same. However, the the power law dependence in the correlation function obtained in Eq. (5.39) suggests that the correlation times can be large compared to the system timescale, and as the correlation function acts as a the kernel of the bath, the environment can have memory and induce a non-Markovian dynamics.

Aiming to explore the non-Markovian dynamics, in the following we estimate the relevant timescales (correlation time of the bath and relaxation time of the system) to

characterise the regime of the dynamics.

We estimate the correlation time of the reservoir as the time τ_B at which $\alpha(\tau_B) = \alpha(0)/e$, as shown in Fig. 5.1 obtaining

$$\tau_B \omega = \frac{m_b}{m_a}\sqrt{e^{4/3}-1} = 1.67\frac{m_b}{m_a}. \tag{5.40}$$

In the units used, this result depends only on the ratio between the masses, since the other parameters are included in the maximum value of the correlation function

$$\alpha(0) = \frac{g_{ab}^2 \rho_0}{4\sqrt{2\pi}\hbar^{5/2}}\sqrt{m_a \omega}. \tag{5.41}$$

For the case $m_a = m_b$, we obtain the correlation time of the reservoir $\tau_B \omega \approx 1.67$.

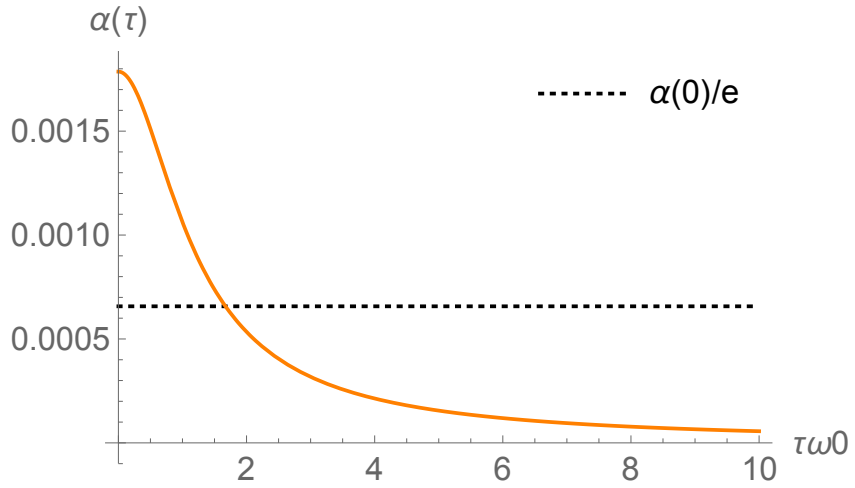

Figure 5.1: Correlation function (solid line) obtained from Eq. (5.39) as a function of τ (in units of the trapping frequency of the impurity ω), obtained for a value of $\omega = 0.5$. The constant value $\alpha(0)/e$ defined by the dashed line was used to estimate the correlation time of the bath, defined from $\alpha(\tau_B) = \alpha(0)/e$, giving $\tau_B \omega = m_b/m_a\sqrt{e^{4/3}-1} \approx 1.67$ with the parameters used here ($m_b = m_a$).

In order to estimate the relaxation time of the system, we consider the dynamics in the Markovian regime, as in this limit the correlation function is delta-correlated and gives rise to an exponential decay with a rate that determines the relaxation time.

In the Markovian limit, the probability amplitude $c_{10}(t)$ can be estimated from the

relation

$$\dot{c}_{10}(t) = -c_{10}(t)\int_0^\infty \alpha(t-s)ds = -\frac{c_{10}(t)}{2}\int_{-\infty}^\infty \alpha(t-s)ds = -\frac{g_{ab}^2\rho_0 m_b^{3/2}e^{-m_b/m_a}}{(2\pi)^2\sqrt{2\omega\hbar^5}m_a}c_{10}(t), \tag{5.42}$$

which gives an exponential decay of the form

$$c_{10}(t) = c_{10}(0)e^{-\Gamma t}, \tag{5.43}$$

with the decay rate

$$\Gamma = \frac{g_{ab}^2\rho_0 m_b^{3/2}e^{-m_b/m_a}}{2(2\pi)^2\sqrt{2\omega\hbar^5}m_a}, \tag{5.44}$$

from which we can define the relaxation time of the impurity as $\tau_R = 1/\Gamma$.

From Eq. (5.39) we can see that the information on the spatial confinement given by the width l_z disappeared as a result of the integration over the continuum in the k space. We could look at the effect that changing different parameters has on the dynamics of the system, but here we limit our study to the changes of the impurity trapping frequency ω. This allows us to explore, within the secular approximation, different regimes depending on the ratio τ_B/τ_R between the correlation time of the reservoir and the relaxation time of the system. As previously discussed in Chapter 3, the Markov approximation is valid in the limit $\tau_B/\tau_R \ll 1$, therefore we expect that going beyond this condition, to the limit $\tau_B/\tau_R \gtrsim 1$, we would observe features of non-Markovian dynamics.

From the decay rate in Eq. (5.44), obtained with the Markov approximation, we see that this decreases for increasing trapping frequency ω, so the exponential decay of the occupation probability of the excited state is determined by longer relaxation times. It is convenient to write this in units of the oscillation period for a better comparison with the correlation time of the reservoir in Eq. (5.40). We expect that when the relaxation time τ_R and the correlation time τ_B become comparable, non-Markovian features arise, therefore in the following we compare the dynamics obtained within the Markov approximation with the dynamics generated by Eq. (5.24), for different values of the impurity trapping frequency ω.

From Fig. 5.2 we observe that an increase of the frequency implies a longer decay time τ_R, consistently with the prediction given by the decay rate of Eq. (5.44).
Comparing this to the value of the correlation time of the bath $\tau_B\omega \approx 1.67$ obtained in Eq. (5.40), we can explain the non-Markovian features observed in Fig. 5.2. The dynamics is Markovian for higher values of the frequency $\omega = 0.5$, corresponding to a relaxation time $\tau_R\omega \approx 54$, implying $\tau_B/\tau_R \approx 0.03$. In the intermediate case $\omega = 0.1$, the relaxation time $\tau_R\omega \approx 5$ starts becoming comparable to the correlation time of the bath ($\tau_B/\tau_R \approx 0.33$) and we can see that at earlier times the decay is not exactly exponential and presents some deviations from the Markovian limit. Finally, when $\omega = 0.01$, corresponding to a relaxation time $\tau_R\omega \approx 0.15$ ($\tau_B/\tau_R \approx 11$), we clearly see a non-Markovian dynamics with oscillations of the probability amplitude. These oscillations characterise the backflow of information induced by the environment, which can happen only if memory effects are taken into account.

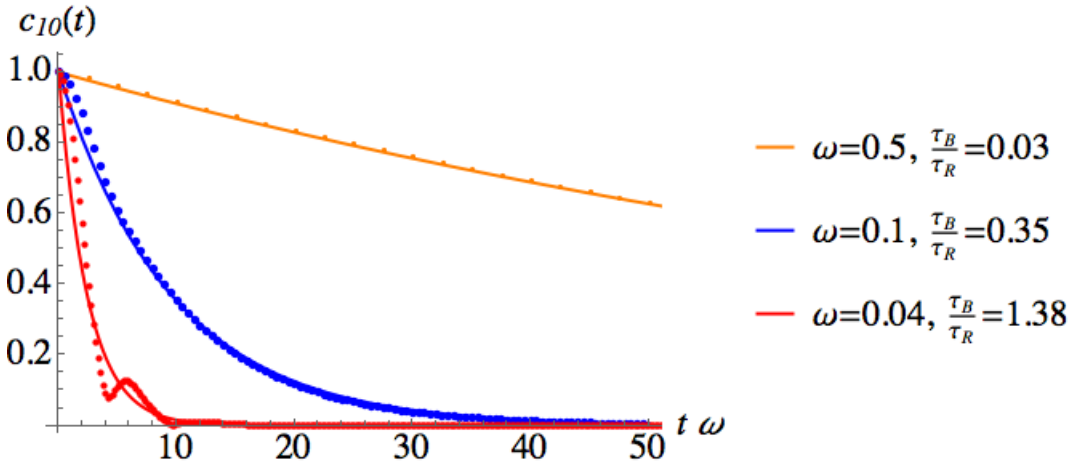

Figure 5.2: Occupation probability obtained with the Markov approximation (solid lines) and non-Markovian case (dotted lines) for different values of ω, as a function of time in units of ω. Increasing the oscillation length gives rise to non-Markovianity as a consequence of the fact that the relaxation and the bath correlation time respectively decreases and increases, yielding an overall increase of τ_B/τ_R. Non-Markovian effects appear when $\tau_B/\tau_R > 1$. The non-Markovian case was computed by using the inverse Laplace transform method with Stehfest algorithm from Eq. (5.34), with $N = 16$.

5.4 Conclusions

We presented some preliminary calculations identifying non-Markovian effects induced by a superfluid reservoir on an impurity, modeled as a two-level atom initially excited. In particular we observed how changing the trapping of the impurity can lead to changes in the dynamics from Markovian to non-Markovian, as a result of the ratio between the correlation time of the bath and the relaxation time of the system. These calculations are a good starting point to study non-Markovian dynamics induced by changes in other physical parameters, such as the coupling strength between the impurity and the superfluid. Another possibility to study non-Markovian behaviours is given by changes in the size of the reservoir, where considering coupling to a finite number of modes allows us to reach the limit of a system analogous to an atom in a multimode cavity, but with the possibility to observe regimes where the environment can have either a linear or quadratic dispersion relation. Other future perspectives include the study of the impurity trapped in 2D and 3D reservoirs, as well as the study of more impurities in the reservoir.

Non-Markovian dynamics has been experimentally observed, in the context of dual species experiments and in particular polaron physics [157, 175], showing that different dimensional confinements and strong interactions can induce features of non-Markovian dynamics, such as Rabi oscillations.

Overall, this system provides an incredibly useful platform, even with experimental perspectives, to conduct a plethora of studies on non-Markovian dynamics. This is due to the fine control that we have, even experimentally, over different parameters, which allows us to explore different regimes relevant to reservoirs with memory effects.

Chapter 6

Collective oscillations of a trapped BEC in tilted ring potentials

6.1 Introduction

Since the realisation of BEC in cold atoms, lots of attention has been oriented towards the study of the collective amplitude oscillations of trapped condensates, both theoretically [97–104] and experimentally [105–107] in order to explore different novel collective properties of this system. In particular, the interaction between the atoms generating nonlinear dynamics has been observed to give rise to phenomena such as frequency shifts of the oscillations [97–101, 103, 176], collapse and revivals of the density oscillations [103, 176] and mode coupling inducing harmonic generation due to transfer of population to higher modes[109, 177].

The study of collective oscillations gives us tools to understand how the dynamics and the thermodynamics of a BEC are affected by the interactions, for different geometrical configurations and different regimes determined by the interaction strength. Most of the studies of collective excitations, both experimentally and theoretically, were done for dynamics of BECs trapped in harmonic potentials in different configurations, from spherically symmetric isotropic traps [97] to anisotropic axially symmetric potentials

[98, 99, 103, 109, 110].

Different approaches were used for these theoretical studies, which include numerical solutions of the Bogoliubov-Hartree theory [102], solving the wave equation obtained from the hydrodynamic equations [97], or using a variational method to study the lowest modes of the system's dynamics through minimisation of the action, given the Lagrangian of the system and an ansatz [98]. In all of these cases the main feature observed is that the frequencies of oscillations are shifted due to the interaction between the particles of the condensate, and these shifts vary depending on the interaction strength, the geometry of the potential and the symmetry of the system.

Finite temperature models have also been studied, both theoretically, and explicitly in experiments as a function of temperature [106, 178–180], to understand how thermal excitations affect damping and frequency shifts of the collective excitations. Different theories were provided, using a mean-field collisionless description in the Popov approximation [181] where the thermal cloud is considered static [182–184], as well as considering the coupled dynamics of both the BEC and the thermal cloud [185, 186], showing how the symmetry of the trapping potential has a strong influence on the damping of the collective excitations [187].

Collective oscillations of trapped BEC were mainly studied for harmonic trapping potentials, in both isotropic and anisotropic configurations, but not as much attention has been devoted towards the case of anharmonic trapping potentials. In the latter case however, the interplay between two non-linear terms with different origins (one related to the anharmonicity of the potential, and one due to the interaction within the BEC) gives rise to a different kind of dynamics compared to the harmonic potential case, affecting frequency shifts, coupling between the modes and collapse and revivals of the wavepackets [121, 122]. These effects will be subject of the investigations in this chapter.

The study of Bose-Einstein Condensates dynamics in anharmonic traps is gaining more attention, in particular after the achievement of neutral atom storage in tilted ring traps [21–23, 115, 116], as well as the realisation of exciton-polariton condensates in microcavity rings [114], which we discuss in Chapter 7 and played a large part in the motivation

of this study. Ring potentials have been shown to be a powerful platform for developments in the field of atomtronics, with the realisation of atom "circuits" [45] due to the achievement of stable persistent flow [23] and in the context of atom interferometry [118, 119], in particular for the study of Sagnac interferometry [117]. Motivated by these opportunities, a detailed understanding of the Bose-Einstein Condensate induced dynamics in this geometry is therefore particularly important. In this chapter we extend the study of collective oscillations to the case of a tilted ring potential of the form $V_{ring}(\theta) = \frac{V_0}{2}(1-\cos(\theta))$, for oscillations at small angles around the bottom of the ring. Using the Gross-Pitaevskii Equation (GPE) to simulate the dynamics of the out-of-equilibrium BEC in the ring, we study the collective oscillations analysing the Fourier frequency spectra of the density in time, at different points in the ring. This allows us to study the oscillation frequency of the center of mass and the width of the wavepacket, related respectively to the dipole and monopole mode. We observe how the non-linearity intrinsically included in the anharmonic potential, combined with the one given by the repulsive interaction within the BEC, affects the dynamics of the dipole mode, which in the harmonic trapping configuration is left invariant, and of the monopole mode. For the latter, we find an empirical relation between the frequency shift of the width oscillation and its revival frequency.

This chapter is organised as follows. In Section 6.2 we introduce the model for the trap geometry examined, and considering a quartic anharmonic potential as perturbation of the harmonic oscillator for a single particle system, we use a perturbation theory approach to the first order in the anharmonic parameter, seeing how this gives rise to a revival of the density oscillations in the dynamics of a single particle wavefunction. We use this approach to define the revival frequencies of the center of mass and width of the wavepacket determined exclusively by the anharmonicity of the potential.

In Section 6.3 we introduce the methods used to study the lower-frequency modes, which include analytical, semi-analytical and numerical approaches. In particular, we simulate numerically the dynamics of a wavepacket in the harmonic oscillator and ring potential using the Gross-Pitaevskii Equation, and introduce an analytical method that relies on the use of a variational approach for the Lagrangian of the system, based on

a Gaussian ansatz [98]. We discuss the calculations for the 1D harmonic potential and extend these to the case of the quartic anharmonic potential. We furthermore present the Fourier transform scheme used to study the frequency modes of the density oscillations.

In Section 6.4 we introduce the central and non-central configurations that we use in our study, and simulate the dynamics in the two cases for both the ring and the HO potentials, observing, from the GPE simulations, how the kind of potential changes the dynamics and has effect on phenomena such as collapse and revivals in the oscillations. In Section 6.5 and Section 6.6 we discuss, separately, some features identified by the analysis of the frequency spectra obtained from the density oscillations of the wavepacket in the different potentials and configurations. These include the observation of sidebands, frequency shifts of the modes and changes in the revival frequency with increasing interaction strength. For this analysis, we compare the numerical results obtained with the GPE and the analytical results provided by an approach that uses perturbation theory and the variational method.

6.2 Model

The ring potential that we consider is given by

$$V_{ring}(\theta) = \frac{V_0}{2}(1 - \cos(\theta)), \tag{6.1}$$

where V_0 is fixed and it is the potential energy at the top of the ring ($\theta = \pi$).

If the motion is confined to small angles around the bottom of the ring ($\theta = 0$), then the above potential can be expanded in a Taylor series as

$$V_{\text{ring}}(\theta) \simeq \frac{V_0}{2}\left(1 - \left(1 - \frac{\theta^2}{2!} + \frac{\theta^4}{4!} - \frac{\theta^6}{6!} + ...\right)\right). \tag{6.2}$$

Retaining the terms up to the second order, we obtain the potential of a harmonic oscillator

$$V_{HO} = \frac{1}{4}V_0\theta^2 = \frac{1}{2}m\omega_{ho}^2 R^2\theta^2, \tag{6.3}$$

where

$$V_0 = 2m\omega_{ho}^2 R^2, \tag{6.4}$$

with m being the mass of the BEC atoms, R the radius of the ring and

$$\omega_{ho} = \sqrt{\frac{V_0}{2mR^2}}, \tag{6.5}$$

the trapping frequency of the harmonic oscillator potential.
Going to the next order in the Taylor expansion, we obtain the Quartic Anharmonic Oscillator (QAO) potential of the form

$$V_{QAO} = \frac{V_0}{2}\left(\frac{\theta^2}{2} - \frac{\theta^4}{4!}\right) = \frac{1}{2}m\omega_{ho}^2\left(R^2\theta^2 - \frac{R^4\theta^4}{12R^2}\right) = \frac{1}{2}m\omega_{ho}^2\left(z^2 - \frac{1}{12R^2}z^4\right). \tag{6.6}$$

The form of the ring potential and its approximations to the HO and QAO are represented in Figure 6.1. For the numerical simulations we use the full form of the ring potential, but as presented in the next sections, we use the quartic approximation to find the correction to the energy of the harmonic oscillator. This is a good approximation for the case analysed, as we do not consider rotational dynamics of the BEC around the whole ring and we only study cases where the BEC expands in the region $\theta < 2$ and $\theta > 4$, where the quartic potential is still a good approximation of the ring.

6.2.1 First order perturbation theory for the quartic potential

We make use of time-independent perturbation theory to the first order to study the energy spectrum of the quartic anharmonic oscillator for a single particle and we show how this implies a shift of the unperturbed harmonic oscillation energy spectrum, and also how from this we can obtain the emergence of phenomena such as revivals (and similarly super-revivals going to higher orders of the expansion in Eq. (6.2)). Noticing that Eq. (6.6) has the form

$$V_{QAO} = V_{ho} + V_4 = \frac{1}{2}m\omega^2\left(R^2\theta^2 - \frac{R^4\theta^4}{12R^2}\right) = \frac{1}{2}m\omega^2\left(z^2 + \zeta z^4\right), \tag{6.7}$$

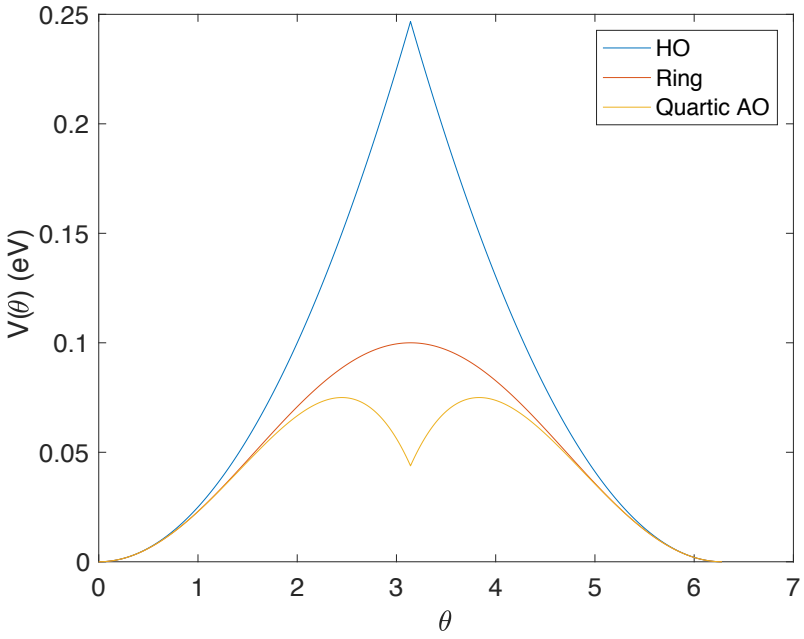

Figure 6.1: Comparison between ring potential, harmonic and quartic approximations for small values of the angle around the center. The values used are $V_0 = 0.1$ eV and $R = 2$ μm. Although these parameters are not typical of experiments (for experiments on polaritons, as discussed in the next chapter, experimental parameters for potential and radius are $V_0 = 1$ eV and $R = 40 - 60$ μm), we used them to access a regime where we could observe revivals at convenient timescales. To be consistent with the applications to polariton BECs covered in Chapter 7, we consider the mass $m = 8.3 \times 10^{-5} m_e$, where $m_e c^2 = 0.51$ MeV is the electron rest-mass energy.

with $\zeta = -\dfrac{1}{12R^2}$, we can consider the quartic term V_4 as a perturbation to the harmonic oscillator Hamiltonian (we neglect the interaction between the atoms of the BEC for the moment and consider the case of a single particle in the harmonic potential),

$$H_{QAO} = \frac{p^2}{2m} + \frac{1}{2} m\omega_{ho}^2 z^2 + \frac{1}{2} m\omega_{ho}^2 \zeta z^4. \tag{6.8}$$

Using the definition of the position operator $\hat{z}$ in terms of the construction and annihilation operators $\hat{a}, \hat{a}^\dagger$ on number states,

$$\hat{z} = \sqrt{\frac{\hbar}{2m\omega_{ho}}} (\hat{a} + \hat{a}^\dagger), \tag{6.9}$$

the correction to the first order of the energy is given by

$$E_n^{(1)} = \langle n|V_4|n\rangle = -\frac{V_0}{48R^4}\langle n|\hat{z}^4|n\rangle = -\frac{V_0}{48R^4}\frac{\hbar^2}{4m^2\omega_{ho}^2}\langle n|(\hat{a}+\hat{a}^\dagger)^4|n\rangle\,. \tag{6.10}$$

The only non-zero terms in the matrix element are the ones that conserve the number of excitations, giving $\langle n|(\hat{a}+\hat{a}^\dagger)^4|n\rangle = 3(2n^2+2n+1)$, hence

$$E_n^{(1)} = -\frac{V_0}{48R^4}\frac{\hbar^2}{4m^2\omega_{ho}^2}3(2n^2+2n+1) = -\frac{\hbar^2}{32mR^2}(2n^2+2n+1), \tag{6.11}$$

where in the last equality the definition of V_0 from Eq. (6.4) was used.
The energy spectrum of Eq. (6.8) corrected to the first order is then

$$E_n = E_n^{(0)} + E_n^{(1)} = \hbar\omega_{ho}\left(n+\frac{1}{2}\right) - \frac{\hbar^2}{16mR^2}\left(n^2+n+\frac{1}{2}\right). \tag{6.12}$$

In Figure 6.2 we show the eigenvalues of the Hamiltonians with the different potentials discussed so far.
As previously mentioned, the particularity of the ring potential that we analyse here is that, even in absence of a non-linear term given by the interactions, it exhibits revivals and super revivals due to the higher order terms in Eq. (6.2). The timescales associated with these can be estimated by expanding the eigenvalues of the harmonic oscillator corrected with higher order terms around a quantum number $n_0 \gg 1$ (defining the average occupied state), so that

$$E(n) \approx E(n_0) + E'(n_0)(n-n_0) + \frac{E''(n_0)}{2}(n-n_0)^2 + \frac{E'''(n_0)}{6}(n-n_0)^3 + ..., \tag{6.13}$$

where $E^p(n_0) = (d^pE_n/dn^p)_{n=n_0}$. The classical, revival and super-revival periods are respectively defined as

$$T_{\rm cl} = \frac{2\pi\hbar}{|E'(n_0)|}; \quad T_{\rm rev} = \frac{2\pi\hbar}{|E''(n_0)|/2}; \quad T_{\rm sup} = \frac{2\pi\hbar}{|E'''(n_0)|/6}. \tag{6.14}$$

For the unperturbed harmonic oscillator, since the energy spectrum has the form $E_n = \hbar\omega_{\rm ho}(n+1/2)$, we recover, from the term $E'(n_0) = \hbar\omega_{\rm ho}$ in Eq. (6.13), the classical

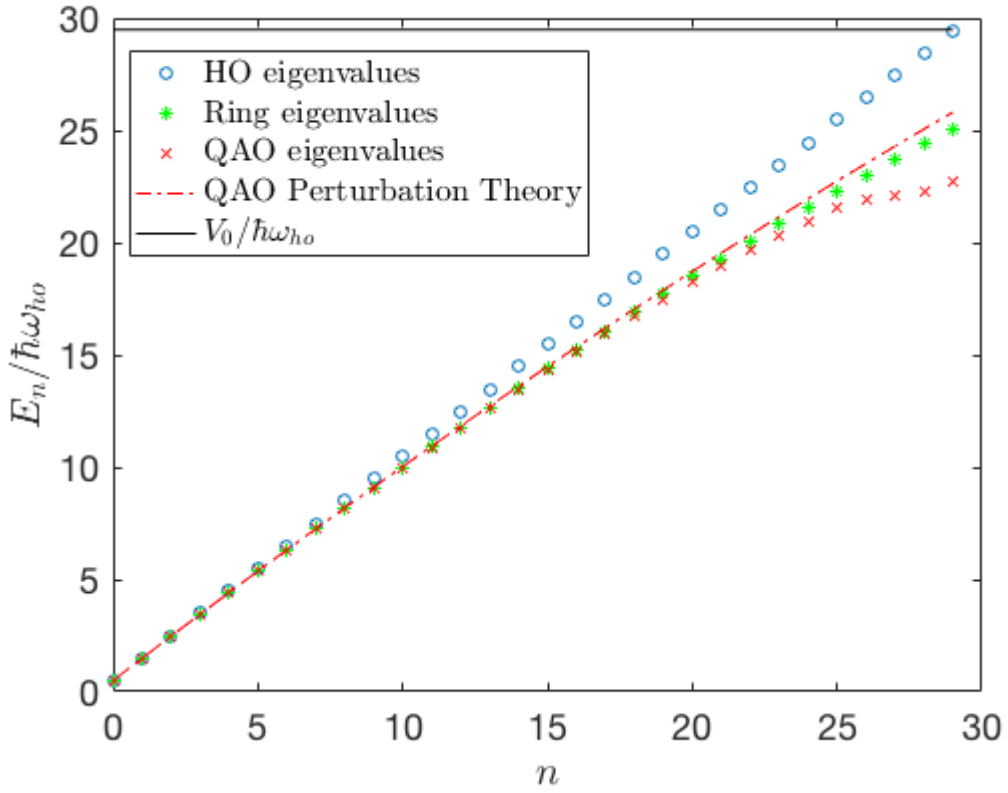

Figure 6.2: Eigenenergies in units of the harmonic oscillator energy spacing for harmonic oscillator, ring, and quartic anharmonic oscillator, the latter being estimated both numerically and from the first order perturbation theory as in Eq. (6.12). The parameters used here are $V_0 = 0.1$ and $R = 2$, and the number of bound states with these is $V_0/\hbar\omega_{ho} \sim 29$ (black solid line) if we consider equally separated energy levels. The steps in the eigenvalues of the QAO potential are due to the fact that the peak of the potential, as seen in Fig. 6.1 is lower, so the number of bound states in these cases is $3V_0/4\hbar\omega_{ho} \sim 22$. In the following we will limit our study to the case where the system does not reach such excited states, staying in the regime $n < 18$, where we can see that the eigenvalues of the QAO, evaluated with both methods, are very close to the ones of the ring.

oscillation period $T_{\rm cl}^{(\rm ho)} = \dfrac{2\pi}{\omega_{\rm ho}}$. If we consider the energy spectrum of the quartic anharmonic oscillator as in Eq. (6.12), we find, however, that

$$E'(n_0) = \hbar\omega_{ho} - \frac{\hbar^2}{16mR^2}(2n_0 + 1). \tag{6.15}$$

From Eq. (6.13) we obtain the corrected classical frequency of the quartic harmonic

oscillator

$$\omega_{\rm cl}^{\rm (QAO)} = \omega_{\rm ho} - \frac{\hbar}{16mR^2}(2n_0+1), \tag{6.16}$$

which is then shifted compared to the harmonic potential case, with a shift that depends on the average occupied state n_0.

From Eq. (6.13) the term at the second order then corresponds to

$$\frac{E''(n_0)}{2} = \frac{d^2E_n}{2dn^2}\bigg|_{n=n_0} = -\frac{\hbar^2}{16mR^2}, \tag{6.17}$$

giving the revival frequency

$$\omega_{\rm rev} = \frac{\hbar}{16mR^2}, \tag{6.18}$$

and the revival period

$$T_{\rm rev} = \frac{32\pi mR^2}{\hbar}. \tag{6.19}$$

By substituting (6.18) in (6.12), this can be rewritten as

$$E_n = \hbar\omega_{\rm ho}\left(n+\frac{1}{2}\right) - \hbar\omega_{\rm rev}\left(n^2+n+\frac{1}{2}\right), \tag{6.20}$$

and we observe that the classical frequency (6.16) can then be rewritten as

$$\omega_{\rm cl}^{\rm (QAO)} = \omega_{\rm ho} - \omega_{\rm rev}(2n_0+1), \tag{6.21}$$

depending on the average occupied state n_0. The revival period, in units of the classical oscillation period, is then given by

$$\frac{T_{\rm rev}}{T_{\rm cl}} = \frac{2|E'|}{|E''|} = \frac{\omega_{\rm cl}^{\rm (QAO)}}{\omega_{\rm rev}} = \frac{\omega_{\rm ho}}{\omega_{\rm rev}} - (2n_0+1). \tag{6.22}$$

Analogously, if we had to consider the next order in Eq. (6.2) for the sixth power, we would obtain another shift in the harmonic oscillator frequency, giving a classical and a revival frequency dependent on n_0^2 and n_0 respectively, and a super-revival frequency not dependent on n_0.

6.3 Methods

6.3.1 Variational method for the evaluation of the lowest mode frequencies

The problem of finding analytical forms for the collective excitations of a BEC in different potentials and geometries has been of vast interest since the achievement of Bose-Einstein Condensation of alkali atoms. Some analytical solutions have been found in certain limits and have shown good agreement with the experimental observations. Different approaches have been used to study collective modes theoretically, mostly using the hydrodynamic equations [97, 101, 103, 110, 188] to derive analytical expressions for spherical and anisotropic harmonic traps, or using the linear-response theory for a condensate with an oscillatory perturbation and solving the equations numerically [99], or by using a variational approach [98]. We use the latter method to find the lowest modes in the case of quartic (anharmonic) trapping potential, so that we can compare these results with the ones obtained from the full dynamics in the ring. The variational approach method consists minimizing the action, given the Lagrangian and an ansatz that takes the form of a Gaussian,

$$\psi(z,t) = \sqrt{\frac{N}{\sqrt{\pi}\sigma(t)}} e^{-(z-z_0(t)^2)/2\sigma^2(t) + i\alpha(t)z + i\beta(t)z^2}, \tag{6.23}$$

where the imaginary components of the slope (α) and of the curvature ($\beta^{-1/2}$) have been shown to be necessary for more precise predictions [189]. After inserting this into the Lagrangian of the form

$$L = \int dz \left[\frac{i}{\hbar} \left(\psi^* \frac{\partial \psi}{\partial t} - \psi \frac{\partial \psi^*}{\partial t} \right) - \frac{\hbar^2}{2m} |\nabla \psi|^2 + V(z)|\psi|^2 + \frac{g}{2}|\psi|^4 \right], \tag{6.24}$$

we use the Euler-Lagrange equation

$$\frac{\partial L(t, q_i(t), \dot{q}_i(t))}{\partial q_i} - \frac{d}{dt} \frac{\partial L(t, q_i(t), \dot{q}_i(t))}{\partial \dot{q}_i} = 0, \tag{6.25}$$

for all the variables of the Gaussian in order to obtain the equations of motion for those. The differential equations obtained for the width σ and the center of the Gaussian z_0 (corresponding to the center of mass), will then give respectively the breathing and the dipole frequencies. We summarise the results obtained with this procedure for the QHO and compare them to the ones obtained for the anharmonic oscillator with a quartic term.

Variational method for the 1D mean-field case in a harmonic potential

Since we extend the the approach used for the anisotropic harmonic oscillator [98] to the anharmonic potential, we start by summarising the results obtained for the case of an anisotropic harmonic potential in the 1D limit $\lambda = \omega_z/\omega_\perp < 1$, where $\omega_\perp = \omega_x = \omega_y$ is the radial frequency and $\omega_z = \omega_{\rm ho}$. We assume that the system is in the 1D mean field approximation, determined by the condition

$$N\lambda a/l_\perp \ll 1, \tag{6.26}$$

where $l_\perp = \sqrt{\hbar/m\omega_\perp}$ is the radial oscillation length and a is the scattering length. In the 1D mean field approximation we assume that only one mode (the ground state) in the radial direction is populated, so that we can describe the wavefunction in the radial direction as a Gaussian whose widths and centers are always at equilibrium radially, assuming that the radial potential is harmonic. Conversely, for the axial direction z, we will use the ansatz of Eq. (6.23). We therefore consider the Lagrangian as in Eq. (6.24) for the dynamics in one direction only, using the value of the interaction strength in 1D, defined as $g_{1D} = \dfrac{g_{3D}}{2\pi l_\perp^2}$, and the potential has the form

$$V(z) = \frac{1}{2}m\omega_z^2 z^2. \tag{6.27}$$

By using the Euler-Lagrange equations for the variables $\alpha(t)$ and $\beta(t)$ of Eq. (6.23), we

obtain

$$\alpha(t) = -\frac{mz_0'(t)}{\hbar} - 2\beta(t), \tag{6.28}$$

$$\beta(t) = -\frac{m\sigma(t)\sigma'(t) + 2mz_0(t)z_0'(t) + 2\hbar\alpha(t)z_0(t)}{2\hbar\sigma(t)^2 + 4\hbar z_0(t)^2}, \tag{6.29}$$

which can be rearranged in the form

$$\alpha(t) = \frac{mz_0(t)\sigma'(t) - m\sigma(t)z_0'(t)}{\hbar\sigma(t)}, \tag{6.30}$$

$$\beta(t) = -\frac{m\sigma'(t)}{2\hbar\sigma(t)}. \tag{6.31}$$

For the Euler-Lagrange equations of the two remaining variables σ and z_0, we insert in these the forms of $\alpha(t)$ and $\beta(t)$ and obtain the two differential equations

$$\sigma''(t) = -\omega_z^2\sigma(t) + \frac{g_{1D}N}{\sqrt{2\pi}m\sigma(t)^2} + \frac{\hbar^2}{m^2\sigma(t)^3}, \tag{6.32}$$

$$z_0''(t) = -\omega_z^2 z_0(t), \tag{6.33}$$

consistent with the 1D limit of the results reported in [98]. It can be immediately seen that the center of mass z_0 will still oscillate with the same frequency ω_z and therefore the dipole mode has a frequency

$$\omega_D = \omega_z, \tag{6.34}$$

which is unaffected by interactions in this limit. Conversely, the oscillations of the width of the Gaussian, which describe monopole oscillations, are affected by the interaction strength and by the number of particles. The correct dynamics of these two quantities can be computed using numerical methods for the solution of differential equations (e.g. Runge-Kutta), which we will use in the next sections for the anharmonic potential. More approximate analytical solutions can also be found by linearising the equations around the stationary points. In particular, after seeing that the dipole frequency is not affected by finite interactions, in order to find an analytical form of the monopole frequency, from Eq. (6.32), imposing $\sigma''(t) = 0$, we find the stationary points σ_e (including

both stable and unstable solutions)

$$\omega_z^2\sigma_e - \frac{g_{1D}N}{\sqrt{2\pi}m\sigma_e^2} - \frac{\hbar^2}{m^2\sigma_e^3} = 0. \tag{6.35}$$

From the expansion around these points we can proceed with the linearisation of the differential equations of the kind

$$\frac{d^2\sigma}{dt^2} = \frac{d^2(\sigma-\sigma_e)}{dt^2} = f(\sigma) \simeq f(\sigma_e) + f'(\sigma_e)(\sigma-\sigma_e), \tag{6.36}$$

where, since $f(\sigma_e) = 0$ by definition, we obtain

$$\sigma''(t) = -\omega_z^2\left(1 + \frac{2g_{1D}N}{\sqrt{2\pi}m\omega_z^2\sigma_e^3} + \frac{3\hbar^2}{m^2\omega_z^2\sigma_e^4}\right)\sigma(t). \tag{6.37}$$

It is then straightforward to see that solving this gives a monopole frequency of the form

$$\omega_M = \omega_z\sqrt{\left(1 + \frac{2g_{1D}N}{\sqrt{2\pi}m\omega_z^2\sigma_e^3} + \frac{3\hbar^2}{m^2\omega_z^2\sigma_e^4}\right)}, \tag{6.38}$$

where we see that in the zero interaction limit, as the equilibrium width of the Gaussian is the harmonic oscillator length $l_z = \sqrt{\frac{\hbar}{m\omega_z}}$ defining the ground state, we obtain $\omega_M = 2\omega_z$ [1].

Variational method for the 1D mean field anharmonic (quartic) potential

Let us add now a quartic term to the harmonic potential, consistent with the expansion of the ring potential for small angles, where we neglect higher orders. We define this potential as

$$V_q(z) = \frac{m\omega_z}{2}\left(z^2 + \zeta z^4\right), \tag{6.39}$$

where $\zeta = -\dfrac{1}{12R^2}$ and R is the radius of the ring. We use the same approach we used in the previous section, again considering a Gaussian ansatz of the form Eq. (6.23). Adding the extra quartic term in the Lagrangian Eq. (6.24) and using again the Euler-Lagrange equations to find the equations of motion for the variables, we find that,

[1] In the opposite limit, when the interaction strength dominates over the kinetic energy, we should get $\omega_M = \sqrt{3}\omega_z$.

while the expressions for $\alpha(t)$ and $\beta(t)$ are still given by Eq. (6.30) and Eq. (6.31), the equations of motion for the width and the center of the Gaussian are now given by

$$\sigma''(t) = -\omega_z^2\sigma(t)\left(1 + 6\zeta z_0(t)^2 + 3\zeta\sigma^2(t)\right) + \frac{g_{1D}N}{\sqrt{2\pi}m\sigma^2(t)} + \frac{\hbar^2}{m^2\sigma^3(t)} \tag{6.40}$$

$$z_0''(t) = -\omega_z^2 z_0(t)\left(1 + 3\zeta\sigma^2(t) + 2\zeta z_0^2(t)\right). \tag{6.41}$$

By comparing these equations with Eq. (6.32) and Eq. (6.33) we notice the appearance of additional terms with respect to the previous case. In particular we observe that, while in the harmonic oscillator case the dipole mode is not affected by the interactions, now the anharmonicity of the potential affects the dynamics of the center of mass and couples the two differential equations for the width and center of the Gaussian.

As in the harmonic case, we followed the same linearisation approach, based on the expansion in Eq. (6.36), to expand the above differential equations around the equilibrium solutions. This derivation and the results obtained with this approach are shown in Appendix C (Fig. C.1). By comparing these analytical solutions with numerical solutions, we found significant disagreement between the results, which suggests that the order at which we consider the approximation of these solutions, with simple linearisation (as in Eq. (6.36)), is not sufficient. The coupling between the differential equations in this case makes them more sensitive to higher orders in $(\sigma - \sigma_e)$ and $(z_0 - z_{0_e})$ (see Eq. (6.36)).

We can improve the analytical results obtained with a linearisation of both the differential equations for $\sigma(t)$ and $z_0(t)$ around the equilibrium points, presented in Appendix C, by using the linearisation around the equilibrium point to solve only the differential equation $\sigma''(t)$, while we use a more precise solution for $z_0''(t)$, with a different method that we discuss in the following. We refer to this approach as the semi-linearised variational method.

In order to solve Eq. (6.41), instead of expanding this around the equilibrium point $z_{0_{eq}} = 0$, we consider a differential equation of the same form:

$$x''(t) + \omega_0^2 x(t) = -\gamma x(t)^3. \tag{6.42}$$

It can be shown [190], using perturbation theory or the method of averaging [191], that this has solutions with a leading term of the form $x = a\cos(\omega t)$, with

$$\omega = \omega_0 + \Delta\omega = \omega_0 + \frac{3\gamma a^2}{8\omega_0}, \tag{6.43}$$

and $a = x(0)$. In our case, following the mappings $x(t) \to z_0(t)$, $\gamma \to 2\zeta\omega_z^2$ and $\omega_0^2 \to \omega_z^2(1 + 3\zeta\sigma^2)$, we obtain solutions of the form $z_0(t) = z_0(0)\cos(\omega_D t)$, with the initial condition $z_{0_i} = z_0(0)$ and a dipole frequency given by

$$\omega_D = \omega_z\sqrt{1 + 3\zeta\sigma_e^2}\left(1 + \frac{3\zeta z_{0_i}^2}{4(1 + 3\zeta\sigma_e^2)}\right). \tag{6.44}$$

Comparing this result to the harmonic oscillator case $\omega_D = \omega_z$, it can be seen that, because of the anharmonicity given by ζ that couples this to σ, the dipole frequency is now affected by changes of the interaction strength. Different to the linearised case of Eq. (C.5), the dipole mode here shows a dependence on the initial position z_{0_i}, and the existence condition of the solutions is discussed in Appendix C. The monopole frequency, on the other side, is the same as the linearised case:

$$\omega_M = \omega_z\sqrt{1 + 6\zeta z_{0_e}^2 + 9\zeta\sigma_e^2 + \frac{3\hbar^2}{m^2\sigma_e^4\omega_z^2} + \frac{\sqrt{2}g_{1D}N}{\sqrt{\pi}m\sigma_e^3\omega_z^2}}. \tag{6.45}$$

After deriving these analytical results for the dipole and monopole frequencies, we can have better comparisons with the ones obtained for the dynamics in the harmonic potential, and see how the anharmonicity affects them. However, as these analytical methods for the solutions of the differential methods rely on approximations, in the following we use numerical methods to solve the coupled differential equations Eq. (6.40) and Eq. (6.41).

6.3.2 GPE dynamics of a BEC in the 1D HO and ring potentials

We simulate the dynamics of a Bose-Einstein Condensate in the two trapping potentials discussed, by means of the Gross-Pitaevskii equation in one dimension

$$i\hbar\frac{\partial\psi(\theta,t)}{\partial t} = \left(-\frac{\hbar^2\nabla^2}{2m} + V_{ext}(\theta) + g_{1D}|\psi(\theta,t)|^2\right)\psi(\theta,t), \tag{6.46}$$

where we will use the potentials $V_{\text{ext}} = V_{\text{ring}}$ as in Eq. (6.1) and $V_{\text{ext}} = V_{\text{HO}}$ (Eq. (6.3)) respectively for the case of the tilted ring and the harmonic oscillator. The one dimensional description is motivated by the fact that the oscillation length in the radial direction $l_\perp = \sqrt{\hbar/m\omega_\perp}$ is much smaller than the healing length $\xi = \frac{1}{\sqrt{8\pi n_0 a}}$, or equivalently, that $\mu = \frac{\hbar}{2m\xi^2} \ll \hbar\omega_\perp$. Furthermore, as previously mentioned, we limit our study to the 1D mean field case, given by the the condition

$$N\lambda a/a_\perp = \frac{Ng_{1D}\lambda}{2\hbar\omega_\perp l_\perp} \ll 1, \tag{6.47}$$

where we used the definition of the one dimensional interaction strength $g_{1D} = g_{3D}/(2\pi l_\perp^2)$. In the following we will use $\lambda = \omega_z/\omega_\perp = 0.1$, so that the condition Eq. (6.47) is satisfied for $g = g_{1D}/(2\hbar\omega_\perp l_\perp) \ll 10$. For the numerical simulation of the GPE we used the split-step Fourier transform method, which is discussed in Appendix B.

As discussed at the beginning of this chapter, we aim to characterise the collective oscillations by means of the frequency spectra obtained by Fourier transforming the density in time. We therefore simulate the dynamics for different initial configurations in both the ring and harmonic oscillator potential and compare the characteristic features.

Different to previous studies of collective excitations where the wavepacket was subjected to a driving at a determined frequency, here we simply start with a wavepacket out of equilibrium by using an initial Gaussian wavefunction normalised to the number of atoms N,

$$\psi(\theta) = \sqrt{\frac{N}{\sqrt{\pi}\sigma}}e^{-R^2(\theta-\theta_0)^2/(2\sigma^2)}, \tag{6.48}$$

centered at θ_0 and having a width $\sigma = wl_{\text{ho}}$, where $l_{\text{ho}} = \sqrt{\frac{\hbar}{m\omega_{\text{ho}}}}$ is the oscillation length associated with the harmonic potential and w is a factor. In the following we

set $w = 2$, so that we do not start with the ground state of the system (in absence of interaction).

Because of the normalisation of the wavefunction, the interaction term depends on the product Ng, so for simplicity we set $N = 1$ and vary only the values of g. As already mentioned, in order to find a regime where we can more easily observe revival frequencies for the values of g used here with convenient computational times, we consider the 1D dynamics in a ring potential with parameters $V_0 = 0.1$ and $R = 2$.

6.3.3 Evaluation of frequency spectra of the density evaluated at particular points around the ring

In our study we characterise the frequencies at which the condensate oscillates in the trap by analysing the frequency spectra obtained from the evolution of the density at particular points around the ring. Here we describe how the frequency spectra $n(\theta, \nu)$ are obtained from the density $n(\theta, t) = |\psi(\theta, t)|^2$. We use a Suzuki-Trotter decomposition with time steps δt for the numerical evolution of a wavepacket (see Appendix B) in a time $T_{\text{fin}} = n_t \delta t$. In the frequency space the frequency interval is $\delta\nu = 1/T_{\text{fin}}$ and the final frequency for the sampling is given by $\nu_{fin} = 1/\delta t = n_\nu \delta\nu$. The frequency spectrum of the density $n(\theta, t)$ is given by the discrete Fourier Transform, defined as

$$n(\theta, \nu) = \sum_{j_t=0}^{n_t-1} n(\theta, j_t) e^{-i\frac{2\pi}{n_t} j_t \nu}. \tag{6.49}$$

The frequency spectrum obtained is symmetric around the Nyquist frequency defined as $\nu_{Nyq} = \nu_{fin}/2$, and in order to avoid "aliasing" phenomena in the data, we make sure that the time samples are small enough to satisfy the relation $\delta t < 1/(2\nu_{max})$, where ν_{max} is the highest occupied frequency, so that $\nu_{max} < \nu_{Nyq}$.

6.4 Density oscillations in central and non-central configurations

We simulate the dynamics of the wavefunction in two different configurations, depending on the position of the initial Gaussian wavepacket $\psi_{\theta_0}(\theta)$, as pictured in Fig. 6.3, in order to capture the main features of the oscillations and study different modes.

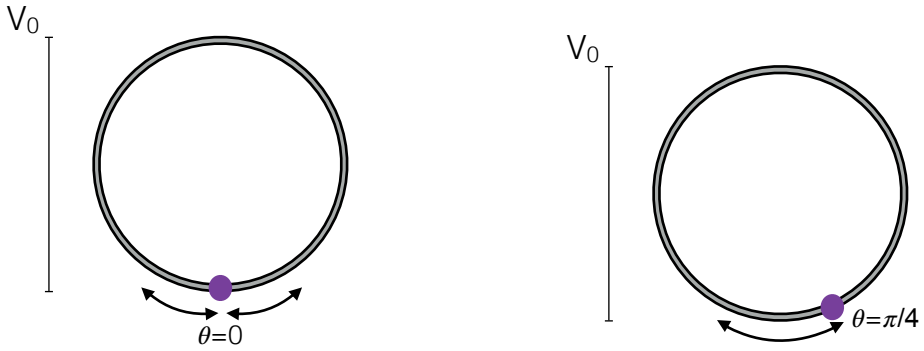

(a) (b)

Figure 6.3: Different configurations of the initial wavepackets $\psi_0(\theta)$ (a) and $\psi_{\pi/4}(\theta)$ (b) used to study central and non-central dynamics in the ring, respectively.

In particular, at first we study the dynamics of a BEC at the bottom of the trap ($\theta_0 = 0$), which we indicate with the notation $\psi_{\theta_0}(\theta) = \psi_0(\theta)$, aiming to characterise the effect of the interaction on the modes with an odd number of nodes (breathing mode and its harmonics) that do not involve the motion of the center of mass (see Fig. 6.3(a)).

Secondly, we study the out of equilibrium dynamics of a wavepacket initially placed at $\theta_0 = \pi/4$, indicated with the notation $\psi_{\pi/4}(\theta)$, for different values of the interaction strength, in both the harmonic oscillator case and the tilted ring potential (Fig. 6.3(b)). The density of the condensate in time and space, obtained with simulation of the dynamics via the GPE, for different values of the interaction strength, is shown in Fig.6.4 and Fig.6.5 for the two initial conditions $\psi_0(\theta)$ and $\psi_{\pi/4}(\theta)$, respectively.

The results presented in both figures have been averaged in space over a grid having a size of $\sim 1\%$ the length of the ring, making the round profile obtained from the sinusoidal oscillations more sharp and triangular. This is however only an effect of

averaging in both position and momentum space.

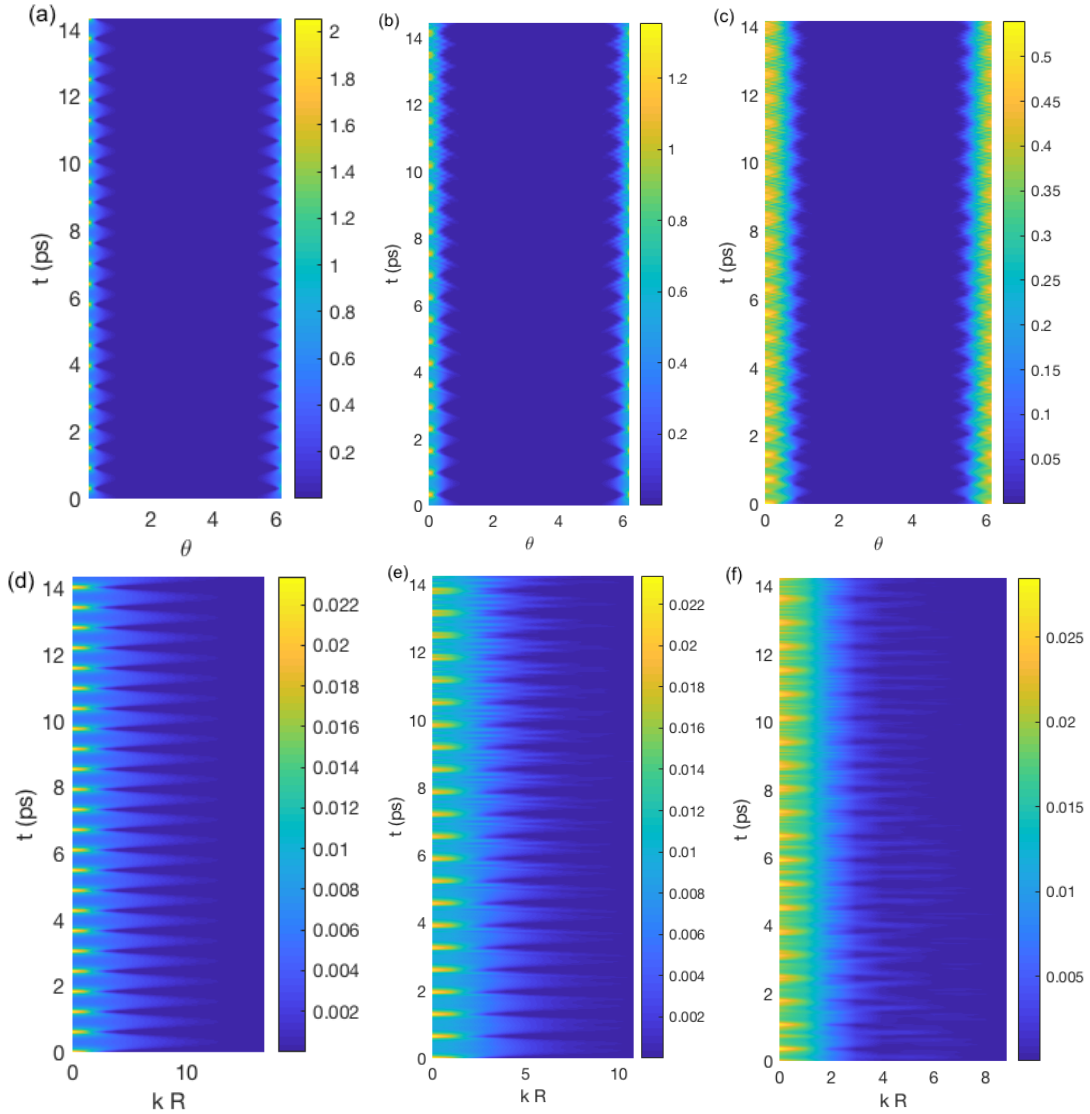

Figure 6.4: Density in position (a-c) and momentum space (d-f) obtained simulating the dynamics with the GPE, for an initial wavepacket $\psi_0(\theta)$ and for different values of the interaction strength $g_{1D}/(2\hbar\omega_\perp l_\perp) = 0, 0.54, 4.5$ (from left to right).

In the case shown in Figure 6.4, where the initial Gaussian is at the bottom of the ring, only the central moments are involved in the dynamics, and we can see how, while at $g = 0$ the Gaussian wavepacket presents breathing but mantains its shape, for increasing values of the interaction strength, interference effects can be observed and the wavepacket form is no longer Gaussian. Although the dynamics here are simulated

using the ring potential in the GPE evolution, we remark that, as the motion is confined at the bottom of the ring for sufficiently small oscillations, we can still treat the system in the harmonic oscillator approximation. Because of the central symmetry, in the following we will refer to this configuration where the wavepacket is initially at $\theta = 0$ as the central harmonic oscillator case.

Conversely, for the case of a wavepacket initially placed at $\theta = \pi/4$, where the anharmonicity becomes relevant in the ring potential, we observe, by comparing the dynamics in the HO and in the ring potentials (Figure 6.5) that this is affected by non-linearity due to the potential itself, in addition to the interaction. More specifically, we see that the dynamics between the two cases is visibly different for lower (panels b-e) and zero (panels a-d) values of the interaction strength, where the wavepacket in the ring potential presents dephasing and loses the Gaussian shape, in contrast to the harmonic potential, where it is preserved. For higher values of the interaction strength however (panel f), the wavepacket starts becoming more stable due to the repulsive interaction energy becoming more relevant, bringing to a dynamics significantly closer to the one observed for the harmonic oscillator. This will be further discussed in the next sections, investigating the first four moments of the distribution in time.

More insights on these effects in the configurations presented here can be obtained by looking at the frequency spectra of the density in the two cases, and we will see how this can be helpful to provide deeper understanding of effects such as frequency shifts of collective modes.

6.4.1 Observation and definition of the revival frequencies in the ring potential

In Section 6.2.1 we discussed the effect of anharmonic corrections to the harmonic potential and showed how the dynamics of a single particle in the quartic potential leads to revivals of the wavefunction at timescales larger than the classical oscillation period, $T_{\mathrm{rev}} > T_{\mathrm{cl}}$. The revival frequency in Eq. (6.18) was estimated with perturbation theory to the first order in the anharmonicity parameter ζ. With the values used in this chapter, reported in the caption of Fig. 6.1, Eq. (6.18) gives a prediction of the

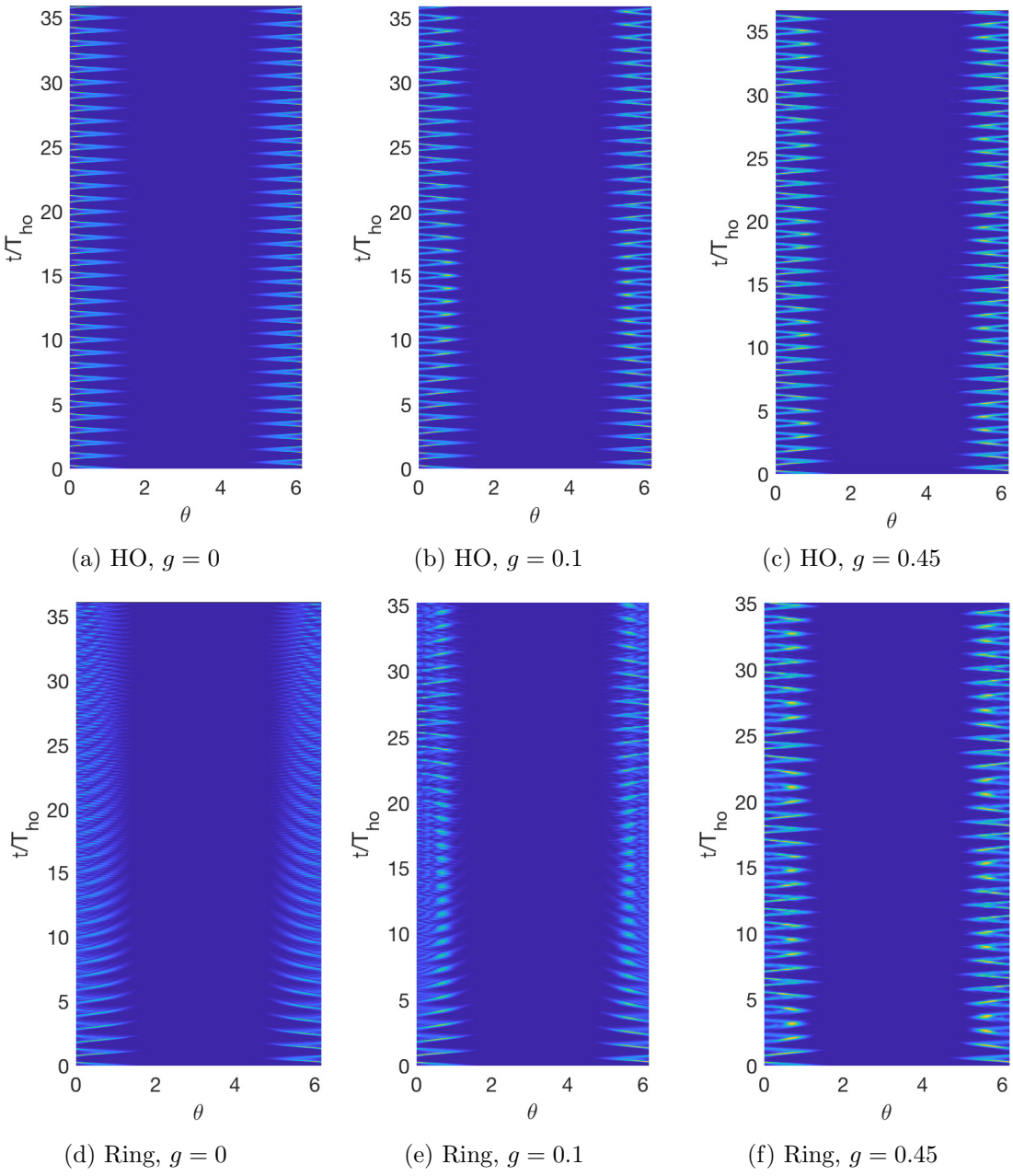

(a) HO, $g = 0$ (b) HO, $g = 0.1$ (c) HO, $g = 0.45$

(d) Ring, $g = 0$ (e) Ring, $g = 0.1$ (f) Ring, $g = 0.45$

Figure 6.5: Density in position space obtained simulating the dynamics with the GPE, for an initial wavepacket $\psi_{\pi/4}(\theta)$, for different values of the interaction strength $g = g_{1D}/(2\hbar\omega_\perp l_\perp)$ in the harmonic and ring potential, as captioned.

revival frequency $\omega_{\rm rev} = 0.0042\,\omega_{\rm ho}$, corresponding to a revival period $T_{\rm rev} = 236 T_{\rm ho}$. As we will frequently talk about the revival frequency in the rest of the chapter, it is important to clarify here some definitions related to revivals.

Here we compare the revival period of the center of mass obtained from the numerical simulation of a wavepacket in the ring with the revival time predicted in Section 6.2.1 using a perturbation theory approach. After simulating the dynamics of a Gaussian wavepacket $\psi_{\pi/4}(\theta)$, as was seen in the previous section (Fig. 6.5(b)), we evaluate the motion of the center of mass from the expectation value

$$\langle\theta(t)\rangle = \frac{\langle z_0(t)\rangle}{R} = \int_{-\pi}^{\pi} |\psi(\theta,t)|^2 \theta R d\theta. \tag{6.50}$$

The dynamics of the center of mass is shown in Fig. 6.6. The revival period obtained numerically is $T_{\mathrm{R-D}} \simeq 107\, T_{\mathrm{ho}}$, which has a 10% discrepancy from $T_{\mathrm{rev}}/2 = 118\, T_{\mathrm{ho}}$ predicted from perturbation theory[2]. The reason why we compare this to $T_{\mathrm{rev}}/2$ and not T_{rev} is that the revival observed from the center of mass dynamics is a "mirror revival" [192], determined by the fact that the wavepacket, after that time $T_{\mathrm{R-D}} \simeq T_{\mathrm{rev}}/2$ has reassembled on the other side of the potential, mirroring its initial condition.

As we will not limit our studies to the dipole mode, related to the oscillations of the center of mass, we also introduce the revival frequency relative to the monopole mode, determined by the oscillations of the amplitude of the wavepacket. In order to determine it, we estimate the variance from the equation

$$\sigma^2(t) = R^2(\langle\theta^2(t)\rangle - \langle\theta(t)\rangle^2), \tag{6.51}$$

where $\langle\theta(t)\rangle$ was defined in Eq. (6.50) and analogously

$$\langle\theta^2(t)\rangle = \frac{\langle z_0^2(t)\rangle}{R^2} = \int_{-\pi}^{\pi} |\psi(\theta,t)|^2 \theta^2 R^2 d\theta. \tag{6.52}$$

The width σ of the wavepacket in time, describing the breathing oscillations during the dynamics, is shown in Fig. 6.7(a). In contrast to the center of mass oscillations, here the first revival is observed at $T_{\mathrm{R-M}} \sim 52 T_{\mathrm{ho}}$. It can be shown [121] that for terms of the form $\langle z_0^p(t)\rangle$, revivals occur at times $t \approx \frac{m T_{\mathrm{R-D}}}{j}$, where $m \geq 1$ is an integer and

[2]Going to the second order in the perturbation, the revival frequency would take the form $\omega_{\mathrm{rev}}^{(2)} = \frac{\hbar}{16mR^2} + \frac{3\hbar^2}{216m^2\omega_{\mathrm{ho}}R^4}(2n_0+1)$. With the numerical values used, this would be $\omega_{\mathrm{rev}}^{(2)} = 0.0049\,\omega_{\mathrm{ho}}$, corresponding to $T_{\mathrm{rev}}^{(2)} = 202 T_{\mathrm{ho}}$, having a 5% discrepancy with $2T_{\mathrm{R-D}}$ observed numerically.

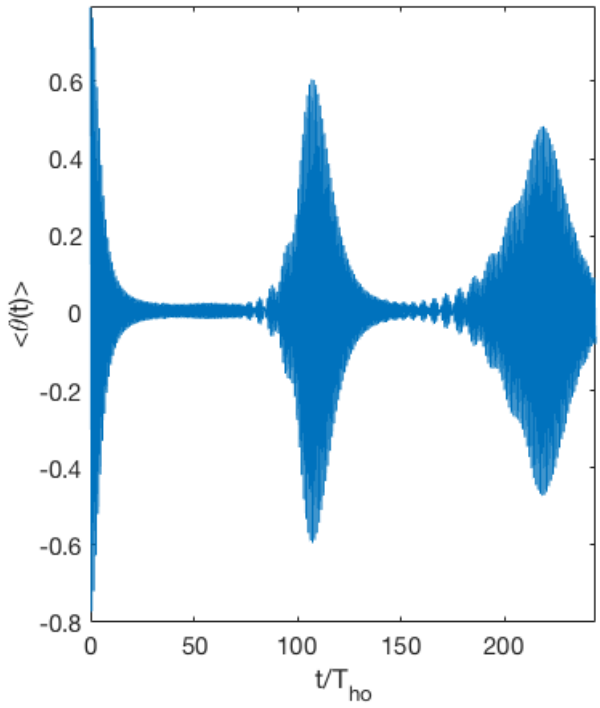

Figure 6.6: Oscillations of the center of mass of the initial Gaussian wavepacket $\psi_{\pi/4}(\theta)$, centered in $\theta_0 = \pi/4$ and with width $\sigma = 2l_{\rm ho}$, obtained from Eq. (6.50) after simulating the evolution with the GPE. The revivals appear after a time $T_{\rm R-D} \simeq 107 T_{\rm ho}$.

$j = 2, 4, ..., p$ for even p and $j = 1, 3, ..., p$ for odd p. As a consequence, the oscillations of the width of the wavepacket, according to the definition of Eq. (6.51), will present revivals at the times $T_{\rm R-M} = \frac{T_{\rm R-D}}{2} = \frac{T_{\rm rev}}{4}$ and integer multiples of this. It is therefore important to stress the fact that we refer to different revival frequencies $T_{\rm R-D}$ and $T_{\rm R-M}$ when talking respectively about dipole and monopole mode oscillations. The revivals in the oscillations of σ are captured by the frequency spectrum of its dynamics, as shown in Fig. 6.7(b), with the emergence of a peak at frequencies close to 0. In the following, the frequency spectra of the moments of the wavefunction will be analysed to determine, from the position of the peaks, the frequencies associated with the dipole and monopole modes, as well as the revival frequencies.

In addition to evaluating the dynamics from the GPE, we simulated the oscillations of the center of mass and the width of a Gaussian wavepacket by solving numerically[3]

[3]We used the library "ode5" on Matlab, which is the fifth order Dormand-Prince method (similar

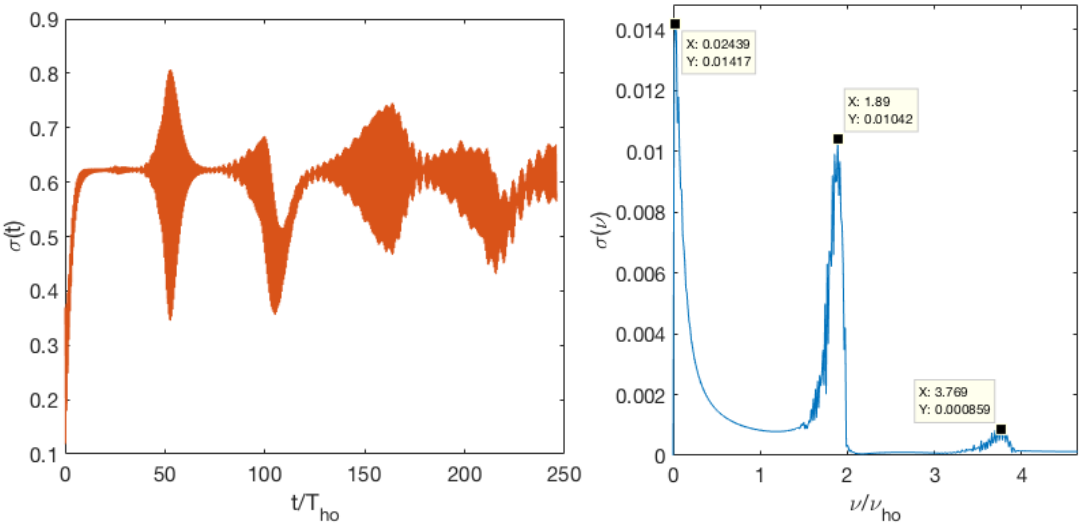

(a) (b)

Figure 6.7: (a) Oscillations of the width of an initial Gaussian wavepacket $\psi_{\pi/4}(\theta)$, centered in $\theta_0 = \pi/4$ and with width $\sigma = 2l_{\rm ho}$, obtained from Eq. (6.51) after simulating the evolution with the GPE without interaction. The revival time observed is $T_{\rm R-M} \sim 52T_{\rm ho}$. (b) Frequency spectrum of $\sigma(t)$, obtained from Eq. (6.49), with a final time $T_{\rm fin}/T_{\rm ho} \simeq 82$, and a sampling frequency $\delta\nu/\nu_{\rm HO} \simeq 0.012$.

the differential equations of Eq. (6.41) and Eq. (6.40). The results are shown in Appendix C.2.

6.5 Characterization of the frequency spectra and observation of sidebands

6.5.1 Dynamics of a central wavepacket at the bottom of the ring

Using the GPE (Eq. (6.46)), we simulate the dynamics of a Gaussian wavepacket (Eq. (6.48)) initially centered at $\theta_0 = 0$, as shown in Fig. 6.3(a), and we numerically evaluate the Fourier transform of the density observed (as a function of time) at the bottom of the ring, $n(0,t) = |\psi(0,t)|^2$, to obtain its frequency spectrum $n(0,\nu) = |\psi(0,\nu)|^2$. We show this in Fig. 6.8, for different values of the interaction strength.

As stressed in Section 6.3.3, for the evaluation of the frequency spectra it is important

to Runge-Kutta).

to pay attention to use long enough time for the dynamics in order to reduce the grid size in frequency space.

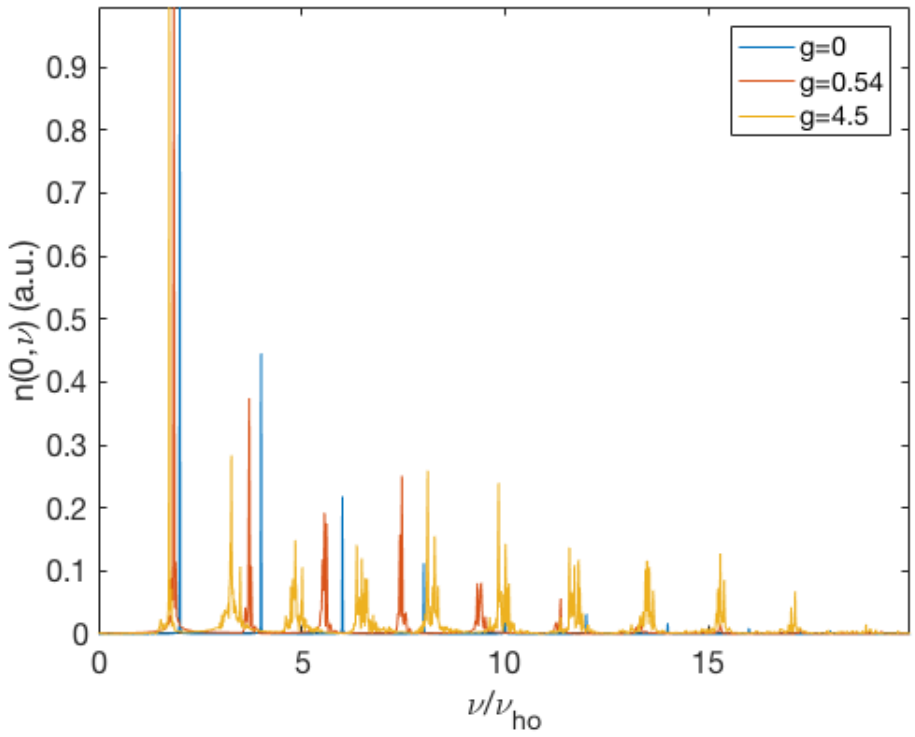

Figure 6.8: Frequency spectra of the density at $\theta = 0$ for different interaction strengths $g = g_{1D}/(2\hbar\omega_\perp l_\perp)$ as in legend, obtained from the Fourier transform (Eq. (6.49)) of the density $n(0,t)$, simulated with a GPE from an initial Gaussian wavepacket $\psi_0(\theta)$ centered at $\theta_0 = 0$. The final time for the simulation $T_{\rm fin} = 82T_{\rm ho}$ gives a frequency interval $\delta\nu \approx 0.012\nu_{\rm ho}$.

The frequency spectra present harmonics (at multiples of the breathing frequency) already for zero interaction, consistently with the occupation distribution $|\langle\phi_n(\theta)|\psi_0(\theta,0)\rangle|^2$ of the initial wavefunction $\psi_0(\theta,0)$, evaluated projecting this on the eigenstates ϕ_n of the harmonic oscillator Hamiltonian, and shown in Fig. 6.9.

As pointed out in the previous section from Fig. 6.4, in the absence of interaction (for $g = 0$) the wavepacket starts shrinking and expanding and in this compressional oscillations we observe the fundamental frequency, given by the breathing mode at $\nu_M = 2\nu = \frac{2\omega_{\rm ho}}{2\pi} = \frac{2}{2\pi}\sqrt{\frac{V_0}{2mR^2}}$, followed by smaller peaks at multiples of this frequency, corresponding to the harmonics. From the definition of $\omega_{\rm ho}$ we see that, in the absence

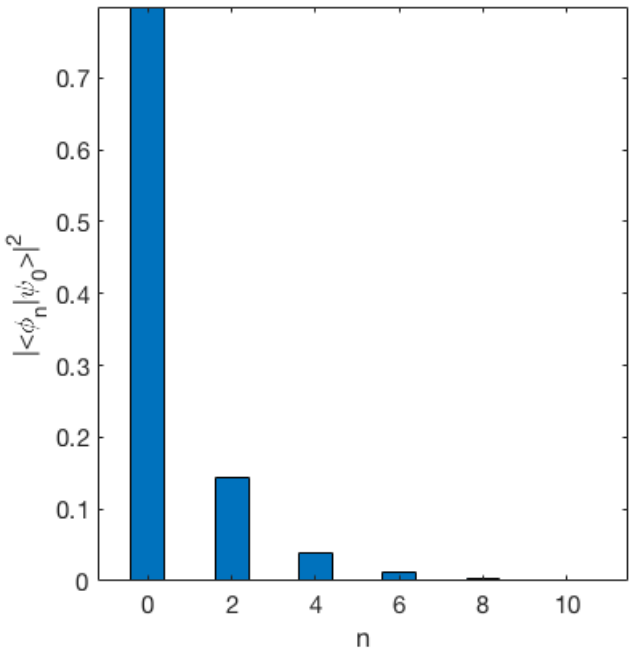

Figure 6.9: Distribution of the occupation number of the initial wavefunction $\psi_0(\theta)$, centered at $\theta = 0$ having a width $\sigma = 2l_{\mathrm{ho}}$. ϕ_n are the eigenstates of the harmonic oscillator, evaluated numerically from the harmonic oscillator Hamiltonian.

of interaction, the frequencies of the modes here do not depend on the choice of the width σ (as long as the dynamics is still within the harmonic oscillator limit). In fact, this would affect only the amplitude of the oscillations, which would be 0 in the case of $\sigma = l_{\mathrm{ho}}$.

As already mentioned, increasing the interaction strength, and consequently the interaction energy, leads to a change in the form of the wavepacket that becomes less Gaussian, hence losing its coherence. This can be observed in the frequency spectrum of Fig. 6.11 from the redistribution of the occupied modes to higher frequency components at higher interactions.

Other interesting features can be observed from the frequency spectrum, such as the broadening of the peaks for finite interactions due to collisions within the BEC, and their progressive shift to lower frequencies, already discussed in Chapter 2 for the case of harmonic oscillator potentials. The study of the latter effect, with comparison to the case of the tilted ring potential, will be further discussed in the next section.

As the wavepacket is centered at zero potential here, and therefore $\langle\theta(t)\rangle = 0$, the dynamics is given only by the even moments, e.g. the variance $\sigma^2(t) = R^2(\langle\theta^2(t)\rangle - \langle\theta(t)\rangle^2)$. We therefore evaluate the width of the wavepacket $\sigma(t)$ for different values of g and its Fourier transform in the frequency space.

We observe that, due to dephasing, for finite values of the interaction strength, the modulation of the oscillations results in collapse and (fractional) revivals, as evident from the evolution of the variance in Fig. 6.10c. This is a purely quantum feature that can be explained if we consider the wavepacket as a superposition of stationary states of different quantum numbers n [122, 176, 193]. Let us consider the evolution of the wavefunction, given by

$$\psi(\theta, t) = \sum_n c_n \phi_n(\theta) e^{-i\omega_n t}, \tag{6.53}$$

where ϕ_n are the eigenstates of the harmonic oscillator Hamiltonian, $\omega_n = E_n/\hbar$ are the frequencies of the energy spectrum and

$$|c_n|^2 = \frac{e^{-n_0} n_0^n}{n!} \approx \frac{1}{\sqrt{2\pi n_0}} e^{-(n-n_0)^2/2n_0}, \tag{6.54}$$

with $n_0 \gg 1$ the average occupied state. The average value of the center of mass position is given by

$$\begin{aligned}
\langle z(t)\rangle =& R\langle\theta(t)\rangle = \sum_n c_n c_{n+1} \cos[(\omega_{n+1} - \omega_n)t] R \int d\theta \phi_n^*(\theta)\phi_{n+1}(\theta)\theta, \\
=& \sqrt{\frac{\hbar}{2m\omega_{\text{ho}}}} \sum_n \sqrt{n+1} c_n c_{n+1} \cos[(\omega_{n+1} - \omega_n)t] \\
=& \sqrt{\frac{\hbar}{2m\omega_{\text{ho}}}} \sqrt{n_0} \sum_n |c_n|^2 \cos[(\omega_{n+1} - \omega_n)t]
\end{aligned} \tag{6.55}$$

where we used the fact that the only contributions come from transitions to state that differ of one excitation ($m = n \pm 1$) and the relation $c_n c_{n+1}\sqrt{n+1} = \frac{\sqrt{n_0} n_0^n e^{-n_0}}{n!} = \sqrt{n_0}|c_n|^2$ derived from Eq. (6.54). For small enough times we can replace the sum over n with an integral. If the energy spectrum is equally spaced, as in the case of the harmonic oscillator, then $\omega_{n+1} - \omega_n = \omega_{\text{ho}}$ does not depend on n. In this case the

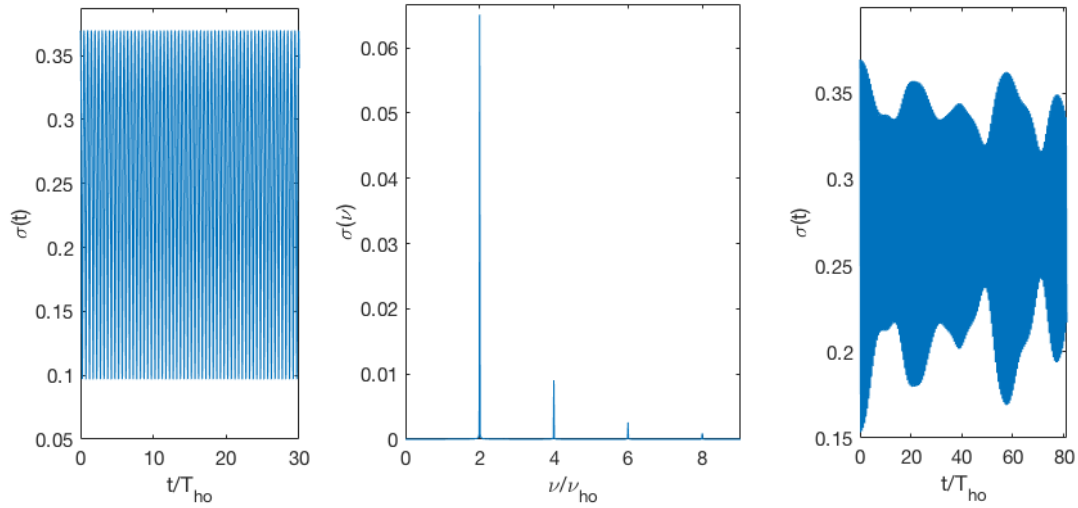

(a) $g = 0$ (b) $g = 0$ (c) $g = 0.54$

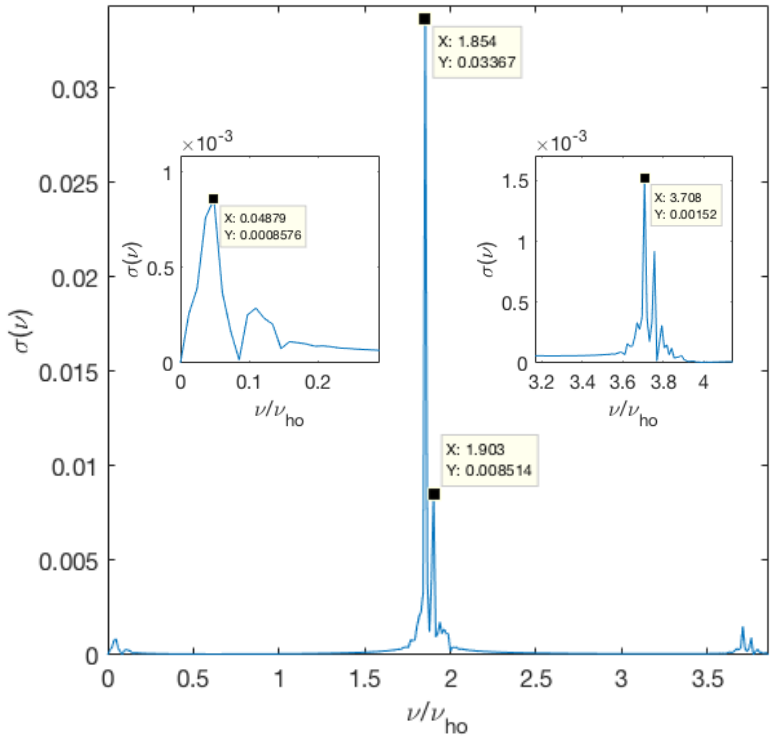

(d) $g = 0.54$

Figure 6.10: Width of the wavepacket (a,c) initially centered at $\theta = 0$ and relative frequency spectra (b,d), computed as in Eq. (6.49) with $T_{\rm fin} = 82\,T_{\rm ho}$ giving a frequency step $\delta\nu \simeq 0.012\nu_{\rm ho}$, for $g = g_{1D}/(2\hbar\omega_\perp l_\perp) = 0$ and $g = 0.54$ as in the legend. Here, and in the following, we set $\omega_\perp = 10\omega_{\rm ho}$.

wavepacket presents reversible dynamics and regains its original shape after a classical period $T_{\rm cl} = 2\pi/\omega_{\rm cl}$. Conversely, when the energy spectrum is not equally spaced (in this case due to the interaction term, or in the ring potential due to the anharmonicity), the classical period will be affected by an energy shift $\Delta\omega$, as it has been shown for the corrections in Eq.(6.21) from the first order perturbation theory in the case of the anharmonic potential, as

$$\omega_{\rm cl} = \omega_{\rm ho} + \Delta\omega = \omega_{\rm ho}\left(1 + \frac{\Delta\omega}{\omega_{\rm ho}}\right) = \omega_{\rm ho}(1 + \kappa E_n) = \omega_{\rm ho}(1 + \kappa\hbar\omega_{\rm ho}^2 n), \tag{6.56}$$

where κ is a coefficient that determines the anharmonicity. We can write the frequencies related to the energy spectrum as $\omega_n = E_n/\hbar = \omega_{\rm ho}\left(n + \frac{\Delta\Omega}{2}n^2\right)$, and using the definition of the classical frequency

$$\omega_{\rm cl} = \frac{\partial E_n}{\hbar\partial n} = \frac{\partial\omega_n}{\partial n}, \tag{6.57}$$

we can integrate Eq. (6.56), obtaining

$$\begin{aligned}\omega_n &= \omega_{\rm ho} n + \frac{1}{2}\hbar\omega_{\rm ho}^2 n\kappa \\ &= \omega_{\rm ho} n + \frac{1}{2}\Delta\Omega n^2,\end{aligned} \tag{6.58}$$

where we defined $\Delta\Omega = \hbar\omega_{\rm ho}^2 n\kappa$. This implies that the argument of the cosine in Eq. (6.55) gains a dependence on n, as $\omega_{n+1} - \omega_n = \omega_{\rm ho} + \Delta\Omega/2 + \Delta\Omega n$. When integrating this over n in Eq. (6.55), we obtain a Gaussian collapse [176] of the oscillations

$$\langle z(t)\rangle \sim e^{-\frac{1}{2}n_0\Delta\Omega^2 t^2} = e^{-(t/T_C)^2}, \tag{6.59}$$

where T_C is the collapse time, defined as

$$T_C = \frac{\sqrt{2}}{\sqrt{n_0}\Delta\Omega}, \tag{6.60}$$

that shows a dependence on the average occupied state n_0, which is influenced by factors such as the displacement of the wavepacket, the change of its width from the oscillation

length, and the interaction strength. The shift $\Delta\omega$ of the frequency induces a change in the periodicity of the oscillations, therefore introducing dephasing, which leads to the observation of collapse and revival periods, as previously discussed. We want to stress the fact that this result of the collapse period was obtained for a general shift of the frequency, without specifying its origin. This is generated by non-linear terms. On one side a non-linearity can be determined by the anharmonic potential even for the single particle dynamics, as previously discussed in Section 6.2.1 and shown in Section 6.4.1. On the other side, the non-linear term can be generated by the interaction strength, as shown in Fig. 6.10d, where the dynamics is still well described within the harmonic approximation in the parameters regime investigated (for a wavepacket initially at $\theta = 0$ and with a sufficiently small width). We will see in the following section how the revival frequencies observed play an important role in the dynamics of the BEC and in the shift of the overall oscillation frequencies.

Aiming to study and compare the effects of these two kinds of non-linearity (given by the interaction and anharmonicity of the potential), for the different trapping potentials, in the following we study the frequency spectra of the density oscillations for the case of a wavepacket initially placed at $\theta = \pi/4$. As can already be seen from the density in Fig. 6.5, this ensures that we have access to the anharmonic part of the potential, but are still in the limit where we can approximate the potential with a quartic term. At the same time, this allows us to study non-central moments, characterised by the change in center of mass position, and therefore allows to study the dipole mode, as well as other modes with an even number of nodes.

6.5.2 Non-central dynamics in HO and ring potentials

In this section we consider the dynamics obtained with the initial wavepacket $\psi_{\pi/4}(\theta, 0)$, as represented in Fig. 6.3(b). Here we study how the difference in the dynamics of Fig. 6.5 for the two different potentials is reflected in the frequency spectra of the density. In particular, we first look at the occupied modes in different points of the potentials by observing the frequency spectra of the density at different coordinates, $n(\theta = 0, \nu)$ and $n(\theta = \pi/4, \nu)$, for the harmonic oscillator and tilted ring potentials.

Dynamics in the Harmonic Oscillator potential

We start by studying the spectrum $n(0,\nu)$ for the dynamics in the harmonic oscillator potential, where, in contrast to the previous case where we had oscillations determined by the breathing mode and their harmonics, here the dynamics comprises a combination of sloshing and breathing of the condensate, together with higher modes.

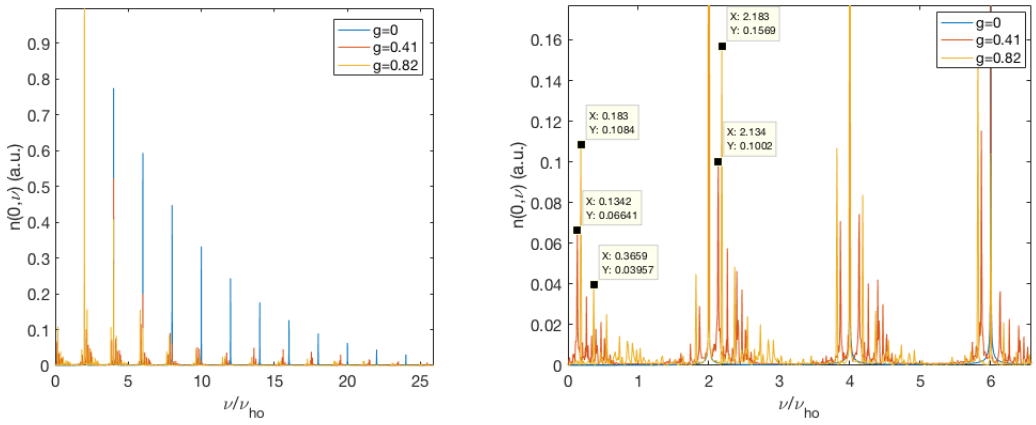

Figure 6.11: Frequency spectrum of the density at the bottom of the harmonic oscillator potential ($\theta = 0$) and zoom in at lower frequencies (right), for different values of the interaction strength, as in legend, and for a wavepacket initially placed at $\theta = \pi/4$ and having a width $\sigma = 2l_{\rm ho}$. The final times used for the simulated dynamics with the parameters $g = 0, 0.41, 0.82$ are respectively $T_{fin} = 164T_{\rm ho}$, $T_{\rm fin} = 123T_{\rm ho}$ and $T_{\rm fin} = 82T_{\rm ho}$ corresponding to the sampling frequencies $\delta_\nu/\nu_{\rm ho} \simeq 0.006, 0.008, 0.012$.

For axially symmetric harmonic traps it has been shown [103] that applying a driving to the system leads to harmonic generations and modes coupling. Starting from the hydrodynamic equations and writing them in terms of the condensate widths in the different directions, it was shown that modulating the trap frequency couples the equations of motion for the widths, therefore inducing coupling between the modes, which depends on the choice of the driving amplitude. [103] Although we do not drive the system out of equilibrium by means of a periodic driving potential, the dynamics depends on the initial condition of the position of the wavepacket in the potential. This defines the out of equilibrium state of the system, and affects the non-linear contribution to the dynamics due to the anharmonic part of the potential, even in the non-interacting case. This can be seen by looking at the occupied state distribution in Figure 6.12,

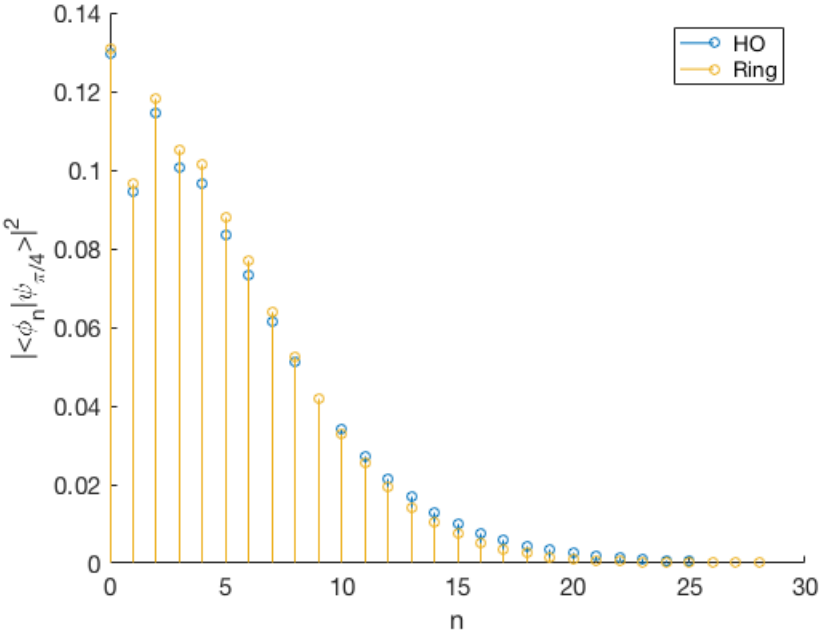

Figure 6.12: Occupation number distribution of the initial state centered at $\theta = \pi/4$ and having width $\sigma = 2l_{\mathrm{ho}}$, in the basis of the eigenstates of both the harmonic oscillator and tilted ring potentials.

where we project the initial state $\psi_{\pi/4}(\theta, 0)$ in the eigenstates basis of the harmonic oscillator and ring potential, through the equation $|\langle\phi_n|\psi_{\pi/4}\rangle|^2$.

From Fig. 6.11 it can also be seen that in the case of non-zero interaction the spectrum presents sidebands, similar to the previous case in Fig. 6.8, but here they seem to have a more defined structure being equally spaced. In particular, we note that their distance from the main peaks is equal to multiple integers of the revival frequency T_R observed in the same dynamics. As discussed in Section 6.4.1, the periodicity of the oscillations envelopes defining the revival frequency depend on the modes we consider (we had previously defined $T_{\mathrm{R-D}}$ and $T_{\mathrm{R-M}}$ for the dipole and monopole modes). The oscillations of the density at a point of the ring is given by a combination of different modes, and as a consequence we observe a main peak close to zero frequency, determining the revival frequency ω_R (having the value shown in the plot of Fig. 6.13 for different interaction strengths), and its multiples $T_{FR} = T_R/p$, determined by fractional revivals associated with the moments involving the terms $\langle z_0^p \rangle$ [122], as explained in

Section 6.4.1. As in the previous case, we notice a shift of the frequencies towards lower values, which progressively affects lower modes for increasing interaction strength. These frequency shifts will be further discussed in the next section.

Dynamics in the ring potential

The frequency spectra $n(0,\nu)$ and $n(\pi/4,\nu)$ of the density at different points of the tilted ring present some differences, compared to the harmonic oscillator case just discussed. As can be seen from Fig. 6.13, sidebands appear already in the non-interacting case.

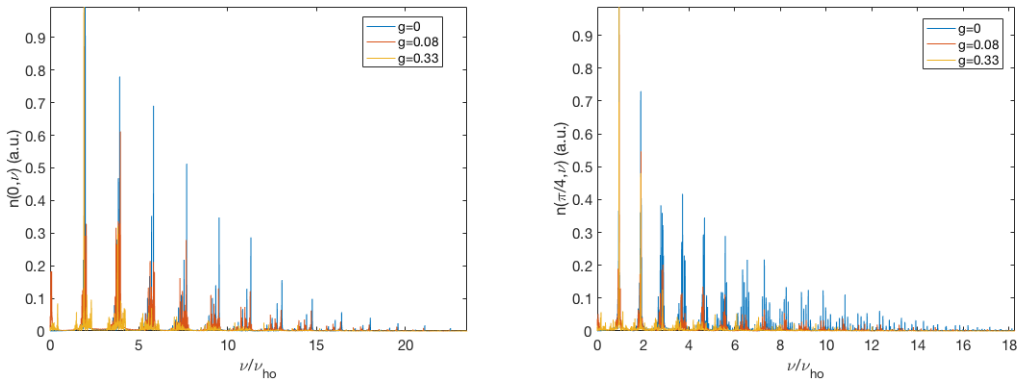

Figure 6.13: Frequency spectrum $n(\theta = 0, \nu)$ and $n(\theta = \pi/4, \nu)$ of the density at the different points in the tilted ring potential, obtained from the dynamics of the Gaussian wavepacket $\psi_{\pi/4}$.

In contrast to the sidebands observed in Fig. 6.11, however, the sidebands associated with every harmonic frequency are not at the same distance from the main peaks. In fact, we observe that this separation progressively increases going to higher frequencies. These features can be related to the dephasing of the condensate at small values of the interaction strength, where different parts of the wavepacket assume different velocities and will therefore have a slightly different periodicity.

Furthermore, we can see that, in contrast to the previous case of central symmetry in Fig. 6.8, higher frequencies become less occupied at higher interaction strengths. This is in agreement with the features of the dynamics shown in Fig. 6.5, where it was seen that increasing the interaction stabilises the condensate, therefore the spectrum is characterised by lower frequency components, which show, as a consequence, more

narrow spectral lines because of the decrease in the dephasing.

In Fig. 6.13 we showed, in addition to $n(0,\nu)$, the frequency spectrum of the density $n(\pi/4,\nu)$ obtained at the point where the wavepacket is originally placed ($\theta = \pi/4$), aiming to gain a better understanding of the effects that the interactions have on the modes with peaks at odd multiples of the oscillation frequency (e.g. the dipole mode). We remark the fact that, in contrast to the previous case of the initial wavepacket $\psi_0(\theta,t)$ initially centered at $\theta = 0$, in this case the frequency observed in proximity of $2\omega_{\rm ho}$ would not be given by the bare breathing mode, but would also contain contributions coming from the sloshing of the center of mass (passing from that point twice in a classical period) and higher modes components. It is therefore clear that the frequency spectra of the density at different spatial points would have a different distribution (see Fig. 6.13), as the contribution to these comes from the excitation of different modes.

In order to study how the lowest modes are affected by the anharmonicity of the potential and by the interaction within the wavepacket, we need to integrate over the whole ring and look at the evolution of the moments in time and their Fourier transforms in the frequency space. We saw that for the central dynamics studied with the initial Gaussian $\psi_0(\theta,0)$, the position of the center of mass is fixed and the only moments contributing to the dynamics are the even moments $E[\theta^{2p}] \propto \sigma^{2p}$, with p integer and positive. Conversely, for a wavepacket initially displaced, the moments to be considered are non-central moments.

We study, for the dynamics of the wavepacket in the ring potential, the moments up to the fourth order, as they generate the peaks observed at lower frequencies. They are defined as follows:

$$E[z] = \langle z_0 \rangle \,, \tag{6.61}$$

$$E[z^2] = \langle z_0 \rangle^2 + \sigma^2, \tag{6.62}$$

$$E[z^3] = \langle z_0 \rangle^3 + 3\,\langle z_0 \rangle\,\sigma^2, \tag{6.63}$$

$$E[z^4] = \langle z_0 \rangle^4 + 6\,\langle z_0 \rangle^2\,\sigma^2 + 3\sigma^4, \tag{6.64}$$

where $\langle z_0 \rangle = R\,\langle \theta_0 \rangle$ is the mean of the center of the distribution. The third and fourth

moment, related to skewness and kurtosis, respectively describe how the position of the peak of the wavefunction and the tails differ from the ones of a normal distribution, therefore providing some information about how the wavepacket loses its initial Gaussian shape and coherence.

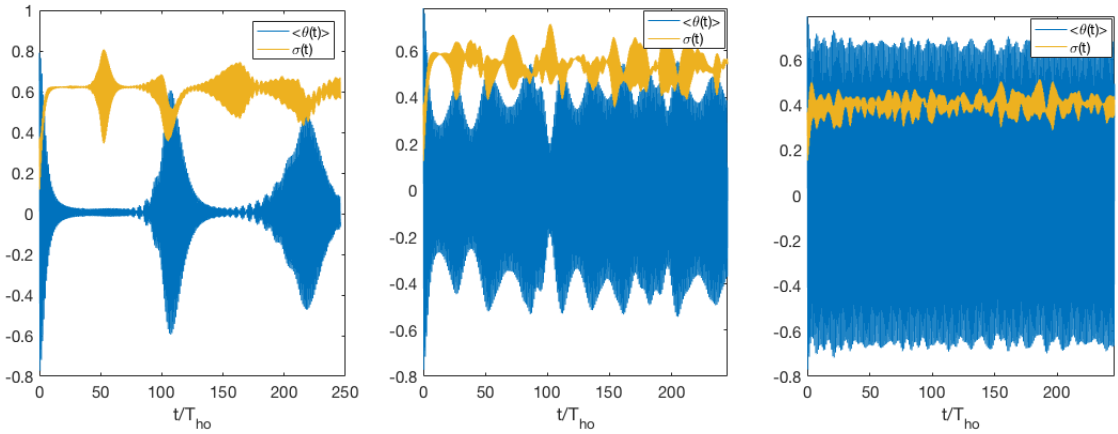

(a) $g = 0$ (b) $g = 0.08$ (c) $g = 0.33$

Figure 6.14: Evolution of the center of mass and width of a wavepacket initially placed at $\theta_0 = \pi/4$ in the ring potential for different values of $g = g_{1D}/(2\hbar\omega_\perp l_\perp)$.

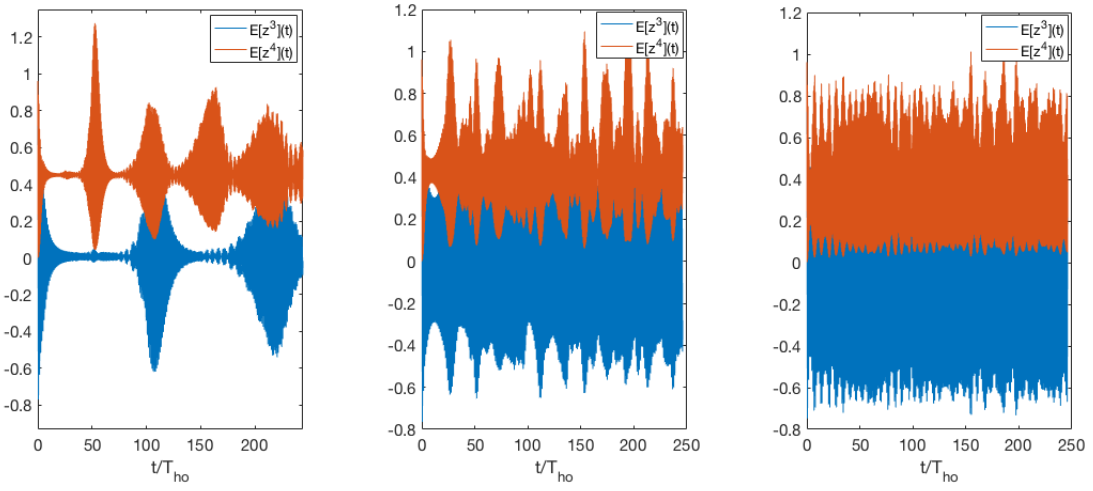

(a) $g = 0$ (b) $g = 0.08$ (c) $g = 0.33$

Figure 6.15: Evolution of the third and fourth moments of a wavepacket initially placed at $\theta_0 = \pi/4$ in the ring potential for different values of $g = g_{1D}/(2\hbar\omega_\perp l_\perp)$.

From Fig. 6.14 we show the behaviour of the width and the center of mass in time,

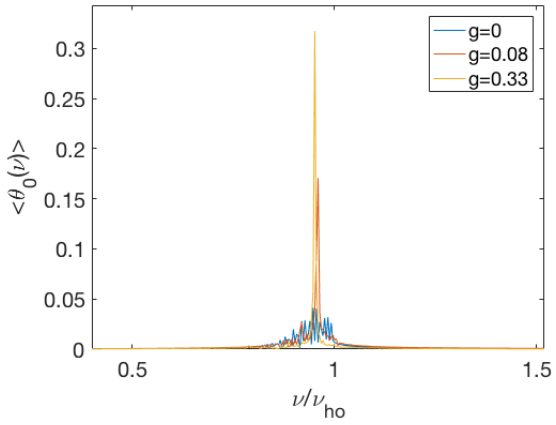

(a) Frequency spectrum of c.o.m. $R\langle\theta_0(t)\rangle$.

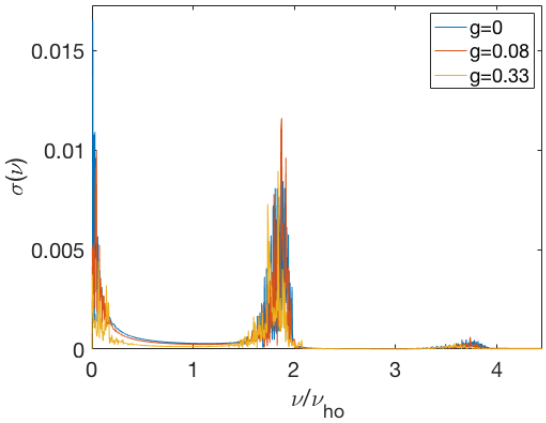

(b) Frequency spectrum of the dynamics of the width $\sigma(t)$.

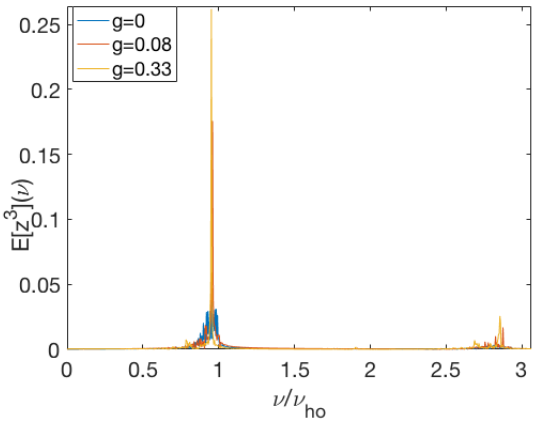

(c) Frequency spectrum of the dynamics of the third moment $E[z^3(t)]$.

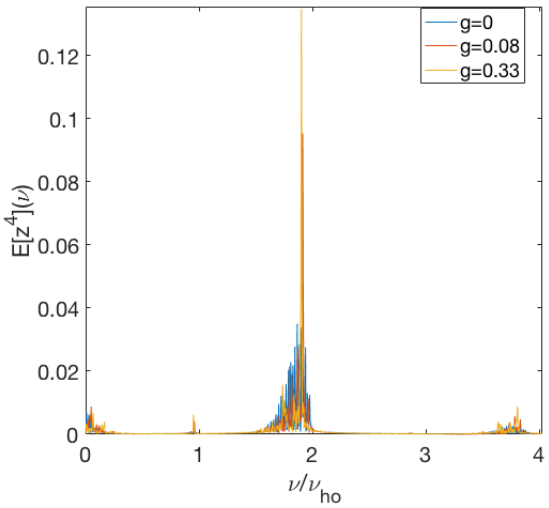

(d) Frequency spectrum of the dynamics of the fourth moment $E[z^4(t)]$.

Figure 6.16: Frequency spectra of the first four moments of Fig. 6.14 and Fig. 6.15 for different values of g. For the evaluation of all the frequency spectra we used a final time $T_{\rm fin} = 246T_{\rm ho}$, corresponding to a sample frequency $\delta\nu = 0.004$. We used σ instead of the second moment $E[z^2(t)]$ for an easier comparison with the variational method results ((to be) shown in Appendix C).

for different values of the interaction strength, as already shown in the single particle (non-interacting) case in Section 6.4.1. From these, we evaluate the higher moments of Fig. 6.15. The dynamics at $g = 0$ of the oscillations for the center of mass and the width was already discussed in Section 6.4.1, where we defined the revival periods $T_{\rm R-D}$ and

$T_{\mathrm{R-M}}$ associated with these. The distortions observed in the revivals at higher times are due to the fact that, as previously discussed, the wavepacket loses its Gaussian shape with increasing time. As a consequence, different parts of the wavepacket move at different speeds, determining the broadening of the envelopes at every cycle and the appearance of higher frequencies.

It can be observed that, for increasing interaction strength, the revival period of all the moments decreases, and more fractional revivals [193] are present. This is consistent with the fact that the collapse time of the wavepacket, as shown in Eq. (6.60), is inversely proportional to the average occupied state n_0, which increases with the interaction strength, as further discussed in Section 6.6.2. Furthermore, we note that the oscillations of the width become smaller when increasing the value of g, and this is consistent with the fact that, as shown in Fig. 6.5, higher interactions in the ring trap stabilise the shape of the wavepacket.

In Fig. 6.16 we compare the frequency spectra of the dynamics of the first four moments shown in Fig. 6.14 and Fig. 6.15, for different interactions. The dipole mode frequency spectrum becomes sharper with increasing interaction, as a consequence of the fact that the wavepacket is less fragmented for higher g, as already discussed. For the even moments, we observe a distribution of sidebands around the peaks of the main frequency modes. The broadening of the peak corresponding to the revival frequency, with the appearance of sidebands, is determined by the appearance of fractional revivals, as well as the fact that the interaction increases the non-linearity, making the revivals more irregular and not identical. We will discuss in the next section their shift towards higher frequencies that can be observed in the frequency spectrum of the width.

6.6 Observation of frequency shifts and relation with the revival frequency

In this part we characterise the frequency shift observed in the previous section by looking at the frequency spectra of the moments, aiming to gain a deeper understanding of this effect. As previously discussed at the beginning of this chapter, frequency

shifts have extensively been studied for collective oscillations of a condensate in the harmonic oscillator potential, in different geometrical configurations and interaction regimes. Here we start by considering the known case of frequency shifts in a 1D mean-field harmonic oscillator [98, 111] to benchmark the results obtained numerically by solving the GPE and extracting the frequency oscillations of the lowest modes from the peaks of the frequency spectra determined from the density. We therefore conduct the same kind of analysis to study the frequency shifts that we observe for the dynamics in the tilted ring potential, and compare these results with the variational method derived at the beginning of this chapter. At the same time, we analyse the effects induced by the non-linearity on the revival frequencies, as already anticipated in the previous section, and find that these affect the shifts of the monopole mode frequency.

6.6.1 Frequency shifts in the 1D harmonic oscillator potential

Central dynamics

We start considering the central dynamics of a wavepacket $\psi_0(\theta, 0)$ in the harmonic oscillator potential. As we noticed from Fig. 6.8, for increasing interaction strengths there is a progressive redshift of the frequencies. In Fig. 6.17 we study, in particular, the shift of the lowest (monopole) mode, as we can compare it with known results from literature, in particular with the variational method results of Eq. (6.38) [98] and with the hydrodynamic limit result $\omega_M = \sqrt{3}\omega_{\rm ho}$ [111].

The frequencies plotted for the GPE numerical method were obtained from the positions of the most populated peaks close to $\omega = 2\omega_{\rm ho}$ of the frequency spectrum $n(0, \nu)$ shown in Fig. 6.8. As the center of mass remains at $\theta = 0$ during the evolution of the wavepacket, only central moments contribute to the dynamics here. We observe that the agreement between the results from the numerical GPE frequency spectra analysis and the analytical predictions is good, and we reach the asymptotic frequency for high values of the interaction strength.

We observe an increase of the monopole frequency for $g_{1D}/2\hbar\omega_\perp l_\perp > 10$. However, as we set $\lambda = \omega_z/\omega_\perp = 0.1$, for those values of the interaction strength we can not consider the system in the mean field anymore, granted by the condition $N\lambda a/l_\perp \ll 1$.

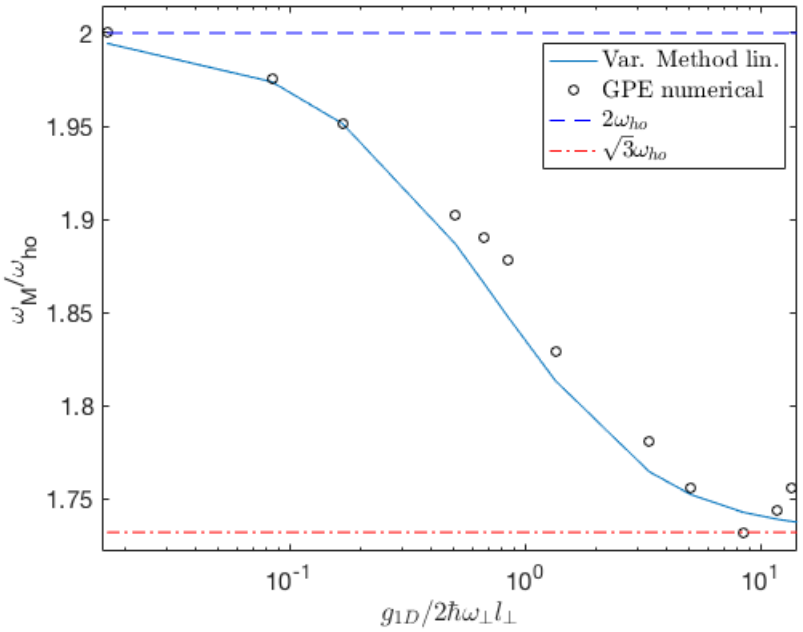

Figure 6.17: Monopole mode as a function of the interaction strength, determined from the frequency spectra of the density $n(0,\nu)$ of a central wavepacket in the harmonic potential, simulated with the GPE (dots), compared with the values calculated from the equation for the monopole mode (Eq. (6.38)), obtained from the linearised variational method (solid line). The dashed-dotted line shows the asymptotic hydrodynamic limit $\omega_M = \sqrt{3}\omega_{\rm ho}$.

In fact, in the opposite limit, for $N\lambda a/l_\perp \gg 1$, we should change our approach going to the Thomas-Fermi regime, which is beyond the aim of this study.

Non-central dynamics

We now conduct the same kind of analysis on the lowest modes through by characterising the frequency spectra obtained for non central dynamics of a wavepacket (initially placed at $\theta = \pi/4$) in both the harmonic oscillator and tilted ring potential.

In the first instance, we study more in detail the frequency shifts observed from the frequency spectra $n(0,\nu)$ shown in Fig. 6.11, for the harmonic oscillator potential. As we pointed out in the previous section, we observe that the distance between the sidebands is equal to the revival frequency, which increases with the interaction strength. Furthermore, we notice that the shifts to lower frequencies, observed for the different

modes, occur in a quantised way. In fact, the dominant frequencies move to lower sidebands for increasing values of g. In order to visualise this more clearly, in Fig. 6.18a we show the frequencies of the even modes observed from the frequency spectrum of $n(0,\nu)$, together with the bare frequencies ω_n observed in the non-interacting case. We also show the frequencies obtained from the equation obtained phenomenologically

$$\omega_n/\omega_{\rm ho} = n - p\omega_R/\omega_{\rm ho}, \tag{6.65}$$

where ω_R is the revival frequency observed in the frequency spectrum $n(0,\nu)$ and p are (positive) integer numbers. We observe that the higher modes frequencies start being redshifted at lower values of the interaction, and progressively, for increasing g, the frequency of lower modes decreases. For all the modes, the shift of the frequencies coincides with multiples of the revival frequencies, which increases with the interaction, as we show in Fig. 6.18b(b). Here we show the revival frequency as a function of the interaction strength, determined from the frequency spectra of the density $n(0,\nu)$ and compare it with the solutions of the revival frequency observed in the frequency spectra of the moments dynamics obtained by solving numerically the differential equation Eq. (6.32), as shown in Appendix C.2.

The above observations suggest that the revival frequency determined from the dynamics of the wavepacket is related to the shift of the frequency modes. Since the frequency spectrum of the density is determined by the contribution from different modes[4], we need to study the frequency spectra of the moments. As seen at the beginning of this chapter, the dipole mode in the harmonic oscillator potential is not affected by finite interactions, therefore we study the Fourier spectrum of the variance for different values of the interaction strength, in order to determine the shift of the monopole frequency $\omega_2 = \omega_M$. We compare this with both the linearised analytical Eq. (6.38) and numerical results coming from the variational method, as well as the hydrodynamic limit $\omega_M = \sqrt{3}\omega_{\rm ho}$ and with $\omega_M = 2\omega_{\rm ho} - \omega_R$.

It can be seen that all the methods used are in agreement and consistent with the

[4]i.e., the frequency at $n = 2$ in Fig. 6.18a is not simply a monopole mode, but here is mixed with contributions that arise from the dipole mode

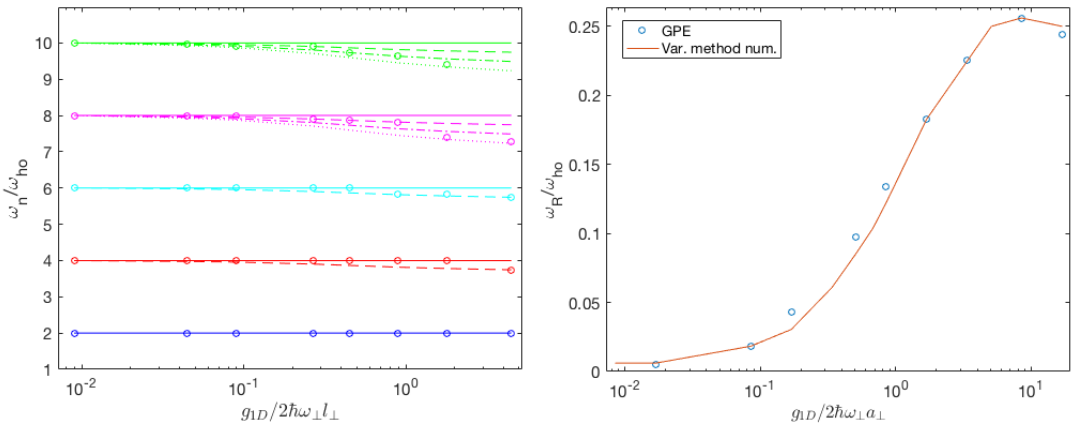

(a) (b)

Figure 6.18: (a) Even frequency modes observed from the frequency spectrum of the density $n(\theta = 0, \nu)$ (dots), obtained from the non-central dynamics of the initial Gaussian $\psi_{\pi/4}(\theta, 0)$ for different values of the interaction strength g_{1D}. The solid lines are the frequencies at $g = 0$, given simply by the harmonics. With the lines from dashed to dotted we represented the frequencies $\omega_n/\omega_{\rm ho} = n - p\omega_R/\omega_{\rm ho}$, with $p = 1, 2, 3$.
(b) Revival frequency observed from the frequency spectrum of the density at $\theta = 0$ (with a dynamics simulated by means of the GPE) and revival frequency obtained from the frequency spectrum of the fourth moment after solving numerically the differential equations obtained from the variational method (see Fig. C.3). Here we determined the revival frequency from the fourth moment since, as discussed in Appendix C.2.1, the dynamics of the amplitude evaluated with the variational method does not present collapse and revival.

results shown for the previous central configuration in Fig. 6.17. While the variational method and the hydrodynamic limit solutions were observed before [98, 111] and shown to be in good agreement with experimental results, the connection with the revival frequency obtained from the frequency spectrum for different interaction strength, to our knowledge, has not been observed before.

As the mechanism is not entirely clear (it is not easy to obtain an analytical form for that) and it is a phenomenological result, in the following we use this to reinforce the concept seeing that we have the same kind of agreement with the data obtained from the GPE, for the tilted ring potential.

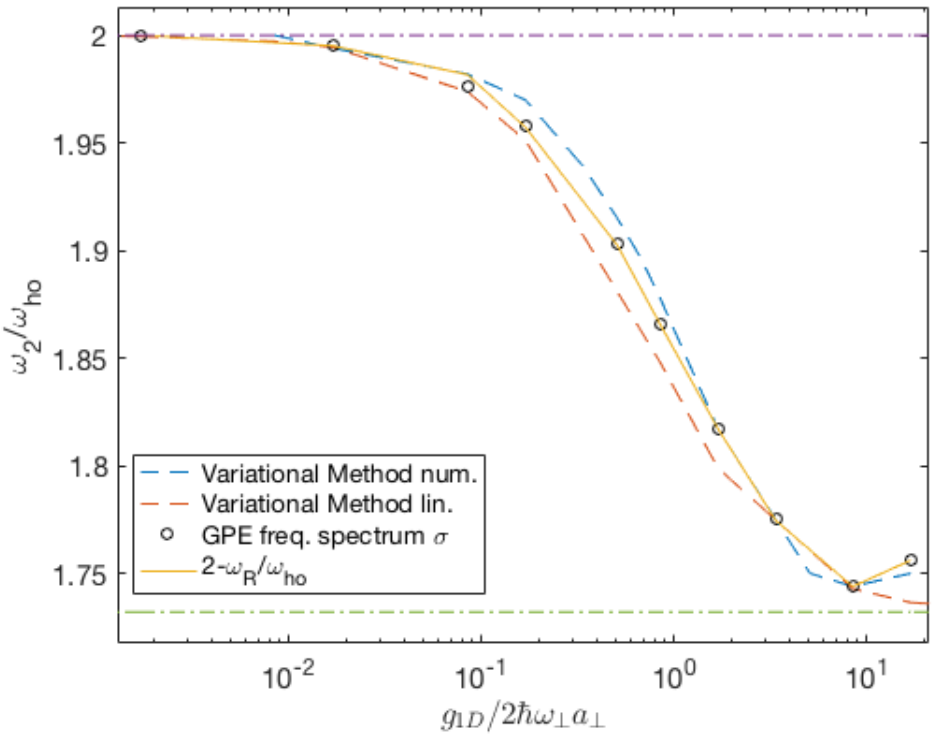

Figure 6.19: Monopole mode as a function of the interaction strength, determined from the frequency spectra of the width of a wavepacket initially placed at $\pi/4$ in the harmonic potential. The same quantity is compared with the numerical and the linearised variational method solutions, with the asymptotic hydrodynamic limit result $\sqrt{3}\omega_{\rm ho}$, and with $2\omega_{\rm ho} - \omega_R$.

6.6.2 Frequency shifts in the tilted ring potential

Under the previous considerations, as we are interested in studying the frequencies of the uncoupled modes (e.g. dipole mode and breathing mode), from the dynamics of the wavefunction derived through the GPE, we obtained the frequency spectra for the center of mass and for the width of the wavepacket, for different values of the interaction strength. This allows us to compare the results obtained from the GPE with the numerical ones derived from the variational method.

As seen in Fig. 6.14, in contrast to the harmonic oscillator case, the motion of the center of mass is affected by the anharmonic potential and the interaction strength. In fact, from Eq. (6.41) we can see that its oscillation frequency is affected by the anharmonicity,

but the center of mass is also coupled to the wavepacket width, which depends explicitly on g. We therefore expect a shift of the dipole frequency. Determining this shift corresponds to finding the correction to the classical oscillation. A contribution to this correction comes from the anharmonicity itself, and as previously discussed at the beginning of this chapter, we can use the result from first order perturbation theory Eq. (6.21). Since this depends on the average occupied state n_0, we determine this after evaluating the energy of the system, found deriving the energy functional

$$E = \int_0^{2\pi} \left(\frac{\hbar^2}{2mR^2} |\nabla\psi(\theta)|^2 + V_{\text{ring}}(\theta)|\psi(\theta)|^2 + \frac{g}{2}|\psi(\theta)|^4 \right) R d\theta. \tag{6.66}$$

In Fig. 6.20 we show the energy for two different values of the interaction strength and the average occupation number varying with g, obtained from mapping the total energy of the system to a harmonic oscillator, so that

$$n_0 = (E_{tot} - 1/2)/\hbar\omega_{\text{ho}}. \tag{6.67}$$

In Fig. 6.21 we compare this result with the dipole frequency obtained from the analysis of the center of mass frequency spectra, derived both with the numerical GPE, and with the numerical solution of the variational method. The errors associated with the frequencies recorded for the GPE numerical simulations are considered as half of the frequency division in the frequency Fourier space, which is determined by the final time used for the simulations[5]. We also report the percent relative differences between the frequencies used with the two aforementioned approaches and the ones obtained from the GPE simulation.

From a comparison between the perturbation theory and the variational method, with reference to the true values considered as the ones given by the GPE simulation, we can see the limits of both of these methods. For small values of the interaction strength, we have seen that the wavepacket decoheres and does not preserve its Gaussianity, hence the variational method, based on a Gaussian ansatz, is not accurate, while it gets closer

[5]The error increasing with the interaction strength is due to the fact that for higher interaction strength we need to decrease the time steps, hence simulating the dynamics for longer times is computationally more demanding in terms of memory.

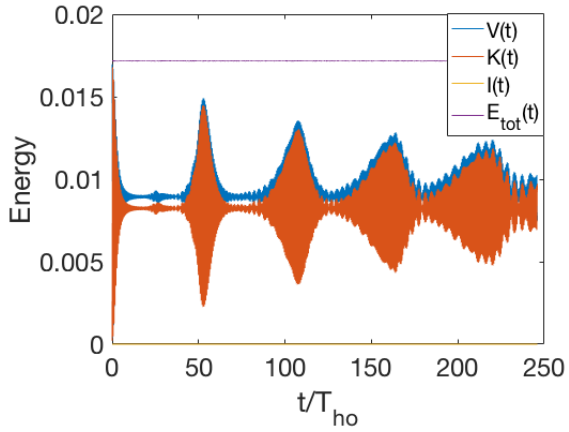

(a) $g_{1D}/2\hbar\omega_\perp l_\perp = 0$

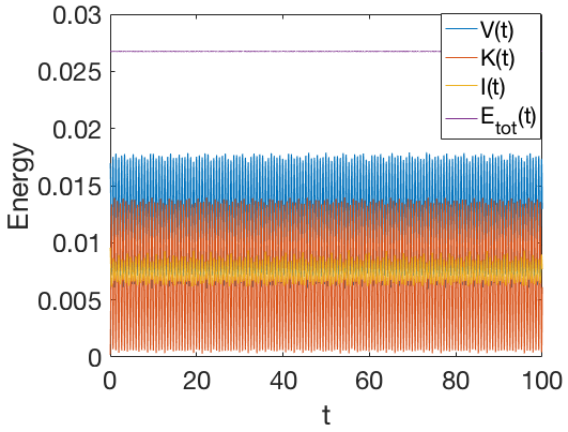

(b) $g_{1D}/2\hbar\omega_\perp l_\perp = 8.7$

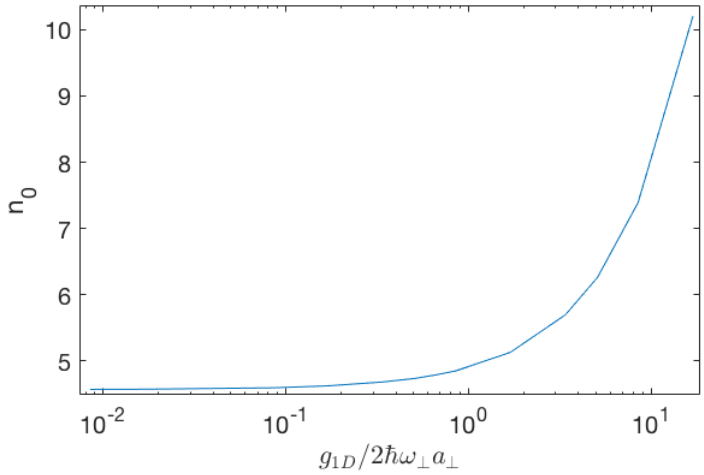

(c)

Figure 6.20: (a-b) Energy components and total energy of the system for different values of the interaction strength as in caption. (c) Average occupation number as a function of g, obtained from mapping the total energy to the harmonic oscillator quantum numbers as in Eq. (6.67).

to the GPE results for higher interactions, when the Gaussian shape is more preserved. For the perturbation theory approach, however, the interaction strength plays a non trivial role. For the frequencies estimated from the GPE simulation, we can see that at $g \sim 10^{-1}$ the value of the dipole mode starts increasing to then drop again, drifting from the expected trend predicted with the perturbation theory. This increase in the dipole mode frequency is therefore consistent with the fact that in Eq. (6.66), the last term corresponding to the interaction energy acts as a perturbation that induces a blue shift

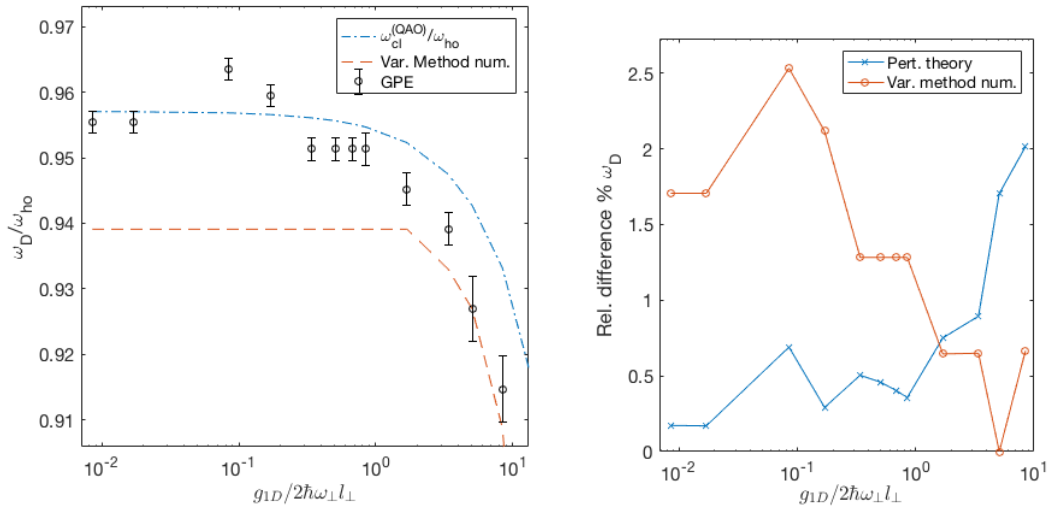

Figure 6.21: (Left) Dipole mode frequency derived from the frequency spectra of the center of mass using GPE and from the variational method numerical solutions, compared with the corrected classical oscillations frequency $\omega_{\rm cl}^{QAO}$ determined with perturbation theory from Eq. (6.20). The errors were determined by using half division of the frequency scale. (Right) Percentage relative difference of perturbation theory and variational method compared to the frequencies observed from the GPE simulation.

of the harmonic oscillator eigenvalues, which depends on the state of the system. In fact, the perturbation theory correction keeps into account the correction to the energy coming from the anharmonic part of the potential treated as a perturbation and not the interaction term. The effect of the interaction, in this model, is kept into account for the effect that it has on the average occupation number. In Fig. 6.22 we show how the interaction energy, defined in Eq. (6.68), changes as a function of the states quantum number n, for eigenstates of both the harmonic and tilted ring potentials, evaluated numerically. Using the definition of the interaction energy

$$E_n^{int} = \frac{g_{1D}}{2}\int |\psi_n(r)|^4 dr, \tag{6.68}$$

we express this in dimensionless units considering the relation

$$\frac{2E_n^{int}}{g_{1D}} = \frac{2E_n^{int}}{\hbar\omega_{\rm ho}}\frac{\lambda\hbar\omega_\perp}{g_{1D}} = \frac{E_{int}}{\hbar\omega_{\rm ho}l_{\rm ho}g}, \tag{6.69}$$

where in the last passage we used the definition of the dimensionless interaction strength already largely used here, $g = g_{1D}/2\hbar\omega_\perp l_\perp$, and $\lambda = \omega_{\rm ho}/\omega_\perp$.

The following drop in the dipole frequency is then determined by the interplay between the shifts given by the interaction strength and the anharmonicity. In fact, if on one side the interaction strength determines a blue shift of the energy, on the other side the interaction energy assumes lower values for states with higher n, as shown in Fig. 6.22, while the anharmonicity determines a red shift of the energy.

As the shift for the dipole frequency is below 10%, the percent relative difference for the two methods analysed here, as shown in Fig. 6.21(b), lies in the range $0 - 2.6\%$ with the variational method and $0.2 - 2\%$ with the perturbation theory approach.

The increasing deviation between the numerical GPE results and the perturbation theory approach, for higher interaction strength, is due to the fact that the unperturbed Hamiltonian considered even in the interacting case is the harmonic oscillator one, and the interaction term enters the perturbation theory correction only in the energy of the system determined to estimate the corresponding average occupied state. This can therefore lead to a lack in accuracy, as we would need to treat also the interaction term as a perturbation in order to give a further correction.

We now study the shift of the monopole mode, comparing the solutions of the aforementioned methods. While in the non-interacting harmonic oscillator case the monopole mode is given by $\omega_M = 2\omega_{\rm ho}$, in the previous section we have seen that, for the harmonic oscillator case, the shift due to the interaction can be reproduced both with a variational method and with a phenomenological result that takes into account the revival frequency ω_R observed, with the relation

$$\omega_M = 2\omega_{\rm ho} - \omega_R. \tag{6.70}$$

Differently from the harmonic oscillator case, however, we see that the dipole frequency, describing the classical oscillations of the center of mass, is shifted in the tilted ring potential even in the non-interacting case, as a result of the anharmonic perturbation to the potential. Here then we have to consider the correction to the center of mass oscillations, which we determined using perturbation theory from Eq. (6.20), obtaining

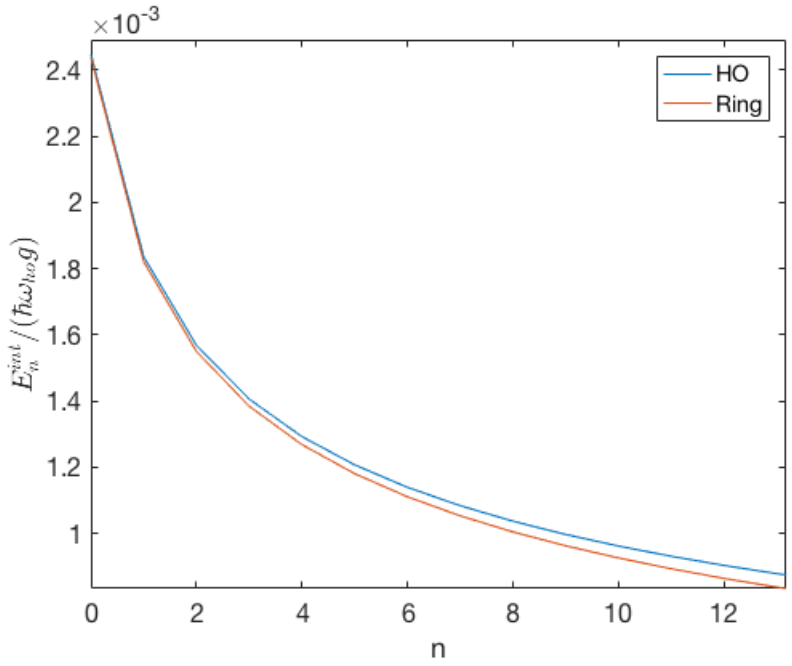

Figure 6.22: Interaction energy of Eq.(6.66) in dimensionless form, evaluated from Eq. (6.68) with the eigenstates of the harmonic oscillator and the ring, estimated numerically from the xHamiltonian in the non-interacting case.

the results shown in Fig. 6.21.

Eq. (6.70) then reduces to

$$\omega_M = 2\omega_{\rm cl}^{(\rm QAO)} - \omega_{R-M}, \tag{6.71}$$

where ω_{R-M} is the revival frequency observed in the frequency spectra of the wavepacket width oscillations.

In Fig. 6.23, in analogy to the previous study of the dipole frequency shift, we show the frequencies obtained from the frequency spectrum of the width of the wavepacket, obtained from the numerical simulation of the GPE. We compare these with the variational method solutions, obtained from the numerical solution of Eq. (6.40), and with the phenomenological result of Eq. (6.71), obtained after considering the perturbation theory correction to the classical oscillation of the wavefunction (Eq. (6.21)).

The revival frequency, determined from the frequency spectra of σ, and used to predict the shift from Eq. (6.71), is shown, as a function of the interaction strength, in Fig. 6.24.

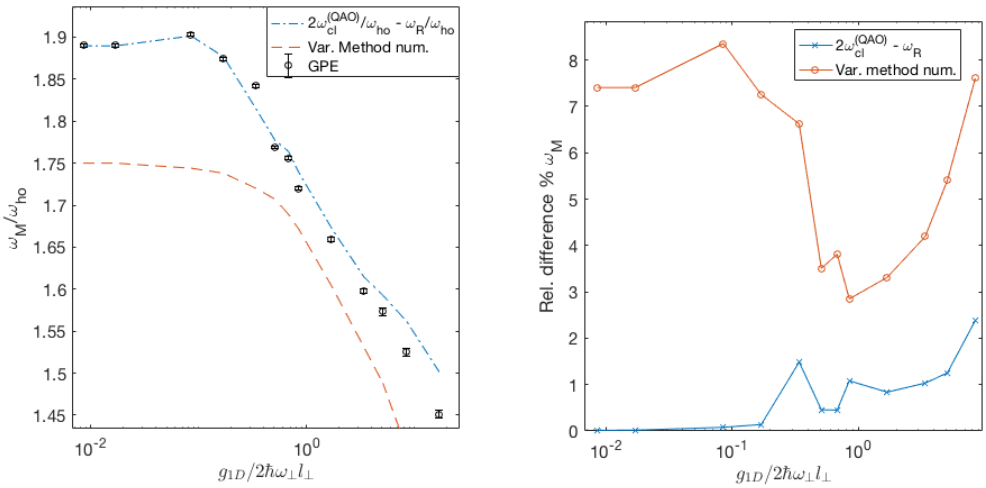

Figure 6.23: (Left) Monopole mode frequency derived from the frequency spectra of the wavepacket width σ using the GPE and from the variational method numerical solutions, compared with the monopole oscillations determined using perturbation theory and the phenomenological formula in Eq. (6.71). The errors were determined by using half division of the frequency scale. (Right) Percentage relative difference of perturbation theory and variational method compared to the monopole frequencies observed from the GPE simulation.

Comparing the two results with the frequencies determined from the GPE simulations, we can see that the variational method fails to give an accurate prediction for the monopole frequency shift, with percent relative errors in the range $3\% - 8.5\%$. From the frequency spectra of the width obtained with the variational method approach, shown in Fig. C.5), it can be seen that the shift in the monopole frequency is consistent with the value of the revival frequency, according to the phenomenological result of Eq. (6.71). However, the discrepancy in the value of the revival frequency ω_{R-M} obtained with the variational method and with the GPE, affects the accuracy in determining the shifts of the monopole mode. In fact, from Fig. 6.24, we can see that the revival frequency obtained with the variational method is ~ 5 times larger than the one obtained with the GPE simulation at low interactions.

This deviation is related to the fact that the wavepacket loses its Gaussian form for lower values of the interaction strength. On the other side, we want to stress the fact that the phenomenological result that we verified in the previous case for the harmonic

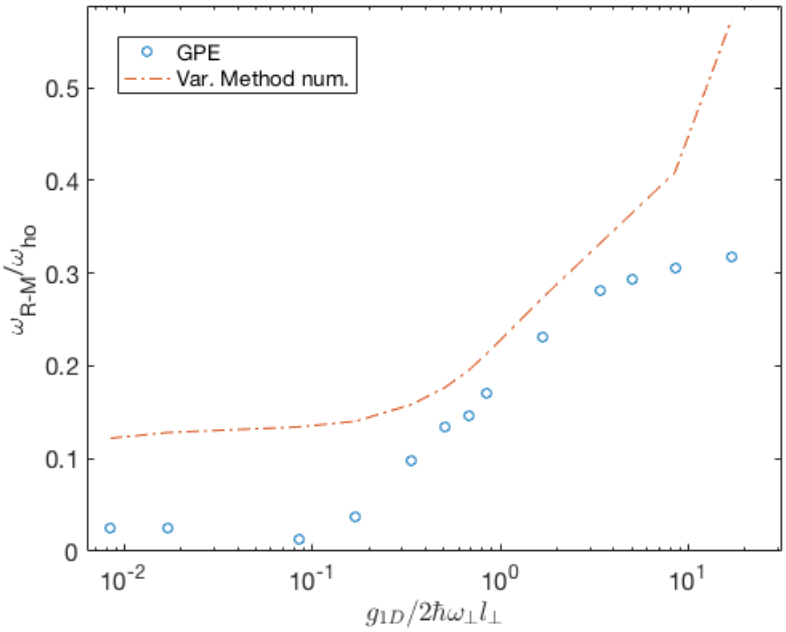

Figure 6.24: Revival frequency computed from the frequency spectra of σ obtained both with the numerical solutions of the GPE (dots) and with the numerical solution of the differential equations Eq. (6.40) and Eq. (6.41) obtained from the variational method. The frequency spectra used to determine the revival frequency with the variational method, obtained from the evolution of the lower moments for some values of the interaction strength, are shown in Fig. C.5.

oscillator, seems to be working quite well, especially for lower values of the interaction strength. In fact, we observe that the percentage relative errors lie in the interval $0 - 2.5\%$, with a higher uncertainty for higher values of g as a consequence of the fact that the prediction of the dipole oscillations obtained from the perturbation theory, in this limit, contains deviations close to this values. This can be seen from the relative difference in Fig. 6.21. The major source of deviation from the numerical solutions given by the GPE is therefore the lack of accuracy in determining the dipole frequency shift, whilst the effect of the revival frequency seems to be playing the major role.

6.7 Conclusion

We have studied the out-of-equilibrium dynamics of a BEC in a tilted ring potential, focusing on collective oscillations that have been investigated in the harmonic oscillator

limit before, with different approaches. Here in particular, we discussed the variational method with the Gaussian ansatz, and the hydrodynamic limit for strong interactions, achieved when the quantum pressure is negligible.

Being able to simulate the full dynamics of the BEC through the Gross-Pitaevskii Equation and to determine the frequency spectrum from its Fourier transform, gives us some advantages compared to aforementioned methods that aim to give an analytical description. One of these is the advantage of not being restrained by a particular form of the ansatz, like in the case of the variational method, where depending on the geometry of the system the same ansatz can lead to inaccurate results (as seen in the latest results of the previous section). On the other side, we do not need to neglect the kinetic term like in the Thomas Fermi approximation in the hydrodynamic limit. The main approximation in this model is therefore given by the fact that we do not consider the non-condensed cloud, as the GPE is a mean field approach.

Taking the results of the 1D harmonic oscillator in mean field as a starting point, we studied the frequency spectra obtained from the GPE simulation to characterise the collective oscillations and the frequency shifts in the tilted ring potential. Comparing the results for the two different potentials allowed us to determine how the different non linear effects, coming from the interaction within the BEC and the anharmonic potential, affect the dynamics. The observation of the spectra turned out to be an invaluable tool to extract the main features of the system dynamics.

We summarise here briefly the main results obtained in this chapter. For the harmonic oscillator we noticed that interactions within the BEC give rise to a damping of the oscillations and a broadening of the peaks, which is determined by the collisions within the BEC. In the tilted ring, the damping is observed even in the non interacting case, due to the anharmonicity that leads to dephasing and decoherence of the initial wavepacket. In both cases the damping is followed by revivals, which give rise to peaks at lower frequencies in the frequency spectra.

We observed, for both potentials, the appearance of sidebands in the frequency spectra of both the density and the moments, whose distance from the main peaks is given by multiples of the revival frequency, but with a different structure in the two potentials.

The frequency shift was also determined, for both cases, from the frequency spectra. While for the harmonic oscillator potential the dipole mode is decoupled from the other modes and the motion of the center of mass does not depend on the interactions, in the tilted ring we saw that the anharmonicity induces a coupling between the even and the odd modes (e.g. dipole and monopole). This was seen also by extending the variational method approach to the case of a harmonic potential perturbed with a quartic term. We therefore observed the shift of the dipole mode due to the collisions within the BEC and predicted the shift with first order perturbation theory, which gives a reasonably good agreement. For the study of the monopole frequency shift, we observed that there is a relation between this and the revival frequency observed. More precisely, we found that the shift of the monopole mode can be derived, both in the harmonic oscillator and in tilted ring traps, by subtracting the revival frequency to the "bare" breathing frequency estimated from twice the classical oscillation frequency, which is dependent on the form of the potential. These phenomenological results are in excellent agreement with the numerical data obtained from the GPE, and in the case of the ring potential we showed that they give a better prediction than the variational method.

Although we do not have yet a deeper understanding of this phenomenological result, the revival frequencies observed close to the zero seem to be the key feature, connecting the structure of the sidebands, which appear at multiples of the revival frequency, and the shift of the frequency modes from the main peaks to the successive lower frequency sidebands, for increasing interaction strengths. In the future it would be interesting to study these effects in more detail, to gain a better understanding of the connection between them.

This study would be interesting considering also the dynamics obtained using different parameters of the ring potential and radius, as well as different initial positions that can allow us to explore regimes that go beyond the quartic approximation of the potential, where the dynamics presents super-revivals. This would allow to see how the interaction affects the dynamics in this limit and whether the frequency shift of the monopole mode could be predicted also by the super-revival frequency, in analogy to the phenomenological relation that includes the revival frequency.

However, going beyond the approximation of small oscillation, to the extreme limit of oscillations of a BEC launched from the top of the trap, would not be ideal for our study, as the splitting and recombination of the cloud at the top of the ring creates interference that generates the so called "quantum carpets" [194, 195]. Analysing the frequency spectra of the density obtained from the dynamics would result in too many frequency components in the frequency spectra (determined by quantum fractional revivals) that would be hard to analyse.

Here we have considered the case of a quasi-one-dimensional ring, where the radial direction is much smaller than the healing length, so that the dynamics in this direction is frozen and the wavefunction along it can be described as the ground state of a harmonic oscillator. However, including the dynamics in the radial direction, either by considering more available states in this dimension or by using a full 2D description, would be interesting to study, for varying interactions, the interplay of the dynamics in the two directions in the tilted ring potential, and see how this changes the frequency of the lowest modes and eventually effects of coupling between the different modes.

The study of this kind of system, because of the anharmonicity, offers a different setup in the investigation of collective oscillations generated by the non linear dynamics, compared with previously studied systems. In particular, the frequency spectra derived from the dynamics in the mean field approximation give a large amount of information on the dynamics of the system and on the physics behind it. Although it was not discussed here, this system presents chaotic behaviour [101], and the appearance of broad band components can be interpreted as a signature of this [196]. Furthermore, we aim to understand if the characterization of collective oscillations can be used to determine the structure factor from the evaluation of the moments.

Chapter 7

Dynamics of an exciton-polariton condensate in a microcavity ring

7.1 Introduction

In this chapter we present the results of a collaboration with the experimental group of David Snoke at the University of Pittsburgh on the study of the dynamics of exciton-polariton condensates in a microcavity ring, which led to the publication in [124]. Although in this thesis we do not aim to focus on the study of polaritons, we give a brief overview to describe these systems, and report the theoretical model used to explain some experimentally observed features. This study played a large part in the motivation for the research reported in Chapter 6.

Alongside ultracold atoms, solid state systems have been proposed as alternative candidates to observe the onset of Bose-Einstein condensation, both with excitons [197] and with exciton-polaritons (polaritons) [198]. Polaritons have low mass, in current semiconductor microcavities, around 10^9 times lighter than rubidium atoms due to the fact that they are hybrid excitations of matter and photons, and because of the bosonic statistics that these quasiparticles have, condensation can be obtained through a thermalization process. Coherent population [199–203] of the lowest single-particle state in polariton systems, in analogy to the case of atomic gases, has been shown, and the emergence of quantum effects such as superfluidity [204] and quantized vortices [205]

were observed.

Polaritons [206] are quasiparticles obtained from strong coupling between photons and excitons (electron-hole pairs), therefore they can be considered as photons dressed with matter fields. The interest in the study of exciton-polariton BEC over exciton BEC has been motivated by the fact that the mass of polaritons ($m_{pol} \sim 10^{-5} m_e$) is around 4 orders of magnitudes lighter than the mass of excitons, and as a consequence the condensation can be achieved even at room temperature [201–203], with temperatures in the range of $1 - 300$ K.

The achievement of condensation in polaritons, under incoherent pumping, relies on a thermalization process assisted by the interaction between the polaritons. This was successfully obtained for the first time in 2006 [199], where a macroscopic occupation of polaritons in lower energy states was observed in the momentum space, together with long range order in real space.

One of the challenges in the achievement of full thermalization, in these systems, is due to the fact that their lifetime, determined by the photon leakage rate from the cavity, is short compared to the thermalization time. These timescales, for typical experiments, have been reported to be respectively $\tau \sim 1 - 10$ ps and $T_{th} \sim 1 - 10$ ps, with a ratio in the range $T_{th}/\tau \sim 0.1 - 10$, in contrast to atomic gas BEC, where this is $T_{th}/\tau \sim 1$ ms/1 s $\sim 10^{-3}$ [207]. This led to controversies in the definition of Bose-Einstein Condensates when discussing the physics of these systems, since they are inherently out-of-equilibrium [208, 209].

However, recently significant progress has been made in limiting the leakage of photons from the cavities, leading to ultralong lifetimes on the order of $\sim 100 - 200$ ps, which, compared to thermalization times $T_{th} \sim 5 - 10$ ps, allowed the observation of Bose-Einstein condensation of polaritons at equilibrium [210].

Another challenge in the study of these systems is the presence of an incoherent reservoir of excitons interacting with the coherent part of the many-body system, which makes it difficult to measure key physical quantities such as the polariton-polariton interaction strength. For this reason, increasing interest has been tailored towards the creation of particular geometries and techniques that make it possible to separate the

two components. Recent experiments, using different methods, such as the propagation of polaritons far from the reservoir [211] and depletion of the incoherent population [212], allowed direct measurements of the polariton-polariton interaction strength.

Motivated by these challenges, the group of David Snoke recently set up a tilted microcavity ring platform, with an effective one-dimensional geometry achieved through etching processes in its structure, to study the dynamics of polaritons with ultralong lifetime of ≈ 200 ps [124]. The dynamics of polaritons in this configuration, which will be the subject of investigation in the rest of the chapter, has many potential interesting aspects. The gradient of the ring potential, combined with the long lifetime of polaritons, allows them to travel distances of the order of hundreds of microns, and to observe their dynamics far from the laser injection spot, where an excitonic hill builds up. Doing so, the condensation can be observed without being attributed to non-linear effects of the laser light, and the polaritons can in principle be separated from the incoherent reservoir of excitons. Studying the physical processes involved in this dynamics is therefore important to understand what novel contributions and advantages we can obtain from this configuration.

Because of their finite lifetime and their creation process, polariton BECs are out-of-equilibrium systems usually described by means of driven-dissipative models. In the following we model the dynamics of polaritons in tilted microcavity rings of different sizes, using a modified Gross-Pitaevskii Equation that accounts for the generation and decay of polaritons, as well as relaxation processes that we describe with a phenomenological term, due to interaction with an excitonic reservoir.

The remainder of this chapter is structured as follows. In Section 7.2 we give a brief background on the exciton-polariton systems. In Section 7.3 we present the model analysed and the theoretical methods used to describe the dynamics of the polaritons in the regime of interest. In Section 7.4 we present the results obtained from the theoretical model, alongside the experimental data obtained by the group of David Snoke, and comment them. Finally, in Section 7.5 we summarise the key results and discuss some future directions.

7.2 Exciton-polaritons

The experimental setup used in the experiments which we study here is constituted by a microcavity, where photons are pumped, and quantum wells of semiconductors placed between the Bragg reflectors, where excitons are generated. In the following we show how the coupling between exciton and cavity photon modes gives rise, through a linear supersposition of these, to polariton modes. Therefore we first obtain the energy dispersion for the cavity photon and the excitons, and then derive the dispersion relations for the polaritons.

Let us consider a photon in a cavity, trapped between two Bragg mirrors separated by a distance D, with refractive index n_0. The energy of the photon in the cavity is

$$E_C = \hbar\omega_C = \hbar\frac{c}{n_0}k = \hbar\frac{c}{n_0}\sqrt{k_\perp^2 + k_\parallel^2}, \tag{7.1}$$

where $k_\perp$ and $k_\parallel$ are the components of the photon momentum in the directions respectively perpendicular and parallel to the mirror surface. The boundary condition along the perpendicular direction fixes the momentum $k_\perp = M\pi/D$, where M is a positive integer. For $k_\parallel \ll k_\perp$ we can write $\sqrt{k_\perp^2 + k_\parallel^2} \simeq k_\perp + \frac{k_\parallel^2}{2k_\perp}$, leading to $E_C = \frac{\hbar c k_\perp}{n_0} + \frac{\hbar^2 k_\parallel^2}{2n_0 k_\perp \hbar}$, therefore obtaining a dispersion relation that depends quadratically on $k_\parallel$, which we can write in the form

$$E_C = E_C^0 + \frac{\hbar^2 k_\parallel^2}{2m_C}, \tag{7.2}$$

where we have introduced a cutoff energy $E_C^0 = \frac{\hbar c k_\perp}{n_0}$ and the effective mass of the cavity field

$$m_C = n_0 k_\perp \hbar = \frac{n_0 \pi M \hbar}{cD}. \tag{7.3}$$

This is typically of the order of $10^{-4} m_e$, where m_e is the electron mass in the vacuum. Polaritons can form when the light trapped in the cavity strongly interacts with an active medium, such as semiconductors layers, exciting the electrons from the valance to the conduction band and leading to the formation of an electron-hole bound state,

an exciton. The exciton energy is given by

$$E_x(k) = E_x(0) + \frac{\hbar^2 k_\parallel^2}{2m_{ex}}, \tag{7.4}$$

where $m_{ex} = m_e m_h/(m_e + m_h)$ is the reduced mass obtained from the electron and hole masses, and $E_x(0) = E_{gap} - E_B$. Here E_{gap} is the energy gap between the two bands and $E_B = \frac{\hbar^2 k^2}{2m_{ex}a_{ex}^2}$ is the binding energy, with a_{ex} the exciton Bohr radius. Since $m_{ex} \approx 10^3 m_C$, the exciton energy can be approximated as constant ($E_x(0)$) with $k_\parallel$. The Hamiltonian for the polaritons can be written as

$$\begin{aligned}\hat{H}_P &= \hat{H}_C + \hat{H}_x + \hat{H}_I \\ &= \sum_{k_\parallel} E_C(k_\parallel)\hat{c}^\dagger_{k_\parallel}\hat{c}_{k_\parallel} + \sum_{k_\parallel} E_x(k_\parallel)\hat{a}^\dagger_{k_\parallel}\hat{a}_{k_\parallel} + \Omega_0 \sum_{k_\parallel}(\hat{c}^\dagger_{k_\parallel}\hat{a}_{k_\parallel} + \hat{a}^\dagger_{k_\parallel}\hat{c}_{k_\parallel}),\end{aligned} \tag{7.5}$$

where we introduced the bosonic annihilation operators for the excitons and the cavity, respectively indicated with $\hat{a}_{k_\parallel}$ and $\hat{c}_{k_\parallel}$, and the coupling Ω_0 between cavity photons and excitons.

This Hamiltonian can be diagonalised by introducing new operators $\hat{P}_{k_\parallel}$ and $\hat{Q}_{k_\parallel}$, as a linear combination of the modes of the cavity photons and the excitons [206]

$$\hat{P}_{k_\parallel} = X(k_\parallel)\hat{a}_{k_\parallel} + C(k_\parallel)\hat{c}_{k_\parallel}, \tag{7.6}$$

$$\hat{Q}_{k_\parallel} = -C(k_\parallel)\hat{a}_{k_\parallel} + X(k_\parallel)\hat{c}_{k_\parallel}, \tag{7.7}$$

leading to eigenvalues of the form

$$E_{LP/UP}(k_\parallel) = \frac{1}{2}\left[E_X(k_\parallel) + E_C(k_\parallel) \mp \sqrt{\Omega^2 + \delta^2(k_\parallel)}\right], \tag{7.8}$$

where $\delta(k_\parallel)$ is the detuning energy, given by

$$\delta(k_\parallel) = E_C(k_\parallel) - E_X(k_\parallel). \tag{7.9}$$

Therefore the Hamiltonian of Eq. (7.5) reduces to the diagonal form

$$\hat{H}_P = \sum_{k_\parallel} E_{LP}(k_\parallel)\hat{P}^\dagger_{k_\parallel}\hat{P}_{k_\parallel} + E_{UP}(k_\parallel)\hat{Q}^\dagger_{k_\parallel}\hat{Q}_{k_\parallel}, \tag{7.10}$$

from which we can clearly see that two kinds of quasiparticles are obtained, after using the above transformation. These quasiparticles are the lower and upper polaritons, whose modes are indicated respectively with the bosonic annihilation operators $\hat{P}_{k_\parallel}$ and $\hat{Q}_{k_\parallel}$.

We can then see more clearly how polaritons can be considered as hybrid quasiparticles having both light and matter components, with proportions determined by the factors $X(k_\parallel)$ and $C(k_\parallel)$, called Hopfield coefficients [206] and satisfying the relation $|X(k_\parallel)|^2 + |C(k_\parallel)|^2 = 1$. These are defined according to the relations

$$f_X(k_\parallel) = |X(k_\parallel)|^2 = \frac{1}{2}\left(1 + \frac{\delta(k_\parallel)}{\sqrt{\delta^2(k_\parallel) + \Omega^2}}\right), \tag{7.11}$$

$$f_C(k_\parallel) = |C(k_\parallel)|^2 = \frac{1}{2}\left(1 - \frac{\delta(k_\parallel)}{\sqrt{\delta^2(k_\parallel) + \Omega^2}}\right), \tag{7.12}$$

which describe respectively the excitonic and the photonic fractions of the lower polaritons. In these equations for convenience we defined $\Omega = 2\Omega_0$. It is therefore evident that changing the detuning δ affects the excitonic and photonic components of the polaritons (for $\delta = 0$ the LP and UP are half exciton and half photon), as well as their effective mass, and therefore the way they interact with each other.

The dispersion curves for the polariton modes, together with the ones of the cavity field and the exciton, are represented qualitatively in Fig. 7.1 for different values of the detuning δ, having fixed the coupling Ω.

7.3 Model

As discussed in Section 7.1, motivated by current experimental realisations with these platforms [124], we study the dynamics of polaritons in an effective one-dimensional

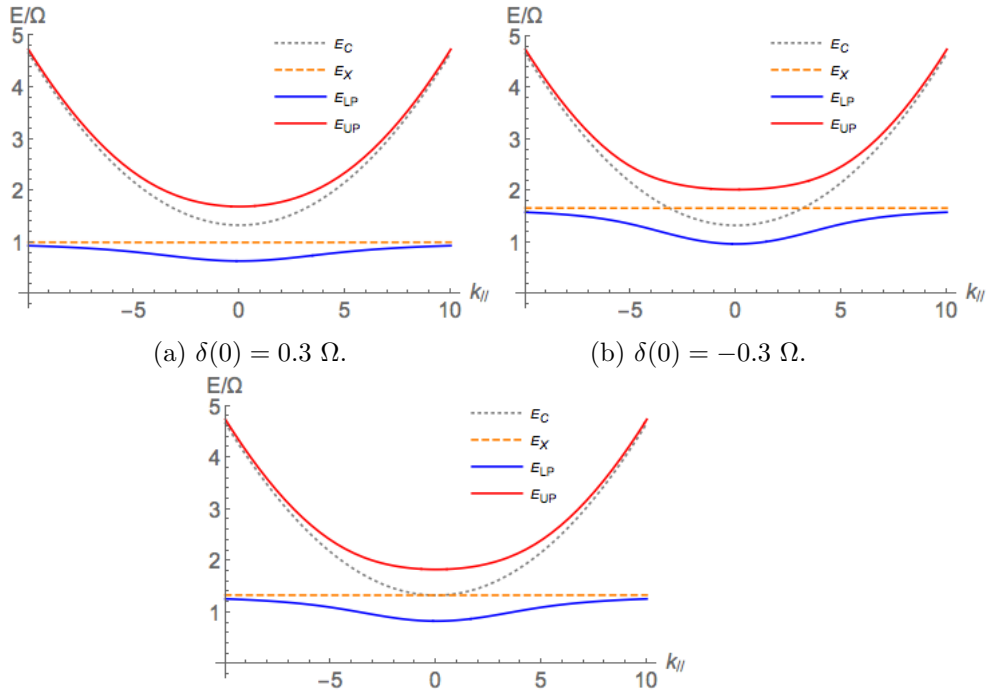

(a) $\delta(0) = 0.3\ \Omega$. (b) $\delta(0) = -0.3\ \Omega$.

(c) $\delta(0) = 0$.

Figure 7.1: Dispersion curves obtained for the polariton modes Eq. (7.8), the cavity field Eq. (7.2) and the exciton energy Eq. (7.4), in units of the coupling Ω, shown qualitatively for a fixed value of this and different detunings δ, and $E_C(0) = 1.3\ \Omega$.

tilted microcavity. The experimental geometry here inspired the choice of geometry for the research in Chapter 6. Therefore, the choice of potential is analogous to the one introduced in Chapter 6, of the form

$$V(\theta) = \frac{V_0}{2}[1 - \cos(\theta)]. \tag{7.13}$$

In contrast with the case studied in Chapter 6, where the number of atoms was conserved, here we have to adopt a slightly different model to account for the generation of polaritons, as well as the decay due to the fact that polaritons have a finite lifetime, given by

$$\tau_{pol} \approx \frac{\tau_C}{f_C}, \tag{7.14}$$

where τ_C is the lifetime of the photons in the cavity. As we show in the schematic representation of Fig. 7.2, the polaritons are created at the top of the ring by means of

a laser directed on the active layer, where excitons are formed. The polaritons travel around the ring and their density is measured at the bottom (at $\theta = 0$), together with their energy ΔE_{LP}.

In this experimental setup the one-dimensional geometry allows polaritons to have a considerably long lifetime of $\tau_{pol} \sim 200$ ps, and to travel distances of the order of tens of microns (we study the dynamics of the polaritons in microcavity rings of different dimensions, having radii of $40, 50$ and 60 μm). In this chapter we estimate the interaction strength between both polaritons and excitons, and we study how the interaction affects the frequency of the oscillations in the polaritons' density.

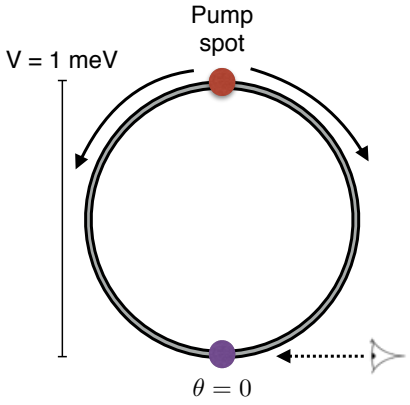

Figure 7.2: Schematic representation of the trapping potential used to study the dynamics of polaritons. The polaritons are generated at the top of the ring and move towards the bottom, where their density is measured by detecting the emitted photons.

In order to describe the dynamics of the polaritons at the $\theta = 0$, we adapt the Gross-Pitaevskii Equation (GPE) introduced in Chapter 2 and used in Chapter 6 to include the pumping and the dissipative terms, together with a phenomenological damping term of the kinetic energy, to account for relaxation due to the presence of a population of an exciton reservoir around the bottom of the ring $\theta = 0$. We therefore use the open-dissipative GPE (ODGPE), having the form

$$i\hbar\frac{\partial\psi(\theta,t)}{\partial t} = \left[-(1-i\alpha)\frac{\hbar\nabla^2}{2m} + V(\theta) + g_{1D}|\psi(\theta,t)|^2 + iG(t) - i\Gamma(t)\right]\psi(\theta,t), \quad (7.15)$$

where

$$G(t) = G_0[1 - e^{-t/\tau_1}]e^{-t/\tau_2}, \tag{7.16}$$

$$\Gamma(t) = \Gamma_0[1 - e^{-t/\tau_3}], \tag{7.17}$$

are respectively the time-dependent feeding and decay terms, and α is a phenomenological factor, first introduced by Pitaevskii [213], and now widely used in the exciton-polariton literature to account for the relaxation, due for example to scattering with phonons and excitons [214–216]. This simplified phenomenological model is aimed to describe the oscillations at the bottom of the ring at $\theta = 0$, where the photon emission is detected experimentally, therefore the generation term here keeps into account the time needed for the polaritons to move from the top to the bottom of the ring. We rewrite the ODGPE of Eq. (7.15) in the dimensionless form, after defining $x = \theta R$ and rescaling time, energy and length with the units $T = 2\pi/\omega$, $E = \hbar\omega$ and $l_0 = \sqrt{\hbar/m_{pol}\omega}$, where $\omega = \sqrt{V_0/(2m_{pol}R^2)}$ is the oscillation frequency defined by the potential V_0 of the tilted ring and the radius R. For convenience, we consider the initial wavefunction to be normalised to one, so that the dimensionless initial wavefunction is rescaled as $\psi l_0/\sqrt{N}$, and we can transfer the dependence of the dynamics on the initial number of polaritons N in the interaction term, as $g_{1D}N$. Furthermore, Therefore, in dimensionless form (where the dimensionless physical quantities are indicated with the subscript 'd'), the ODGPE of Eq. (7.15) reduces to the form

$$i\frac{\partial\psi_d}{\partial t_d} = \left[-(1 - i\alpha)\pi\frac{\partial^2}{\partial x_d^2} + \frac{\pi V_0}{\hbar\omega}[1 - \cos(l_0 x_d/R)] + \frac{2\pi g_{1D}N}{\hbar\omega l_0}|\psi_d|^2 + iG_d(t_d) - i\Gamma_d(t_d)\right]\psi_d, \tag{7.18}$$

where we have used an initial Gaussian wavefunction of the form

$$\psi_d(x_d, 0) = \frac{1}{\sqrt{\sqrt{\pi}\sigma_d \operatorname{erf}(\pi R/\sigma_d l_0)}} e^{-x_d^2/2\sigma_d^2}. \tag{7.19}$$

For the simulation of the ODGPE we use the split-step Fourier transform method discussed in Appendix B, being careful to renormalise the wavefunction after the action of the non-Hermitian evolution given by the damping term proportional to α.

7.4 Results

We use the model described above to simulate the polariton dynamics and caluculate the density at the bottom of the ring. From this we derive the exciton density determined by their excitonic fraction from the relation

$$n_{ex}(\theta, t) = |X(k_{\|})|^2 n_{pol}(\theta, t), \tag{7.20}$$

which we will use in the following to compare the numerical simulation with the experimental data. In order to study the effects that the interaction strength and the phenomenological parameter α in Eq. (7.18) have on the dynamics of the polaritons, we first consider the dynamics in a microcavity ring of radius $R = 50\mu$m, for different values of these parameters, and show the oscillations of the exciton density $n_{exc}(0, t)$ at the bottom of the ring in Fig. 7.3, for the different values considered.

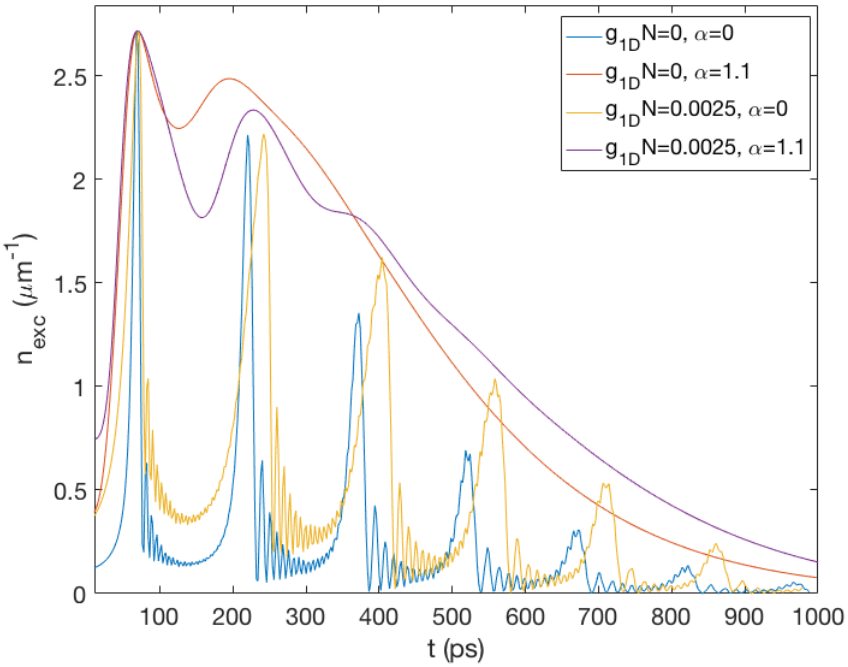

Figure 7.3: Density of excitons (7.20) estimated from the polariton density simulated from Eq. (7.18), for different values of the damping coefficient α and the interaction strength $g_{1D}N$ in eVμm, as in legend, and for the ring with radius $R = 50\mu m$. The other parameters used are the ones reported in Table 7.1.

We observe that, as is consistent with the results discussed in Chapter 6, increasing the interaction generates a red shift of the oscillation frequency and broadens the density peaks. The relaxation term α however is fundamental to match the experimental results and to observe smoother oscillations, as a result of damping higher momentum oscillations due to the interaction with the exciton reservoir, for which we also see evidence in the experiment. The effect that the damping term has on the polariton density in momentum space, for the same parameters used in Fig. 7.3, is shown in Fig. 7.4, where we observe that, while for $\alpha = 0$ the polaritons reach higher values of momentum, which results in sharper oscillations of the density, for finite values of α the momentum is confined to lower values. As a result, we see that the oscillations are almost completely smoothed out for the non-interacting case, but are recovered for a finite value of the interaction.

As mentioned in the previous section, we aim to observe how the interaction affects the dynamics of the polaritons in microcavity rings of different dimensions, and to discuss the interaction strengths observed in this regime, through the estimated value of the exciton-exciton interaction g_{xx}.

7.4.1 Oscillations of polaritons in microcavity rings of different radii

In this part we study the dynamics of low density polaritons and the corresponding density of excitons, obtained from Eq.(7.20). Having experimental data of the exciton density in rings with radii of $40, 50$ and 60μm, we find the best fits for these datasets, using the model of Eq. (7.18) to simulate the dynamics of polaritons, and from $n_{pol}(0,t)$ we extract the exciton density using Eq. (7.11). We therefore determine, by changing the value of the interaction strength g_{1D}, how the frequency of the oscillations changes for every configuration, compared to the non-interacting case. We show the best fits and the experimental data in Fig. 7.5.

The parameters used for the numerical simulations of Eq. (7.18) to obtain the results shown in Fig. 7.5 are reported in Table 7.1. In Table 7.2 we report the values of the periods observed with the values of the interaction strength given by the best fits and compare them with the ones expected in the non-interacting case. The configurations

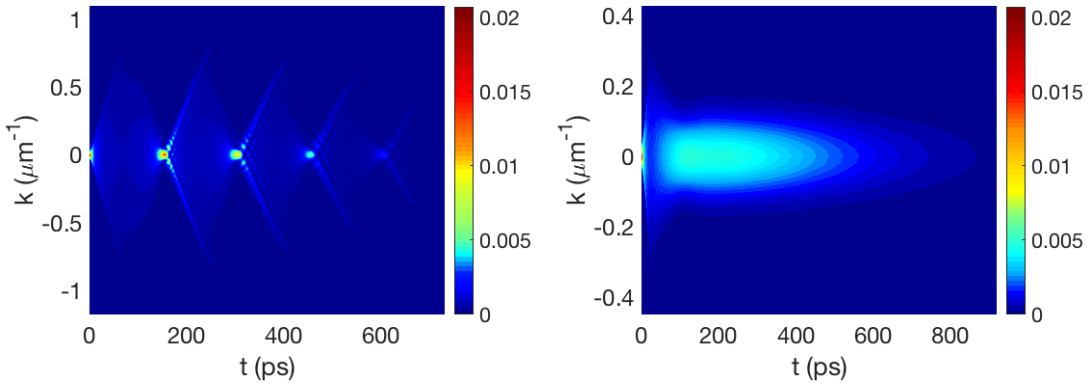

(a) $\alpha = 0$, $g_{1D}N = 0$ eV μm (b) $\alpha = 1.1$, $g_{1D}N = 0$ eV μm

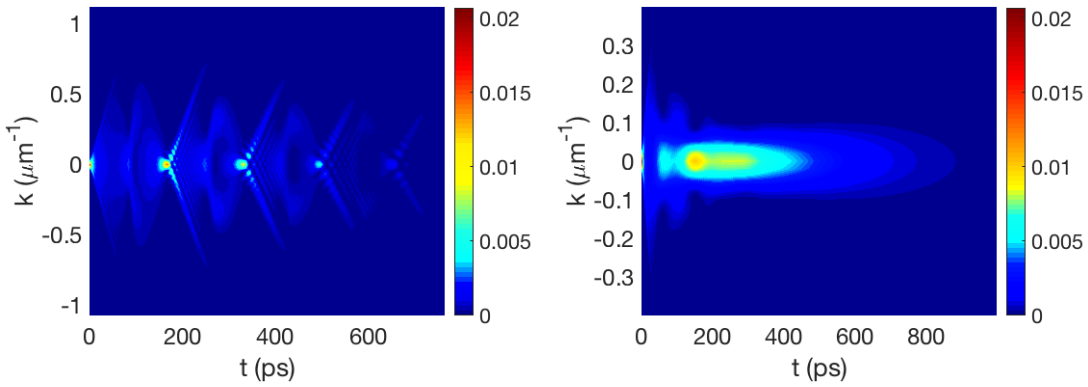

(c) $\alpha = 0$, $g_{1D}N = 0.25 \times 10^{-2}$ eV μm (d) $\alpha = 1.1$, $g_{1D}N = 0.25 \times 10^{-2}$ eV μm

Figure 7.4: Density of polaritons in momentum space, computed using Eq. (7.18) for different values of the interaction strength $g_{1D}N$ and the relaxation coefficient α.

R(μm)	$\omega\tau_1/2\pi$	$\omega\tau_2/2\pi$	$\omega\tau_3/2\pi$	$2\pi G_0/\omega$	$2\pi\Gamma_0/\omega$	α	σ_d	$g_{1D}N$ (eV μm)
40	0.15	0.6	0.5	1.0	0.9	1.1	5	0.50×10^{-2}
50	0.20	0.6	1.5	1.0	1.0	1.1	6	0.25×10^{-2}
60	0.20	0.6	0.5	1.0	1.0	0.8	5	0.25×10^{-2}

Table 7.1: Parameters used to reproduce the dynamics of the polaritons densities represented in Fig. 7.5.

with different radii correspond to non equal values of the energy gradient V_0 and will correspond to different masses of the polaritons m_{pol}. These were determined by estimating the lower polariton dispersion relation from Eq. (7.8) and fitting that with a parabola centered at $k = 0$.

R(μm)	V_0 (meV)	m_{pol} ($\times 10^{-5} m_e$)	T (ps)	T_g (ps)	$g_{1D}N$ (eV μm)
40	0.66	6.7	270	272±5	0.50×10^{-2}
50	0.83	6.4	302	306±5	0.25×10^{-2}
60	0.88	6.0	331	343±5	0.25×10^{-2}

Table 7.2: Comparison between the oscillation period $T = 2\pi/\omega = 2\pi\sqrt{2m_{pol}R^2/V_0}$ expected in the non-interacting case and the period T_g observed experimentally by evaluating the time between the first and the third peak in the oscillations of the experimental densities represented in Fig. 7.5, for different values of the radii. The different sizes of the ring determine different values of the energy gradient V_0 and of the polariton mass m_{pol}, which are also reported.

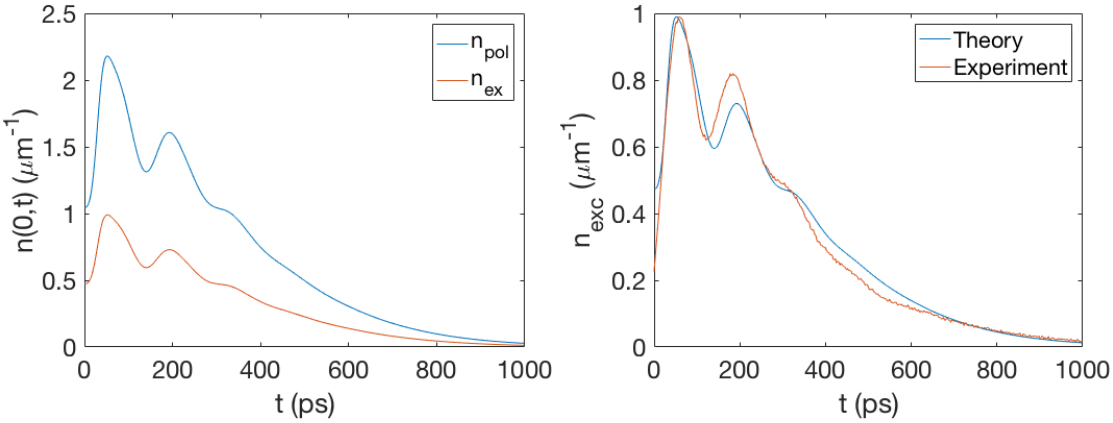

(a) $R = 40, g_{1D}N = 0.5 \times 10^{-2}$ eV μm (b) $R = 40, g_{1D}N = 0.5 \times 10^{-2}$ eV μm

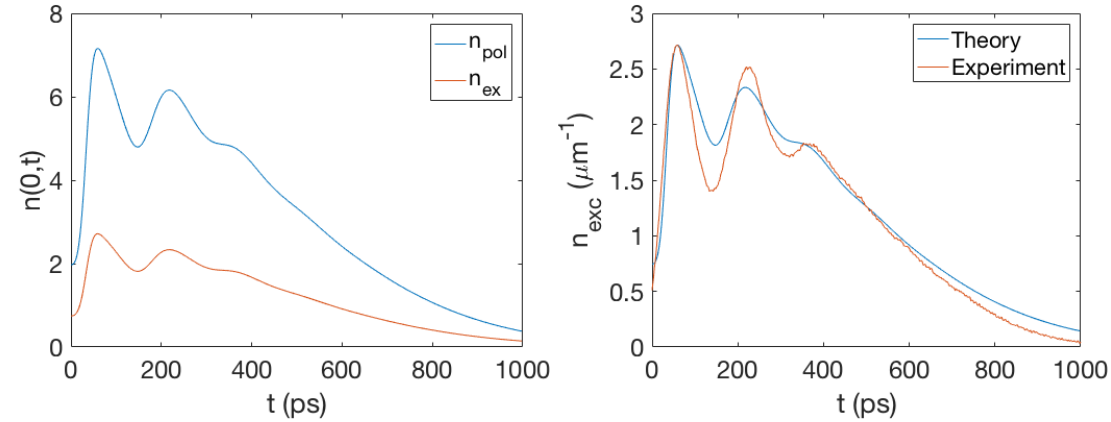

(c) $R = 50, g_{1D}N = 0.25 \times 10^{-2}$ eV μm (d) $R = 50, g_{1D}N = 0.25 \times 10^{-2}$ eV μm

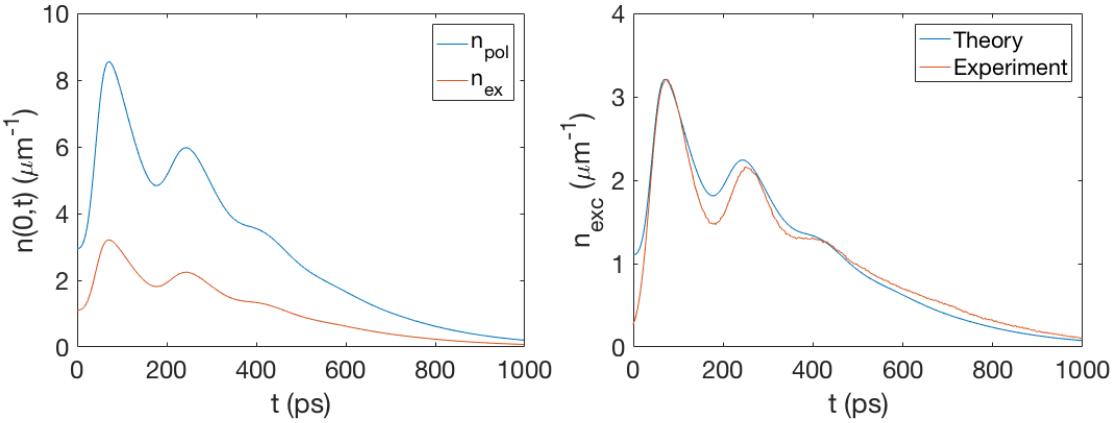

(e) $R = 60, g_{1D}N = 0.25 \times 10^{-2}$ eV μm (f) $R = 60, g_{1D}N = 0.25 \times 10^{-2}$ eV μm

Figure 7.5: Polariton densities at the bottom of the ring $n_{pol}(\theta = 0, t)$ and corresponding exciton densities $n_{ex}(0, t)$ estimated using Eq. (7.20) (left), and comparison between the exciton densities obtained numerically and experimentally (right) for rings with different radii and with the interaction strengths reported in captions. The parameters used for the simulations are reported in Table 7.1.

7.4.2 Estimation of the interaction strength from the energy shift

In the previous section we have determined the value $g_{1D}N$ from the best fit to the exciton density $n_{ex}(\theta = 0, t)$. However, the inability to determine the initial number of polaritons N does not allow us to estimate the effective value g_{1D} of the polariton-polariton interaction strength.

We now consider a different set of experimental data, that in contrast to the previous case have a higher density of polaritons, which are in the regime useful to achieve condensation. For this case, we refer to the experimental datasets of the energy shift caused by the interaction and of the measured densities of polaritons, and discuss the important features in their relation and in the determination of the interaction strength. From the time-independent GPE, the blue shift of the energy, in the Thomas-Fermi regime, is mainly determined by the interaction strength and should be directly proportional to the density of polaritons, according to the equation

$$\Delta E_{LP}(\theta, t) = g_{p-p} n_{pol}(\theta, t), \tag{7.21}$$

therefore we expect the measured blue shift to follow the same trend in the oscillations, compared to the density of polaritons measured. However, from Fig. 7.6 we observe that there is a discrepancy between the experimental measured value of the blue shift and the one trend given by the bare interaction between the polaritons from Eq. (7.21). As we have pointed out in the previous section, however, for a correct description of the dynamics we have to include a phenomenological term that accounts for the interactions with an exciton reservoir. Based on the evidence of the presence of these excitons, we therefore have to include this contribution in the equation for the blueshift, so that

$$\Delta E_{LP} = g_{p-p} n_{pol}(t) + g_{pol-ex} n_{res}(t), \tag{7.22}$$

where $n_{res}(t)$ is the density of excitons in the reservoir. In order to obtain this in a convenient form, where we need to estimate only the interaction strength between

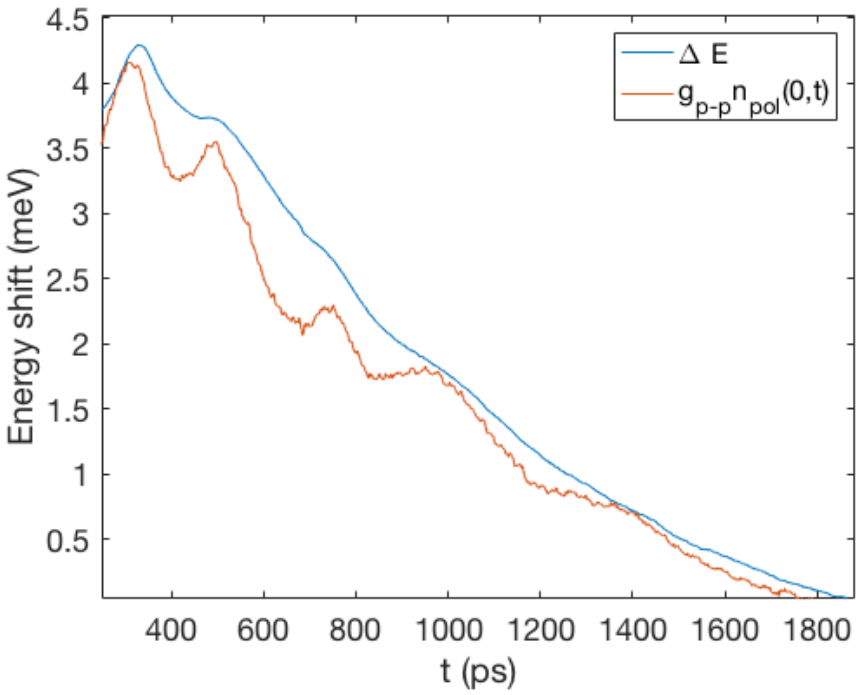

Figure 7.6: Energy shift measured experimentally (blue line) and energy shift obtained from Eq. (7.21), using an indicative guess value $g_{p-p} = 0.25 \times 10^{-2}$ eV μm. We see that in the measured energy shift the oscillation are smoothed out, resulting in a deviation between the predicted and the measured values, which can not simply be accounted for from Eq. (7.21).

the excitons, we transform the polariton population in its excitonic part and convert the interactions g_{p-p} and g_{pol-ex} to exciton-exciton interactions. As the interaction between the polaritons is mainly given by their excitonic fraction, the blueshift in the exciton energy is given by

$$\Delta E_X = g_{xx}(n_{ex}(t) + n_{res}(t)), \tag{7.23}$$

where the exciton component $n_{ex}(t)$ of the polaritons is determined from Eq. (7.20). Defining $\Delta E_{LP}(0) = E'_{LP}(0) - E_{LP}(0)$ and $\delta = E_c - E_x$, from the definition in Eq. (7.8), we obtain

$$\Delta E_{LP} = \frac{\Delta E_x}{2} + \frac{1}{2}[\sqrt{\delta^2 + \Omega^2} - \sqrt{(\delta - \Delta E_x)^2 + \Omega^2}]. \tag{7.24}$$

Using the definitions of the exciton blueshift in Eq. (7.23) and the excitonic frac-

tion $f_x(k_\parallel) = |X(k_\parallel)|^2$ of Eq. (7.11), the lower polaritons blueshift of Eq. (7.22) and Eq. (7.24) can be cast in the form

$$\Delta E_{LP} = g_{p-p} n_{pol}(t) + g_{pol-ex} n_{res}(t) \sim f_x(0) \Delta E_x(t) = f_x(0) g_{xx} [n_{ex}(t) + n_{res}(t)]. \tag{7.25}$$

By defining $g_{fit} = f_x(0) g_{xx}$ it is therefore possible to obtain the interaction between the excitons g_{xx}. More information about how to extract the population of the reservoir can be found in [124]. The exciton-exciton interaction strengths g_{xx} obtained in this set of experiments, for different pump powers beyond the threshold, give values of the order of 10 μeV μm^2, which are consistent with other values observed in the same regime at high densities [211, 212].

7.5 Conclusions

The system considered here presents some novelty due to the effective dynamics in one dimension and the ultralong lifetimes of the polaritons ($\sim$ 200 ps), allowing motion at distances of the order of hundreds of microns, far from the injection spot where the excitonic hill is created. The longer lifetime of the polaritons, compared to the thermalization time, allowed condensation close to equilibrium conditions to be observed in this experimental setup for the first time [210].

To gain a better understanding of the dynamics and the interactions between the components of the system, we have modeled the dynamics of low density polaritons for ring traps of different sizes, using a modified Gross-Pitaevskii Equation that accounts for pumping and dissipation, and we used this to explain some features of the experimental data obtained by D.Snoke's group [124].

We showed how the oscillations are affected by the interaction strength, observing how the period of the oscillations is different from bare classical pendulum oscillations, for different values of the ring radii. Furthermore, we inferred that the shape of the oscillations of the polaritons is strongly affected by relaxation phenomena given by the interaction with an excitonic reservoir. In order to account for this, we added a phenomenological term in the modified GPE.

From the study of the data obtained experimentally for polariton oscillations at higher densities, we observed that the presence of an excitonic reservoir manifests also here, in the measured energy shift. In order to have a match between the blue shift observed and predicted from the density of excitons, the presence of dark excitons was accounted for. From this, a value of the exciton-exciton interaction strength of the order of 10 μeV μm^2 was obtained, showing consistency with other experimental values in literature for polaritons at high densities.

The study of BEC in these platforms is very promising for the impact they can have in quantum devices, due to their compact size and to the fact that condensation with polaritons can in principle be achieved at room temperatures. Furthermore, these 1D geometries offer intriguing opportunities for the realisation of polariton circuits and networks of these, with connected 1D rings.

Chapter 8

Conclusions

The ability to engineer the dimensionality and the geometry of the trapping potentials for cold atoms, together with the control that we have over the interactions, allows us to design highly-controlled systems where we can access desired regimes. In this thesis we have used these possibilities in the context of both open and quantum systems by studying particular geometries and confinements of cold atoms and BEC. In particular, we studied the dissipative dynamics of impurities tightly confired in different dimensions, induced by their interaction with a weakly confined BEC, as well as the dynamics of interacting BECs trapped in one-dimensional tilted ring potentials. These models offer applications for experimental platforms of relevance in the context of quantum simulations and quantum technologies. In this chapter we review the key results of each project and discuss some possible future directions.

In Chapter 4 we studied the induced dissipative dynamics of neutral impurities trapped in different configurations, immersed in a BEC. In particular, motivated by the experimental possibility to control and address the dynamics of individually trapped atoms, we have studied the cooling induced by the coupling to a reservoir gas, which causes initially excited motional states to relax to lower temperature states. Changing the confinement of the trapped neutral impurities we investigated the induced dynamics of the atoms with tight confinement different dimensions, in configurations that are of experimental relevance and currently in place in different experimental groups. We

estimated the cooling rates of the impurities for realistic experimental parameters, and studied the heating effects of a finite temperature reservoir on the cooling process, showing that the timescales obtained for the cooling process can be accessed experimentally. Experimental applications of these cooling schemes then naturally follow.
The long coherence time of these systems allows us to use the induced dissipative dynamics to achieve cooling to lower temperature states, under desired conditions.
In particular, the study of a configuration where the dynamics is reduced along two directions, where one is tightly confined, offers the possibility to extend this study to the case of impurities trapped in a lattice, with the aim to implement dark state cooling [81, 82].

In Chapter 5 we used the same platform of an impurity in a BEC, but with a study tailored towards reservoir engineering and non-Markovian dynamics. Once again, the ability to control the confinement of both the trapped impurity and the reservoir, allows us to access different regimes where some approximations commonly used do not hold. This is the case for the non-Markovian dynamics explored in this chapter, where we have seen how changing the confinement of the impurity immersed in a cigar-shaped BEC, affects the ratio between the relaxation time of the system and the correlation time of the reservoir, leading to a backflow of information. The study conducted offers several possibilities for future directions, including the non-Markovian dynamics of impurities trapped in BEC having higher dimensions or having a finite number of modes to which the motion of the impurity is coupled, as well as the study of non-Markovian dynamics with two or more impurities.
The study of this system offers a promising toolbox for possibilities to explore new elements of non-Markovian dynamics that are not accessible in other platforms, such as atoms in cavities, because of the different nature of the reservoir.

In Chapter 6, motivated by ongoing experiments with BECs in tilted ring traps, we characterised the effect that this geometry has on the collective oscillations of the system. We studied the interplay between the non-linearity coming from the form of the

potential and the interaction between the atoms, and comparing analytical and numerical methods we have characterised the frequencies of the low-lying modes. We have seen how this geometry induces different behaviour compared to the case of harmonic potentials commonly studied, such as the coupling of the center of mass with the internal dynamics of the system.
This study was conducted for a one-dimensional trap and in the regime of small oscillations around the minimum of the potential, where the anharmonic effects are however visible. In future studies it would be interesting to consider more radial modes and study how the coupling to these affects the excitation spectra, but also to study the dynamics of solitons and BEC in tilted ring traps with barriers, with potentially useful applications in the context of atomtronics.

In Chapter 7 we studied the out-of-equilibrium dynamics of polaritons in a tilted ring trap, as a result of a collaboration with an experimental group on the subject. Current progress in these platforms has produced polaritons with long lifetime, making it possible to achieve condensation through thermalization of the polaritons. This possibility, together with the ability to design desired geometries, leads to possible applications in quantum technologies. It is therefore important to understand the physical processes observed for these systems in new geometries, to understand possible limitations in the models and future improvements both in experiments and for theoretical descriptions. In this case, in particular, we observed that the presence of a reservoir of excitons interacting with the polaritons requires the inclusion of thermalisation processes in the description of the out-of-equilibrium driven and dissipative dynamics.
Further directions in the theoretical model include the observation of coupling between the radial modes to see how this would eventually affect the dynamics of the polaritons even in relation to experimental observations. Furthermore, these platforms can be used for building networks of connected rings, which can find application for quantum memories in the context of quantum technologies and quantum computing.

Overall, the high degree of control that we have on these systems allows us to design

desired configurations for the study of the dynamics of ultracold atoms and BEC, in both open and closed quantum systems, offering a plethora of possibilities for advances in quantum technologies.

The system of impurities immersed in a BEC offers many possibilities in the context of quantum simulators, where the development of cooling techniques for producing lower temperature states gives us access to the study of interesting problems in many-body physics. Furthermore, we have seen how this system can be used to explore non-Markovian regimes and investigate novel elements of coherent and dissipative quantum dynamics, with potential applications in the context of state engineering. On the other side, the study of the dynamics in tilted trapped BECs, with both ultracold atoms and polaritons, offers different applications for atomtronics platforms, quantum metrology and sensing, and it provides new opportunities for the study of new aspects in the context of non-equilibrium dynamics.

Appendix A

Evaluation of the decay rates and semi-classical approximation

In Eq. (4.36) we provided the equation for the decay rates $\Gamma_{n1\to m0}$ in the 2D cigar-shaped trap, after using a semi-classical approximation. We discuss this more in detail in the following, and we also derive the decay rates in the fully quantum approach, with an analogous procedure used in the estimation of the transition coefficients in 3D (Eq. (4.32)).

Following previous considerations, in the cigar-shaped potential, based on the assumption that the energy spacing in the radial direction is much larger than the chemical potential, the excitations emitted in the decay from the first excited state in the radial direction can still be considered in the supersonic regime, where the structure factor is $S(k) = (u_k + v_k)^2 = 1$. With calculations similar to the 3D case, for the estimation of the matrix elements, we used the relation in Eq. (4.29). After writing the components of the momentum in the two directions in polar coordinates, as $k_x = k\cos\theta$ and $k_z = k\sin\theta\cos\phi$, and integrating over k using the properties of the delta function involving the energies, we obtain the decay rates

$$\begin{aligned}\Gamma_{n,1\to m,0} =& \frac{2g_{ab}^2\rho_0\sqrt{m_a m_b}}{(2\pi)^2\hbar^3 u}\frac{m_<!}{m_>!}\sqrt{\frac{m_b}{m_a}\big(w+n-m\big)}\sqrt{\omega_x\omega_0} \\ &\times\int_0^\pi d\theta B_\phi(n,m,\theta)e^{-\xi^2(\theta)}\xi^{2|n-m|}(\theta)\sin\theta\big|L_{m_<}^{|n-m|}(\xi^2(\theta))\big|^2, \end{aligned} \tag{A.1}$$

Appendix A. Evaluation of the decay rates and semi-classical approximation

where $w = \dfrac{\omega_z}{\omega_x}$, $m_< = \min(n, m)$, $m_> = \max(n, m)$,

$$\xi^2(\theta) = \frac{x_0^2 k^2 \cos^2\theta}{2} = \frac{m_b}{m_a}(w + n - m)\cos^2\theta, \tag{A.2}$$

and

$$\begin{aligned} B_\phi(n, m, \theta) &= \int_0^{2\pi} d\phi e^{-\zeta^2(\theta)\cos^2\phi}\zeta^2(\theta)\cos^2\phi \\ &= \pi\zeta^2(\theta)e^{-\zeta^2(\theta)/2}\left[I_0\left(\frac{\zeta^2(\theta)}{2}\right) - I_1\left(\frac{\zeta^2(\theta)}{2}\right)\right]. \end{aligned} \tag{A.3}$$

Here

$$\zeta^2(\theta) = \frac{z_0^2 k^2 \sin^2\theta}{2} = \frac{m_b}{m_a w}(w + n - m)\sin^2\theta, \tag{A.4}$$

and I_0 and I_1 are the modified Bessel functions of the first kind, defined as

$$I_\alpha(x) = i^{-\alpha}J_\alpha(ix) = \sum_{m=0}^{\infty}\frac{1}{m!\,\Gamma(m + \alpha + 1)}\left(\frac{x}{2}\right)^{2m+\alpha}. \tag{A.5}$$

From Eq. (A.1) we notice that, differently from the previous 3D case of Eq. (4.32), the decay rates now contain Laguerre polynomials $L_{m_<}^{|n-m|}(x)$ that do not depend only on the difference between the quantum numbers of initial and final states in the radial direction, but also on the particular value of $m_<$. As a consequence, for high values of $m_<$, these terms will oscillate rapidly and make their numerical evaluation complicated. We therefore make use of the semi-classical approximation [79, 162] in order to circumvent this problem, having also the advantage of speeding up the time needed for the numerical evaluation of the matrix elements. The semi-classical approximation consists of describing the motion of the impurity in the trap with a classical trajectory, so that $k_x x = k_x x_{max}\cos(\omega_x t)$. The matrix elements of the axial transitions therefore

Appendix A. Evaluation of the decay rates and semi-classical approximation

are

$$
\begin{aligned}
|\langle m|e^{-ik_x x}|n\rangle|^2 &= \left|\frac{2}{T}\int_0^{T/2} e^{-ik_x x_{max}\cos(\omega_x t)}\cos\left(\frac{2\pi(n-m)t}{T}\right)dt\right|^2 \\
&= \left|\frac{\omega_x}{2\pi}\int_0^{2\pi/\omega_x} e^{-ik_x x_{max}\cos(\omega_x t)}e^{-i\omega_x(n-m)t}dt\right|^2 \\
&= J^2_{n-m}(k_x x_{max}),
\end{aligned} \tag{A.6}
$$

where $J_{n-m}(z)$ are the Bessel functions of the first kind, defined as

$$
J_\alpha(x) = \sum_{m=0}^{\infty}\frac{(-1)^m}{m!\Gamma(m+\alpha+1)}\left(\frac{x}{2}\right)^{2m+\alpha}, \tag{A.7}
$$

with $\Gamma(z) = \int_0^\infty x^{z-1}e^{-x}dx$ the Gamma function. In Eq.(A.6),

$$
x_{max} = x_0\left(\frac{\sqrt{2n+1}+\sqrt{2m+1}}{2}\right), \tag{A.8}
$$

is the average between the initial and final maximum position of the impurity, and $T = 2\pi/\omega_x$ is the period of the oscillations [162]. Inserting this solution of the matrix elements in the decay rates (Eq. (4.26)), we obtain the decay rates of Eq. (4.36).
This approximation was also used for the estimation of the transition coefficients in 1D (for the slower dynamics along the axial direction), with an expression for the decay rates given by

$$
\begin{aligned}
\Gamma_{n\to m} =& \frac{g_{ab}^2\rho_0}{2\pi\hbar}\int_0^\infty dk S(k)k^2\delta(\hbar\omega_x(n-m)-\epsilon_k)\int_0^\pi J^2_{n-m}(k\cos\theta x_{max})\sin\theta d\theta \\
=& \frac{g_{ab}^2\rho_0}{2\pi\hbar^2}\sqrt{\frac{m_b}{2}}\frac{\tilde{\epsilon}k^2S(k)}{\sqrt{(\tilde{\epsilon}^2+\mu_b^2)(\sqrt{\tilde{\epsilon}^2+\mu_b^2}-\mu_b)}}\int_0^\pi J^2_{n-m}(k\cos\theta x_{max})\sin\theta d\theta,
\end{aligned} \tag{A.9}
$$

where in the last line

$$
k = \frac{\sqrt{2m_b}}{\hbar}\sqrt{\sqrt{\epsilon_k^2+\mu_b^2}-\mu_b}. \tag{A.10}
$$

We compare the decay rates obtained in both the fully quantum and semi-classical approximation in order to test the goodness of the latter. We do this for the 1D case, where we can evaluate them both numerically. The quantum expression for the decay

rates, in the most general form reads

$$\Gamma_{n\to m} = \frac{g_{ab}^2 \rho_0 m!}{2\pi\hbar n!}\sqrt{\frac{m_b}{2}}\frac{\tilde{\epsilon}k^2 S(k)}{\sqrt{(\tilde{\epsilon}^2+\mu_b^2)(\sqrt{\tilde{\epsilon}^2+\mu_b^2}-\mu_b)}}\int_0^\pi d\theta e^{-(x_0^2k^2\cos^2\theta)/2} \times \left(\frac{x_0^2k^2\cos^2\theta}{2}\right)^{n-m}\left|L_m^{n-m}\left(\frac{x_0^2k^2\cos^2\theta}{2}\right)\right|^2, \tag{A.11}$$

with k defined as in Eq. (A.10).

In Fig. A.1 and Fig. A.2 we compare the values of the decay rates obtained with both the approaches, for two specific transitions from a higher and from a lower excited state, respectively $\Gamma_{60\to m}$ and $\Gamma_{10\to m}$. As expected from the theory, the semi-classical approximation works very well in the case $|n-m| \ll n$, whilst it is less accurate for $|n-m| \approx n$. More precisely, from Fig. A.1 and Fig. A.2, we can see that the relative difference between quantum and semi-classical results are smaller than 15% in the range $|n-m|/n \leq 0.9$. Fig. A.1(b) shows that the relative difference increases above 40% for $m \leq 4$. However, in this case, the decay rates obtained for these transitions with both methods are respectively of the orders of 10^{-10} and 10^{-8} and can be approximated to 0 being much smaller than the other rates at higher m, as it can be seen from Fig. A.1(a). In general, we notice that, for transitions $n \to m$ in the limit $|n-m|/n \leq 0.9$, the relative difference is below 18%, and transitions to lower energy states m with $|n-m|/n > 0.9$ start becoming more significative for $n \lesssim 12$. We therefore compare in Fig. A.2 the decay rates obtained with the two approaches and their relative difference, for transitions from the initial state $n = 10$.

We see that, while the decay rates are of the order of magnitudes of $10^{-4} - 10^{-3}$, and the relative difference between the two methods results is below 10% for $m > 0$ (corresponding to $|n-m|/m = 0.9$), this increases to 37% only when $|n-m| = n$. Going to even lower initial states n, we observed that the maximum relative difference (at $m = 0$) keeps decreasing with n and lies in the range $0 - 38\%$, while for $m > 0$ we still have a relative difference below 10%. Following this, we can therefore state that the semi-classical approximation has a high accuracy for $|n-m|/n \leq 0.9$, going beyond the condition $|n-m| \ll n$ predicted by the WKB approximation, and the values obtained

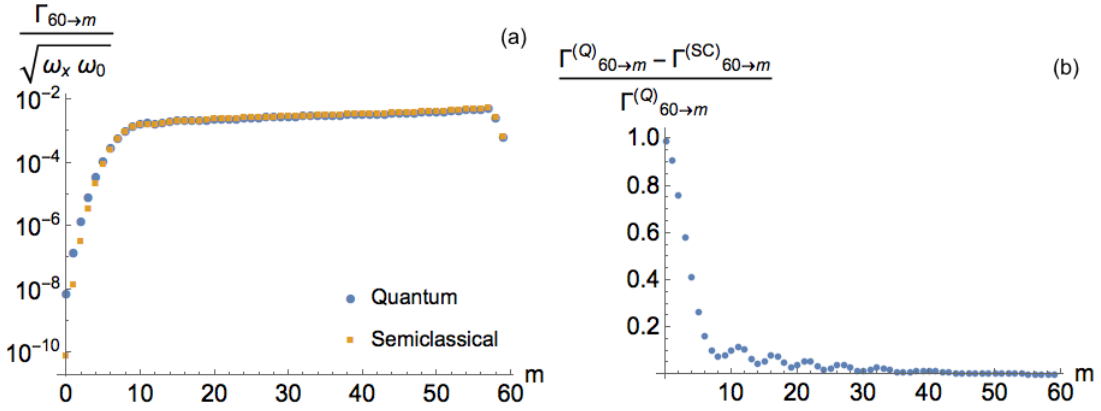

Figure A.1: Comparison (a) and relative difference (b) between decay rates estimated with the fully quantum expression and the semi-classical approximation, for transitions from the state $n = 60$ and for a value of the trapping frequency $\omega_x = \omega_0$.

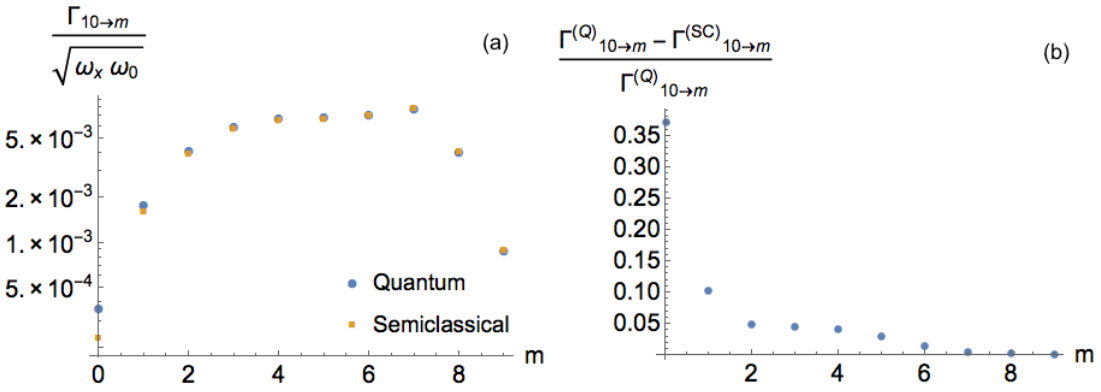

Figure A.2: Comparison (a) and relative difference (b) between decay rates estimated with the fully quantum expression and the semi-classical approximation, for transitions from the state $n = 10$ and for a value of the trapping frequency $\omega_x = \omega_0$.

for non negligible transitions with $|n - m| = n$ have a relative discrepancy varying in the range $0 - 38\%$, getting smaller with n, as the contributions from this transitions increase.

A.1 Evaluation of the 1D decay rates in supersonic and subsonic limits

We can find some simplified expressions for the decay rates in 1D when considering the two limits $\epsilon_k \gg \mu_b$ and $\epsilon_k \ll \mu_b$ for the supersonic and subsonic regimes. Under these

conditions, they are respectively given by [79]

$$\Gamma^{(sup)}_{n\to m} = \frac{g^2_{ab}\rho_0 m_b\sqrt{m_a m_b}}{\pi\hbar^4 l_0}\frac{m!}{n!}\sqrt{\omega_x\omega_0}\int_{-\sqrt{\frac{m_b}{m_a}(n-m)}}^{\sqrt{\frac{m_b}{m_a}(n-m)}} d\xi e^{-\xi^2}\xi^{2(n-m)}\left|L^{n-m}_m(\xi^2)\right|^2, \quad \text{(A.12)}$$

and

$$\Gamma^{(sub)}_{n\to m} = \frac{g^2_{ab}\rho_0 l_0}{4\pi\hbar^2 u^4}\frac{m!}{n!}\sqrt{\frac{2m_a}{m_b}}\omega_x^2(n-m)^2\sqrt{\omega_x\omega_0}\int_{-\frac{x_0\omega_x(n-m)}{\sqrt{2}u}}^{\frac{x_0\omega_x(n-m)}{\sqrt{2}u}} d\xi e^{-\xi^2}\xi^{2(n-m)}\left|L^{n-m}_m(\xi^2)\right|^2, \quad \text{(A.13)}$$

where $l_0 = \sqrt{\frac{\hbar}{m_b\omega_0}}$. For transitions $|1\rangle \to |0\rangle$, Eq. (A.12) reduces to Eq. (4.34).
In the semi-classical approximation, under the considerations discussed in the previous section, they respectively reduce to the two forms

$$\Gamma^{(sc-sup)}_{n\to m} = \frac{g^2_{ab}\rho_0 m_b\sqrt{m_a m_b}}{\pi\hbar^4 l_0(\sqrt{2n+1}+\sqrt{2m+1})}\sqrt{\omega_x\omega_0}\int_{-\sqrt{\frac{m_b}{2m_a}(n-m)}x_{max}}^{\sqrt{\frac{m_b}{2m_a}(n-m)}x_{max}} d\alpha J^2_{n-m}(\alpha), \quad \text{(A.14)}$$

$$\Gamma^{(sc-sub)}_{n\to m} = \frac{g^2_{ab}\rho_0 l_0\omega_x^2(n-m)^2}{2\pi\hbar^2 u^4(\sqrt{2n+1}+\sqrt{2m+1})}\sqrt{\frac{m_a}{m_b}}\sqrt{\omega_x\omega_0}\int_{-\omega_x(n-m)x_{max}/u}^{\omega_x(n-m)x_{max}/u} d\alpha J^2_{n-m}(\alpha). \quad \text{(A.15)}$$

In Chapter 4 we use Eq. A.12 to study the 1D limit of the transitions $\Gamma_{001\to000}$ (see Fig. 4.5) in the disk shaped configuration, having imposed the condition that the system, even in that limit, is in the supersonic regime.
For the dynamics in the cigar-shaped configuration we estimated the 1D transition rates $\Gamma_{n\to m}$ for the decays in the axial direction, but we used the full form of the structure factor without any particular assumptions on the regime.

Appendix B

Split-step Fourier transform method for GPE numerics

In order to compute the dynamics described by the GPE we used a numerical method called split-step Fourier transform, consisting in splitting the evolution in two terms: the kinetic term and the one containing the potential and interaction. The two evolutions are then applied separately in momentum and position space. In this Appendix we show the procedure to implement this algorithm.

We start from the GPE of the form

$$i\hbar\frac{\partial\psi(\theta,t)}{\partial t} = \left(-\frac{\hbar^2\nabla^2}{2m} + V_{ext}(\theta) + g_{1D}|\psi(\theta,t)|^2\right)\psi(\theta,t) = \tag{B.1}$$

$$= \left(-\frac{\hbar^2\partial^2}{2mR^2\partial\theta^2} + V_{ext}(\theta) + g_{1D}|\psi(\theta,t)|^2\right)\psi(\theta,t). \tag{B.2}$$

Since the interaction term determines a contribution to the effective potential, we divide the Hamiltonian in the two terms

$$T = -\frac{\hbar^2}{2mR^2}\frac{\partial^2}{\partial\theta^2} = \frac{\hbar^2k^2}{2m}, \qquad V = V_{ext}(\theta) + g_{1D}|\psi(\theta,t)|^2. \tag{B.3}$$

Using the Suzuki-Trotter expansion [217], the evolution operator can be factorised as

$$U(t) = e^{-iHt/\hbar} \sim \prod_j^n e^{-iH_j\delta}, \tag{B.4}$$

where $\delta = t/n$, so the state at each time increment is determined by

$$\psi(\theta, t+\delta) \simeq e^{-iH(t)\delta/\hbar} = e^{-i(T+V(t))\delta/\hbar}\psi(\theta, t), \tag{B.5}$$

where the time dependence in $V(t) = V_{ext} + g_{1D}|\psi(\theta, t)|^2$ is given by the interaction term, which we consider at the initial time. This gives an error $O(\delta^2)$. The exponential of the sum of the two operators however, is not easy to calculate, and since the operators V and T do not commute, $e^{i(V+T)} \neq e^{iV}e^{iT}$. The split-step method then aims to go around this obstacle, finding a way to factorise the exponentials containing separately the kinetic and potential operators, with the approximation

$$e^{\lambda(A+B)} \simeq e^{\lambda\beta_n B}e^{\lambda\alpha_n A}...e^{\lambda\beta_1 B}e^{\lambda\alpha_1 A}. \tag{B.6}$$

Retaining only three exponentials, with an error $O(\lambda^3)$, it can be found [218] that the condition to be verified for the coefficients must be $\alpha_1 = \alpha_2 = 1/2, \beta_1 = 1$ (or, equivalently, as the choice of which operator associate to A and B is arbitrary, $\beta_1 = \beta_2 = 1/2, \alpha_1 = 1$). Therefore, imposing $A = T$ and $B = V$, Equation B.5 takes the form

$$\psi(\theta, t+\delta) \simeq e^{-iT\delta/2\hbar}e^{-iV\delta/\hbar}e^{-iT\delta/2\hbar}\psi(\theta, t) \tag{B.7}$$

$$= e^{-i\hbar k^2\delta/4m}e^{-iV(t)\delta/\hbar}e^{-i\hbar k^2\delta/4m}\psi(\theta, t). \tag{B.8}$$

Using the kinetic operator in the momentum representation, it is convenient to Fourier transform the wavefunction from position to momentum space $\psi(k, t)$ to evolve it with the kinetic operator evolution and we transform it back to the position representation for the evolution with the potential operator, so the steps for the implementation of

this method are the following:

$$\psi_0(\theta,t) = \psi(\theta,t) \rightarrow \psi_0(k,t) \tag{B.9}$$

$$\psi_1(k) = e^{-i\hbar k^2\delta/4m}\psi_0(k,t) \rightarrow \psi_1(\theta) \tag{B.10}$$

$$\psi_2(\theta) = e^{-i(V_{ext}(\theta)+g_{1D}|\psi_1(\theta)|^2)/\hbar}\psi_1(\theta) \rightarrow \psi_2(k) \tag{B.11}$$

$$\psi_3(k,t+\delta) = e^{-i\hbar k^2\delta/4m}\psi_2(k) \rightarrow \psi_3(\theta,t+\delta) = \psi(\theta,t+\delta). \tag{B.12}$$

This method was used for the results presented in Chapter 6 and Chapter 7, to simulate the dynamics of a BEC in a tilted ring trap. For the polaritons dynamics in Chapter 7, the terms with $G(t)$ and $\Gamma(t)$ in Eq. (7.16) and Eq. (7.17) are contained in the term $V(t)$ of Eq. (B.8), while the relaxation term α of Eq. (7.15) can be included in the term T of Eq. (B.8).

Appendix C

Variational method and comparison with the GPE results

C.1 Linearised solution of the variational method equations

As shown in Chapter 7, analytical solutions of the lowest mode frequencies were obtained for the harmonic oscillator potential after using a variational method approach with a Gaussian ansatz to obtain the differential equations for the width σ and for the center of mass z_0. These were then solved by a linearisation around the equilibrium solutions. Here we use the same proedure for the case of the dynamics in a quartic harmonic oscillator potential. We refer to this approach as the linearised variational method.

We find, even in this case, the stationary solutions needed for the expansion of the differential equations Eq. (6.40) and Eq. (6.41). From Eq. (6.41) we obtain

$$z_{0_e}(t)\left(1+3\zeta\sigma^2(t)+2\zeta z_{0_e}^2(t)\right)=0 \tag{C.1}$$

that admits solutions of the form

$$z_{0_{e1}} = 0 \tag{C.2}$$

$$z^2_{0_{e2,3}} = -\frac{1+3\zeta\sigma^2(t)}{2\zeta}. \tag{C.3}$$

The first is a stable stationary point, while the equation for the two other equilibrium points requires the condition $1+3\zeta\sigma^2(t) \geq 0$ in order to have real solutions, which leads to $\sigma(t) \leq -\sqrt{-1/(3\zeta)}$ and $\sigma(t) \geq \sqrt{-1/(3\zeta)}$. Remembering that in our case $\zeta = -\frac{1}{12R^2}$, the aforementioned condition would imply $\sigma(t) \leq -2R$ and $\sigma(t) \geq 2R$, which are both unphysical conditions. We will therefore consider only the stable stationary point $z_{0_e} = 0$. The other differential equation Eq. (6.40) has both stable and unstable solutions given by

$$\omega_z^2\sigma_e\left(1+6\zeta z_0(t)^2+3\zeta\sigma_e^2\right) - \frac{g_{1D}N}{\sqrt{2\pi}m\sigma_e^2} - \frac{\hbar^2}{m^2\sigma_e^3} = 0. \tag{C.4}$$

By expanding the differential equations Eq. (6.41) and Eq. (6.40) around the equilibrium points, we obtain

$$\omega_D = \omega_z\sqrt{1+3\zeta\sigma_e^2} \tag{C.5}$$

$$\omega_M = \omega_z\sqrt{1+6\zeta z_{0_e}^2+9\zeta\sigma_e^2+\frac{3\hbar^2}{m^2\sigma_e^4\omega_z^2}+\frac{\sqrt{2}g_{1D}N}{\sqrt{\pi}m\sigma_e^3\omega_z^2}} \tag{C.6}$$

where it can be easily noticed that these frequencies are now coupled. In the harmonic oscillator limit $\zeta = 0$ we obtain the same results of Eq. (6.34) and Eq. (6.38). The above solution obtained for the dipole frequency with this method does not depend on the initial position of the wavepacket $z_0(0)$, in contrast to the more accurate result of Eq. (C.5) used in Chapter 6, which predicts a correction given by this term. see that this linearised solution is a correction that depends on the initial position $z_0(0)$.

In Fig. C.1 we compare the shift of the dipole frequency obtained from the linearised solution Eq. (C.5) and from the semi-linearised and numerical solutions of Eq. (6.44) obtained from the variational method, together with the data acquired from the analysis

of the frequency spectra after simulating the dynamics via the GPE.

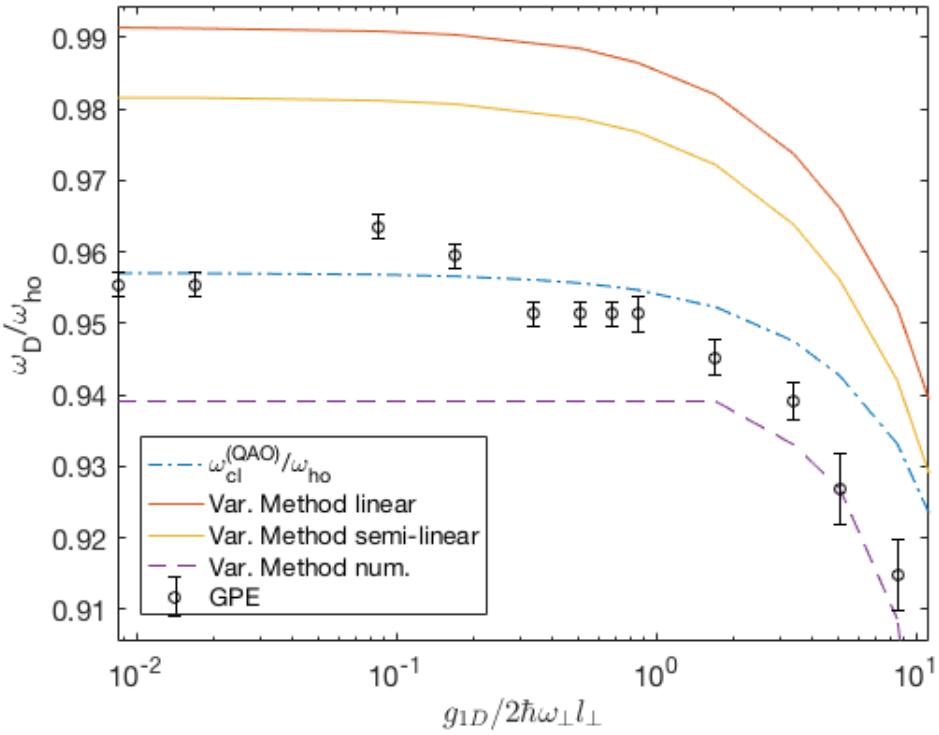

Figure C.1: Dipole frequency as a function of the interaction strength, evaluated from the frequency spectra of the GPE dynamics (black dots), from the perturbation theory correction of Eq. (6.21) (blue line) and compared with the results obtained from the variational method through a linearised solution of Eq. (C.5) and from the semi-linearised and numerical solutions of Eq. (6.44). The relative differences of linear, semi-linear and numerical solutions of the variational method, compared to the GPE data, lie in the range $28-47\%$, $18-36\%$, $0-25\%$ respectively.

C.2 Dynamics and frequency spectra of the moments obtained from the variational method

In this section we present the dynamics of the lowest moments obtained with the numerical solution of the differential equations for the center of mass z_0 and σ obtained with the variational method, applied to the cases of the wavefunction for the harmonic oscillator potential in non-central configurations, and for the quartic anharmonic oscillator potential.

C.2.1 Non-central dynamics in the harmonic oscillator potential

Using the differential equations of Eq. (6.32) and Eq. (6.33), we used a Runge-Kutta algorithm to evaluate numerically the moments evolution, for different values of the interaction strength, as shown in Fig. C.2. The corresponding frequency spectra are shown in Fig. C.3. The amplitude in the oscillations of the width of the wavepacket decreases for increasing interaction strength, but do not present collapse and revivals, in opposition to the dynamics obtained with the GPE. On the other side, the oscillations for the third and fourth moment present collapse and revivals periods that decrease with increasing interaction. The frequency spectrum of the fourth moment shows a peak at low frequencies corresponding to the revival frequency, whose value is equal to the distance between the sidebands and the frequency peaks at $\nu = p\nu_{\mathrm{ho}}$. The shift of the monopole frequency ν_2 (determined by σ) coincides with the frequency value of the sideband appearing for the moment $E[|\theta|^4]$.

C.2.2 Non-central dynamics in the quartic anharmonic oscillator potential

In this section we show the non-central dynamics of the moments obtained by solving numerically, using a Runge-Kutta method, the differential equations Eq. (6.41) and Eq. (6.40), obtained from a variational method with a Gaussian ansatz, as discussed in Chapter 6.3.1. In contrast to the previous case of a wavefunction oscillating in the harmonic oscillator potential, here we see that revivals of the oscillations appear also for the center of mass and variance, and not only for the third and fourth moments. These are shown in Fig. C.4.

From the corresponding frequency spectra, plotted in Fig. C.5, we can observe that there is a shift of the frequency modes already in the non-interacting case, as predicted also from the perturbation theory results in Chapter 6.2.1. Increasing the interaction strength comports an additional redshift of the frequencies, but an increase of the revival frequencies associated with both the variance and the fourth moment. Even in this case sidebands appear at a spacing equal to the revival frequency from the main peaks.

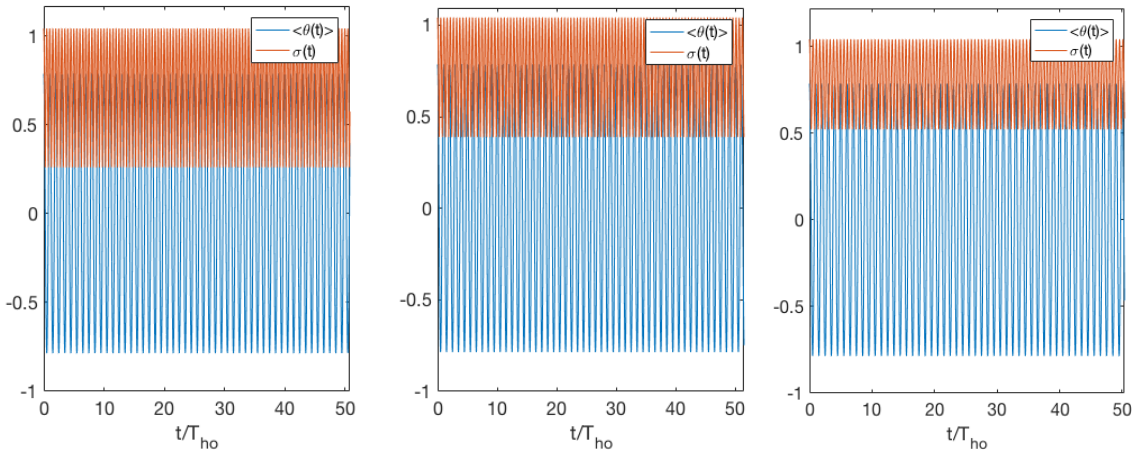

(a) $g = 0$ (b) $g = 0.45$ (c) $g = 0.9$

(d) $g = 0$ (e) $g = 0.45$ (f) $g = 0.9$

Figure C.2: Evolution of the center of mass and width (a-b-c) and of the next non-central moments (d-e-f) defined in Eq. (6.63) and Eq. (6.64), for $g = g_{1D}/2\hbar\omega_\perp l_\perp = 0, 0.45, 0.9$.

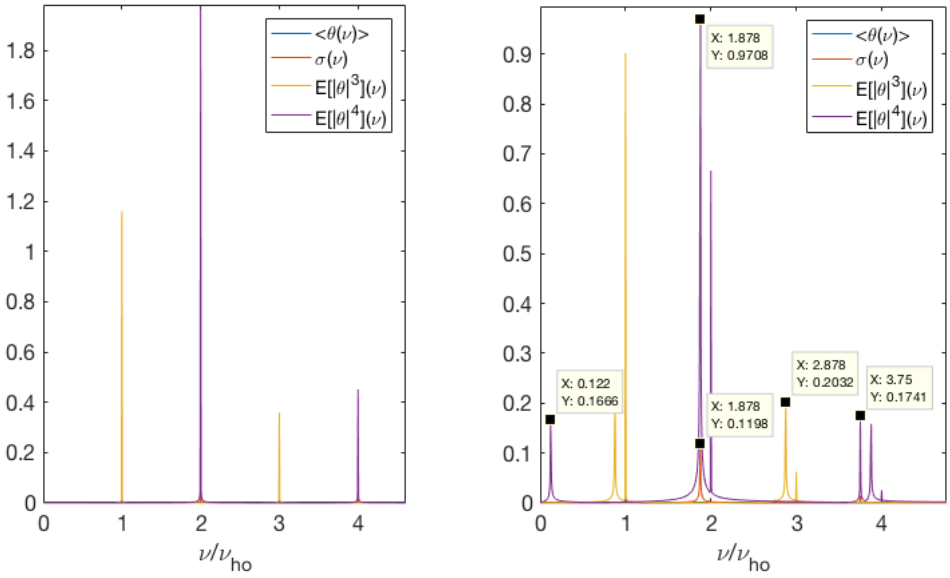

(a) $g = 0$ (b) $g = 0.45$

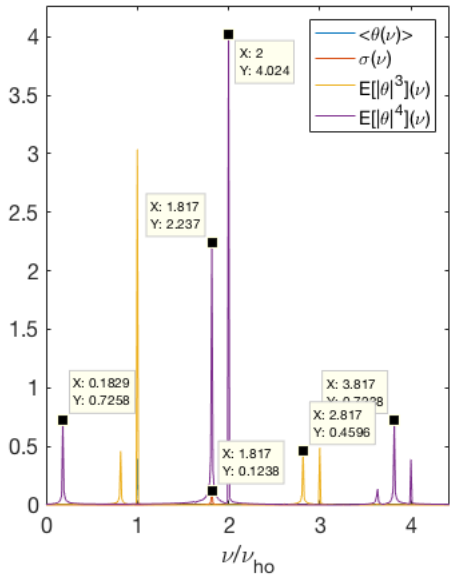

(c) $g = 0.9$

Figure C.3: Frequency spectra of the moments evolution of Fig. C.2, for $g = g_{1D}/2\hbar\omega_\perp l_\perp = 0, 0.45, 0.9$. The sampling frequency used for the Fourier transform is $\delta\nu = 0.012$. The revivals of the fourth moment give rise to the appearance of a revival frequency peak in the frequency spectra, which increases with the interaction strength. Sidebands at a distance from the modes frequencies $n\nu_{\text{ho}}$ equal to the revival frequency appear for finite interaction strength.

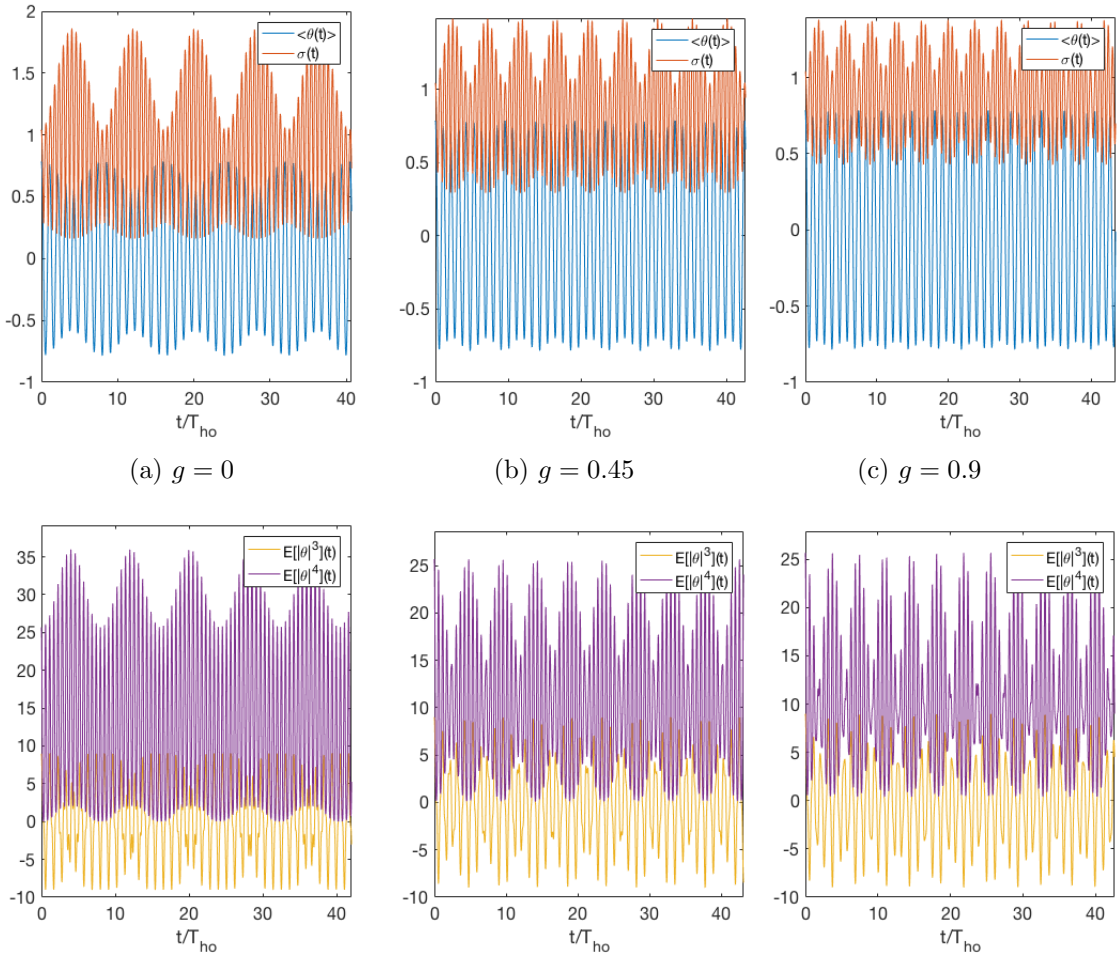

(a) $g = 0$ (b) $g = 0.45$ (c) $g = 0.9$

(d) $g = 0$ (e) $g = 0.45$ (f) $g = 0.9$

Figure C.4: Dynamics of the center of mass $\langle\theta\rangle = \theta_0$ and width σ (a-b-c) and of the third and fourth moment (d-e-f) of the wavefunction in the quartic anharmonic potential, obtained from solving Eq. (6.41) and Eq. (6.40) numerically, with initial conditions $\theta_0 = \pi/4$, $\sigma = 2l_{\rm ho}$ and for different values of $g = g_{1D}/2\hbar\omega_\perp l_\perp = 0, 0.45, 0.9$.

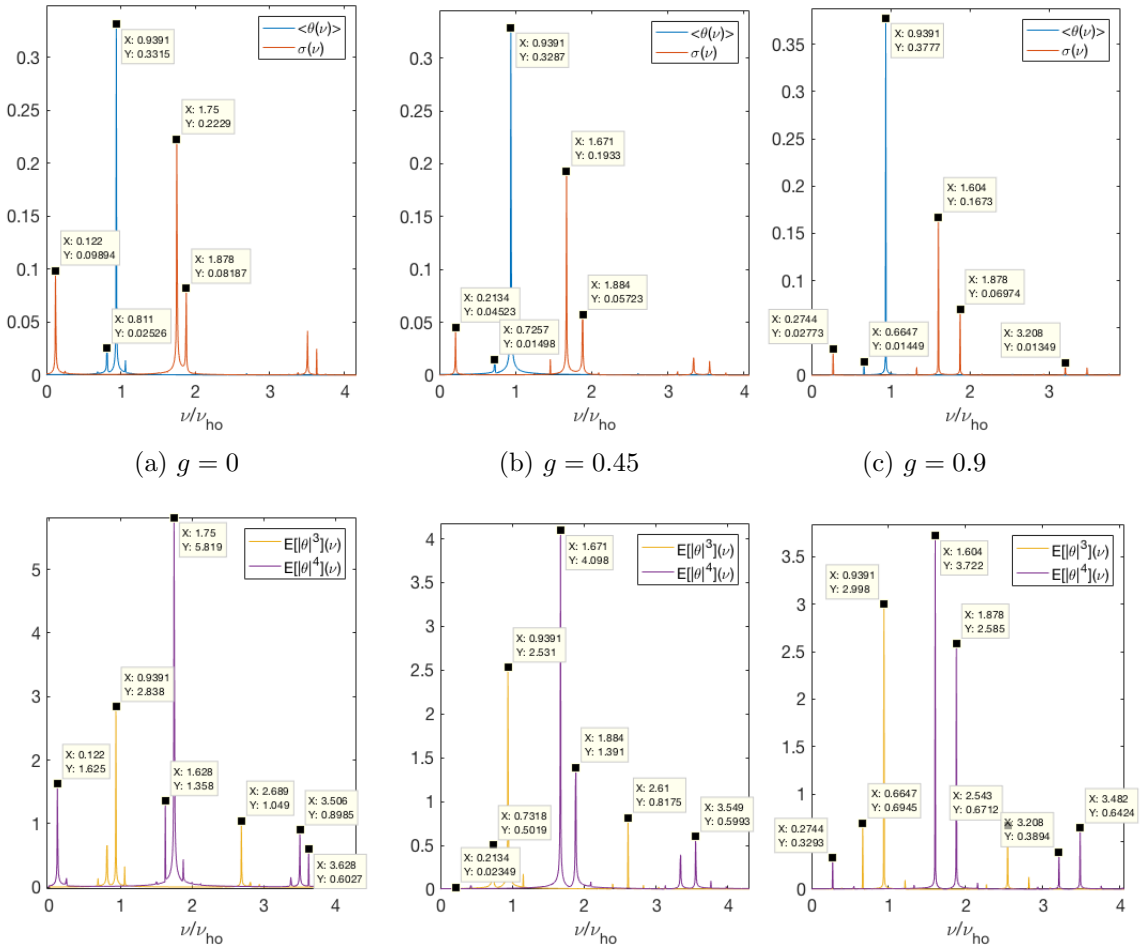

(a) $g = 0$ (b) $g = 0.45$ (c) $g = 0.9$

(d) $g = 0$ (e) $g = 0.45$ (f) $g = 0.9$

Figure C.5: Frequency spectra of the moments evolution of Fig. C.4, for $g = g_{1D}/2\hbar\omega_\perp l_\perp = 0, 0.45, 0.9$. The sampling frequency used for the Fourier transform is $\delta\nu = 0.006$. Here collapse and revivals appear for all the moments, and the peaks associated with these revival can be observed for $\sigma(\nu)$ and $E[|\theta|^4](\nu)$.

Bibliography

[1] S. N. Bose, "Plancks gesetz und lichtquantenhypothese," (1924).

[2] A. Einstein, "Quantentheorie des einatomigen idealen gases," SB Preuss. Akad. Wiss. phys.-math. Klasse (1924).

[3] M. H. Anderson, J. R. Ensher, M. R. Matthews, C. E. Wieman, and E. A. Cornell, "Observation of Bose-Einstein condensation in a dilute atomic vapor," Science , 198 (1995).

[4] K. B. Davis, M.-O. Mewes, M. R. Andrews, N. J. van Druten, D. S. Durfee, D. Kurn, and W. Ketterle, "Bose-Einstein condensation in a gas of sodium atoms," Phys. Rev. Lett. **75**, 3969 (1995).

[5] C. C. Bradley, C. Sackett, J. Tollett, and R. G. Hulet, "Evidence of Bose-Einstein condensation in an atomic gas with attractive interactions," Phys. Rev. Lett. **75**, 1687 (1995).

[6] C. C. Bradley, C. Sackett, and R. Hulet, "Bose-Einstein condensation of lithium: Observation of limited condensate number," Phys. Rev. Lett. **78**, 985 (1997).

[7] W. D. Phillips, "Nobel lecture: Laser cooling and trapping of neutral atoms," Rev. Mod. Phys. **70**, 721 (1998).

[8] D. J. Wineland and W. M. Itano, "Laser cooling of atoms," Phys. Rev. A **20**, 1521 (1979).

[9] F. Diedrich, J. Bergquist, W. M. Itano, and D. Wineland, "Laser cooling to the zero-point energy of motion," Phys. Rev. Lett. **62**, 403 (1989).

[10] H. J. Metcalf and P. van der Straten, "Laser cooling and trapping of atoms," JOSA B **20**, 887 (2003).

[11] W. Ketterle, N. Van Druten, *et al.*, "Evaporative cooling of trapped atoms," Adv. At. Mol. Opt. Phys **37**, 181 (1996).

[12] C. Myatt, E. Burt, R. Ghrist, E. A. Cornell, and C. Wieman, "Production of two overlapping Bose-Einstein condensates by sympathetic cooling," Phys. Rev. Lett. **78**, 586 (1997).

[13] G. Modugno, G. Ferrari, G. Roati, R. J. Brecha, A. Simoni, and M. Inguscio, "Bose-Einstein condensation of potassium atoms by sympathetic cooling," Science **294**, 1320 (2001).

[14] F. Schreck, G. Ferrari, K. Corwin, J. Cubizolles, L. Khaykovich, M.-O. Mewes, and C. Salomon, "Sympathetic cooling of bosonic and fermionic lithium gases towards quantum degeneracy," Phys. Rev. A **64**, 011402 (2001).

[15] I. Bloch, J. Dalibard, and S. Nascimbene, "Quantum simulations with ultracold quantum gases," Nat. Phys. **8**, 267 (2012).

[16] R. Blatt and C. F. Roos, "Quantum simulations with trapped ions," Nat. Phys. **8**, 277 (2012).

[17] C. Gross and I. Bloch, "Quantum simulations with ultracold atoms in optical lattices," Science **357**, 995 (2017).

[18] M. Lewenstein, A. Sanpera, V. Ahufinger, B. Damski, A. Sen, and U. Sen, "Ultracold atomic gases in optical lattices: mimicking condensed matter physics and beyond," Advances in Physics **56**, 243 (2007).

[19] P. Courteille, R. Freeland, D. J. Heinzen, F. Van Abeelen, and B. Verhaar, "Observation of a Feshbach resonance in cold atom scattering," Phys. Rev. Lett. **81**, 69 (1998).

[20] C. Chin, R. Grimm, P. Julienne, and E. Tiesinga, "Feshbach resonances in ultracold gases," Rev. Mod. Phys. **82**, 1225 (2010).

[21] S. Gupta, K. Murch, K. Moore, T. Purdy, and D. Stamper-Kurn, "Bose-Einstein condensation in a circular waveguide," Phys. Rev. Lett. **95**, 143201 (2005).

[22] A. S. Arnold, C. S. Garvie, and E. Riis, "Large magnetic storage ring for Bose-Einstein condensates," Phys. Rev. A **73**, 041606 (2006).

[23] C. Ryu, M. Andersen, P. Clade, V. Natarajan, K. Helmerson, and W. D. Phillips, "Observation of persistent flow of a Bose-Einstein condensate in a toroidal trap," Phys. Rev. Lett. **99**, 260401 (2007).

[24] M. Greiner, O. Mandel, T. Esslinger, T. W. Hänsch, and I. Bloch, "Quantum phase transition from a superfluid to a Mott insulator in a gas of ultracold atoms," Nature **415**, 39 (2002).

[25] M. Albiez, R. Gati, J. Fölling, S. Hunsmann, M. Cristiani, and M. K. Oberthaler, "Direct observation of tunneling and nonlinear self-trapping in a single bosonic Josephson junction," Phys. Rev. Lett. **95**, 010402 (2005).

[26] R. Gati and M. Oberthaler, "A bosonic Josephson junction," J. Phys. B **40**, R61 (2007).

[27] W. S. Bakr, J. I. Gillen, A. Peng, S. Fölling, and M. Greiner, "A quantum gas microscope for detecting single atoms in a Hubbard-regime optical lattice," Nature **462**, 74 (2009).

[28] J. F. Sherson, C. Weitenberg, M. Endres, M. Cheneau, I. Bloch, and S. Kuhr, "Single-atom-resolved fluorescence imaging of an atomic Mott insulator," Nature **467**, 68 (2010).

[29] Z. Hadzibabic, P. Krüger, M. Cheneau, B. Battelier, and J. Dalibard, "Berezinskii–Kosterlitz–Thouless crossover in a trapped atomic gas," Nature **441**, 1118 (2006).

[30] T. Kinoshita, T. Wenger, and D. S. Weiss, "Observation of a one-dimensional Tonks-Girardeau gas," Science **305**, 1125 (2004).

[31] B. Seaman, M. Krämer, D. Anderson, and M. Holland, "Atomtronics: Ultracold-atom analogs of electronic devices," Phys. Rev. A **75**, 023615 (2007).

[32] L. Amico, G. Birkl, M. Boshier, and L.-C. Kwek, "Focus on atomtronics-enabled quantum technologies," New J. Phys. **19**, 020201 (2017).

[33] R. Pepino, J. Cooper, D. Anderson, and M. Holland, "Atomtronic circuits of diodes and transistors," Phys. Rev. Lett. **103**, 140405 (2009).

[34] Y. Qian, M. Gong, and C. Zhang, "Quantum transport of bosonic cold atoms in double-well optical lattices," Phys. Rev. A **84**, 013608 (2011).

[35] J. A. Stickney, D. Z. Anderson, and A. A. Zozulya, "Transistorlike behavior of a Bose-Einstein condensate in a triple-well potential," Phys. Rev. A **75**, 013608 (2007).

[36] R. Pepino, J. Cooper, D. Meiser, D. Anderson, and M. Holland, "Open quantum systems approach to atomtronics," Phys. Rev. A **82**, 013640 (2010).

[37] A. Micheli, A. Daley, D. Jaksch, and P. Zoller, "Single atom transistor in a 1d optical lattice," Phys. Rev. Lett. **93**, 140408 (2004).

[38] J.-S. You, R. Schmidt, D. A. Ivanov, M. Knap, and E. Demler, "Atomtronics with a spin: Statistics of spin transport and nonequilibrium orthogonality catastrophe in cold quantum gases," Phys. Rev. B **99**, 214505 (2019).

[39] A. Ruschhaupt and J. Muga, "Atom diode: A laser device for a unidirectional transmission of ground-state atoms," Phys. Rev. A **70**, 061604 (2004).

[40] R. Labouvie, B. Santra, S. Heun, S. Wimberger, and H. Ott, "Negative differential conductivity in an interacting quantum gas," Phys. Rev. Lett. **115**, 050601 (2015).

[41] L. Amico, A. Osterloh, and F. Cataliotti, "Quantum many particle systems in ring-shaped optical lattices," Phys. Rev. Lett. **95**, 063201 (2005).

[42] K. C. Wright, R. Blakestad, C. Lobb, W. Phillips, and G. Campbell, "Driving phase slips in a superfluid atom circuit with a rotating weak link," Phys. Rev. Lett. **110**, 025302 (2013).

[43] S. Eckel, J. G. Lee, F. Jendrzejewski, N. Murray, C. W. Clark, C. J. Lobb, W. D. Phillips, M. Edwards, and G. K. Campbell, "Hysteresis in a quantized superfluid 'atomtronic'circuit," Nature **506**, 200 (2014).

[44] S. Franke-Arnold, J. Leach, M. J. Padgett, V. E. Lembessis, D. Ellinas, A. J. Wright, J. M. Girkin, P. Öhberg, and A. S. Arnold, "Optical ferris wheel for ultracold atoms," Opt. Express **15**, 8619 (2007).

[45] A. Ramanathan, K. C. Wright, S. R. Muniz, M. Zelan, W. T. Hill, C. J. Lobb, K. Helmerson, W. D. Phillips, and G. K. Campbell, "Superflow in a toroidal Bose-Einstein condensate: An atom circuit with a tunable weak link," Phys. Rev. Lett. **106**, 130401 (2011).

[46] A. S. Arnold, "Extending dark optical trapping geometries," Opt. Lett. **37**, 2505 (2012).

[47] C. Ryu, P. Blackburn, A. Blinova, and M. Boshier, "Experimental realization of Josephson junctions for an atom SQUID," Phys. Rev. Lett. **111**, 205301 (2013).

[48] F. Jendrzejewski, S. Eckel, N. Murray, C. Lanier, M. Edwards, C. J. Lobb, and G. K. Campbell, "Resistive flow in a weakly interacting Bose-Einstein condensate," Phys. Rev. Lett. **113**, 045305 (2014).

[49] I. Carusotto and C. Ciuti, "Quantum fluids of light," Rev. Mod. Phys. **85**, 299 (2013).

[50] G. Modugno, M. Modugno, F. Riboli, G. Roati, and M. Inguscio, "Two atomic species superfluid," Phys. Rev. Lett. **89**, 190404 (2002).

[51] M. Taglieber, A.-C. Voigt, T. Aoki, T. Hänsch, and K. Dieckmann, "Quantum degenerate two-species Fermi-Fermi mixture coexisting with a Bose-Einstein condensate," Phys. Rev. Lett. **100**, 010401 (2008).

[52] E. Wille, F. Spiegelhalder, G. Kerner, D. Naik, A. Trenkwalder, G. Hendl, F. Schreck, R. Grimm, T. Tiecke, J. Walraven, *et al.*, "Exploring an ultracold fermi-fermi mixture: interspecies feshbach resonances and scattering properties of Li 6 and K 40," Phys. Rev. Lett. **100**, 053201 (2008).

[53] Z. Hadzibabic, C. A. Stan, K. Dieckmann, S. Gupta, M. W. Zwierlein, A. Görlitz, and W. Ketterle, "Two-species mixture of quantum degenerate Bose and Fermi gases," Phys. Rev. Lett. **88**, 160401 (2002).

[54] M. K. Tey, S. Stellmer, R. Grimm, and F. Schreck, "Double-degenerate Bose-Fermi mixture of strontium," Phys. Rev. A **82**, 011608(R) (2010).

[55] I. Ferrier-Barbut, M. Delehaye, S. Laurent, A. T. Grier, M. Pierce, B. S. Rem, F. Chevy, and C. Salomon, "A mixture of Bose and Fermi superfluids," Science (2014).

[56] D. McCarron, H. Cho, D. Jenkin, M. Köppinger, and S. Cornish, "Dual-species Bose-Einstein condensate of Rb 87 and Cs 133," Phys. Rev. A **84**, 011603 (2011).

[57] K. Mertes, J. Merrill, R. Carretero-González, D. Frantzeskakis, P. Kevrekidis, and D. Hall, "Nonequilibrium dynamics and superfluid ring excitations in binary Bose-Einstein condensates," Phys. Rev. Lett. **99**, 190402 (2007).

[58] S. Papp, J. Pino, and C. Wieman, "Tunable miscibility in a dual-species Bose-Einstein condensate," Phys. Rev. Lett. **101**, 040402 (2008).

[59] M. Lewenstein, L. Santos, M. Baranov, and H. Fehrmann, "Atomic Bose-Fermi mixtures in an optical lattice," Phys. Rev. Lett. **92**, 050401 (2004).

[60] K. Günter, T. Stöferle, H. Moritz, M. Köhl, and T. Esslinger, "Bose-Fermi mixtures in a three-dimensional optical lattice," Phys. Rev. Lett. **96**, 180402 (2006).

[61] S. Ospelkaus, C. Ospelkaus, O. Wille, M. Succo, P. Ernst, K. Sengstock, and K. Bongs, "Localization of bosonic atoms by fermionic impurities in a three-dimensional optical lattice," Phys. Rev. Lett. **96**, 180403 (2006).

[62] A. Chikkatur, A. Görlitz, D. Stamper-Kurn, S. Inouye, S. Gupta, and W. Ketterle, "Suppression and enhancement of impurity scattering in a bose-einstein condensate," Phys. Rev. Lett. **85**, 483 (2000).

[63] N. Spethmann, F. Kindermann, S. John, C. Weber, D. Meschede, and A. Widera, "Dynamics of single neutral impurity atoms immersed in an ultracold gas," Phys. Rev. Lett. **109**, 235301 (2012).

[64] R. Scelle, T. Rentrop, A. Trautmann, T. Schuster, and M. K. Oberthaler, "Motional coherence of fermions immersed in a bose gas," Phys. Rev. Lett. **111**, 070401 (2013).

[65] D. Mayer, F. Schmidt, D. Adam, S. Haupt, J. Koch, T. Lausch, J. Nettersheim, Q. Bouton, and A. Widera, "Controlled doping of a bosonic quantum gas with single neutral atoms," J. Phys. B **52**, 015301 (2018).

[66] A. Klein, M. Bruderer, S. R. Clark, and D. Jaksch, "Dynamics, dephasing and clustering of impurity atoms in Bose–Einstein condensates," New J. Phys. **9**, 411 (2007).

[67] M. Cirone, G. De Chiara, G. Palma, and A. Recati, "Collective decoherence of cold atoms coupled to a Bose-Einstein condensate," New J. Phys. **11**, 103055 (2009).

[68] A. Klein and M. Fleischhauer, "Interaction of impurity atoms in Bose-Einstein condensates," Phys. Rev. A **71**, 033605 (2005).

[69] J. Tempere, W. Casteels, M. Oberthaler, S. Knoop, E. Timmermans, and J. Devreese, "Feynman path-integral treatment of the BEC-impurity polaron," Phys. Rev. B **80**, 184504 (2009).

[70] M. Hohmann, F. Kindermann, B. Gänger, T. Lausch, D. Mayer, F. Schmidt, and A. Widera, "Neutral impurities in a Bose-Einstein condensate for simulation of the Fröhlich-polaron," EPJ Quantum Technol. **2**, 23 (2015).

[71] F. Cucchietti and E. Timmermans, "Strong-coupling polarons in dilute gas Bose-Einstein condensates," Phys. Rev. Lett. **96**, 210401 (2006).

[72] J. Wang, X.-J. Liu, and H. Hu, "Roton-induced Bose polaron in the presence of synthetic spin-orbit coupling," Phys. Rev. Lett. **123**, 213401 (2019).

[73] J. P. Gordon and A. Ashkin, "Motion of atoms in a radiation trap," Phys. Rev. A **21**, 1606 (1980).

[74] Y. Castin, J. I. Cirac, and M. Lewenstein, "Reabsorption of light by trapped atoms," Phys. Rev. Lett. **80**, 5305 (1998).

[75] S. Wolf, S. J. Oliver, and D. S. Weiss, "Suppression of recoil heating by an optical lattice," Phys. Rev. Lett. **85**, 4249 (2000).

[76] F. Gerbier and Y. Castin, "Heating rates for an atom in a far-detuned optical lattice," Phys. Rev. A **82**, 013615 (2010).

[77] H. Pichler, A. J. Daley, and P. Zoller, "Nonequilibrium dynamics of bosonic atoms in optical lattices: Decoherence of many-body states due to spontaneous emission," Phys. Rev. A **82**, 063605 (2010).

[78] D. C. McKay and B. DeMarco, "Cooling in strongly correlated optical lattices: Prospects and challenges," Rep. Prog. Phys. **74**, 054401 (2011).

[79] A. J. Daley, P. O. Fedichev, and P. Zoller, "Single-atom cooling by superfluid immersion: A nondestructive method for qubits," Phys. Rev. A **69**, 022306 (2004).

[80] D. Chen, C. Meldgin, and B. DeMarco, "Bath-induced band decay of a Hubbard lattice gas," Phys. Rev. A **90**, 013602 (2014).

[81] A. Griessner, A. J. Daley, S. R. Clark, D. Jaksch, and P. Zoller, "Dark-state cooling of atoms by superfluid immersion," Phys. Rev. Lett. **97**, 220403 (2006).

[82] A. Griessner, A. Daley, S. Clark, D. Jaksch, and P. Zoller, "Dissipative dynamics of atomic Hubbard models coupled to a phonon bath: dark state cooling of atoms within a Bloch band of an optical lattice," New J. Phys. **9**, 44 (2007).

[83] M. Okano, H. Hara, M. Muramatsu, K. Doi, S. Uetake, Y. Takasu, and Y. Takahashi, "Simultaneous magneto-optical trapping of lithium and ytterbium atoms towards production of ultracold polar molecules," Appl. Phys. B **98**, 691 (2010).

[84] V. D. Vaidya, J. Tiamsuphat, S. L. Rolston, and J. V. Porto, "Degenerate Bose-Fermi mixtures of rubidium and ytterbium," Phys. Rev. A **92**, 1 (2015).

[85] J. Poyatos, J. I. Cirac, and P. Zoller, "Quantum reservoir engineering with laser cooled trapped ions," Phys. Rev. Lett. **77**, 4728 (1996).

[86] S. McEndoo, P. Haikka, G. De Chiara, G. Palma, and S. Maniscalco, "Entanglement control via reservoir engineering in ultracold atomic gases," EPL (Europhys. Lett.) **101**, 60005 (2013).

[87] A. Orieux, A. d'Arrigo, G. Ferranti, R. L. Franco, G. Benenti, E. Paladino, G. Falci, F. Sciarrino, and P. Mataloni, "Experimental on-demand recovery of entanglement by local operations within non-Markovian dynamics," Sci. Rep. **5**, 1 (2015).

[88] M. T. Mitchison, T. H. Johnson, and D. Jaksch, "Probing the dynamic structure factor of a neutral Fermi superfluid along the BCS-BEC crossover using atomic impurity qubits," Phys. Rev. A **94**, 063618 (2016).

[89] Q. Bouton, J. Nettersheim, D. Adam, F. Schmidt, D. Mayer, T. Lausch, E. Tiemann, and A. Widera, "Single-atom quantum probes for ultracold gases boosted by nonequilibrium spin dynamics," Phys. Rev. X **10**, 011018 (2020).

[90] D. McKay and B. DeMarco, "Thermometry with spin-dependent lattices," New Journal of Physics **12**, 055013 (2010).

[91] L. A. Correa, M. Mehboudi, G. Adesso, and A. Sanpera, "Individual quantum probes for optimal thermometry," Phys. Rev. Lett. **114**, 220405 (2015).

[92] M. Mehboudi, A. Lampo, C. Charalambous, L. A. Correa, M. Á. García-March, and M. Lewenstein, "Using polarons for sub-nk quantum nondemolition thermometry in a Bose-Einstein condensate," Phys. Rev. Lett. **122**, 030403 (2019).

[93] S. Beattie, S. Moulder, R. J. Fletcher, and Z. Hadzibabic, "Persistent currents in spinor condensates," Phys. Rev. Lett. **110**, 025301 (2013).

[94] A. Lampo, C. Charalambous, M. Á. García-March, and M. Lewenstein, "Non-Markovian polaron dynamics in a trapped Bose-Einstein condensate," Phys. Rev. A **98**, 063630 (2018).

[95] M. Schecter, D. M. Gangardt, and A. Kamenev, "Quantum impurities: from mobile Josephson junctions to depletons," New J. Phys. **18**, 065002 (2016).

[96] A. Lampo, S. H. Lim, M. Á. García-March, and M. Lewenstein, "Bose polaron as an instance of quantum Brownian motion," Quantum **1**, 30 (2017).

[97] S. Stringari, "Collective excitations of a trapped Bose-Condensed gas," Phys. Rev. Lett. **77**, 2360 (1996).

[98] V. M. Pérez-García, H. Michinel, J. I. Cirac, M. Lewenstein, and P. Zoller, "Low energy excitations of a Bose-Einstein condensate: A time-dependent variational analysis," Phys. Rev. Lett. **77**, 5320 (1996).

[99] M. Edwards, P. Ruprecht, K. Burnett, R. Dodd, and C. W. Clark, "Collective excitations of atomic bose-einstein condensates," Phys. Rev. Lett. **77**, 1671 (1996).

[100] K. G. Singh and D. S. Rokhsar, "Collective excitations of a confined Bose condensate," Phys. Rev. Lett. **77**, 1667 (1996).

[101] M. Fliesser, A. Csordás, P. Szépfalusy, and R. Graham, "Hydrodynamic excitations of Bose condensates in anisotropic traps," Phys. Rev. A **56**, R2533 (1997).

[102] L. You, W. Hoston, and M. Lewenstein, "Low-energy excitations of trapped Bose condensates," Phys. Rev. A **55**, R1581 (1997).

[103] F. Dalfovo, C. Minniti, S. Stringari, and L. Pitaevskii, "Nonlinear dynamics of a Bose condensed gas," Phys. Lett. A **227**, 259 (1997), 9612175 [cond-mat] .

[104] M. Fliesser, A. Csordás, R. Graham, and P. Szépfalusy, "Classical quasiparticle dynamics in trapped Bose condensates," Phys. Rev. A **56**, 4879 (1997).

[105] D. S. Jin, J. R. Ensher, M. R. Matthews, C. E. Wieman, and E. A. Cornell, "Collective excitations of a Bose-Einstein condensate in a dilute gas," Phys. Rev. Lett. **77**, 420 (1996).

[106] D. S. Jin, M. R. Matthews, J. R. Ensher, C. E. Wieman, and E. A. Cornell, "Temperature-dependent damping and frequency shifts in collective excitations of a dilute Bose-Einstein condensate," Phys. Rev. Lett. **78**, 764 (1997).

[107] M.-O. Mewes, M. Andrews, N. Van Druten, D. Kurn, D. Durfee, C. Townsend, and W. Ketterle, "Collective excitations of a Bose-Einstein condensate in a magnetic trap," Phys. Rev. Lett **77**, 988 (1996).

[108] L. Pitaevskii and S. Stringari, *Bose-Einstein condensation and superfluidity*, Vol. 164 (Oxford University Press, 2016).

[109] F. Dalfovo, C. Minniti, and L. P. Pitaevskii, "Frequency shift and mode coupling in the nonlinear dynamics of a Bose-condensed gas," Phys. Rev. A **56**, 4855 (1997), 9709010 [cond-mat] .

[110] S. Stringari, "Dynamics of Bose-Einstein condensed gases in highly deformed traps," Phys. Rev. A **58**, 2385 (1998).

[111] C. Menotti and S. Stringari, "Collective oscillations of a one-dimensional trapped Bose-Einstein gas," Phys. Rev. A **66**, 6 (2002).

[112] G. De Rosi and S. Stringari, "Collective oscillations of a trapped quantum gas in low dimensions," Phys. Rev. A **92**, 053617 (2015).

[113] W. Heathcote, E. Nugent, B. Sheard, and C. Foot, "A ring trap for ultracold atoms in an RF-dressed state," New J. Phys. **10**, 043012 (2008).

[114] G. Liu, D. W. Snoke, A. Daley, L. N. Pfeiffer, and K. West, "A new type of half-quantum circulation in a macroscopic polariton spinor ring condensate," Proc. Natl. Acad. Sci. U.S.A. **112**, 2676 (2015).

[115] J. A. Sauer, M. D. Barrett, and M. S. Chapman, "Storage ring for neutral atoms," Phys. Rev. Lett. **87**, 270401 (2001).

[116] K. Henderson, C. Ryu, C. MacCormick, and M. Boshier, "Experimental demonstration of painting arbitrary and dynamic potentials for Bose–Einstein condensates," New J. Phys. **11**, 043030 (2009).

[117] G. Sagnac, "L'éther lumineux démontré par l'effet du vent relatif d'éther dans un interféromètre en rotation uniforme," CR Acad. Sci. **157**, 708 (1913).

[118] A. D. Cronin, J. Schmiedmayer, and D. E. Pritchard, "Optics and interferometry with atoms and molecules," Rev. Mod. Phys. **81**, 1051 (2009).

[119] J. L. Helm, T. P. Billam, A. Rakonjac, S. L. Cornish, and S. A. Gardiner, "Spin-orbit-coupled interferometry with ring-trapped Bose-Einstein condensates," Phys. Rev. Lett. **120**, 063201 (2018).

[120] L. Amico, D. Aghamalyan, F. Auksztol, H. Crepaz, R. Dumke, and L. C. Kwek, "Superfluid qubit systems with ring shaped optical lattices," Sci. Rep. **4**, 4298 (2014).

[121] M. Herrera, T. M. Antonsen, E. Ott, and S. Fishman, "Echoes and revival echoes in systems of anharmonically confined atoms," Phys. Rev. A **86**, 023613 (2012).

[122] A. Bakman, H. Veksler, and S. Fishman, "Collapse and revival for a slightly anharmonic Hamiltonian," Phys. Lett. A **381**, 2298 (2017).

[123] R. G. Lena and A. J. Daley, "Dissipative dynamics and cooling rates of trapped impurity atoms immersed in a reservoir gas," Phys. Rev. A **101**, 033612 (2020).

[124] S. Mukherjee, D. M. Myers, R. G. Lena, B. Ozden, J. Beaumariage, Z. Sun, M. Steger, L. Pfeiffer, K. West, A. J. Daley, *et al.*, "Observation of nonequilibrium motion and equilibration in polariton rings," Phys. Rev. B **100**, 245304 (2019).

[125] C. J. Pethick and H. Smith, *Bose–Einstein condensation in dilute gases* (Cambridge university press, 2008).

[126] V. Bagnato, D. E. Pritchard, and D. Kleppner, "Bose-Einstein condensation in an external potential," Phys. Rev. A **35**, 4354 (1987).

[127] E. Fermi, "Sullo spostamento per pressione dei termini elevati delle serie spettrali (on the pressure displacement of higher terms in spectral series)," Nuovo Cimento **11**, 157 (1934).

[128] C. Cohen-Tannoudji, J. Dupont-Roc, and G. Grynberg, *Atom-photon interactions: basic processes and applications* (Wiley, New York, 1998) p. 678.

[129] H. Carmichael, *An open systems approach to quantum optics: lectures presented at the Université Libre de Bruxelles, October 28 to November 4, 1991*, Vol. 18 (Springer Science & Business Media, 2009).

[130] C. Gardiner, P. Zoller, and P. Zoller, *Quantum noise: a handbook of Markovian and non-Markovian quantum stochastic methods with applications to quantum optics*, Vol. 56 (Springer Science & Business Media, 2004).

[131] V. May and O. Kühn, *Charge and energy transfer dynamics in molecular systems*, Vol. 2 (Wiley Online Library, 2011).

[132] A. Nitzan, *Chemical dynamics in condensed phases: relaxation, transfer and reactions in condensed molecular systems* (Oxford university press, 2006).

[133] M. A. Nielsen and I. L. Chuang, "Quantum computation and quantum information," Phys. Today **54**, 60 (2001).

[134] A. Chin, J. Prior, R. Rosenbach, F. Caycedo-Soler, S. F. Huelga, and M. B. Plenio, "The role of non-equilibrium vibrational structures in electronic coherence and recoherence in pigment–protein complexes," Nat. Phys. **9**, 113 (2013).

[135] M. Desouter-Lecomte and X. Chapuisat, "Quantum-mechanical statistical theories for chemical reactivity: overlapping resonances," Phys. Chem. Chem. Phys. **1**, 2635 (1999).

[136] N. Michel, W. Nazarewicz, J. Okołowicz, and M. Płoszajczak, "Open problems in the theory of nuclear open quantum systems," J. Phys. G **37**, 064042 (2010).

[137] V. Gorini, A. Kossakowski, and E. C. G. Sudarshan, "Completely positive dynamical semigroups of N-level systems," J. Math. Phys. **17**, 821 (1976).

[138] G. Lindblad, "On the generators of quantum dynamical semigroups," Comm. Math. Phys. **48**, 119 (1976).

[139] H.-P. Breuer, F. Petruccione, *et al.*, *The theory of open quantum systems* (Oxford University Press on Demand, 2002).

[140] C. W. Gardiner and M. Collett, "Input and output in damped quantum systems: Quantum stochastic differential equations and the master equation," Phys. Rev. A **31**, 3761 (1985).

[141] M. Collett and C. Gardiner, "Squeezing of intracavity and traveling-wave light fields produced in parametric amplification," Phys. Rev. A **30**, 1386 (1984).

[142] J. Dalibard, Y. Castin, and K. Mølmer, "Wave-function approach to dissipative processes in quantum optics," Phys. Rev. Lett. **68**, 580 (1992).

[143] M. B. Plenio and P. L. Knight, "The quantum-jump approach to dissipative dynamics in quantum optics," Rev. Mod. Phys. **70**, 101 (1998).

[144] A. J. Daley, "Quantum trajectories and open many-body quantum systems," Adv. Phys. **63**, 77 (2014).

[145] G. Roati, F. Riboli, G. Modugno, and M. Inguscio, "Fermi-Bose quantum degenerate ^{40}K−^{87}Rb mixture with attractive interaction," Phys. Rev. Lett. **89**, 150403 (2002).

[146] M. Müller, S. Diehl, G. Pupillo, and P. Zoller, "Engineered open systems and quantum simulations with atoms and ions," in *Adv. Atom. Mol. Opt. Phys.*, Vol. 61 (Elsevier, 2012) pp. 1–80.

[147] A. J. Daley, "Quantum trajectories and open many-body quantum systems," Adv. Phys. **63**, 77 (2014).

[148] S. Diehl, A. Micheli, A. Kantian, B. Kraus, H. P. Büchler, and P. Zoller, "Quantum states and phases in driven open quantum systems with cold atoms," Nat. Phys. **4**, 878 (2008).

[149] B. Kraus, H. P. Büchler, S. Diehl, A. Kantian, A. Micheli, and P. Zoller, "Preparation of entangled states by quantum Markov processes," Phys. Rev. A **78**, 042307 (2008).

[150] F. Verstraete, M. M. Wolf, and J. Ignacio Cirac, "Quantum computation and quantum-state engineering driven by dissipation," Nat. Phys. **5**, 633 (2009).

[151] W. Yi, S. Diehl, A. J Daley, and P. Zoller, "Driven-dissipative many-body pairing states for cold fermionic atoms in an optical lattice," New J. Phys. **14**, 055002 (2012).

[152] V. D. Vaidya, J. Tiamsuphat, S. L. Rolston, and J. V. Porto, "Degenerate Bose-Fermi mixtures of rubidium and ytterbium," Phys. Rev. A **92**, 043604 (2015).

[153] C. Zipkes, S. Palzer, C. Sias, and M. Köhl, "A trapped single ion inside a Bose-Einstein condensate," Nature **464**, 388 (2010).

[154] S. Schmid, A. Härter, and J. H. Denschlag, "Dynamics of a cold trapped ion in a Bose-Einstein condensate," Phys. Rev. Lett. **105**, 133202 (2010).

[155] S. J. Schowalter, A. J. Dunning, K. Chen, P. Puri, C. Schneider, and E. R. Hudson, "Blue-sky bifurcation of ion energies and the limits of neutral-gas sympathetic cooling of trapped ions," Nat. Commun. **7**, 1 (2016).

[156] Z. Meir, T. Sikorsky, R. Ben-Shlomi, N. Akerman, Y. Dallal, and R. Ozeri, "Dynamics of a ground-state cooled ion colliding with ultracold atoms," Phys. Rev. Lett. **117**, 243401 (2016).

[157] G. Lamporesi, J. Catani, G. Barontini, Y. Nishida, M. Inguscio, and F. Minardi, "Scattering in mixed dimensions with ultracold gases," Phys. Rev. Lett. **104**, 153202 (2010).

[158] N. Spethmann, F. Kindermann, S. John, C. Weber, D. Meschede, and A. Widera, "Inserting single Cs atoms into an ultracold Rb gas," Appl. Phys. B **106**, 513 (2012).

[159] F. Schmidt, D. Mayer, T. Lausch, D. Adam, Q. Bouton, M. Hohmann, F. Kindermann, J. Koch, J. Nettersheim, and A. Widera, "Motional and spin dynamics of individual neutral impurities in an ultracold gas," Phys. Status Solidi B **256**, 1800710 (2019).

[160] H. Carmichael, "An open system approach to quantum optics, vol. m 18 of lecture notes in physics," (1993).

[161] S. Barnett and P. M. Radmore, *Methods in theoretical quantum optics*, Vol. 15 (Oxford University Press, 2002).

[162] A. B. Migdal, *Qualitative methods in quantum theory* (WA Benjamin, Inc., Reading, MA, 1977).

[163] W. Greiner, L. Neise, and H. Stocker, *Thermodynamics and Statistical Mechanics* (Springer, 1997).

[164] D. Jaksch, C. W. Gardiner, and P. Zoller, "Quantum kinetic theory. II. Simulation of the quantum Boltzmann master equation," Phys. Rev. A **56**, 575 (1997).

[165] J. Hope, G. Moy, M. Collett, and C. Savage, "Steady-state quantum statistics of a non-Markovian atom laser," Phys. Rev. A **61**, 023603 (2000).

[166] K. H. Madsen, S. Ates, T. Lund-Hansen, A. Löffler, S. Reitzenstein, A. Forchel, and P. Lodahl, "Observation of non-Markovian dynamics of a single quantum dot in a micropillar cavity," Phys. Rev. Lett. **106**, 233601 (2011).

[167] W. Coish and D. Loss, "Hyperfine interaction in a quantum dot: Non-Markovian electron spin dynamics," Phys. Rev. B **70**, 195340 (2004).

[168] J. Förstner, C. Weber, J. Danckwerts, and A. Knorr, "Phonon-assisted damping of Rabi oscillations in semiconductor quantum dots," Phys. Rev. Lett. **91**, 127401 (2003).

[169] H. Lee, Y.-C. Cheng, and G. R. Fleming, "Coherence dynamics in photosynthesis: protein protection of excitonic coherence," Science **316**, 1462 (2007).

[170] T. Yu and J. Eberly, "Sudden death of entanglement: classical noise effects," Opt. Commun. **264**, 393 (2006).

[171] M. P. Almeida, F. de Melo, M. Hor-Meyll, A. Salles, S. Walborn, P. S. Ribeiro, and L. Davidovich, "Environment-induced sudden death of entanglement," Science **316**, 579 (2007).

[172] B. Bellomo, R. L. Franco, and G. Compagno, "Non-Markovian effects on the dynamics of entanglement," Phys. Rev. Lett. **99**, 160502 (2007).

[173] S. Maniscalco, F. Francica, R. L. Zaffino, N. L. Gullo, and F. Plastina, "Protecting entanglement via the quantum Zeno effect," Phys. Rev. Lett. **100**, 090503 (2008).

[174] H. Stehfest, "Algorithm 368: Numerical inversion of Laplace transforms [D5]," Comm. ACM **13**, 47 (1970).

[175] F. Scazza, G. Valtolina, P. Massignan, A. Recati, A. Amico, A. Burchianti, C. Fort, M. Inguscio, M. Zaccanti, and G. Roati, "Repulsive Fermi polarons in a resonant mixture of ultracold Li 6 atoms," Phys. Rev. Lett. **118**, 083602 (2017).

[176] L. P. Pitaevskii, "Phenomenological theory of mode collapse-revival in a confined Bose gas," Phys. Lett. A **229**, 406 (1997).

[177] S. Morgan, S. Choi, K. Burnett, and M. Edwards, "Nonlinear mixing of quasiparticles in an inhomogeneous Bose condensate," Phys. Rev. A **57**, 3818 (1998).

[178] D. Stamper-Kurn, H.-J. Miesner, S. Inouye, M. Andrews, and W. Ketterle, "Collisionless and hydrodynamic excitations of a Bose-Einstein condensate," Phys. Rev. Lett. **81**, 500 (1998).

[179] O. Maragò, G. Hechenblaikner, E. Hodby, and C. Foot, "Temperature dependence of damping and frequency shifts of the scissors mode of a trapped Bose-Einstein condensate," Phys. Rev. Lett. **86**, 3938 (2001).

[180] F. Chevy, V. Bretin, P. Rosenbusch, K. W. Madison, and J. Dalibard, "Transverse breathing mode of an elongated Bose-Einstein condensate," Phys. Rev. Lett. **88**, 4 (2002).

[181] V. N. Popov and V. N. Popov, *Functional integrals and collective excitations* (Cambridge University Press, 1991).

[182] D. A. W. Hutchinson, E. Zaremba, and A. Griffin, "Finite temperature excitations of a trapped Bose gas," Phys. Rev. Lett. **78**, 1842 (1997).

[183] R. J. Dodd, M. Edwards, C. W. Clark, and K. Burnett, "Collective excitations of Bose-Einstein-condensed gases at finite temperatures," Phys. Rev. A **57**, R32 (1998).

[184] S. Giorgini, L. Pitaevskii, and S. Stringari, "Thermodynamics of a trapped Bose-condensed gas," J. Low Temp. Phys. **109**, 309 (1997).

[185] A. Minguzzi and M. Tosi, "Linear density response in the random-phase approximation for confined Bose vapours at finite temperature," J. Phys. Condens. Matter **9**, 10211 (1997).

[186] S. Giorgini, "Damping in dilute Bose gases: A mean-field approach," Phys. Rev. A **57**, 2949 (1998).

[187] P. Fedichev, G. Shlyapnikov, and J. Walraven, "Damping of low-energy excitations of a trapped Bose-Einstein condensate at finite temperatures," Phys. Rev. Lett. **80**, 2269 (1998).

[188] A. Csordás and R. Graham, "Collective excitations in Bose-Einstein condensates in triaxially anisotropic parabolic traps," Phys. Rev. A **59**, 1477 (1999).

[189] M. Desaix, D. Anderson, and M. Lisak, "Variational approach to collapse of optical pulses," JOSA B **8**, 2082 (1991).

[190] L. D. Landau and E. M. Lifshitz, *Mechanics (3rd edition)* (Butterworth-Heinemann, 1976).

[191] N. M. Krylov and N. N. Bogoliubov, *Introduction to non-linear mechanics*, 11 (Princeton University Press, 1949).

[192] R. W. Robinett, "Quantum wave packet revivals," Phys. Rep. **392**, 1 (2004).

[193] I. S. Averbukh and N. Perelman, "Fractional revivals: Universality in the long-term evolution of quantum wave packets beyond the correspondence principle dynamics," Phys. Lett. A **139**, 449 (1989).

[194] F. Großmann, J.-M. Rost, and W. P. Schleich, "Spacetime structures in simple quantum systems," J. Phys. A **30**, L277 (1997).

[195] I. Marzoli, F. Saif, I. Bialynicki-Birula, O. M. Friesch, A. E. Kaplan, and W. P. Schleich, "Quantum carpets made simple," Acta Phys. Slovaca **48**, 323 (1998).

[196] J. Crutchfield, D. Farmer, N. Packard, R. Shaw, G. Jones, and R. Donnelly, "Power spectral analysis of a dynamical system," Phys. Lett. A **76**, 1 (1980).

[197] E. Hanamura and H. Haug, "Condensation effects of excitons," Phys. Rep. **33**, 209 (1977).

[198] A. Imamoglu, R. Ram, S. Pau, Y. Yamamoto, *et al.*, "Nonequilibrium condensates and lasers without inversion: Exciton-polariton lasers," Phys. Rev. A **53**, 4250 (1996).

[199] J. Kasprzak, M. Richard, S. Kundermann, A. Baas, P. Jeambrun, J. Keeling, F. Marchetti, M. Szymańska, R. André, J. Staehli, *et al.*, "Bose-Einstein condensation of exciton polaritons," Nature **443**, 409 (2006).

[200] R. Balili, V. Hartwell, D. Snoke, L. Pfeiffer, and K. West, "Bose-Einstein condensation of microcavity polaritons in a trap," Science **316**, 1007 (2007).

[201] S. Christopoulos, G. B. H. Von Högersthal, A. Grundy, P. Lagoudakis, A. Kavokin, J. Baumberg, G. Christmann, R. Butté, E. Feltin, J.-F. Carlin, *et al.*,

"Room-temperature polariton lasing in semiconductor microcavities," Phys. Rev. Lett. **98**, 126405 (2007).

[202] S. Kéna-Cohen and S. Forrest, "Room-temperature polariton lasing in an organic single-crystal microcavity," Nat. Photonics **4**, 371 (2010).

[203] J. D. Plumhof, T. Stöferle, L. Mai, U. Scherf, and R. F. Mahrt, "Room-temperature Bose–Einstein condensation of cavity exciton–polaritons in a polymer," Nat. Mater. **13**, 247 (2014).

[204] A. Amo, J. Lefrère, S. Pigeon, C. Adrados, C. Ciuti, I. Carusotto, R. Houdré, E. Giacobino, and A. Bramati, "Superfluidity of polaritons in semiconductor microcavities," Nat. Phys. **5**, 805 (2009).

[205] K. G. Lagoudakis, M. Wouters, M. Richard, A. Baas, I. Carusotto, R. André, L. S. Dang, and B. Deveaud-Plédran, "Quantized vortices in an exciton–polariton condensate," Nat. Phys. **4**, 706 (2008).

[206] J. Hopfield, "Theory of the contribution of excitons to the complex dielectric constant of crystals," Phys. Rev. **112**, 1555 (1958).

[207] H. Deng, H. Haug, and Y. Yamamoto, "Exciton-polariton Bose-Einstein condensation," Reviews of Modern Physics **82**, 1489 (2010).

[208] T. Byrnes, N. Y. Kim, and Y. Yamamoto, "Exciton–polariton condensates," Nat. Phys. **10**, 803 (2014).

[209] D. Sanvitto and S. Kéna-Cohen, "The road towards polaritonic devices," Nat. Mater. **15**, 1061 (2016).

[210] Y. Sun, P. Wen, Y. Yoon, G. Liu, M. Steger, L. N. Pfeiffer, K. West, D. W. Snoke, and K. A. Nelson, "Bose-Einstein condensation of long-lifetime polaritons in thermal equilibrium," Phys. Rev. Lett. **118**, 016602 (2017).

[211] Y. Sun, Y. Yoon, M. Steger, G. Liu, L. N. Pfeiffer, K. West, D. W. Snoke, and K. A. Nelson, "Direct measurement of polariton–polariton interaction strength," Nat. Phys. **13**, 870 (2017).

[212] E. Estrecho, T. Gao, N. Bobrovska, D. Comber-Todd, M. Fraser, M. Steger, K. West, L. Pfeiffer, J. Levinsen, M. Parish, *et al.*, "Direct measurement of polariton-polariton interaction strength in the Thomas-Fermi regime of exciton-polariton condensation," Phys. Rev. B **100**, 035306 (2019).

[213] L. Pitaevskii, "Phenomenological theory of superfluidity near the l point," Sov. Phys.—JETP **8**, 282 (1959).

[214] M. Wouters and I. Carusotto, "Excitations in a nonequilibrium Bose-Einstein condensate of exciton polaritons," Phys. Rev. Lett. **99**, 140402 (2007).

[215] M. Wouters, T. Liew, and V. Savona, "Energy relaxation in one-dimensional polariton condensates," Phys. Rev. B **82**, 245315 (2010).

[216] M. Wouters, "Energy relaxation in the mean-field description of polariton condensates," New J. Phys. **14**, 075020 (2012).

[217] M. Suzuki, "Generalized Trotter's formula and systematic approximants of exponential operators and inner derivations with applications to many-body problems," Comm. Math. Phys. **51**, 183 (1976).

[218] J. Javanainen and J. Ruostekoski, "Symbolic calculation in development of algorithms: split-step methods for the Gross–Pitaevskii equation," J. Phys. A **39**, L179 (2006).